



The
University
Of
Sheffield.

**Investigation of Plasma Electrolytic Oxidation Processes
for Production of Porous Biocompatible Coatings on Ti
alloys**

By:

Wing Kiu Yeung

A thesis submitted in partial fulfilment of the requirements
for the degree of

Doctor of Philosophy

The University of Sheffield

Department of Materials Science and Engineering

March 2016

Abstract

Plasma electrolytic oxidation (PEO) attracts increasing interest in biomedical applications as it can form porous TiO₂ coatings incorporated with Ca and P on Ti alloy substrates. However, the formation of PEO coatings containing crystalline apatite phases using a single stage PEO process is difficult. The aim of the present study was two-fold. Firstly, to expand the cyclic voltammetry (CV) approach into high anodic potentials to achieve a better understanding of the electrochemical behaviour of Ti alloy electrodes under the conditions of PEO. Secondly, to develop a range of novel electrolytic plasma processes to produce biocompatible coatings for Ti implants.

Initially, the CV method was employed to identify characteristic potential ranges corresponding to differential behaviour of Ti alloy electrodes in the sodium orthophosphate electrolyte containing additives of Ca salts of various carboxylic acids. The two Ca salts have then been identified to be suitable for PEO electrolytes and during this progressive study a method to produce uniformly porous CaP containing PEO coatings using a single stage PEO treatment has been developed. Finally, this mode has been adopted for PEO treatments of Ti in electrolytes containing particulate additives of hydroxyapatite (HA).

Coatings produced were examined using scanning electron microscopy (SEM), electron dispersive spectroscopy, X-ray diffraction analysis and glow discharge optical emission spectroscopy. Minkowski functionals were used to analyse the morphological features in the surface-plane SEM images, which allowed subjective interpretation of the coating morphology to be eliminated. The proliferation and viability of human osteosarcoma (MG-63s) and mouse osteoblast (MC3T3-E1) cells cultured on selected PEO coatings were studied and showed these characteristics to be comparable to those of the cells cultured on tissue culture plastic control.

This study has substantially expanded the understanding of electrochemical processes that occur during the PEO treatment of Ti and broadened the range of electrolytes for production of apatite containing PEO coatings for orthopaedic and orthodontic implant applications. These results provide a benchmark against which further work investigating different aspects of PEO processing of Ti and other materials could be undertaken.

Acknowledgements

I would firstly like to thank both my supervisors Dr. Aleksey Yerokhin and Dr. Gwen Reilly for giving me the opportunity to undertake this project and for their guidance, support, patience and encouragement.

I would like to thank my PhD financial sponsor, the Engineering and Physical Science Research Council (EPSRC), which out I would not have been able to carry out this research.

Parts of the work related to evaluation of hydroxyapatite-titania films produced in electrolytes with particle additions (Chapter 7) have been performed within the framework of collaborative research projects with the IDIR Institute at the University of Windsor (Canada), Department of Powder Metallurgy and Functional Coatings at NUST 'MISiS' and Blokhin Cancer Research Centre (both Moscow, Russia). I would like to thank researchers at these organisations, D. Dzhurinskiy, I.V. Sukhorukova, D.V. Shtansky, E.A. Levashov, I.Y. Zhitnyak, N.A. Gloushankova, P.V. Kiryukhantsev-Korneev, M.I. Petrzhik for their help with coating characterisation and useful discussions.

I would also like to thank Dr. Julian Dean for his help with FEM modelling, which enabled me to develop a better understanding of electric field distribution in PEO coatings.

My gratitude also goes to members of the Research Centre in Surface Engineering (Dr. Chen-Jui Liang, Dr. Yonghao Gao, Mr Ming Sun, Mr Jack Cooper, Mr Xingguan Liu, Mr Chang Liu, Mr Lian Liu) and members from INSIGNEO Institute (Dr. Sasima Puwunan and Mr Robert Owen). My sincere thanks also goes to my friends Mr Daniel Yip, Mr Alexander Bayntun-Lees, Mr Christopher Spencer for putting up with me and providing so much help over these years. I would like to thank my family for their understanding, I appreciate everything they have done for me.

I would like to thank Dr. Yerokhin again, you have been so supportive and patience of me from the start, and I am really grateful for giving me this opportunity

Contents

| | |
|--|-----------|
| ABSTRACT..... | 1 |
| ACKNOWLEDGEMENTS | 2 |
| CONTENTS..... | 3 |
| FIGURE CAPTIONS..... | 6 |
| TABLE CAPTIONS..... | 15 |
| CHAPTER 1: INTRODUCTION..... | 17 |
| 1.1 AIM AND OBJECTIVES..... | 17 |
| 1.2 THESIS OVERVIEW | 18 |
| CHAPTER 2: LITERATURE REVIEW | 20 |
| 2.1 THE PLASMA ELECTROLYTIC OXIDATION PROCESS..... | 20 |
| 2.2 DEVELOPMENT OF PEO PROCESS | 20 |
| 2.3 PHYSICAL AND CHEMICAL FUNDAMENTALS OF PEO PROCESS..... | 21 |
| 2.4 DISCHARGE PHENOMENA | 25 |
| 2.5 THE EFFECT OF ELECTRO-PHYSICAL AND CHEMICAL PROPERTIES OF ELECTROLYTE TO PEO TREATMENT | 26 |
| 2.6 EFFECT OF ELECTROLYTE COMPOSITION | 27 |
| 2.6.1 ELECTROLYTES PROVIDING ANIONIC AND CATIONIC COMPONENTS INTO THE COATING..... | 28 |
| 2.6.2 SUSPENSIONS PROVIDING PARTICLES THAT CONTRIBUTE TO THE COATING COMPOSITION | 33 |
| 2.7 INFLUENCE OF ALLOY COMPOSITION | 38 |
| 2.8 INFLUENCE OF POWER SOURCE | 39 |
| 2.8.1 GALVANOSTATIC AND POTENTIOSTATIC REGIMES..... | 39 |
| 2.8.2 EFFECTS OF ELECTRICAL PARAMETERS | 39 |
| 2.8.2.1 DC AND PULSED DC MODE | 40 |
| 2.8.2.2 AC AND PBP MODES | 41 |
| 2.9 ANALYSIS OF PEO SURFACE MORPHOLOGY | 42 |
| 2.10 SUMMARY ON PEO | 44 |
| CHAPTER 3: MATERIALS AND GENERAL METHODS | 45 |
| 3.1 MATERIALS | 45 |
| 3.2 GENERAL METHODS | 45 |
| 3.2.1 PEO TREATMENT EQUIPMENT..... | 45 |
| 3.2.2 COATING CHARACTERISATION..... | 47 |
| 3.2.2.1 MEASUREMENT OF COATING THICKNESS AND SURFACE ROUGHNESS..... | 47 |
| 3.2.2.2 X-RAY DIFFRACTION ANALYSIS..... | 47 |
| 3.2.2.3 ANALYSIS OF COATING MORPHOLOGY AND ELEMENTAL COMPOSITION | 48 |

| | | |
|---------|---------------------------------------|----|
| 3.2.3.4 | ASSESSING CELL VIABILITY | 51 |
| 3.2.3.5 | ALKALINE PHOSPHATASE (ALP) ASSAY..... | 51 |
| 3.2.3.6 | MORPHOMETRIC ANALYSIS | 52 |
| 3.2.4 | STATISTICAL ANALYSIS..... | 52 |

CHAPTER 4: EFFECT OF CALCIUM SALTS IN THE ELECTROLYTE ON THE CHARACTERISTICS OF PEO PROCESS AND RESULTING COATINGS.....53

| | | |
|-------|---|----|
| 4.1 | INTRODUCTION | 53 |
| 4.2 | RESULTS | 58 |
| 4.2.1 | INFLUENCE OF CALCIUM SALT TO THE ELECTROLYTE CHARACTERISTICS..... | 58 |
| 4.2.2 | INFLUENCE OF CALCIUM SALT IN THE ELECTROLYTE TO THE CYCLIC VOLTAMMETRY BEHAVIOUR OF Ti ANODES | 59 |
| 4.2.3 | EFFECT OF CALCIUM SALT TO THE COATING MORPHOLOGY AND ELEMENTAL COMPOSITION | 65 |
| 4.3 | DISCUSSION | 69 |
| 4.3.1 | INFLUENCE OF SUBSTRATE ALLOYING TO THE CHEMICAL REACTIONS DURING THE PEO TREATMENT | 69 |
| 4.3.2 | ANODIC OXIDATION OF VARIOUS CALCIUM SALT SOLUTION DURING THE PEO TREATMENT..... | 71 |
| 4.4 | SUMMARY | 75 |

CHAPTER 5: PEO TREATMENTS OF Ti ALLOYS IN THE CALCIUM PROPIONATE CONTAINING ELECTROLYTES AND RESULTING COATINGS .76

| | | |
|--------|---|-----|
| 5.1 | INTRODUCTION | 76 |
| 5.2 | RESULTS AND DISCUSSION..... | 76 |
| 5.2.1 | INFLUENCE OF CALCIUM PROPIONATE CONCENTRATION TO ELECTROLYTE CHARACTERISTICS AND CYCLIC VOLTAMMETRY BEHAVIOUR OF Ti ANODES | 76 |
| 5.2.2 | INFLUENCE OF CALCIUM PROPIONATE CONCENTRATION IN THE ELECTROLYTE TO THE COATING PHASE COMPOSITION AND SURFACE MORPHOLOGY. | 81 |
| 5.2.3 | SUMMARY..... | 85 |
| 5.2.4 | APPLICATION OF CV METHOD TO UNDERSTAND THE COATING FORMATION MECHANISM | 86 |
| 5.2.5 | OPTIMISATION OF ELECTRICAL PARAMETERS USING CP-Ti SUBSTRATE | 93 |
| 5.2.7 | INFLUENCE OF NEGATIVE BIAS TO THE COATING CHARACTERISTICS..... | 105 |
| 5.2.8 | UNDERSTANDING AND EXPLORING THE APPLICATION OF THE CALCIUM PROPIONATE BASED ELECTROLYTE TO THE TREATMENTS OF Ti-6Al-4V ALLOY..... | 111 |
| 5.2.9 | APPLICATION OF THE TWO-STEP CONTROL PEO PROCESS..... | 114 |
| 5.2.10 | IN VITRO EXPERIMENTS FOR COATINGS PRODUCED USING CALCIUM PROPIONATE BASED ELECTROLYTE | 119 |
| 5.2.11 | IN VITRO BIOLOGICAL RESPONSE OF COATINGS PRODUCED USING CALCIUM PROPIONATE BASED ELECTROLYTE | 122 |
| 5.3 | CONCLUSION | 123 |

CHAPTER 6: PEO TREATMENTS OF Ti ALLOYS IN THE CALCIUM L-LACTATE CONTAINING ELECTROLYTE AND RESULTING COATINGS.....124

| | | |
|---|---|------------|
| 6.1 | INTRODUCTION | 124 |
| 6.2 | RESULTS AND DISCUSSION..... | 124 |
| 6.2.1 | INFLUENCE OF CALCIUM L-LACTATE CONCENTRATION TO ELECTROLYTE CHARACTERISTICS AND CYCLIC VOLTAMMETRY BEHAVIOUR OF Ti ANODES | 124 |
| 6.2.2 | APPLICATION OF GALVANOSTATIC MODE TO PEO TREATMENTS OF CP-Ti SUBSTRATE IN CALCIUM L-LACTATE ELECTROLYTE..... | 128 |
| 6.2.3 | PEO PROCESS AND COATING OPTIMISATION..... | 131 |
| 6.2.3.1 | THE CHARACTERISTICS OF COATING GROWTH BEHAVIOUR UNDER THE TWO-STEP CONTROL METHOD | 131 |
| 6.2.3.2 | EFFECTS OF CURRENT DENSITY TO THE COATING MORPHOLOGY AND PHASE COMPOSITION..... | 136 |
| 6.2.3.3 | EFFECT OF Ca/P RATIO IN THE ELECTROLYTE TO THE COATING GROWTH BEHAVIOUR..... | 140 |
| 6.2.4 | FORMATION OF HA CONTAINING PEO COATING..... | 149 |
| 6.2.5 | UNDERSTANDING SUBSTRATE EFFECTS AND EXPLORING THE APPLICATION OF CALCIUM L-LACTATE ELECTROLYTE FOR PEO TREATMENT OF Ti-6Al-4V ALLOY | 154 |
| 6.2.6 | IN VITRO EXPERIMENTS FOR COATINGS PRODUCED USING CALCIUM L-LACTATE BASED ELECTROLYTE | 159 |
| 6.2.7 | IN VITRO BIOLOGICAL RESPONSE OF COATINGS PRODUCED USING CALCIUM L-LACTATE BASED ELECTROLYTE | 164 |
| 6.3 | CONCLUSIONS | 165 |
| | | |
| CHAPTER 7: PEO TREATMENT OF Ti ALLOYS IN HA CONTAINING ELECTROLYTE | | 166 |
| 7.1 | INTRODUCTION | 166 |
| 7.2 | RESULTS | 166 |
| 7.2.1 | UNDERSTANDING THE USE OF DISODIUM PHOSPHATE BASED ELECTROLYTE TO CYCLIC VOLTAMMETRY BEHAVIOUR OF Ti-6Al-4V ANODE | 166 |
| 7.2.2 | EFFECT OF CONTROL MODES ON THE PEO PROCESS..... | 169 |
| 7.2.3 | INFLUENCE OF HA MICRO-POWDER ADDITION TO THE COATING CHARACTERISTICS | 174 |
| 7.2.4 | EFFECTS OF THE NEGATIVE BIAS TO THE COATING CHARACTERISTICS | 182 |
| 7.3 | CONCLUSION | 189 |
| 7.4 | THE EFFECT OF HA NANO-POWDER ADDITION IN THE ELECTROLYTE TO THE COATING CHARACTERISTICS | 189 |
| 7.4.1 | RESULTS AND DISCUSSION | 190 |
| 7.4.2 | INFLUENCE OF HA PARTICLE SIZE TO THE BIOLOGICAL PROPERTIES OF PEO COATINGS..... | 195 |
| 7.5 | CONCLUSION | 204 |
| | | |
| CHAPTER 8: CONCLUSIONS AND FUTURE WORK..... | | 206 |
| 8.1 | CONCLUSIONS | 206 |
| 8.2 | FUTURE WORK..... | 208 |
| | | |
| REFERENCE..... | | 210 |

Figure Captions

| | |
|---|----|
| Figure 1 Current-Voltage diagram for the discharge phenomena during PEO process. [8].... | 23 |
| Figure 2 Schematic of the voltage transient with subsequent discharge phenomena and coating microstructure developed during PEO process. [9] | 24 |
| Figure 3 Surface morphology of TiO ₂ implant by TiUnite..... | 28 |
| Figure 4 Surface morphology of PEO coatings (a) as formed and (b) after hydrothermal treatment at 190°C for 15h. [50] | 31 |
| Figure 5 Surface morphology of PEO coating formed on Ti-6Al-4V alloy in the electrolyte containing calcium acetate monohydrate and β-glycerophosphate. [51]..... | 32 |
| Figure 6 Visual inspection of the coatings produced from electrolytes with Sr/(Sr + Ca) ratios of (a) 0%, (b) 3%, (c) 7%, (d) 15%, (e) 25%, (f) 50%, (g) 75%, and (h) 100%. [57] | 33 |
| Figure 7 Surface morphology of the coating produced on cp-Ti substrate in the electrolyte with HA powder addition. [62]..... | 36 |
| Figure 8 Schematic diagram of electrical waveforms commonly used in PEO research | 40 |
| Figure 9 Schematic diagram of the PEO system. | 46 |
| Figure 10 Skeletal structure of the calcium salts considered in this study. | 55 |
| Figure 11 Cyclic voltammogram of cp-Ti and Ti-6Al-4V substrate in calcium formate and acetate based electrolytes, the direction of arrow represent the direction of scan. | 59 |
| Figure 12 Cyclic voltammogram of cp-Ti and Ti-6Al-4V substrate in calcium propionate and L-lactate based electrolytes, the direction of the arrow represent the direction of scan. | 60 |
| Figure 13 XRD spectra of coatings formed in calcium formate, acetate, propionate and L-lactate based electrolytes on (a) cp-Ti and (b) Ti-6Al-4V substrates. (A, anatase; R, rutile; Ti, titanium and alloy; T, tri-calcium phosphate; CT, calcium titanate; H, hydroxyapatite) | 63 |
| Figure 14 Surface morphology of coatings produced on cp-Ti and Ti-6Al-4V substrates in calcium formate and acetate based electrolytes. | 66 |

| | |
|--|----|
| Figure 15 Surface morphology of coatings produced on cp-Ti and Ti-6Al-4V substrates in calcium propionate and L-lactate based electrolytes. | 67 |
| Figure 16 Cyclic voltammogram of cp-Ti and Ti-6Al-4V anodes in the sodium orthophosphate electrolyte with various calcium propionate content, directions of arrows represent the direction of scan. | 78 |
| Figure 17 XRD spectra of coatings formed on cp-Ti substrate in calcium propionate containing electrolytes with different Ca/P ratios; (a) 0.5, (b) 1, (c) 1.67 and (d) 2. (A is anatase; R is rutile; Ti is titanium; H is hydroxyapatite; T is tri-calcium phosphate) | 81 |
| Figure 18 Surface and cross-sectional morphology of coatings produced on cp-Ti substrate using calcium propionate electrolytes with Ca/P ratios of (a, e) 0.5, (b,f) 1, (c,g) 1.67 and (d,h) 2..... | 83 |
| Figure 19 Visual inspection of coatings produced on cp-Ti substrate by 3 min PEO treatment in the calcium propionate electrolyte at 440, 450 and 460 V. | 88 |
| Figure 20 SEM micrograph of PEO coatings produced on cp-Ti substrate in calcium propionate based electrolyte with Ca/P ratio 1.67 at 440 V (a,d), 450 V (b,e) and 460 V (c,f) in Ca/P 1.67 for 3 mins. | 88 |
| Figure 21 Surface EDX spectrum of the coating formed on cp-Ti substrate in the calcium propionate based electrolyte with Ca/P ratio of 1.67 at 450 V for 3min. | 90 |
| Figure 22 An SEM image of the coating produced in the calcium propionate based electrolyte with Ca/P=1.67 for 3 min and the elemental composition of the doughnut-like shape feature. | 92 |
| Figure 23 XRD spectra of coatings on cp-Ti substrate produced at 440 and 450V in the calcium propionate electrolyte with Ca/P ratio of 1.67 for 3 min. (A, anatase; R, rutile; Ti, titanium; H hydroxyapatite)..... | 92 |
| Figure 24 Typical examples of (a) pulsed unipolar voltage waveforms with duty cycles set at 90, 50 and 20% and corresponding current signals for voltage pulse magnitudes. | 95 |

Figure 25 Current density transients recorded during PEO treatments of cp-Ti in the calcium propionate based electrolyte with Ca/P=1.67 using PUP voltage with various duty cycles and magnitude set at (a) 450V and (b) 460V.....96

Figure 26 XRD spectra of coatings produced using pulsed unipolar mode (a) 450V and (b) 460V in calcium propionate electrolyte with Ca/P ratio set at 1.67 with various duty cycles. (A, anatase; R, rutile; Ti, titanium and alloy; H, hydroxyapatite; T, tricalcium phosphate) ...97

Figure 27 SEM micrographs of coatings produced using pulsed unipolar voltage mode (V+=450V) with duty cycles of (a,d) 90, (b,e) 50 and (c,f) 20% and corresponding Minkowski functionals (g-i) C(ρ), L(ρ)X5 and E(ρ)X10. 102

Figure 28 SEM micrographs of coatings produced using pulsed unipolar voltage mode (V+=460V) with duty cycles of (a,d) 90, (b,e) 50 and (c,f) 20% and respective Minkowski functionals (g-i) C(ρ), L(ρ)X5 and 10E(ρ)X10..... 103

Figure 29 Typical examples of pulsed bipolar voltage waveform with frequency set at (a) 300 and (c) 450 Hz and corresponding current signals for voltage pulse magnitudes. 105

Figure 30 Current transients recorded during PEO treatments of cp-Ti substrate in the calcium propionate electrolyte with Ca/P ratio of 1.67 using the PBP voltage mode with pulse frequencies of 300 and 450Hz. 106

Figure 31 XRD spectra of coatings produced on cp-Ti substrate by PBP PEO treatments in the calcium propionate based electrolyte with Ca/P=1.67 at various pulse frequencies. (A, anatase; R, rutile; Ti, titanium; H, hydroxyapatite; C, calcium carbonate) 107

Figure 32 SEM micrographs of coatings produced on cp-Ti substrate by PBP PEO treatments in the calcium propionate based electrolyte with Ca/P=1.67 at voltage pulse frequencies of (a, b) 300Hz and (c,d) 450Hz..... 109

Figure 33 Cyclic voltammograms of Ti-6Al-4V anode in the calcium propionate based electrolytes with various Ca/P ratios and corresponding SEM images of coatings produced at different voltages. 113

Figure 34 Current and voltage transients recorded during the two-step PEO treatment of Ti-6Al-4V substrate in the calcium propionate based electrolyte, with stage I carried out at 250V and stage II – at 50 mA/cm², for various times..... 115

Figure 35 XRD spectra of coatings produced on Ti-6Al-4V substrate using the two-step control method in the calcium propionate electrolyte with Ca/P ratio of 1.67. (A is anatase, R is rutile, Ti is titanium alloy and C is calcium carbonate) 116

Figure 36 Surface plane SEM images of the PEO coating on Ti-6Al-4V substrate produced at 250V for 15s. 117

Figure 37 SEM micrographs of coatings produced on Ti-6Al-4V substrate using the two-step control method with treatment times set at 5(c) and 10 min (d), with respective Minkowski functionals (c,d) C(ρ), 5L(ρ) and 10E(ρ). 118

Figure 38 The mean average surface roughness of PEO coatings produced for biological examination (* $p > 0.005$, indicating statistically significant difference from both CP1 and CP2, n=3)..... 120

Figure 39 SEM micrographs of coatings produced on cp-Ti substrate in calcium propionate electrolyte selected for in vitro assays with respective Minkowski functionals C(ρ), L(ρ)X5 and E(ρ)x10..... 121

Figure 40 Viability of MG63 cells on the PEO coatings assessed using PrestoBlue assay at days 1 and 21. The resulting PrestoBlue stain was measured at 590nm. * indicates statistically significant difference ($p < 0.05$) from CP 1, CP 2 and tissue culture plastic control. (n=3) .. 122

Figure 41 Cyclic voltammogram of cp-Ti and Ti-6Al-4V anodes in sodium phosphate electrolyte with varied calcium L-lactate content. The direction of arrows represent the direction of scan..... 125

Figure 42 Voltage transient recorded during galvanostatic treatments of cp-Ti substrate in calcium L-lactate electrolyte with Ca/P ratio of 2 with different current densities. The inset shows a part of the cyclic voltammogram highlighting the corresponding region examined. 129

Figure 43 XRD spectra of PEO coatings produced on cp-Ti substrates for 3min in the calcium L-lactate electrolyte with Ca/P ratio of 2 using a galvanostatic DC mode with different current densities. (A, anatase; R, rutile; Ti, titanium and alloy; H, hydroxyapatite)..... 130

Figure 44 Voltage and current transients recorded during PEO treatments of cp-Ti using the two-step control method in the calcium L-lactate electrolyte with Ca/P 1.67 at the current density of 100 mA/cm² during Stage II with various treatment time. 132

Figure 45 XRD spectra of coatings produced in two-step control method on cp-Ti substrate in the calcium L-lactate electrolyte with Ca/P=1.67 at current density of 100 mA/cm² during Stage II of the treatment with different treatment times. (A, anatase; R, rutile; Ti, titanium and alloy; H, hydroxyapatite) 133

Figure 46 An image of a typical coating produced on cp-Ti substrate in the calcium L-lactate electrolyte with Ca/P=1.67 with treatment time above 7 min. 135

Figure 47 SEM micrographs of coatings produced using two-step control method on cp-Ti substrate in the calcium L-lactate electrolyte with Ca/P ratio of 1.67 at the current density of 100mA/cm² during Stage II at different treatment times and respective Minkowski functionals C(ρ), L(ρ)X5 and E(ρ)x10..... 136

Figure 48 Voltage and current transients recorded during PEO treatments of cp-Ti using the two-step control method in the calcium L-lactate electrolyte with Ca/P=1.67 for 7 min at various current densities during Stage II of the treatment. 137

Figure 49 XRD spectra of cp-Ti with PEO coatings produced in two-step control method in the calcium L-lactate electrolyte with Ca/P=1.67 for 7 min at the current density of (a) 50, (b) 60 and (c) 100 mA/cm² during Stage II of the treatment. (A, anatase; R, rutile; Ti, titanium and alloy; H, hydroxyapatite; T, tricalcium phosphate) 138

Figure 50 An SEM micrograph of the coating produced using the two-step control method on cp-Tii substrate in the calcium L-lactate electrolyte with Ca/P ratio of 1.67 at current density of 60 mA/cm² and respective Minkowski functionals C(ρ), L(ρ)X5 and E(ρ)x10..... 139

Figure 51 SEM micrographs of coatings produced in the calcium L-lactate electrolyte on the cp-Ti substrate at stage I using DC potentiostatic mode at 250V for 15s..... 142

Figure 52 Voltage and current transients recorded during PEO treatments using the two-step control method on cp-Ti substrate in the calcium L-lactate electrolytes with Ca/P ratio 2 at current density of 100 mA/cm² during Stage II carried out for (a) 3, (b) 5 (c) 6 and (d) 10 min.143

Figure 53 The mean average value of surface roughness of PEO coatings produced with various treatment time. (**p* <0.05, indicating statistically difference from coating produced in 3 min).....143

Figure 54 XRD spectra of PEO coatings produced on cp-Ti substrate using the two-step control method in the calcium L-lactate electrolyte with Ca/P ratio 2 at the current density of 100 mA/cm² during Stage II for different treatment times. (A, anatase; R, rutile; Ti, titanium H, hydroxyapatite)144

Figure 55 SEM micrographs of PEO coatings on cp-Ti substrate produced using the two-step control method in the calcium L-lactate electrolyte with Ca/P ratio 2 at the current density of 100 mA/cm²during Stage II for various treatment times and respective Minkowski functionals C(ρ), L(ρ)X5 and E(ρ)x10.....146

Figure 56 Higher-magnification surface-plane images of coatings shown in Figure 54.147

Figure 57 Voltage and current transients recorded during 10 min PEO treatments of cp-Ti with the two-step control method in the calcium L-lactate electrolyte with Ca/P=2 at the current densities of 50 and 100 mA/cm² during Stage II of the treatment.151

Figure 58 XRD spectra of coating produced on cp-Ti substrate using the two-step control PEO treatment for 10 min in the calcium L-lactate electrolyte with Ca/P=2 at the current density of 50 mA/cm². (A, anatase; R, rutile; Ti, titanium and alloy; H, hydroxyapatite) ..152

Figure 59 SEM micrographs of coatings produced using two-step control method of cp-Ti substrate in the calcium L-lactate electrolyte with Ca/P ratio 2 for 10 min at the current density of 50 mA/cm² during Stage II and respective Minkowski functionals C(ρ), L(ρ)X3 and E(ρ)x5.....153

Figure 60 Voltage and current transients recorded during PEO treatments of the Ti-6Al-4V substrate using the two-step control method in the calcium L-lactate electrolyte with Ca/P=2 at the current density of 100 mA/cm² during Stage II for different durations.154

Figure 61 XRD spectra of Ti-6Al-4V samples with PEO coatings produced using the two-step control method in the calcium L-lactate electrolyte with Ca/P=2 at current density of 100mA/cm² for various times. (A, anatase; R, rutile; Ti, titanium and alloy; H, hydroxyapatite) 156

Figure 62 SEM micrographs of PEO coatings produced on Ti-6Al-4V using the two-step control method in the calcium L-lactate electrolyte with Ca/P=2 at the current density of 100 mA/cm² for various times. 158

Figure 63 Visual inspection of coating produced on cp-Ti substrate in the calcium L-lactate electrolyte used for biological assessment. 160

Figure 64 The mean average surface roughness of the A-TiO₂, B-TiO₂ and CaP PEO coatings. (**p* < 0.05, indicating statistically difference from the B-TiO₂ and CaP PEO coating, n=3) 161

Figure 65 SEM micrographs of coatings produced on cp-Ti substrate in calcium L-lactate electrolyte selected for *in vitro* assays with respective Minkowski functionals C(ρ), L(ρ)X5 and E(ρ)x10..... 162

Figure 66 Cell viability on coatings and tissue culture plastic (TCP) control at day 1 and 21 using PrestoBlue, measuring at 590nm. (n = 3)..... 164

Figure 67 Cyclic voltammogram of Ti-6Al-4V anode in 6g/L Na₂HPO₄ electrolyte, the directions of arrows represent the direction of scan. 167

Figure 68 Voltage transients recorded during DC PEO treatments of Ti-6Al-4V alloy in 6g/L Na₂HPO₄ electrolyte at different current densities. 168

Figure 69 Oscillograms of pulsed unipolar and pulsed bipolar current output used in PEO treatment. 170

Figure 70 Voltage and current transients recorded during pulsed current PEO treatments of Ti-6Al-4V in 6g/L Na₂HPO₄ electrolyte containing 10g/L of HA micro-powder, with anodic current density set at 35 mA/cm² (a) pulsed unipolar mode and (b) pulsed bipolar mode with cathodic current density of 11.7 mA/cm². 171

| | |
|---|-----|
| Figure 71 SEM micrographs of coatings produced by pulsed current PEO treatments with anodic current density of 35 mA/cm ² : (a) – pulsed unipolar mode; (b) – pulsed bipolar mode with cathodic current density of 11.7 mA/cm ² ; (c,d) – respective Minkowski functionals(c,d) C(ρ), L(ρ)X5 and E(ρ)X10. | 172 |
| Figure 72 A typical EDX spectrum of the studied PEO coatings..... | 173 |
| Figure 73 Voltage and current transients recorded during PEO treatments of Ti-6Al-4V alloy using pulsed bipolar current treatment in the 6g/L Na ₂ HPO ₄ electrolyte containing 10g/L (solid line), 20g/L (dotted line) and 30g/L (broken line) of HA..... | 176 |
| Figure 74 The mean average values of thickness (a) and surface roughness (b) for PEO coatings produced in electrolytes with 10g/L, 20g/L and 30g/L HA micro-powder addition. (* p<0.05)..... | 177 |
| Figure 75 SEM micrographs of PEO coatings produced in 6g/L Na ₂ HPO ₄ electrolyte with (a) 10g/L (b) 20g/L and (c) 30g/L addition of HA micro-powder and the respective Minkowski functionals (d-f) C(ρ), 5L(ρ) and 10E(ρ). | 178 |
| Figure 76 (a) Schematic representation of the FEM model of the metal-oxide electrolyte system, (b) typical electric field distribution at 2 kHz, (c) frequency dependence of the ratio of minimum to maximum current density at the electrolyte-oxide interface and (d) current density distributions in the surface layer at different frequencies. | 181 |
| Figure 77 Voltage and current transients recorded during PEO treatments of Ti-6Al-4V alloy in the 6g/L Na ₂ HPO ₄ electrolyte containing 30g/L HA micro-powder addition using pulsed bipolar current treatment with various negative duty cycles at step II. | 184 |
| Figure 78 Images of coating produced using PBP PEO treatments with negative duty cycles of 4% and 10%..... | 184 |
| Figure 79 The mean average value of thickness (a) and surface roughness (b) of PEO coatings produced on Ti-6Al-4V substrate using the two-step control method, with the negative duty cycle set at 4%, 10% and 16% during step II. (* p<0.05)..... | 186 |
| Figure 80 SEM micrographs of coatings produced on Ti-6Al-4V substrate in the electrolyte with 30g/L HA micro-powder addition using the two-step control method, with the negative | |

| | |
|---|-----|
| duty cycle set at (a) 4%, (b) 10% and (c) 16% during the step II, with respective Minkowski functions (d-f) C(ρ), 5L(ρ) and 10E(ρ). | 187 |
| Figure 81 Voltage and current transients recorded during PEO treatments of Ti-6Al-4V alloy using the pulsed bipolar current mode in the 6g/L Na ₂ HPO ₄ electrolyte containing 10 and 15 g/L HA nano-powder additions. | 191 |
| Figure 82 Surface morphology of coatings produced on Ti-6Al-4V substrate using the two-step control PEO mode in the electrolyte with 10g/L HA nano-powder addition. | 193 |
| Figure 83 A SEM and backscattered electron micrograph of the coating produced on Ti-6Al-4V substrate using the two-step control PEO mode in the electrolyte with 15g/L HA nano-powder addition. | 193 |
| Figure 84 SEM micrographs of (a) TiO ₂ (b) TiO ₂ + μ HA and (c) TiO ₂ + nHA PEO coatings with respective Minkowski functionals C(ρ), 5L(ρ) and 10E(ρ). | 197 |
| Figure 85 The mean average values of surface roughness of TiO ₂ , TiO ₂ + μ HA and TiO ₂ + nHA coatings. * means comparison with TiO ₂ + μ HA coatings and showed $p < 0.05$; + means comparison to TiO ₂ +nHA showed $p < 0.05$. (Data is mean \pm SD, n=3) | 199 |
| Figure 86 GDOES profiles of selected elements in the (a) TiO ₂ (b) TiO ₂ + μ HA, and (c) TiO ₂ +nHA coatings. | 200 |
| Figure 87 Biocompatibility of coatings (a) Morphometric analysis of MC3T3-E1 cells after 24h in culture on control and PEO coated surfaces. Projected mean cell area from 30 cells on random fields. (b) ALP activity of cells cultured for 14 days on surfaces of TiO ₂ , TiO ₂ + μ HA and TiO ₂ + nHA. * means comparison with control and shown $p < 0.05$; + means comparison to TiO ₂ +nHA and shown $p < 0.05$. | 203 |

Table Captions

| | |
|--|-----|
| Table 1 Composition of Ti alloys used in this experiment. | 45 |
| Table 2 List of calcium salts of interest. | 54 |
| Table 3 The effect of calcium salt in the electrolyte to the electrolyte properties. | 58 |
| Table 4 Relative atomic percentages of elements on the surface of the coatings produced on (a) cp-Ti and (b) Ti-6Al-4V substrates. | 68 |
| Table 5 Effects of calcium propionate concentration to electrolyte properties. | 76 |
| Table 6 The peak locations deduced from the cyclic voltammogram of cp-Ti and Ti-6Al-4V anodes in Figure 1 with different Ca/P ratios in the electrolyte. | 79 |
| Table 7 Relative atomic percentages of elements in the surface of the PEO coatings produced using electrolytes with various Ca/P ratios. | 85 |
| Table 8 Relative atomic percentages of elements in the surfaces of PEO coatings produced in the calcium propionate based electrolyte with Ca/P=1.67 at 440, 450 and 460 V for 3 min. . | 91 |
| Table 9 Chemical composition of PEO coatings produced at different duty cycles. | 104 |
| Table 10 Relative atomic percentages of elements in the surfaces of PEO coatings produced on cp-Ti substrate in the calcium propionate based electrolyte with Ca/P=1.67 at various frequencies. | 110 |
| Table 11 Processing conditions of Ti-6Al-4V substrates selected for <i>in vitro</i> assessment. .. | 119 |
| Table 12 Effects of calcium L-lactate concentration to the electrolyte properties. | 124 |
| Table 13 Peak locations deduced from the cyclic voltammogram of cp-Ti and Ti-6Al-4V anodes in Figure 41 with various Ca/P ratio in the electrolyte. | 126 |
| Table 14 The processing conditions selected for <i>in vitro</i> assessment. | 159 |
| Table 15 The chemical composition of PEO coatings produced with different electrical modes. | 173 |

| | |
|---|-----|
| Table 16 The effect of HA micro-powder concentration in the electrolyte to the electrolyte properties in the temperature range from 15 to 30°C..... | 175 |
| Table 17 Chemical composition of PEO coatings produced using difference HA micro-powder addition. | 182 |
| Table 18 Chemical composition of PEO coatings produced using Ti-6Al-4V substrate with 30g/L HA micro-powder addition electrolyte using the two-step control method, with various negative duty cycles during the Step II..... | 188 |
| Table 19 The effect of HA nano-powder concentration in the electrolyte to the electrolyte properties..... | 190 |
| Table 20 The processing conditions on Ti-6Al-4V substrate selected for in vitro assessment. | 196 |

Chapter 1: Introduction

The use of implants dates back into ancient civilisations where gold was used as bone tissue replacement. Since then attempts at using materials to replace bone tissue lost through injury or disease began in aim to improve the quality of life [1].

The basic building block of bone is the organic component of collagen extra-cellular matrix (ECM) and the inorganic component which is largely made up of calcium phosphate (CaP) in the form of hydroxyapatite (HA, $\text{Ca}_{10}(\text{PO}_4)_6(\text{OH})_2$) along with a large quantity of water [2, 3]. Compared with synthetic HA, naturally occurring biological apatite is non-stoichiometric and contains ions other than its base component, such as carbonates, sodium and silicon ions. The osseointegration property of HA has been suggested to be a result of the HA dissolution and precipitation of the apatite layer which leads to ion exchange as well as absorption and incorporation of biological molecules. These improve adhesion of osteoblasts (matrix-producing cells) on the surface and differentiation, extracellular matrix formation and mineralization of the cells. Unfortunately, the inherent brittle characteristics of HA limits their use as implants in load-bearing applications.

Today, titanium is considered to be a biocompatible material which has been used in the field of orthopaedic and orthodontic implants for a long time to replace joints, stabilise fractures and reduce pain. In order to reduce the issues of corrosion and release of metal ions into the tissue inflicting additional problems with bare metal implants, surface coatings are widely used. Although synthetic HA is not identical to biological apatite, it is still the most commonly used for coatings in the orthopaedic and orthodontic field. The use of HA coating on metallic substrate combines the advantage of the strength provided by the metal and ability to form a direct bond with living bone tissue [4]. Furthermore, after implantation, the ‘race for the surface’ between bacterial colonization and tissue integration [5] can be shifted towards the latter, which marks the success of the implant. The application of a bioactive layer which enhances the cell adhesion can reduce implant infection and loosening.

1.1 Aim and Objectives

The overall aim of this project is to deepen understanding of electrochemical behaviour of ‘metal electrode – electrolyte’ systems over a wide range of anodic potentials and develop on this basis novel electrolytic plasma processes for production of bioactive coatings for Ti

implants. This involves determination of the role of various calcium sources in the electrolyte for the deposition of calcium phosphate (CaP) compounds by the Plasma Electrolytic Oxidation (PEO) process and optimisation of the process parameters including electrolyte composition and electrical regimes.

The objectives of this project are to:

1. Investigate possibilities for rapid evaluation and analysis of the electrochemical response of the studied electrochemical system over a wide range of anodic potentials, including a high-voltage domain.
2. Expand the range and explore capabilities of Ca and P containing electrolyte systems to meet essential criteria for production of bioactive PEO coatings using a single-stage treatment, without compromising the process stability.
3. Evaluate *in vitro* biological response of the coatings produced to understand the effects of surface chemistry and morphology in provision of biocompatibility of PEO-coated Ti alloys.

1.2 Thesis Overview

Chapter 2 presents an overview of the PEO process and associated mechanisms with emphasis on the types of electrolyte currently used in PEO processes for biological applications. It also overviews current methods to analyse the electrochemical behaviour of the system and resulting surface morphologies. The advantages and disadvantages of these approaches are discussed.

Chapter 3 provides details of experimental procedures utilised in the present work. The experimental methods include sample preparation, cyclic voltammetry analysis, general plasma electrolytic oxidation process, coating thickness measurements, SEM and EDX analysis. Furthermore, techniques for analysing both the morphological images and the biological response to various coatings are presented.

Chapter 4 introduces the effect of calcium salts in the electrolyte on the characteristics of the PEO process and resulting coatings. The cyclic voltammograms recorded for Ti alloys in various calcium based electrolytes are compared and analysed. The calcium propionate and L-lactate based electrolytes are selected for further investigations based on their stability over the range of voltages during the cyclic voltammetry analysis.

Chapter 5 discusses the use of calcium propionate based electrolytes for PEO treatments of cp-Ti and Ti-6Al-4V alloy substrates, including the effect of calcium content in the electrolyte, electrical mode (pulsed unipolar, bipolar) and frequency range. The surface morphologies are analysed using the Minkowski functionals approach. Electrolyte composition is optimised and the novel two-step control PEO method is developed and employed for further investigations. Selected coatings undergo biological examinations to understand the influence of surface morphologies on the osteoblastic-like cell response.

Chapter 6 discusses the use of the novel calcium L-lactate based electrolytes for PEO treatments of Ti alloys and demonstrates success in forming hydroxyapatite (HA) containing PEO coatings using the single-stage PEO process. The voltammograms of processes carried out in the electrolytes with various Ca/P ratios are studied and compared. The effect of current density applied in two-step control PEO treatments on characteristics and the *in vitro* biological response of resulting coatings is examined.

Chapter 7 compares the effect of HA micro- and nano-powder in the sodium hydrogen-phosphate electrolyte to the coating produced by pulsed bipolar (PBP) current PEO treatments with various frequencies and amplitudes of negative bias. It concludes that the use of HA nano-powder in the electrolyte for PEO treatment shows promising results in terms of HA incorporation in the coating. Coatings produced in both HA micro- and nano-powder containing electrolytes exhibit good biocompatibility and bioactivity *in vitro*.

Chapter 8 summarises the main conclusions based on the results and discussions in this study, and provides the outlook for further research.

Chapter 2: Literature review

2.1 The plasma electrolytic oxidation process

Plasma Electrolytic Oxidation (PEO) is a novel surface modification technique for valve metals. The term ‘valve metals’ designates a group of metals, including titanium, magnesium, aluminium and some others, which form semi-conductive oxide films on the surface when in contact with air. The PEO process involves submerging the metal substrate which acts as an anode into an aqueous electrolyte contained in a stainless steel tank which also acts as the cathode. An external power supply is connected to the two electrodes and provides power to trigger the oxidation processes on the metal substrate. The PEO treatment operates at higher potentials and current densities compared to conventional anodising; this allows discharges to occur at the anode-electrolyte interface, resulting in the unique porous surface morphology produced by this modification technique, which has triggered significant interest in the biomedical field.

The following chapter reviews and discusses the scientific progression to understand the growth phenomena and formation mechanisms of PEO coatings. Furthermore, it reviews the current research on PEO treatment for orthopaedic and orthodontic applications using Ti alloy substrates.

2.2 Development of PEO process

PEO is an electrochemical conversion process, transforming the surface of the metal substrate into an oxide ceramic layer. It attracts increasing interest in the formation of oxide ceramic coatings on light alloys due to its versatility, low cost and environmental friendliness. The development of PEO technique began with the investigation of the spark discharges on the metal electrodes under high voltage by Gunterschultze and Betz (1934)[6]. Another well-known documentation by McNeill and Nordbloom [7], who utilised spark discharges for deposition of cadmium niobate on a cadmium anode in a potassium niobate electrolyte. During early stages of PEO research, acid based electrolytes were mainly used, which resulted in poor coating uniformity; along with inherent disadvantages of lab-scale DC power supplies, this restricted the upscaling of PEO treatment.

Significant improvement and development to the PEO process occurred during the 1970s in Russia, where researchers have noted that under certain conditions, discharges occurred can

promote growth of anodic oxides and enhance mechanical properties of the coatings produced. There has been a rapid growth of research in the PEO process as the electrolytes used have shifted from acidic to alkaline based and the use of pulse current (which enhances the coating formation process) has become available. Thereafter, the potential of the PEO process had been recognised and researches from other countries also became involved in this field.

The initial applications of PEO coatings focused on the aerospace and automotive industries such as rotors, pistons and gears due to the high wear and corrosion resistance of the coating. In the last decades, there has been growing interest in the use of PEO coatings in the biomedical field. Compared with other coating methods commonly used in the orthopaedic and orthodontic fields such as sol-gel and plasma spraying, the use of PEO method is more favourable. The inherent coating growth mechanism provides strong adhesion with substrate, reducing the chance coating of delamination. Moreover, PEO coatings are known for the uniformly porous morphology which is beneficial for cell attachment and proliferation. Although considerable research has been done on the PEO process in relation to biomedical applications, the results have opened up further questions and the need to explore the potential of this technique has become apparent.

2.3 Physical and chemical fundamentals of PEO process

PEO is an electrochemical process which is accompanied by the formation of spark discharges and forms anodic oxide film on the metal surface during the process. The nature of the spark discharge occurring at high voltages is proposed to be a result of electronic avalanche initiated by the impact or thermal ionisation. Therefore, numerous of studies have attempted to understand the spark discharge using a range of approaches. However, it is highly difficult to locate and analyse an individual sparking event, therefore up to now the sparking nature is not fully understood. The following section discusses the commonly accepted coating formation mechanism and current methods to characterise and understand the electrochemical behaviour of the ‘metal electrode-electrolyte’ system during the PEO process.

Figure 1 displays the current–voltage characteristic behaviour of the electrochemical system during the PEO treatment proposed by Yerokhin *et al* [8]. It summarises the range of discharge phenomena that occur on the substrate surface in a wide range of voltages. At a

relatively low applied voltage ($<U_1$), the system complies to Ohm's law where voltage increases linearly with the resistance of the growing oxide film during the process. At U_1 , the peak marks the point where passive film begins to dissolve. As the voltage continues to increase ($U_1 - U_2$), the current drops, which is a result of a porous oxide film growth across the surface. At this stage, the titanium substrate is oxidised similarly to conventional anodising;



At point U_2 , the electric field strength in the oxide film reaches a critical value and beyond that, the film is broken through due to impact on atoms and achieve the electric avalanche breakdown. This marks the end of conventional anodising and further increase in voltage will begin sparking stage.

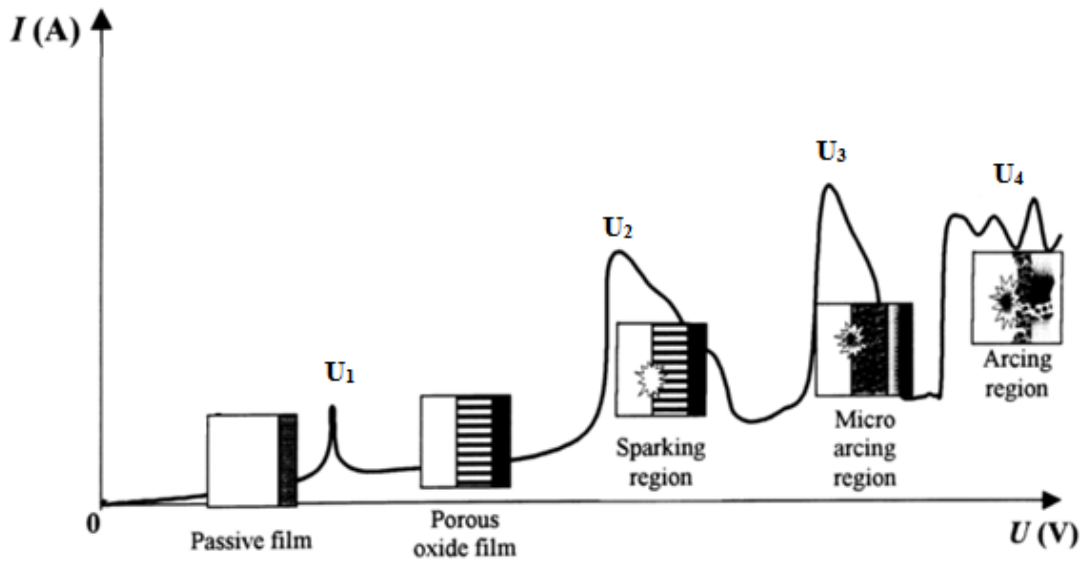


Figure 1 Current-Voltage diagram for the discharge phenomena during PEO process. [8]

The number of defects within the barrier layer increases, resulting in formation of a conductive path, as a result the temperature in the local region rises and thermal damage becomes possible which would cause further defects on the surface. These events are characterised by small sparks moving rapidly across the metal surface. At U_3 , the mechanism of impact ionisation is supported by the onset of thermal ionisation process and short-lived but larger arcing discharge is observed. At the metal oxide interface, Ti is ejected via the discharge channels into the electrolyte where it reacts with electrolyte species forming titanium oxides and hydroxides that are deposited back onto the surface.

In the region $U_3 - U_4$, negative charge builds up in the bulk of the thickening oxide film, resulting in discharge decaying. At U_4 , the arc micro-discharge transforms into powerful arcing, which may lead to destructive effects such as thermal cracking of the coating. This summarises the discharge phenomena that occur during the PEO process and shown during different stages of the PEO process it is accompanied by a change in the resistivity of the coating.

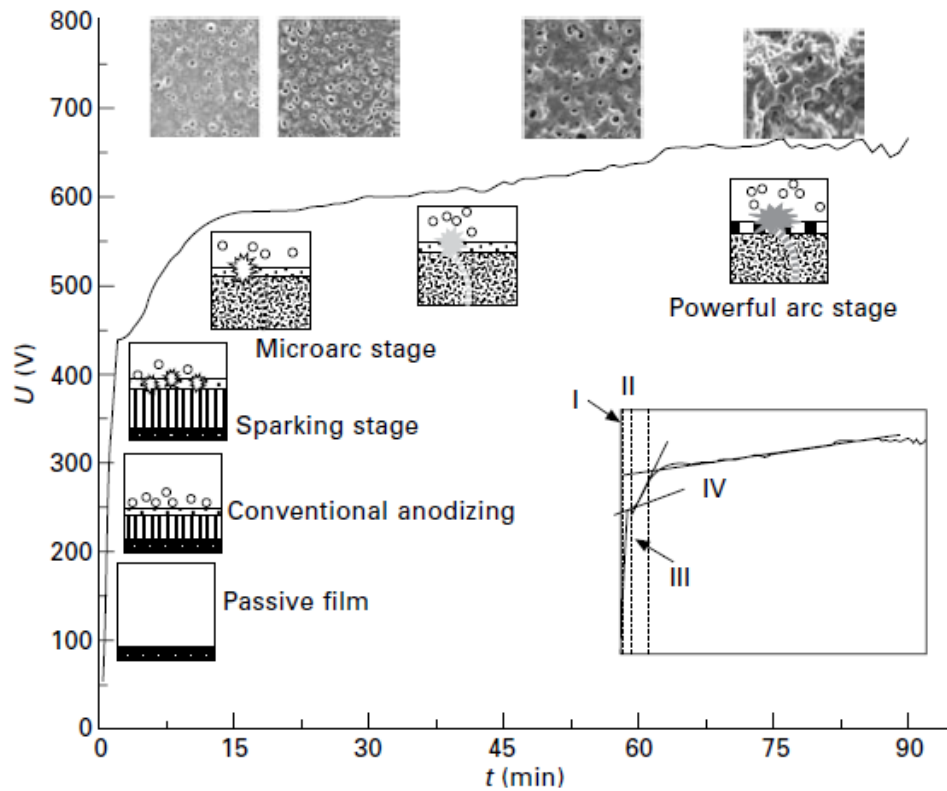


Figure 2 Schematic of the voltage transient with subsequent discharge phenomena and coating microstructure developed during PEO process. [9]

In most studies, the voltage/current transient of the treatment is recorded for further analysis. Figure 2 reveals the schematic diagram of the voltage transient recorded during a galvanostatic PEO treatment. The purpose of this is to determine the electrochemical behaviour of the system during oxide growth under specific processing conditions using principles similar to those discussed for Figure 1, where different stages of the process can be identified by changes in the coating resistance.

In short, at the beginning of the treatment (Region I) the anodic forming voltage increases rapidly with time, which corresponds to the conventional anodising stage as mentioned previously. Thereafter the voltage growth rate begins to decrease (Region II), which marks the competition between the coating growth and dissolution. Visible sparks begin to appear at the voltage range where a flex is observed in the voltage transient curve. As the voltage continues to be forced to increase (Region III), it passes the threshold voltage range and results in micro-regional instability across the surface. In Region IV, the voltage becomes stable, and is associated with the micro-arc stage. When the oxidation process continues, disturbance in voltage can be observed, which marks the powerful arcing stage.

Comparison of voltage transients between treatments carried out with different parameters allows the process reproducibility to be determined and a quantitative analysis of the influence of electrolyte composition and electrical parameters to the coating growth behaviour to be provided [10-13]. Sul *et al* [14] has found the voltage growth rate and the final anodic voltage to be highly dependent on the electrolyte and electrical parameters, but the differences between electrolytes employed makes it difficult to compare between studies.

2.4 Discharge phenomena

Each discharge event during the PEO treatment corresponds to a chain of thermal and chemical reactions resulting in breakdown, melting and solidification effects. The characteristics of each spark therefore have a significant influence to the phase formation, coating morphology and phase distribution. Therefore the understanding of spark characteristics has been of great interest in PEO related research. However, the difficulty to identify characteristics individual sparks remains a problem and makes it difficult to study. Current research in discharge behaviour focuses on understanding the size and spatial density of discharge channels by optical imaging. The results have shown to be affected by the setup of the imaging system and the exposure time. The following section discusses processes that occur during the discharge and factors influencing the discharge characteristics.

PEO coatings usually grow both inward and outward from the original substrate surface. The inner coating growth can be described as the formation of a nano-crystalline layer from the substrate. Meanwhile the outer coating growth is due to chemical reactions occurring during the discharge and the melted oxide products solidify on the inner wall of the discharge channel and/or spray out and solidify at the coating surface.

The discharge occurs at the coating/substrate interface, therefore it had been accepted that discharges do not alter the bulk substrate microstructure. Yerokhin *et al* [15] proposed the discharge initiation to be electron emission from the electrolyte interface with a gaseous phase rather than development of impact ionisation in growing oxide film. Under rapid cooling by the electrolyte, the melted oxide would solidify at the surface. During the treatment, due to discharge induced repeated melting and solidification process, the temperature in the discharge channel would increase and allow formation of complex compounds, crystallisation of and phase transformations in oxide phases (such as anatase to rutile transition). The discharge channel within the oxide layer would exhibit a gradient of

temperature zones, and the reactions may occur depending on the temperature of the region. The discharge characteristics can be influenced by a number of factors as discussed below. It is interesting however to note the correlation between the intensity of the micro-discharge and the number of sparks on the surface. Matkyina *et al* [13, 16] have proposed if the number of micro-discharge increases, the current passing through each channel should decrease to maintain the same total current.

2.5 The effect of electro-physical and chemical properties of electrolyte to PEO treatment

The electrolyte is one of the most influential factors in PEO treatment. It provides a medium for conducting current completing the circuit, promotes metal passivation to form a thin insulating film which is a pre-requisite for dielectric breakdown and provides oxygen source to form an oxide ceramic coating.

A passive oxide layer is formed on the substrate surface, and depending on the electrolyte and the substrate properties, the discharge events will exhibit different behaviour. Consequently, this will influence the coating properties. PEO treatment usually operates in an alkaline environment, this allows the use of environmentally friendly chemicals compared to those used in conventional anodising. The shift in the electrolyte pH from acidic to alkaline over the years results in improvement to the coating morphology and allows formation of uniformly porous structures. The importance of electrolyte pH in the PEO process is highlighted in [17]. Neupane *et al* [18] suggest an increase in the electrolyte pH enhances formation of crystalline phases, aiding oxide stability on the surface, as well as changing the electrolytic dissociation of the compounds in the electrolyte altering the way it interacts with metal surface.

The pH can have an influence to the dissociation of compounds and the level of ions present, therefore numerous of studies used additives such as KOH to modify the electrolyte pH to the desired range. As a result it is difficult to isolate the discussion of the electrolyte pH from the PEO process. The concentration of the electrolyte is also an important factor to the subsequent discharge behaviour. According to Yerokhin *et al* [8] the electrolyte concentration is related to the breakdown voltage (U_2 in Figure 1) $U_2 \cong \frac{E}{\alpha} \ln \frac{z}{a\eta C^b}$, where a and b are constants. C is the electrolyte concentration, z is the elemental charge and η is the

electron current fraction of the total current passing through the system. Therefore it can be assumed the increase in concentration will decrease the breakdown voltage.

Sul *et al* [14] suggested the influence of electrolyte concentration can be explained by the ‘electrical double layer’ model, where a double layer is formed at the coating/electrolyte interface. On one side, there is an excess of electrons from the titanium metal and on the other an excess of ions at the electrolyte region. During the PEO treatment, a certain gradient of ions in the electrolyte is formed at the coating/electrolyte interface. However if the concentration increased sufficiently to influence that gradient, this can accelerate the rate of electrochemical processes that occur, which will subsequently reduce the electrical resistance at the local region. This complies with the results from Shi *et al* [19], where electrolyte containing calcium glycerophosphate and acetate monohydrate was employed, which showed an increase in concentration of both compounds favours the anatase-to-rutile transformation and increase in the average coating surface roughness. This can be assumed to be a combination of the increase in concentration gradient across the initial passive film, which reduces the breakdown voltage with increased thermal impact from more energetic plasma discharge.

It is difficult to trace simple correlations between the electrolyte pH, conductivity, concentration and the electrochemical response of the system because these properties can influence the current-voltage characteristics, and favour various processes, e.g. surface passivation or anodic dissolution, which would have opposite effects on the coating formation process.

2.6 Effect of electrolyte composition

Another major factor of the electrolyte would be the chemical composition. Yerokhin *et al* [8] categorised electrolytes that can be considered for the PEO process as;

1. Electrolytes that provide fast dissolution of metal
2. Electrolytes that provide slow metal dissolution
3. Electrolytes providing metal passivation in a narrow range of voltages
4. Electrolytes promoting weak passivation of the metal
5. Electrolytes promoting strong metal passivation

It was further discussed that electrolytes from groups 3-5 allow sparking voltage to be easily reached therefore are beneficial for the PEO process. These electrolytes were classified in consideration of biomedical application as follows;

1. Electrolytes containing anionic and cationic components incorporated into the coating
2. Suspensions providing transportation of particles which contribute to the coating composition

The following sections discuss the research trends with and limitations of these electrolytes;

2.6.1 Electrolytes providing anionic and cationic components into the coating

TiO₂ PEO coatings with enriched phosphorous content are commercially available from TiUnite. The coatings are characterised by an open porous structure, as shown in Figure 3 and show enhanced osseointegration and anchorage with surrounding bone [20-22]. When compared to other commercially available TiO₂ based implants such as Osseotite implants, they appear to enhance the removal torque and new bone formation [23].

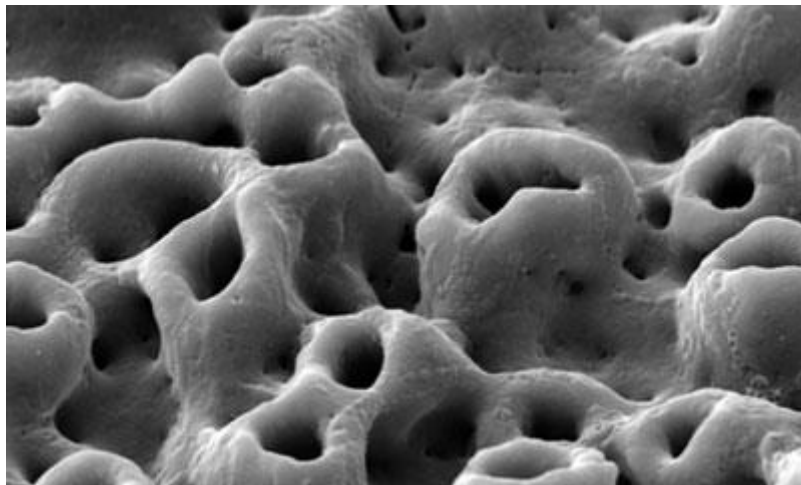
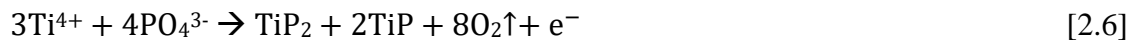


Figure 3 Surface morphology of TiO₂ implant by TiUnite.

Phosphate based electrolytes are commonly used to produce TiO₂ PEO coatings [14, 24, 25], because of their ability to promote passivation and provide –OH groups to the surface. The biocompatibility of Ti is a result of the chemical stability and corrosion resistance of this dense and protective oxide film. TiO₂ PEO coatings have the potential to attract Ca²⁺ ions in the body to form amorphous CaP. It had been proposed the amorphous CaP could potentially

transform into apatite when the Ca/P ratio in the local region reaches 1.67 [26]. The TiO₂ PEO coatings have been suggested to have negatively charged –OH groups incorporated, which improves the hydrophilic ability of the surface, which is beneficial for protein adsorption thereby cell adhesion [27-29]. By changing processing parameters, the surface roughness of the coating can be tailored, which has been shown to play a significant role in anchoring cells and shorten the healing period.

During the PEO treatment, it is assumed that the PO₄³⁻ ions in the electrolyte would be adsorbed onto the positively charged substrate at a low voltage range. As the voltage increases, the PO₄³⁻ would transport by ‘short circuit’ to the substrate-coating interface by migrating through discharge channels under high electric field effect. As a result, a layer enriched with P is commonly observed at the coating-substrate interface [30]. It had been proposed that Ti reacts with the PO₄³⁻ as follows;



At the same time, Ti would form TiO₂ phases in the coating via a range of reactions described in Equations [2.1 – 2.5]. The two TiO₂ phases commonly observed on PEO coatings are the metastable anatase and the stable rutile phase. The ratio and content of these two phases in the coating depends on the processing parameters such as applied voltage and treatment time. The increase in applied voltage would result in stronger discharge intensity, therefore this would increase thermal and stress effects; this can therefore be assumed to facilitate the anatase-to-rutile transformation.

Some studies proposed that crystal structure of anatase is particularly suitable for apatite formation, resulting in a comparatively higher bone-bonding strength during the post-operative period [26, 31, 32]. Meanwhile, others suggest rutile based coatings can enhance the proliferation and ALP activity of osteoblast cells *in vitro* and improve bone growth *in vivo* [33, 34]. Yang *et al* [35] proposed the biological response of TiO₂ coatings is due to the thickness rather than the crystalline structure of the coating, which was supported by Kossenko *et al* [36] who also suggested that the ability of TiO₂ surface to nucleate HA is dependent on the number of hydroxyl groups present on the coating. Despite numerous studies investigating the benefits of anatase [37, 38] and rutile [39] to osteoblastic behaviour, the influence of coating characteristics such as surface morphology and roughness has not been taken into consideration, therefore it is difficult to compare between studies. As a

result, the isolated effects of the two phases to the osteoblastic behaviour are still inconclusive.

The ability to incorporate both anionic and cationic elements from the electrolyte in the PEO coating has become one of the great advantages in the biomedical field. It potentially allows the incorporation of Ca and phosphate ions in the electrolyte and formation of crystalline HA phases in the coating. Therefore numerous studies have focused on formation of CaP containing PEO coatings in aim to improve the osteoconductivity and stability of Ti implants.

The most common calcium source used for such PEO treatments is calcium acetate. The main source of phosphate can be the same as calcium (Ca β -glycerphosphate, calcium phosphate) or sodium phosphates [40-42]. Many studies uses ethylenediamine tetra acetic acid (EDTA) or other strong complexing agents to prevent precipitation of Ca- and P-containing compounds in the electrolyte [43-46]. However results have shown the use of EDTA and other complexing agents can inhibit the crystallisation of TiO₂.

The concept of using soluble calcium and phosphate salts such as calcium acetate and sodium phosphate is that the salt would undergo electrolytic dissociation in the aqueous solution. This would lead to formation of Ca²⁺, PO₄³⁻ and/or PO₄²⁻ and/or HPO₄²⁻ and OH⁻ ions in the electrolyte, these ions would react in the electrolyte forming precipitates;



Furthermore, repeated melting and re-solidification processes occur during the treatment, which can transform the amorphous calcium phosphate phases into crystalline phases [47]. It is proposed that the incorporation of HA and formation of TiO₂ phases occur simultaneously and result in the porous PEO coating with crystalline HA incorporation.

Although much work has been done to date, the results are rather disappointing. These can be categorised into two branches, the first are porous coatings that reveal a large range of calcium phosphate phases such as TCP, CaTiO₃ [14, 22, 48, 49] shown in Figure 4a. The relative low crystallinity of the PEO coatings with amorphous calcium phosphate layers led to a range of research into the use of post-treatments such as hydrothermal treatment to

enhance the crystallinity of phases in the coating. The advantage of this method consists in formation of HA crystals inside the pores without compromising the porous structure as shown in Figure 4b. Results show the surface roughness of the coatings after the hydrothermal treatment is often lower than that of the PEO coated samples [50], moreover it may lead to a depletion of Ca and P concentration just beneath the surface, which was suggested to be due to migration of Ca and P from the coating towards the surface to form crystalline HA during the hydrothermal treatment. Although the use of post-treatment has shown to enhance the crystallinity of the coating without comprising the surface morphology, however the introduction of additional processing step could result in variation of properties between batches.

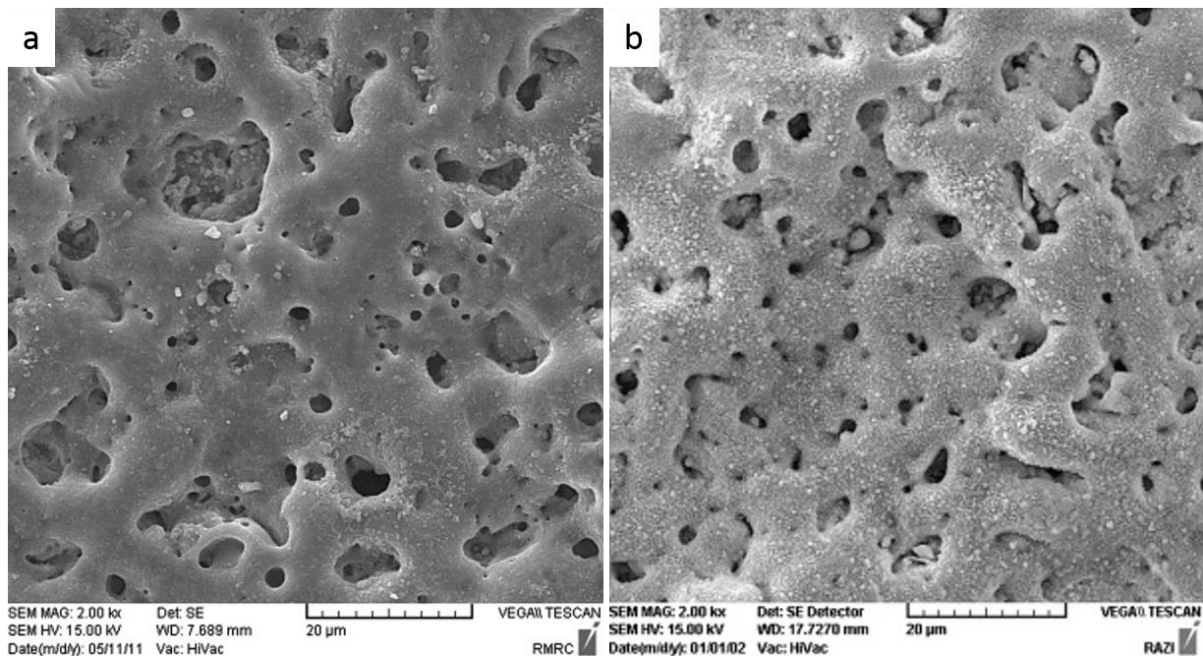


Figure 4 Surface morphology of PEO coatings (a) as formed and (b) after hydrothermal treatment at 190°C for 15h. [50]

Another branch of studies demonstrated the success in direct formation of HA containing coatings, however HA tends to agglomerate on the surface [51], as shown in Figure 5. Ni *et al* [52] proposed the formation of HA layer to be a result of continuous re-melting during the PEO treatment, therefore it would display a dense layer. However this does not explain the formation of agglomerates on the surface. Nevertheless, substantial studies have been done on the optimisation of the electrolyte and electrical regimes in aim to improve the surface morphology while enhancing the crystallinity of HA on the PEO-treated surface.

Shi *et al* [19] used a range of Ca-GP and calcium acetate electrolytes and showed the increase in concentration would increase the number of micro-pores present in and the average surface roughness of the coatings produced. This could be explained by a change in electrolyte conductivity and possible variation in pH, however details of the electrochemical and physical property of the electrolyte are lacking in this research. The use of electrical parameters such as AC and PBP current modes were explored in aim to enhance the level of Ca content in the coating. Further influence of electrical parameters to the discharge characteristics and the coating morphology is discussed in later sections.

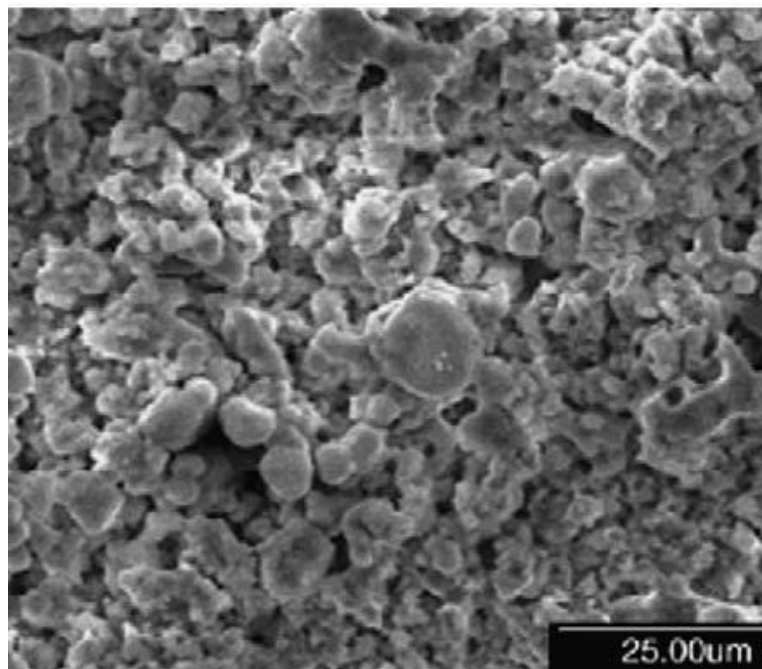


Figure 5 Surface morphology of PEO coating formed on Ti-6Al-4V alloy in the electrolyte containing calcium acetate monohydrate and β -glycerophosphate. [51]

As the demand for improvement continues to increase, it makes researchers to explore the potential of producing PEO coatings containing HA added with trace elements such as Sr^{2+} , Mg^{2+} due to natural bone is not stoichiometric HA. Strontium is clinically used for osteoporotic patients [53], therefore the introduction of Sr into the coating can potentially depress osteoclast proliferation [54]. Numerous studies used strontium hydroxide or acetate additives to the calcium acetate based electrolyte. Results showed the addition of Sr alters the apatite layer formation mechanism [55], although some studies suggest the ability to form porous PEO coatings, coarse features correlated to powerful arcing can be observed [56].

Chung and Long [57] reveal visual images of coatings that have regions of coating peeled off (Figure 6), deposited and re-growth, suggesting further work is required to improve the overall treatment.

Current literature contains a vast amount of studies optimising processing parameters to produce HA containing PEO coatings from calcium acetate based electrolytes. Despite that, the success is still limited, as the formation of crystalline HA appears to proceed at the expense of the uniformly porous morphology. Therefore it is important to return to the fundamental principles of the electrochemical interaction between ions in the electrolyte and the substrate to understand the reasoning behind the failure.

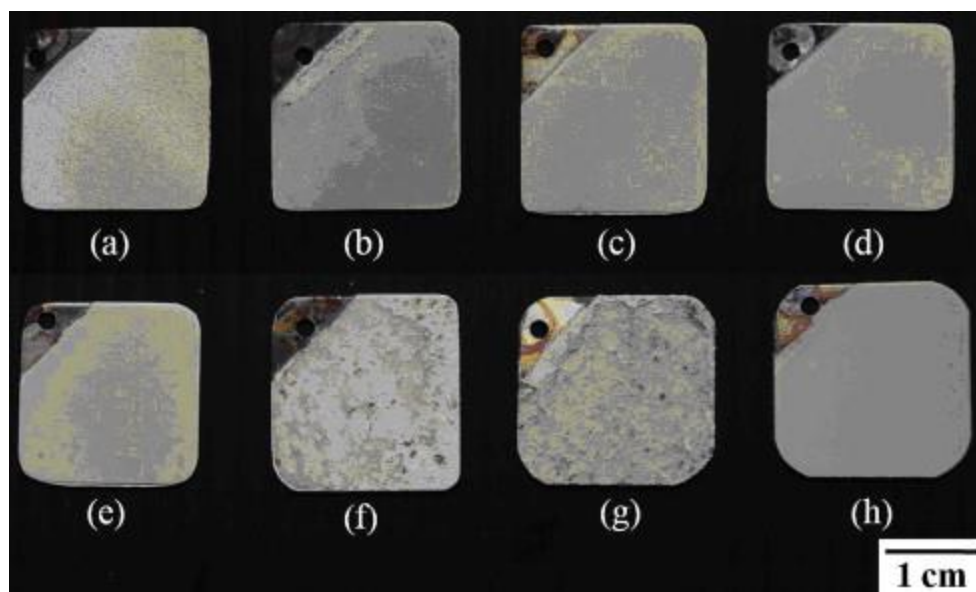


Figure 6 Visual inspection of the coatings produced from electrolytes with Sr/(Sr + Ca) ratios of (a) 0%, (b) 3%, (c) 7%, (d) 15%, (e) 25%, (f) 50%, (g) 75%, and (h) 100%. [57]

2.6.2 Suspensions providing particles that contribute to the coating composition

The issue with the balance of crystalline HA formation and porous PEO morphology have led to the use of calcium phosphate and HA containing slurry electrolytes. The principle of using these electrolytes is a combination of electrophoretic deposition (EPD) with PEO treatment. The use of hybrid EPD+PEO processing is attracting increasing interest due to the simplicity of equipment and its ability to control the coating thickness. Moreover, as PEO operates in the anodic regime it does not facilitate an efficient mass transfer of calcium cation. Therefore the use of negatively charged particles could potentially overcome this deficiency.

Electrophoretic deposition is possibly one of the oldest coating methods. The early use of PEO+EPD involves a duplex treatment [58], where a previously formed porous PEO coating was placed in an HA suspension to be treated at a high voltage for 5-10 min. The resulting coating features a dense HA/TiO₂ layered structure, although results reveal excellent adhesion between the HA and the TiO₂ layer, the favourable porous structure is lost. Furthermore, additives such as EDTA are required to stabilise the suspension and prevent sedimentation of HA particles in the electrolyte. It must be stressed that the long-term influence of EDTA to the electrochemical process and the *in vivo* response is still unknown, therefore a simple alkaline electrolyte would be preferred.

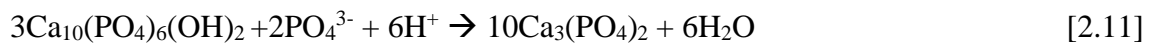
Nevertheless, the investigation of the single-step approach began in aim to produce HA containing PEO coating. The mechanism of hybrid EPD+PEO processing takes advantages of the alkaline based electrolyte required for PEO method. Since the isoelectric point of HA is approximately pH= 7, therefore it can be assumed that HA particles attain a negative charge as follows;



Coating growth mechanism in the PEO treatment relies on the anodic regime, therefore negatively charged HA particles will be attracted to the substrate. Simultaneously, TiO₂ is produced at the surface as described in Equations [2.2] to [2.5]. The coating formation mechanism in a slurry electrolyte can be assumed to vary from that in the electrolyte based on soluble salts discussed above. This could be a result of particle addition and may not have a significant influence over the electrolyte electrochemical and physical properties. Furthermore during the initial stage of PEO treatment, (<U₁ in Figure 1) negatively charged HA particles would migrate towards the substrate in the form of individual particles. As the treatment continues, the number of HA particles on the surface would increase and form small agglomerates on the surface. At the same time, the increase in the HA layer thickness, the deposition rate would decrease, and the agglomerates begin to nucleate. When the voltage reaches the threshold point, it can be assumed that a layer of HA particles is present on the surface. Therefore under strong electric field HA could be integrated into the coating. At the same time, negatively charged HA particles in the electrolyte would be attracted into discharge channels to facilitate particle incorporation throughout the coating. As the voltage increases, the HA particles would continue to be attracted to the substrate and experience repeated local heating, melting and resolidification due to the micro-discharging activity at

the surface. In the later micro-arcing stage, the longer life sparks result in a looser coating and despite HA particle could deposit within the porous structure. According to literature, the incorporation of HA particles in the PEO coating is more complex. Gas evolution at the anode would obstruct the HA particles attaching to the surface and lead to suspension destabilisation [58-60].

Kim *et al* [59] and Bai *et al* [61] suggested the addition of high zeta potential chemicals such as ethanol is required in the electrolyte to prevent HA particles settling due to gravity. Coatings were produced in a β -glycerophosphate pentahydrate based electrolyte with NH_4OH and HA particles. These electrolytes showed the ability of incorporating HA particles onto the coating without compromising the porous structure, however XRD spectra of the coating produced shown weak HA peaks, suggesting limited HA particles were incorporated onto the coating. Furthermore, Shin *et al* [62] proposed the low HA content in the coating could be attributed to HA particles reacting with phosphate ions in the electrolyte or titanium oxide and decomposing as treatment time and/or temperature increase as follows;



Furthermore, the thermal and structural stress caused by the HA particles have shown to destroy the coating. As a result of these studies it was proposed to use polymer additives to reduce the thermal and structural differences [63]. However, the long term effect of the additives and the biological influence is still unknown, therefore further investigation is needed.

The principle driving forces of EPD are the charge and the electrophoretic mobility of the particles in the electrolyte under the influences of the applied electric field. Therefore the suspension characteristics such as particle size and concentration are highly influential factors to the coating formation mechanism. Shin *et al* [62] proposed that a change in the concentration of the HA particles in the electrolyte would trigger a different coating growth mechanism. Figure 7 shows the surface morphology of the coating produced in the HA containing slurry electrolyte. It reveals a porous structure as shown in Figure 7 (region A) and agglomerates in region B. Results suggest as the particle concentration increases, the particles would not react with the phosphate ions or TiO_2 , instead forming a layer of HA

covering the whole surface. However, different electrolytes were used in the experiment, therefore it is difficult to isolate the influence of HA concentration to the coating mechanism.

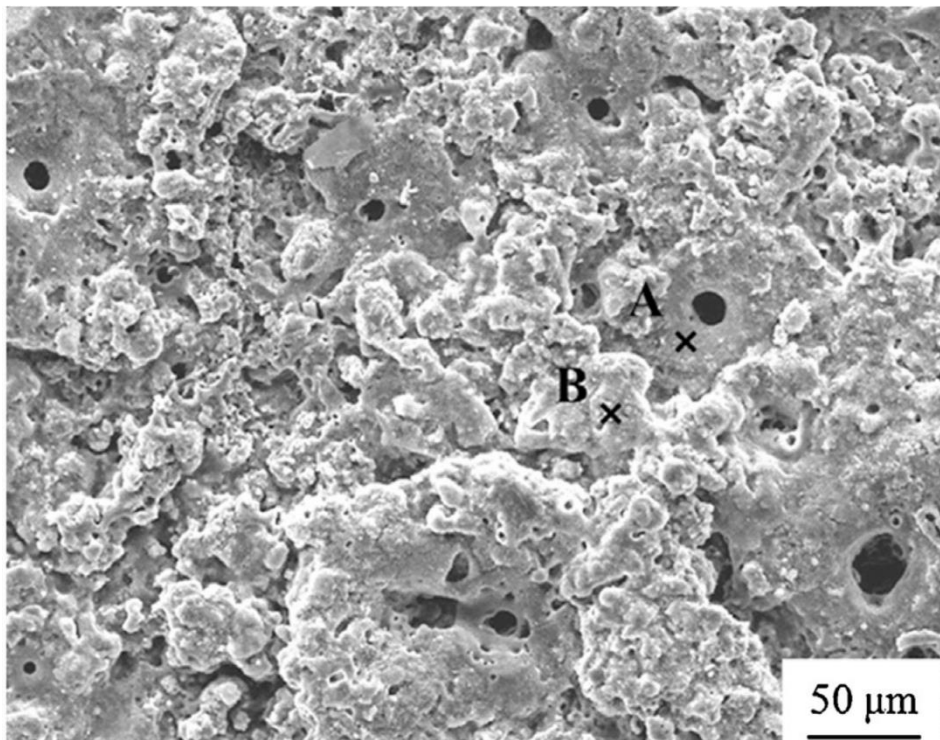


Figure 7 Surface morphology of the coating produced on cp-Ti substrate in the electrolyte with HA powder addition. [62]

The electrophoretic velocity of the charged particle can be described as;

$$v = \frac{QU}{4\pi r\eta} \quad [2.13]$$

Where Q , U , r , η represent the charge, applied voltage, particle radius and viscosity of the electrolyte, respectively. In electrolytes with low particle addition, the viscosity can be assumed constant. Therefore the particle size becomes the major factor affecting the movement during the treatment. Furthermore, it can be assumed that larger particles are more susceptible to settling in the electrolyte due to gravity, therefore it is comparatively more difficult to attain a uniform deposition [64]. As a result the use of nano particles has been extensively investigated. It was observed that the use of HA nano-powder can reduce the mismatch in thermal expansion [65]. HA nano-powders have shown to be more suitable due to the enhanced surface to volume ratio and reduced the chance of sedimentation formation. But the need for EDTA still remains, moreover results suggest the apatite forming

ability of resulting coatings is poor [66], with chemical treatment required to enhance the surface bioactivity.

Additionally, methods to minimise the incidence of infection through surface engineering are also explored as the infection caused by bacteria continues to be an issue in medical devices. Silver (Ag) is a well-established anti-microbial agent which has been extensively used in the form of metallic silver and/or salt. In short, Ag can penetrate through the cell wall, bind to the bacteria DNA chain and disable its replication ability, which will eventually kill the micro-organism. As a result, some research has looked into incorporation of nano-Ag particles in PEO coatings, despite the advantages, it had been reported that the maximum concentration of Ag for human cells is 10 mg/l, above which is cytotoxic to the surrounding cells [67, 68]

Factors that influences the stability of nano-Ag include the particle size, concentration, pH and zeta potential. It had been proposed at pH 12.6, the zeta potential of Ag particles was -26.8 mV indicating a good dispersion stability due to the strong repulsive forces between particles. The results of PEO treatments of Mg alloy carried out using AC power supply under galvanostatic conditions with current density at 3 A/dm² indicate that it is feasible to form Ag incorporated PEO coatings [69]. Necula *et al* [70] proposed the use of 0.3 g/l nano-Ag particle addition to the calcium acetate and glycerophosphate based electrolyte. PEO treatments were also carried out in the galvanostatic AC mode at a current density of 20 A/dm² on Ti alloy substrate (Ti-6Al-7Nb). The results suggest addition of Ag nano-particles does not significantly influence the surface morphology and coatings have shown to provide good osteoblast viability. Alternatively, some researchers synthesise AgHA nano-particles [71] for PEO treatment, and showed AgHA deposition on PEO coating as a layer of dense matrix, this brings back the issue of compensating the porous PEO morphology and the deposition of AgHA onto the coating.

As current literature shows, there are issues with producing HA incorporated coatings with porous morphology. Additional research is required to understand the influence of electrophoretic velocity of suspension and particle concentration to the plasma discharge behaviour and local properties such as electric field distribution in the vicinity of the particles, in order to expand the use of PEO+EDP treatment. Therefore it is useful to study these effects on formation and properties of PEO coatings as a whole system rather than isolated factors.

2.7 Influence of alloy composition

The basis of PEO treatment is built on the breakdown of the anodic oxide film on the substrate surface and allow sparking to occur at the interface with electrolyte. This leads to the coating growing simultaneously both above and below the original substrate surface. Therefore the anodic film formed on the substrate can determine the coating formation mechanism during the PEO process.

Hussein *et al* [11] proposed that discharge formation process differs depending on the metal composition and results from Jovovic *et al* [72, 73] also comply with such observation and further imply the importance of substrate alloying to PEO treatment. It had been suggested that the microstructure could play an important role when using high energy treatment such as PEO [74]. Duan *et al* [75] used AZ91D alloy to investigate the influence of substrate alloy microstructure to the PEO coating growth process and found higher coating growth rate on α -phase than those on β -phase, which suggests a higher content of Mg in the α -phase attributes the higher growth rate. Studies on Mg and its alloys have shown inconsistency e.g. some found coatings produced on pure Mg in phosphate based electrolytes to possess better corrosion resistance than those on silicate [76], while others obtained opposite results on Mg alloys [77]. The disagreement between various studies may arise from differences in microstructure and chemical composition of substrate materials.

In the orthodontic and orthopaedic industry, the two most commonly used Ti alloys are cp-Ti and Ti-6Al-4V. The former contains alpha Ti phase only, while Ti-6Al-4V is an alpha-beta alloy; α -phase has a hexagonal close-packed structure, whereas β phase has a body centred cubic structure. Alloying to stabilise both α solid solution and β phase in the ($\alpha + \beta$) structure increases the alloy strength. Studies comparing the coatings produced using cp-Ti and a newly developed titanium-zirconium (Ti - 12-15% Zr) alloy, showed inconsistencies between the surface morphology and the wettability of the coating [78]. Metikoš-Huković and Piljac [79] suggest the passive film on Ti-6Al-4V alloy is formed by diffusion of vacancies on the oxide layer due to dissolution of vanadium oxide. Blackwood *et al* [80] suggested that high defect densities are associated with rapid coating growth rate using titanium rod. It can therefore be assumed that at higher anodic potentials, such as those applied in PEO, the influence on the electrochemical behaviour would be more apparent. This also complies with theory from Sato [81], where it was proposed the breakdown of the passive film to be sensitive to the chemical composition of the substrate and the anion adsorption.

These studies highlight the importance of substrate alloying to the PEO process. Yet there is surprising lack of attention to the influence of alloying on the coating formation mechanism.

2.8 Influence of power source

2.8.1 Galvanostatic and potentiostatic regimes

The two typical electrical control modes used in electrochemical processing are potentiostatic (constant voltage) and galvanostatic (constant current) mode.

The main advantage of the potentiostatic mode consists in controlling voltage within a desired range, however the control over the surface discharge characteristics would be limited. Moreover the application of potentiostatic control restricts process scaling and transfer to different equipment as the voltage drop across electrolyte often remains unknown. These disadvantages could be avoided using galvanostatic approach, wherein a constant electric field across the growing coating is maintained regardless of other conditions. However, the use of galvanostatic approach is limited by the minimum required current density, below which sparking cannot commence.

For effective breakdown to occur in the galvanostatic mode, high current densities are often applied, and the resulting voltage is forced to increase. Thereafter the voltage transient is recorded over the treatment for further analysis. Shin *et al* [82] used AC conditions for 300s at current density from 100 to 250 mA/cm². Their results show as the applied current density increases pit-like pores become dominating on the surface, a larger variation in pore size was observed and the coating thickness increased from 4 to 13 μm. Results show an increase in current density is often associated with development of a larger pore size due to a comparatively larger discharge energy.

2.8.2 Effects of electrical parameters

The power source for PEO treatment plays a decisive role in the resulting coating characteristics. DC power supplies were used in the early PEO research, but the limitation in the control over the surface discharge limited the development of PEO technique. Since then DC pulsed, AC, and pulsed bipolar sources had been developed which allow better control of discharge characteristics during the process. The following section discusses the effect of electrical parameters to the coating formation mechanism and the subsequent coating characteristics.

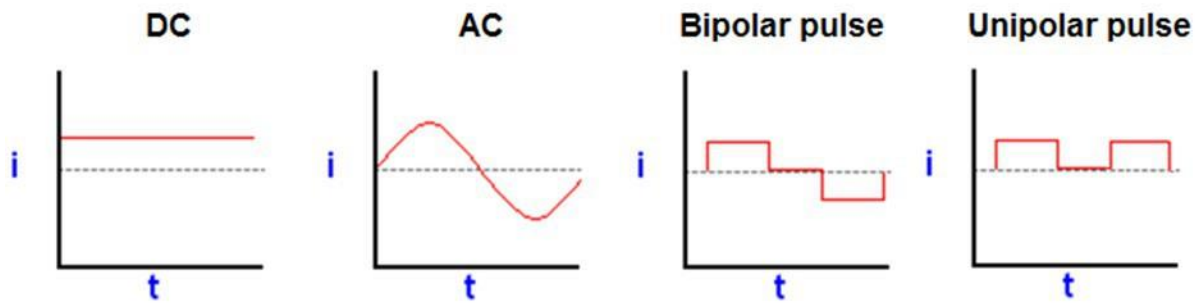


Figure 8 Schematic diagram of electrical waveforms commonly used in PEO research

2.8.2.1 DC and pulsed DC mode

DC-PEO process is the simplest electrical model for PEO treatment, and had been extensively investigated at early stages of PEO research. Due to the limited control over discharge energy, resulting in development of long-lived micro-discharges at the surface. The resulting coatings often possess a coarse structure with defects, which is associated with the thermal ionisation at the surface and therefore local over heating [15, 83]. As the treatment continues, the increase in the net resistance of the dense layer would weaken the micro-discharge activity. The use of DC-PEO process allows a high rate transfer of negatively charged PO_4^{3-} ions to the positively charged substrate, which results in formation of Ti-OH groups on the surface. Furthermore, it is likely that calcium phosphate would precipitate in the electrolyte near the electrode, where the local combination of pH change induced by electrochemical processes with high concentration of Ca and phosphate ions would favour the formation of calcium phosphate similar to that described by Equation [2.9].

Despite this, the prolonged discharge during DC-PEO process is still undesirable, moreover CaP phases such as HA had been suggested to decompose due to high temperature. As a result, the use of pulsed unipolar mode had been explored. The positive pulse promotes the growth of the passive oxide film, while the introduction of off-time not only reduces energy consumption by interrupting discharges but can also allow cooling to occur thus reducing local overheating. Factors such as the duty cycle, treatment time and current density/voltage will all influence coating microstructure and composition, allowing its properties to be tailored to specific applications.

The duty cycle of the positive pulse can be defined as

$$\delta_+ = \frac{t_+^{\text{on}}}{t_{\text{total}}} \quad [2.15]$$

where t_+^{on} is the pulse on time and t_{total} is the total time for the selected frequency.

An increase in the duty cycle would therefore result in stronger discharges [84], therefore it is commonly associated with greater pore size. On the other hand, reduction in the duty cycle would result in weaker but more populous discharges [13, 16]. The increase in the single pulse discharge energy by increasing voltage/current pulse magnitude would have a similar influence; moreover, the rise in the local temperature could induce in a stronger plasma effect.

2.8.2.2 AC and PBP modes

The introduction of the negative bias in the PEO treatment using AC and PBP modes can reduce the additional polarisation of the electrode and gain further control over the discharge duration. Sah *et al* [85] proposed that AC regime is preferred for as the porous structure developed during the cathodic breakdowns healed by the molten oxide formed in the subsequent anodic pulse, therefore reduces the crack formation. It is interesting to note that studies have suggested AC mode would result in a loss of inner coating material [86], however further investigation is required to understand the coating mechanism. Nevertheless, studies have also suggested the use of AC mode allows formation of thicker coatings and enhances the adhesion strength between the coating and the substrate. But despite the advantages, the use of AC mode in PEO studies is not wide spread, this is because of the limitation in the power and current frequency which restricts the commercial upscaling.

This lead to the development of the novel pulsed bipolar source (PBP), which had been shown to supply higher power and provide a wide range of frequencies. Compared to the AC mode, it had been suggested to improve the coating growth rate and surface morphology [87]. The use of PBP mode has therefore attracted a great interest as it allows independent adjustment of different current pulse parameters which can further help tailoring the characteristics of micro-discharge events and thereby the coating morphology. It was suggested that the higher frequency current pulses allow formation of shorter and more energetic micro-discharge events, which can enhance the micro-hardness of the coating.

It can be assumed that the positive pulse plays a crucial role in the micro-discharge events and the formation of the coating microstructure. Meanwhile the negative pulse would interrupt the spark discharge and allow the surface to cool, whereas the negatively charged calcium phosphate and HA particles as well as hydroxylated metal ions $Me(OH)_m^{n-}$ formed in alkaline electrolytes will be repelled from the surface. During the negative pulse, gas liberation such as hydrogen and oxygen would be generated. This would have two-fold effect, it could alter the local pH and temperature at the coating surface, this would influence the chemical reactions that could occur in the local region and influence the melting and re-solidification process of the outer layer [11, 88]. In calcium and phosphate containing electrolytes, it can be assumed the use of PBP mode allows the attraction of both Ca^{2+} and PO_4^{3-} ions, in particular enhance Ca transfer. When HA containing slurry is employed, the introduction of the negative bias would allow local cooling which could potentially reduce HA decomposition.

The introduction of negative bias has shown to enhance the ability to attract positively charged Ca ions onto the surface during the treatment. However the research using PBP mode is still in its early development, therefore further investigation is required to provide a more insight into the coating formation behaviour when PBP is used.

2.9 Analysis of PEO surface morphology

Coating characteristics, such as porosity, are dependent on the spark discharge as mentioned in previous section, for some applications surface porosity is not favourable as it reduces the coating stiffness and the wear and corrosion resistance because it allows penetration of corrosive liquid through the pores. In contrast, for orthopaedic and orthodontic applications, this characteristic favours osteoblast attachment and enhances osseointegration by allowing body fluid transport through the pores and sufficient bone ingrowth [89]. Nevertheless, the optimum surface morphology and pore size are still unclear.

Shin *et al* [90] used current density ranging from 100 to 250 mA/cm² to form porous coatings. Treatments at 100 mA/cm² resulted in porous coatings featured areas of dense matrix and craters, whereas the coatings formed at 250 mA/cm² appear to be smooth with larger pores. The results suggest smaller crater-like pores with diameter ~2 µm are suitable for cell anchoring, but omits the differences in pore shape. Meanwhile Teixeira *et al* [91] suggest surfaces with 62 µm pore size yield higher expression of osteoblast phenotype. From

the findings in current literature, it follows that as the osteoblast cell becomes in contact the implant surface a range of cellular behaviour occurs, therefore the architecture of the porous structure is as important as the pore size itself.

The most common image analysis approach used in PEO research consists of measuring the average pore size and corresponding statistics (standard deviations or pore size distributions) [92] or evaluation of its fractal dimension [93, 94]. The advantage of measuring the average pore size is the simplicity of this approach, although its physical meaning towards the discharge phenomena is limited to circumstances. Moreover, it is difficult use to a single value to analyse the complex PEO porous morphology and this method cannot take into account differences in pore shape and relationships with surface roughness.

The second method is based on using fractal theory, which allows to measure the heterogeneity of the surface and had also been shown to be useful in quantifying the structure of naturally occurring objects such as trabecular bone [95] and seeds [96]. Since development of traditional linear fractal method to mass fractal dimension, this approach can now be used for PEO research. Fractal dimension is a parameter used to quantitatively assess fractal geometry, looking at the self-similarity on an image. The concept of self-similarity is based on the orderliness of the surface, therefore assuming the homogeneity of the surface is related to the probability distribution of height which is independent of local surface [97]. Therefore, in relation to PEO research, fractal dimension is often associated with average coating roughness.

There are various fractal methods, however the box-method is most suitable and therefore most often used to assess PEO coatings. This approach uses a number of 'boxes' with grid size r to cover the image, and the total number of squares along the image is $N(r)$. A log-log graph was used to determine fractal dimension (D) from the slope as the dimension (D) is defined as $D = \lim_{r \rightarrow 0} \frac{\ln(N(r))}{\ln(r)}$. Since PEO coatings occupy a large volume and have a rough surface, the single value of resulting fractal dimension is in the range of 2 to 3, with lower values corresponding to smoother surfaces and the higher ones (~ 3) to more irregular surfaces.

Many factors affect the fractal dimension, for example fractal analysis is highly magnification dependent, as the 'roughness' and 'branching' of the pore at a particular magnification, may appear to be different in higher magnification. In application to PEO

coatings, where various pore morphologies are often observed, fractal dimension does not provide any morphological specification, therefore it is not possible to differentiate, e.g. non-uniformly distributed circular pores from grooved-like porous morphology, and different porous structures could result in similar D values. It must be noted that the surface morphology of PEO coatings are often assessed from SEM images which are grey-scale, however this method requires to convert these grey-scale images to binary (black and white), which could potentially lose details of some surface features.

While there is a strong link between the pore size and coating ‘self-similarity’ to the coating formation process and/or resulting biological behaviour, the application of these image analysis techniques is limited by circumstances and often neglects the influence of pore shape in attempts to quantify the range of porous features observed using a single value. To overcome these shortcomings, a new approach that allow simple and quick analysis of PEO coatings using a range of grey-scale images and taking into account the pore shape would be preferable.

2.10 Summary on PEO

Plasma Electrolytic Oxidation (PEO) is an attractive surface modification technique that is not only environmentally friendly but also highly flexible to allow tailoring surface properties. Although numerous of studies have been performed on the optimisation of processing parameters, these are focused onto effects of one or two variables influencing the discharge behaviour and/or correlation between the two parameters to provide desired PEO coating morphology and phase composition. These narrowly focused studies lack manufacturing value in terms of advancing the use of PEO technology for commercial applications. A means to provide insights into electrochemical behaviour of materials during PEO processing is therefore highly important to allow better understanding of the fundamental aspects of this technology. This can advance the scientific understanding of the PEO process, which could allow better design and exploration PEO treatments and resulting coatings.

Chapter 3: Materials and General Methods

3.1 Materials

Thermally annealed commercially pure ASTM Grade II and Grade V Ti alloy bars from Advanced Titanium Materials Ltd were used in this study. Although the precise thermal histories were not available, and the microstructures were not assessed, these are likely to have been rolled or extruded to bar form, leading to axially elongated microstructures. While these may have recrystallised under the annealing treatment, the possibility of anisotropy in the grain structure cannot be discounted. The composition of the materials is shown in Table 1. The bars were cut into disks of 7 mm thickness and 1cm diameter, polished using abrasive paper with 240 to 1200 grit to achieve surface finish of $R_a \approx 0.1 \mu\text{m}$. The samples were cleaned in acetone, isopropanol and distilled water, then air dried.

Table 1 Composition of Ti alloys used in this experiment.

| Wt (%) | Grade II | Grade V |
|--------|----------|---------|
| Ti | Balance | Balance |
| C | 0.03 | 0.02 |
| Fe | 0.08 | 0.132 |
| N | 0.015 | 0.013 |
| O | 0.12 | 0.12 |
| H | 0.001 | 0.001 |
| Al | - | 6.00 |
| V | - | 4.00 |

3.2 General methods

3.2.1 PEO treatment equipment

PEO treatments were conducted using a power module comprising of two DC power supply units (Advanced Energy MDX II 15kW and 30kW) connected to a pulse generator SPIK 2000A (Melec GmbH). The DC units were remotely controlled by the computer through a NI-PXI-8430 card, the current and voltage signals were acquired by Tektronix A6303 current

and voltage probes and logged into PC through a NI-PXI-5922 card. The voltage and current transient behaviour was recorded during the PEO treatment and submitted for further analysis.

The schematic diagram of the set-up is displayed in Figure 9. A cylindrical stainless steel tank ($\text{\O} 160 \times 140 \text{ mm}$) was used in the system to contain the electrolyte and act as the counter electrode. Electrolyte temperature during the PEO treatment was carefully monitored and regulated by the water cooling system to prevent interference in the treatment processes with fluctuation in the thermal energy. For this purpose, during processing the electrolyte bath was cooled by water passed through stainless steel coil, with electrolyte temperature maintained in the range of $25 \pm 5 \text{ }^\circ\text{C}$. A magnetic stirrer was also employed, which had two-fold function; firstly to provide a uniform electrolyte composition and prevent sedimentation of species in the electrolyte throughout the treatment; secondly, to provide electrolyte circulation and enhance the cooling process.

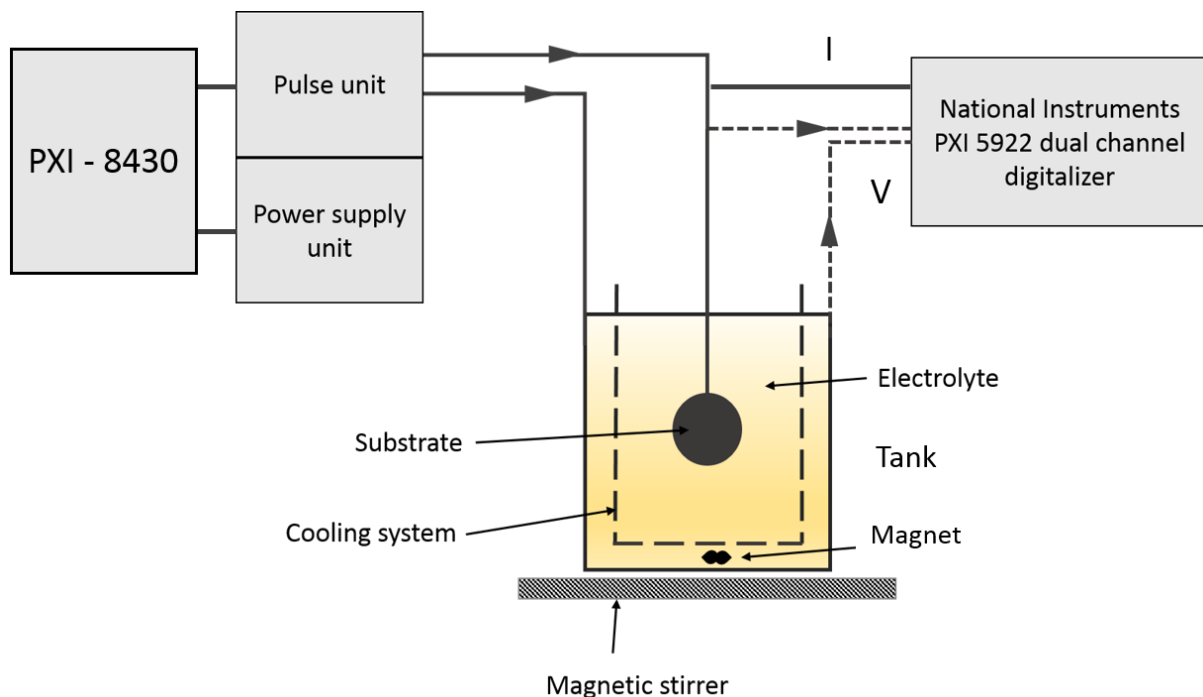


Figure 9 Schematic diagram of the PEO system.

Various electrolytes have been prepared in this work, details of composition for which as well as specific electrical parameters of the process are presented in the related chapters. In short, the chemicals used were weighted using an electronic balance (DENVER Instrument MXX-2001) with precision of $\pm 0.1\text{g}$. The electrolyte conductivity and pH were measured

using a conductivity meter (HANNA HI9835) and pH meter (HANNAH pH 211), respectively.

3.2.2 Coating characterisation

3.2.2.1 Measurement of coating thickness, surface roughness and wettability

The coating thickness was analysed using an Electrometer 355 Coating Thickness Gauge equipped with N4 standard anodisers probe with an accuracy of $\pm 1 \mu\text{m}$. The probe uses a relative high frequency signal to generate an alternating electric field in the substrate beneath the coating. The field causes eddy currents to circulate in the substrate, which is converted into magnetic field and is calibrated as the substrate. When coated samples are examined, it causes an electrical impedance changes that are dependent on the coating thickness. The results were expressed as the average coating thickness from 10 randomly selected places with standard deviation.

A Veeco Dektat 1500 profilometer operated in standard scan mode with resolution of minimum $0.40\mu\text{m}/\text{sample}$. A force of 3 mg applied to stylus with radius of $12.5 \mu\text{m}$ was used to examine the average surface roughness of coatings produced. Six measures were made per coating, and the results are displayed as the mean average \pm standard deviation (SD) values of roughness.

The surface wettability of the coatings was measured with distilled water at the central regions of the samples using a Rame-Hart angle goniometer. Three measurements were taken per coating surface, with the results displayed as the average \pm standard deviation (SD) values of contact angle ($^{\circ}$).

3.2.2.2 X-ray diffraction analysis

The phase composition of the coatings was examined by X-ray diffraction (XRD) using a Siemens D5000 diffractometer operated with Cu $K\alpha$ radiation ($\lambda=1.54\text{\AA}$) at a 40kV acceleration voltage and 30 mA filament current. Normal coupled $\theta - 2\theta$ scans were performed with step size of 0.02 and dwell time 2 s/step. The patterns obtained were analysed using PDF-4+ software, which is designed for phase identification. This allows identification of different calcium phosphate and TiO_2 phases present in the coating.

3.2.2.3 Analysis of coating morphology and elemental composition

The surface and cross sectional morphologies of the coatings were analysed by Scanning Electron Microscopy (SEM) using JEOL 6400 and FEI Inspect F SEM instruments operated at an accelerated voltage of 15-20 kV. For cross-sectional imaging, the coated samples were first cut in half using ISOMET 5000 precision saw. Thereafter the samples were cold mounted using epoxy resin (MetPrep Ltd.) and subjected to grinding and polishing. Due to the low conductivity of PEO coatings, carbon was sputtered onto the samples to form a thin conductive layer which would prevent accumulation of static electric field during SEM imaging.

The coating chemical compositions were analysed using a semi-quantitative analysis method known as energy dispersive X-ray (EDX) spectroscopy using appropriate detectors attached to the SEM. The obtained EDX spectra were used to evaluate atomic percentages of elements detected.

3.2.2.4 Image analysis using Minkowski Measures

Surface plane SEM images of coatings were further analysed using various methods to derive and evaluate different morphological characteristics. As mentioned in Chapter 2, morphological evaluation of PEO coatings currently relies on qualitative analysis with additional information of the number of pores and average pore size measurement from ImageJ (or similar software) analysis. Therefore discussions of PEO coating morphologies are prone to bias morphological examination moreover it is difficult to compare coating morphologies between studies.

In this work, the surface plane images were analysed using the Minkowski functional method. The functionals were calculated as a function of the image binarization threshold (ρ), this allows detailed information to be obtained about the structure of the coating from the grey scale images. The features present in the image between thresholds can vary drastically, therefore application of Minkowski functionals can eliminate the use of arbitrary definitions to describe a continuous feature.

The functionals used included the surface coverage (C), it is the ratio of the image containing features and background matrix (dark and white), and therefore the surface coverage is a pure number between 0 to 100% for all images. The second measurement L describes as the

boundary length, this is related to the perimeter of the features in the image and correlated to the curvature of the boundaries. The third is the Euler characteristic (E), which represents the topological properties of the imaged pattern. Since the boundary length is associated with the curvature of the boundary, the larger the boundary length L measure it represents for a given E_{\min} , the more domains are distorted, suggesting the feature becomes elongated. These quantities have been calculated in MATLAB using the source code developed by Salerno and Banzato [98]. As these functionals would vary between images, they were normalised.

The surface coverage (C), for all images varies between 0 to 100%, corresponding to the all white and black background, respectively. Therefore the maximum of C value within each image is normalised to 1. The boundary length (L) measure can also defined as the number of edge pixels joined by black and white pixels, therefore the boundary length (L) measure varies between images and cannot be normalised internally to L like that of surface coverage (C), because it will lead to the loss of the relative intensity L_{\max} . For images with i - j pixel, the total number of edges on both orthogonal directions of a 2D image will be $(i-1)j + (j-1)i$. The Euler (E) measure is also a dimensionless quantity, but it accounts for the analysis of the surface area, therefore it is normalised to the total number of pixel (ij) of the SEM image. Due to the subtle variations obtained for the $L(\rho)$ and $E(\rho)$ curve could represent various surface morphology, therefore the resulting functional curves are displayed as $C(\rho)$, $5L(\rho)$ and $10 E(\rho)$. The C_{flex} , L_{\max} and E_{\min} were identified in the curves, and the corresponding ρ values were noted.

3.2.3 Biological testing using osteoblast-like cells

The success or failure of the implant is highly dependent on the biocompatibility of the surface, which can be reflected by the cell adhesion and proliferation on the surface. In the present work, the biocompatibility and cytotoxicity of the selected coatings will be assed using *in vitro* cell culture method.

3.2.3.1 Materials

1. MG63 human osteosarcoma cells
2. MC3T3-E1 mouse osteoblast cells
3. MG63 basal culture media consists of Dulbecco's Modified Eagle's Medium (DMEM) (Biosera, East Sussex, UK) supplemented with 10% Fetal Calf serum (FCS), 1% 2mM L-

Glutamine (L-g) and 1% 100mg/ml penicillin and streptomycin (P/S) (All obtained from Sigma, UK).

4. MC3T3-E1 basal culture media consist of Dulbecco's Modified Eagle's Medium (DMEM) (Invitrogen) supplemented with 10% FCS (PAA Laboratories).
5. Osteogenesis Media (OM) for MG63s: basal media supplemented with 50µg/ml AA, 5mM βGP and 100nM Dexamethasone (Dex) (Sigma, UK).
6. Osteogenesis Media (OM) for MC3T3-E1: α-MEM supplemented with 10% FCS, 50µg/ml AA, 5mM βGP (Sigma, UK).

3.2.3.2 General cell culture condition

All cells were cultured in T75 flasks using appropriate basal media and incubated at 37°C with 5% CO₂. Media was changed every 2-3 days along and the cell morphology and density were visually examined. Cells were passaged when they were confluence, this was done by removing cell media and washing the cells with PBS twice before adding 2 ml of trypsin-EDTA and leaving to incubate for 5 min to allow cells to detach. Cell morphology was observed to ensure cells were detached from the flask before adding media to halt the trypsin-EDTA reaction.

The detached cells in suspension were then centrifuged at 1000rpm for 5 mins, and the supernatant was poured away. The remaining cells were suspended in a known volume of media and a cell count was performed using a haemocytometer. The remaining cells were split 1:10 to new T75 flasks. Basic culture media were added to give a total volume of 12ml per flask and were incubated

Cells to be used in future experiments were suspended in a 10% DMSO in FCS solution and placed in a isopropanol jacket and stored at -80 °C for 24 h before moving to the liquid nitrogen for long term storage.

To defrost cells, a vial was taken from the liquid nitrogen and placed in the water bath until the contents melted. The vial was then rinsed with 1ml media to a T75 flask, which was placed in an incubator at 37°C and 5% CO₂. After 5h, the media was removed and replenish in fresh media to remove any remaining DMSO. After 24 h the medium was removed from the flask and cells were rinsed twice with PBS.

3.2.3.3 Sample preparation and seeding

Selected PEO samples were sterilised in a culture dish with 70% ethanol and rocked steadily for 3 h. After sterilisation, the samples were washed three times with PBS to remove any remaining ethanol and rocked for 20 min. The samples were then submerged in culture media containing serum and kept overnight in the incubator. Excess media was removed before seeding.

The low volume seeding method was employed in this study. The appropriate volume of cell suspension (with required number of cells) were dispensed onto the centre of the sample. The cells were allowed to attach for at least 60 min before scaffolds were submerged in fresh media. The samples were transferred to new well-plates 24 h after seeding, and replenished with fresh media with the required supplements added.

When the cells are introduced to a surface, they attach to the surface via non-specific electrostatic forces, which had been suggested to be influenced by surface roughness. This is followed by cell spreading, proliferation and differentiation. Although the time scale for these processes can vary between cell lines and passage number it is commonly accepted that cell attachment can be measured up to 24 h after seeding and proliferation can be measured at 7 and 21 days [99].

3.2.3.4 Assessing cell viability

PrestoBlue Cell (Invitrogen, UK) viability assay is a rapid evaluation method to measure the viability and proliferation of cells. The assay is resazurin based, where the reagent is reduced by metabolically active cells. The PrestoBlue assay was performed by removing media from cells and washing with PBS to remove any residue. Before incubating with diluted 1:10 of PrestoBlue reagent and culture media for 50 min at 37 °C with 5% CO₂. The fluorescence of the resulting solution was determined using a 96-well plate reader at 590 nm, with excitation wavelength of 560 nm.

3.2.3.5 Alkaline phosphatase (ALP) assay

Alkaline phosphatase is an early marker of osteogenic differentiation using a colorimetric assay involving the conversion of p-nitrophenol phosphate substrate to p-nitrophenyl and recording the rate of colour change from colourless to yellow. Cells were detached from the sample using trypsin/EDTA solution, and washed with PBS three times, the re-suspend in 200 µl of 0.1% Triton X-100, 10 mM Tris-Cl (pH = 7.5), 1 mM MgCl₂ and underwent 4

cycles of freeze-thaw and sonication. After that, 100 μ l of *p*-nitrophenyl phosphate (pNPP) was added to 10 μ l of cell lysate followed by incubation for 30 min at 37 °C. The reaction was stopped by adding 0.4 M of NaOH and the plate was read at a wavelength of 405 nm by Stat Fax 3200 microplate reader (Awareness Technology Inc). The ALP activity was determined as a rate of *p*-nitrophenol liberation from *p*-nitrophenyl phosphate and expressed as nmol of *p*-nitrophenol formation per minute per milligram of cellular protein. All measurements were reported as the mean average value \pm standard deviation.

3.2.3.6 Morphometric analysis

Cells were fixed by formaldehyde after 24 h and was examined using an Axioplan microscope (ZEISS) equipped with 40 \times objective and Olympus DP-100 camera. ImageJ software was used to determine the average area of individual cells cultivated on the samples, 30 cells in total were analysed per sample.

3.2.4 Statistical analysis

To test whether differences were statistically significant, one-way ANOVA was performed followed by Tukey's post-hoc test. Unless otherwise is stated, the graphs are plotted as the mean average value \pm SD, with significant differences marked $p < 0.05$.

Chapter 4: Effect of calcium salts in the electrolyte on the characteristics of PEO process and resulting coatings

This chapter concerns the selection of appropriate calcium salts for PEO processing of Ti alloys. It discusses the main preliminary work that was performed to study electrolyte characteristics and the electrochemical behaviour of titanium alloys using the cyclic voltammetry (CV) method. The CV approach is a well established technique in electrochemistry, however up to now it has been mainly overlooked in PEO related research. We are among the first to apply it to the PEO process in an attempt to understand its utility for process development.

4.1 Introduction

Calcium acetate is one of the most common calcium salts used for PEO treatment of Ti and numerous studies continue to optimise the coating and/or post treatment parameters to form HA on the surface [40, 41, 100]. The reasoning behind using calcium acetate based electrolyte for PEO treatment is still unclear. Apart from the use in PEO treatment, calcium acetate is a pharmaceutical buffering agent which is commonly administered orally as a source of calcium and phosphate binder. Therefore, the combination of the pharmaceutically approved compounds with good solubility of all acetate salts could attribute to the interest in using this salt for the PEO treatment to form bioactive coatings. Nevertheless, in order to expand the range of calcium salts suitable for PEO treatment, calcium compounds that are known to be dietary sources or used in biomedical field with reasonable ranges of solubility in water, are discussed below.

Table 2 shows a range of calcium compounds that are already being in use clinically or as food additives, and their molecular weights and solubilities are compared with those of the commonly used calcium acetate. Compounds with only calcium cations are discussed here to simplify the initial search. The list includes calcium ascorbate or more commonly known as Vitamin C, which plays a crucial role for human to promote healthy skin, teeth and bone [101]. Low level of Vitamin C will result in scurvy. Calcium formate has been suggested to be used as dietary supplement for prevention and management of osteoporosis [102]. Moreover, it is currently discussed as an alternative to antibiotic growth promoters in animal rations [103], therefore it has been used as calcium source in animal diets for many years. Calcium L-lactate and D-gluconate are used as nutritional supplement to prevent

hypocalcaemia. They are also receiving increasing attention in the food industry as functional food and improve bone and teeth health [8, 104, 105] as it has shown to be able to increase remineralization of tooth enamel.

Table 2 List of calcium salts of interest.

| Chemical compound | Chemical formula | Molecular weight | Solubility (20°C) Per 100 ml H ₂ O |
|---------------------|---|------------------|--|
| Calcium acetate | Ca(C ₂ H ₃ O ₃) ₂ | 176.18 | 34.7g |
| Calcium ascorbate | CaC ₁₂ H ₁₄ O ₁₂ · 2H ₂ O | 426.34 | 50g |
| Calcium formate | Ca(HCOO) ₂ | 130.11 | 16.6g |
| Calcium D-gluconate | CaC ₁₂ H ₂₂ O ₁₄ | 430.37 | Low |
| Calcium hydroxide | Ca(OH) ₂ | 74.09 | 0.173g |
| Calcium lactate | CaC ₆ H ₁₀ O ₆ · 5H ₂ O | 218.22 | 5g |
| Calcium propionate | CaC ₆ H ₁₀ O ₄ | 186.22 | 49g |

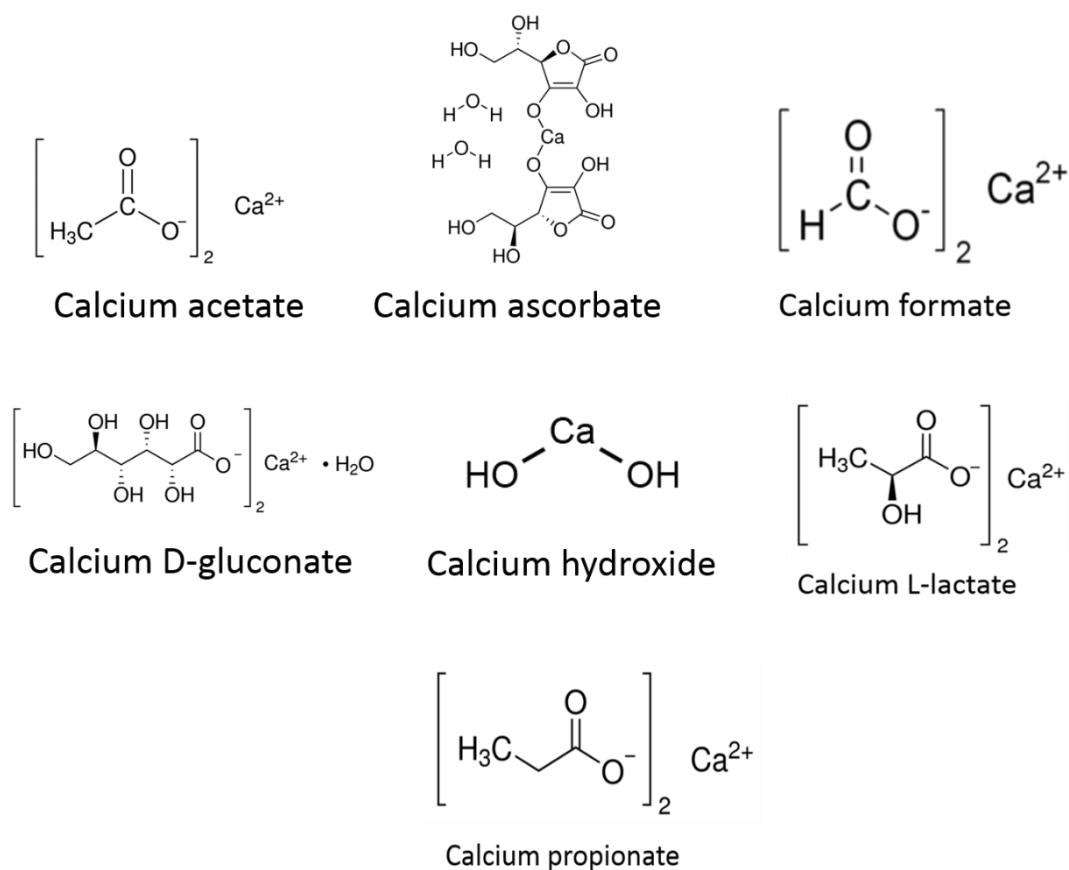


Figure 10 Skeletal structure of the calcium salts considered in this study.

Apart from the safety of the chemical compound, the cost and reactivity must also be taken into consideration. From the manufacturing economic perspective calcium ascorbate is highly expensive (~ £48 for 100 mg) and therefore it is not commercially viable for PEO treatment as a large quantity is required. From the perspective of chemical compound behaviour, calcium D-gluconate contains a gluconic acid group, the addition of hydroxyl groups when compared to calcium acetate could potentially aid the formation of crystalline HA on the PEO coating surface, although further investigations are required. Solubility is influenced by the chemical chain length of the compound [104], and therefore when compared to other calcium compounds containing hydroxyl groups, calcium D-gluconate shows inferior property. Other calcium sources such as oxalate and citrate which also contain oxygen and carboxyl groups, respectively were not considered here due to the toxicity and low solubility of the compounds.

In order to perform a systematic study to the range calcium sources suitable for PEO processing of Ti alloys, the electrolyte concentration is chosen to be the same (0.2 M of

calcium salt and 0.1 M of sodium orthophosphate). Calcium formate, acetate and propionate are all calcium salts of carboxylic acid with increasing number of carbon atoms. Therefore, comparison of these compounds allows to analyse the effects of chain length in the compound on the electrochemical behaviour of Ti alloys in a wide voltage range. Calcium L-lactate is also selected for further investigation as it contains a hydroxyl group, which, as mentioned previously, could potentially be beneficial for HA formation.

Apart from electrolyte composition, the electrical parameters also have a crucial role in the PEO process. As a result, numerous studies focus on optimising the processing parameters to form bioactive coatings using calcium acetate based electrolytes are conducted, whereas little attention is paid to understanding of the fundamental electrochemical processes occurring during the treatment. The fundamentals of the PEO process, as described in Chapter 2, are based upon the studies of the formation mechanisms from electrochemistry point of view [8], taking into account discharge characteristics, e.g. by using in-situ impedance spectroscopy which allows understanding discharge events and their effect on the coating formation [106]. However, the results are still inconclusive due to the complexity of both the analytical technique and the PEO process itself. An alternative approach consists in using the corresponding voltage/current transient to correlate the discharge phenomena and coating microstructure [15]. Based on these approaches, the system behaviour and coating growth rate during conventional anodising and sparking stages can be categorised [14, 107].

A vast amount of work is conducted to understand discharge phenomena and the growth mechanism of coatings. This however provides information limited to a set of boundary conditions and would require extensive analysis of raw data to develop understanding of the physical meaning of each component in the system.

For that reason, new methods that can provide a rapid identification of electrochemical process occurring in the range of potentials are required in PEO related research. The cyclic voltammetry method was adopted to understand the complex coating formation process during PEO such as the underlying metal-electrolyte interactions. CV is a common technique used to investigate mechanisms and kinetics of electrochemical processes [108-110]. It is conventionally conducted by sweeping between two potentials at a relatively narrow range (approximately -0.2 to 1.5 V) using Pt as anode. In our work, CV technique is adapted to understand the complexity of the coating formation mechanism involved during the PEO process. Therefore a large voltage range is used in CV experiment employing cp-Ti and Ti-

6Al-4V anodes, the two Ti alloys most commonly used in biomedical field. These experiments aim to examine the metal and electrolyte interactions throughout the range of voltages used for PEO treatment. The electrochemical behaviour of both cp-Ti and Ti-6Al-4V alloys in various electrolytes is examined, as there is a surprising lack of studies addressing the influence of substrate alloying elements on the coating formation process for biomedical purposes, despite strong evidence indicating that PEO treatment is strongly dependent on the passive film formed on the surface of the valve metal [8, 80, 81, 111]. Yet, current studies appear to cross-reference the results deduced on the formation of bioactive coatings from one alloy to another.

Single cycle voltammetry (SCV) was conducted as positive sweep only, starting at 0 V and moving into the anodic direction to 500 V, followed by a short halt, and returning back to 0 V. The large voltage range was used to investigate the series of discharge phenomena that appear during plasma electrolysis, moreover as coating formation process essentially occurs during oxidation, the CV approach was modified to only examine the mechanisms and kinetics in the anodic region. The analysis of the current response in the voltammogram, and the presence of current peak is known to correlate to a specific electrode process occurring in a given range of electrode potentials. The voltammograms were recorded at a single scan rate of 2 V/s. A variation in the scan rate could alter the kinetics of the reactions at the surface and is commonly used to understand mechanisms of charge transfer and evaluate reaction rate constants as well as electrochemical behaviour of chemicals in aqueous solutions. However, this was not pursued at this stage of the study that aims primarily at phenomenological characterisation of electrochemical behaviour of Ti alloys in calcium formate, acetate, propionate and L-lactate based electrolytes and its correlation with the mechanisms underlying the PEO process.

4.2 Results

4.2.1 Influence of calcium salt on the electrolyte characteristics

Table 3 The effect of calcium salt in the electrolyte on the electrolyte properties.

| Electrolyte composition | | Electrolyte property | | |
|-------------------------|--------------------|------------------------------|----------------------|----------|
| | | pH | Conductivity (mS/cm) | |
| 0.2M | Calcium formate | Sodium orthophosphate (0.1M) | 9.11±0.4 | 27.5±1.3 |
| | Calcium acetate | | 9.18±0.2 | 24.4±2.5 |
| | Calcium propionate | | 7.6±0.1 | 26.0±2.0 |
| | Calcium L-lactate | | 10.79±0.8 | 18.8±0.8 |

Table 3 displays the influence of calcium salt on the electro-physical properties of electrolytes in the temperature range from 15 to 30 °C, which is the typical electrolyte working temperature during the PEO treatment. It had been proposed that the Ca content has a significant influence over the formation of calcium phosphate phases and the discharge behaviour during the PEO treatment. Therefore the Ca/P ratio of the electrolyte was set at 2 for simplicity.

Results in Table 3 show that all electrolytes are mildly alkaline, meanwhile the calcium propionate based electrolyte is weakly alkaline. The calcium L-lactate based electrolyte shows a comparatively stronger alkalinity. This could be attributed to the presence of the hydroxyl group (-OH) in the calcium L-lactate (shown in Figure 10f), which could potentially increase the alkalinity of the electrolyte.

4.2.2 Influence of calcium salt in the electrolyte to the cyclic voltammetry behaviour of Ti anodes

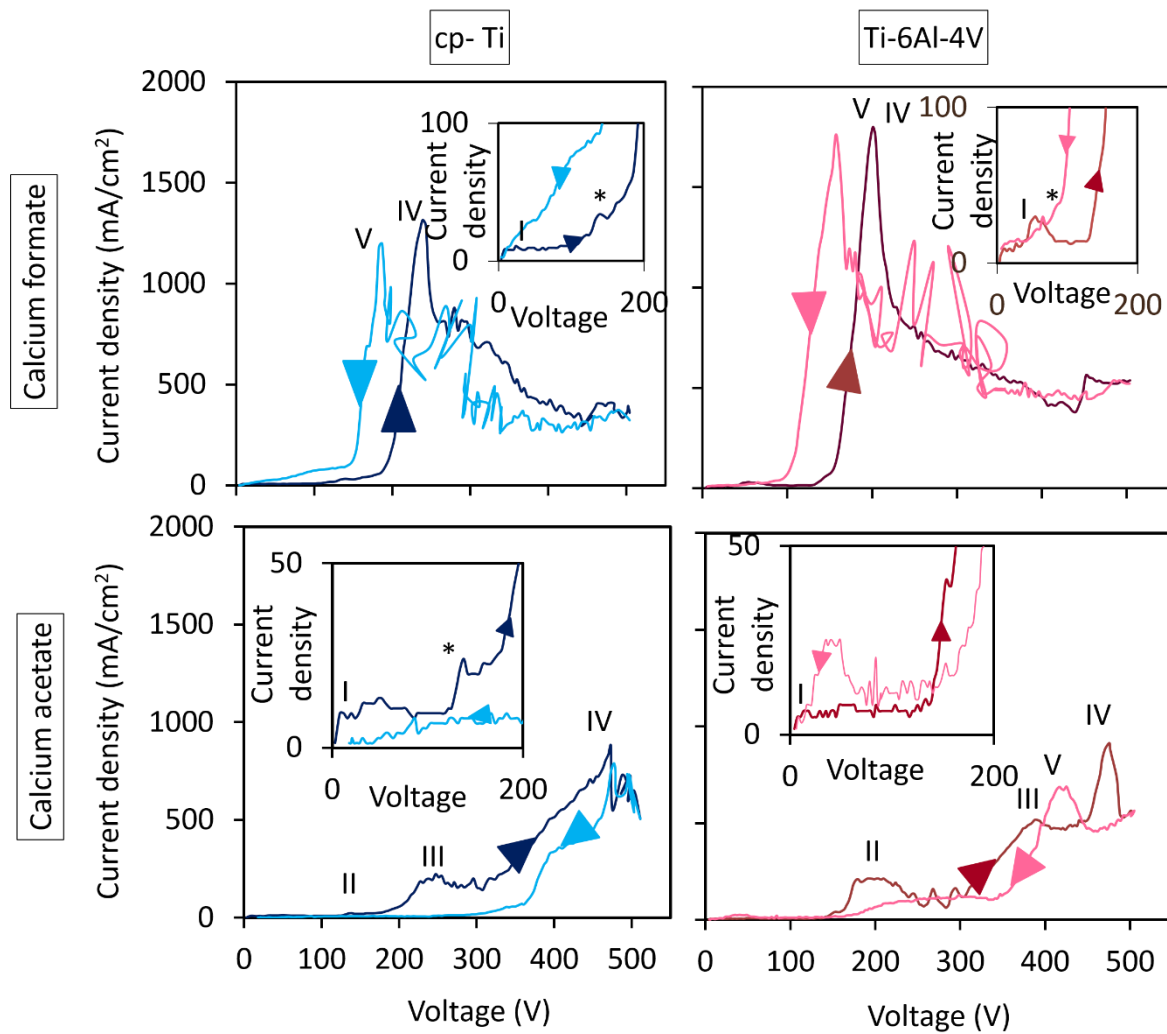


Figure 11 Cyclic voltammogram of cp-Ti and Ti-6Al-4V substrate in calcium formate and acetate based electrolytes, the direction of arrow represent the direction of scan.

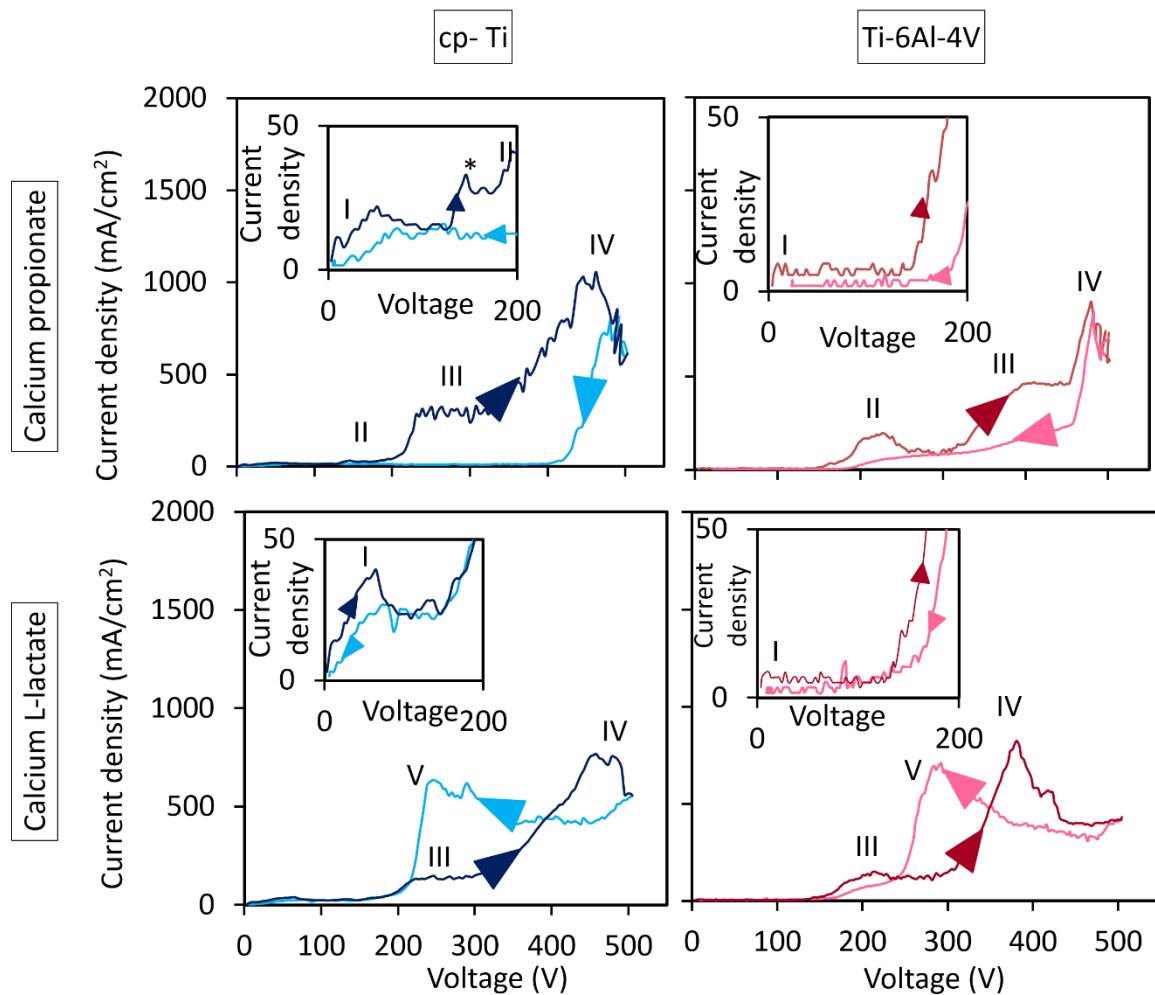


Figure 12 Cyclic voltammogram of cp-Ti and Ti-6Al-4V substrate in calcium propionate and L-lactate based electrolytes, the direction of the arrow represent the direction of scan.

Figure 11 and 12 reveal the current response to the voltage sweep of the two commonly used clinical Ti alloys in the studied electrolytes. The experiments were conducted to determine the kinetics of electrochemical processes over the wide range of anodic potentials. The CV curves can be categorised as the forward (voltage increasing) and reverse (voltage decreasing) scans. The direction of arrows represent the direction of the scan. It is hoped that the peaks in the scan can give an indication of the reactions occur at the surface of the anode within the electrolyte. In the forward scan, a small peak I at approximately 20 V was observed in all curves, this peak was suggested to be related to the electrochemical adsorption of phosphate ions from the electrolyte [112].

A sharp peak in the voltammogram at approximately 80 to 150 V which is marked by the asterisk can be observed in some curves. This small peak does not appear to be a result of

oxide formation leading to disturbance in the potential profile at the anode surface. Instead, it could be a result of oxygen generation during anodising. Habazaki *et al* [113] and Teh *et al* [114] proposed that anodic processes occurring at around 20 to 50 V correspond to oxygen generation during amorphous to crystalline transition in the oxide film during anodising of Ti alloy. In our study, among the sharp peaks observed at around 80 to 150 V, those developed on the cp-Ti anode appear to locate at a higher voltages compared to the Ti-6Al-4V anode.

Peak II is observed in the voltammograms in the range from 130 to 220 V; this peak was suggested to be related to a multi-electron oxidation process [109, 110]. This could be associated with dissolution of previously formed passive film resulting in a reduction of the system's resistance [8]. It may be that within this voltage range, defects are formed on the surface, contributing sites for subsequent dielectric breakdown. The intensities of peaks II are higher on Ti-6Al-4V anodes than on cp-Ti. This could be explained by the comparatively higher resistance to the migration of O^{2-} and OH^- ions at the metal/oxide interface at the initial stages of the treatment due to the microstructure of Ti-6Al-4V alloy [113, 115, 116]. The fact that peak II is located at higher voltages when Ti-6Al-4V anode was used confirms that alloying elements present in the substrate have significant impact to the properties of the passive film [8].

A plateau region III can be observed in the cyclic voltammogram for both anodes when calcium acetate, propionate and L-lactate based electrolytes were employed. This region corresponds to the occurrence of micro-arcing and is observed from approximately 200 V on cp-Ti anode, while it is varied from 150 to 300 V on Ti-6Al-4V. Beyond region III, the current increases up to the final peak IV which is observed in the high voltage range (350 to 500 V). It can be assumed that the high current growth rate in that region corresponds to more vigorous reactions associated with PEO treatments. Peak IV is defined as the region above which powerful arcing would occur, which would lead to intense rupture and spallation of the oxide film, which would at least partly destroy the coating. Its location appears to be dependent on both electrolyte composition and anode material. In the reverse scan, peak V is observed in some curves; this is an indicator of reversible electrochemical behaviour in the system. It is possibly a result of soluble products formed on the electrode surface during the forward scan, which were dissolved during the reverse scan.

When calcium formate was used in the electrolyte, the current density increased dramatically in a very narrow voltage range of the forward scan (200 – 210 V for cp-Ti and 150 – 200 V

for Ti-6Al-4V) up to peak IV before showing a disturbance and drop in the current density in the CV curves. This suggests the electrolyte is highly unstable at voltages as low as 150 V, and therefore is not suitable for the PEO treatment, which usually operates in a high voltage range. When Ti-6Al-4V anode was used, peak V is observed in the reverse scan, at approximate range to peak IV in the forward scan, indicating the reaction corresponding to this potential region is reversible.

For calcium acetate containing electrolyte, the current-voltage behaviour showed features consistent with irreversible electrochemical processes when cp-Ti anode was used, while reversible behaviour was observed on the Ti-6Al-4V anode. This further confirms the influence the substrate alloy has on the PEO process. The cyclic voltammogram of cp-Ti anode in calcium propionate based electrolyte revealed disturbance in the current response over a range of voltages, which is an indicator of the anode surface undergoing localised unstable reactions which do not appear to influence the overall electrochemical reactions at the surface.

When calcium L-lactate was used in the electrolyte, a well-defined peak V can also be noted in the voltammogram, pointing to the reversibility of the anodic process in this voltage range [117]. In the reverse scan, peak V was detected at a much lower voltage range, suggesting possible depolarisation of the electrochemical process when compared to that in the electrolyte containing calcium formate. When cp-Ti anode was used in the calcium L-lactate electrolyte, the shape of peaks IV and V becomes broader than those observed on the Ti-6Al-4V anode. This suggests more than one electrochemical process may be occurring at the anode [110]. Meanwhile, barely defined peaks II on the voltammograms of both anodes suggests the possible adsorption of electrolyte ions at the surfaces could mask the influence of the passive film behaviour, suppressing ruptures occurring in the oxide.

It is interesting to observe a less defined oxidation peak II on the cp-Ti anode and a higher peak voltage when the Ti-6Al-4V anode was used, which indicates significant influence of substrate material on the PEO process, implying the oxidation is facilitated on the cp-Ti compared to the Ti-6Al-4V anode.

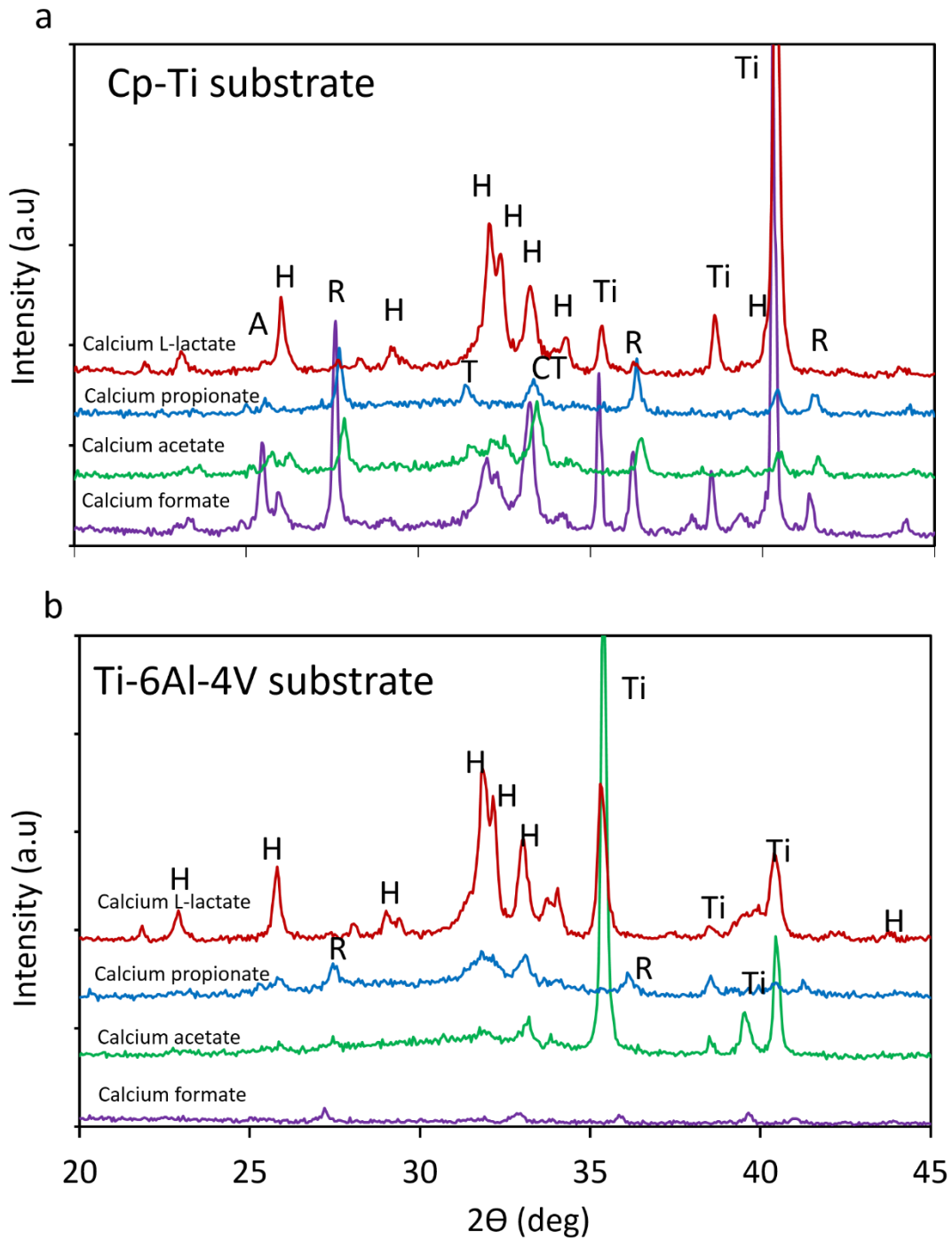


Figure 13 XRD spectra of coatings formed in calcium formate, acetate, propionate and L-lactate based electrolytes on (a) cp-Ti and (b) Ti-6Al-4V substrates. (A, anatase; R, rutile; Ti, titanium and alloy; T, tri-calcium phosphate; CT, calcium titanate; H, hydroxyapatite)

Figure 13 reveals phase compositions of coatings produced using the CV technique on cp-Ti and Ti-6Al-4V substrates in the electrolytes with the studied calcium salts. Figure 13a and b illustrate the impact of alloying elements in the substrate to the coating phase composition. Peaks corresponding to anatase and rutile are observed in the XRD spectra of the coatings formed on the cp-Ti substrate, with rutile peaks being systematically higher than those of anatase. It has been proposed that the anatase to rutile phase transformation is a time dependent process, which is consistent with the wider separation between peaks III and IV observed for the cp-Ti substrate in Figure 11 and 12, allowing longer micro-arc region to enhance nucleation of rutile [118]. In general, it can be noted that coatings produced on the cp-Ti substrate feature more crystalline phases compared to those produced on the Ti-6Al-4V substrate. This could be a result of the presence of aluminium in the latter, which is known to suppress the nucleation and growth of crystalline oxide of the TiO₂ phase [113].

The XRD spectrum of the coating produced using calcium acetate based electrolyte on the cp-Ti substrate reveals intensity of Ti peaks to be systematically higher than those in the coating produced on Ti-6Al-4V anode. A comparatively broader peak in the region $2\Theta=30-34^\circ$ suggests presence of crystalline HA with amorphous CaP constituents in the coating on the Ti-6Al-4V alloy.

When calcium propionate based electrolyte was used, TCP and CaTiO₃ peaks were detected in the XRD spectrum of the coating produced on the cp-Ti substrate, meanwhile for the coating produced on the Ti-6Al-4V substrate, the peaks matching the HA phases were observed.

Peaks that correspond to HA can be observed on the coating produced in calcium L-lactate on both cp-Ti and Ti-6Al-4V substrates. This indicates the electrolyte is highly favourable to form crystalline HA phases in the coating. The intensity of Ti peaks in the XRD pattern of the coating formed on cp-Ti (Figure 13a) is systematically higher than those of the coating produced in the same electrolyte on Ti-6Al-4V (Figure 13b).

Overall, it appears that the cp-Ti substrate is more favourable for formation of crystalline phases than Ti-6Al-4V; this confirms the influence of substrate alloying elements to the coating phase composition. The above results suggest that calcium L-lactate based electrolyte is highly favourable for the formation of crystalline HA phase in the coating, but this would require further analysis.

4.2.3 Effect of calcium salt to the coating morphology and elemental composition

Surface morphologies of the coatings produced using different calcium salt based electrolyte are displayed in Figure 14 and Figure 15. Results indicate that substrate alloying elements influence the surface morphology as well as the phase composition.

The coating produced on the cp-Ti substrate in the calcium formate based electrolyte has shown few large pores on the surface which also appears to feature small agglomerates as indicated by the arrows. Moreover, there are structures on the surface that correlate with dehydration of the coating (marked by the blue circle). When the Ti-6Al-4V substrate was used in the same electrolyte, the coating exhibits areas of re-melting. Small porous features are observed sparsely located on the surface, with the majority of the area covered by a dense layer of translucent matrix. The surface morphology of the coatings produced on both alloys in the calcium formate based electrolyte suggests development of destructive powerful arcing during the treatment. Figure 14 reveals the coatings produced in the calcium acetate based electrolyte on both cp-Ti and Ti-6Al-4V substrates exhibit high variation in surface morphological features. Porous morphology can be observed on the coating produced on the cp-Ti, while agglomerates and comparatively denser translucent matrix is observed on the coating produced on Ti-6Al-4V.

Porous features can be observed on the coating produced in the calcium propionate electrolyte, although it must be noted that the structure of the two coatings suggests variations in the intensity of reactions occurred at the surface. Pore-in-pore structures can be observed in the coating produced on cp-Ti; moreover there are doughnut-like features which indicate development of powerful arcing during the treatment. Open pores are also detected in the coating produced on Ti-6Al-4V and shown variation in heights on the surface. It is interesting to note the matrix on the surface displays a comparatively coarser appearance on Ti-6Al-4V than that on cp-Ti.

A porous morphology was also observed for the coating produced on cp-Ti in the calcium L-lactate electrolyte. The pores are comparatively smaller than those observed when same substrate was used in calcium propionate and acetate electrolytes. On the other hand, when Ti-6Al-4V alloy was used, large deposits forming agglomerates can be observed on the surface (Figure 15).

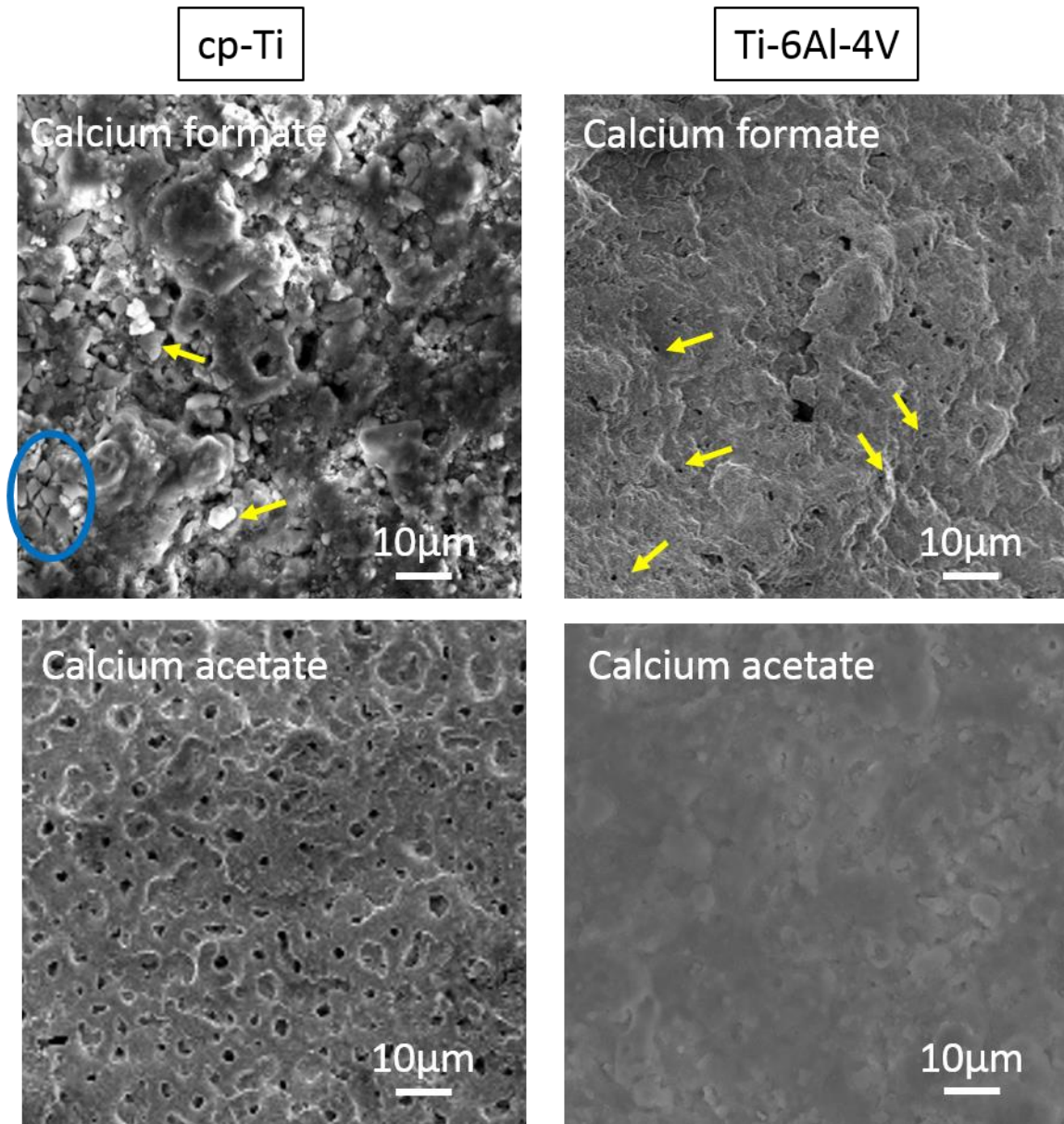


Figure 14 Surface morphology of coatings produced on cp-Ti and Ti-6Al-4V substrates in calcium formate and acetate based electrolytes.

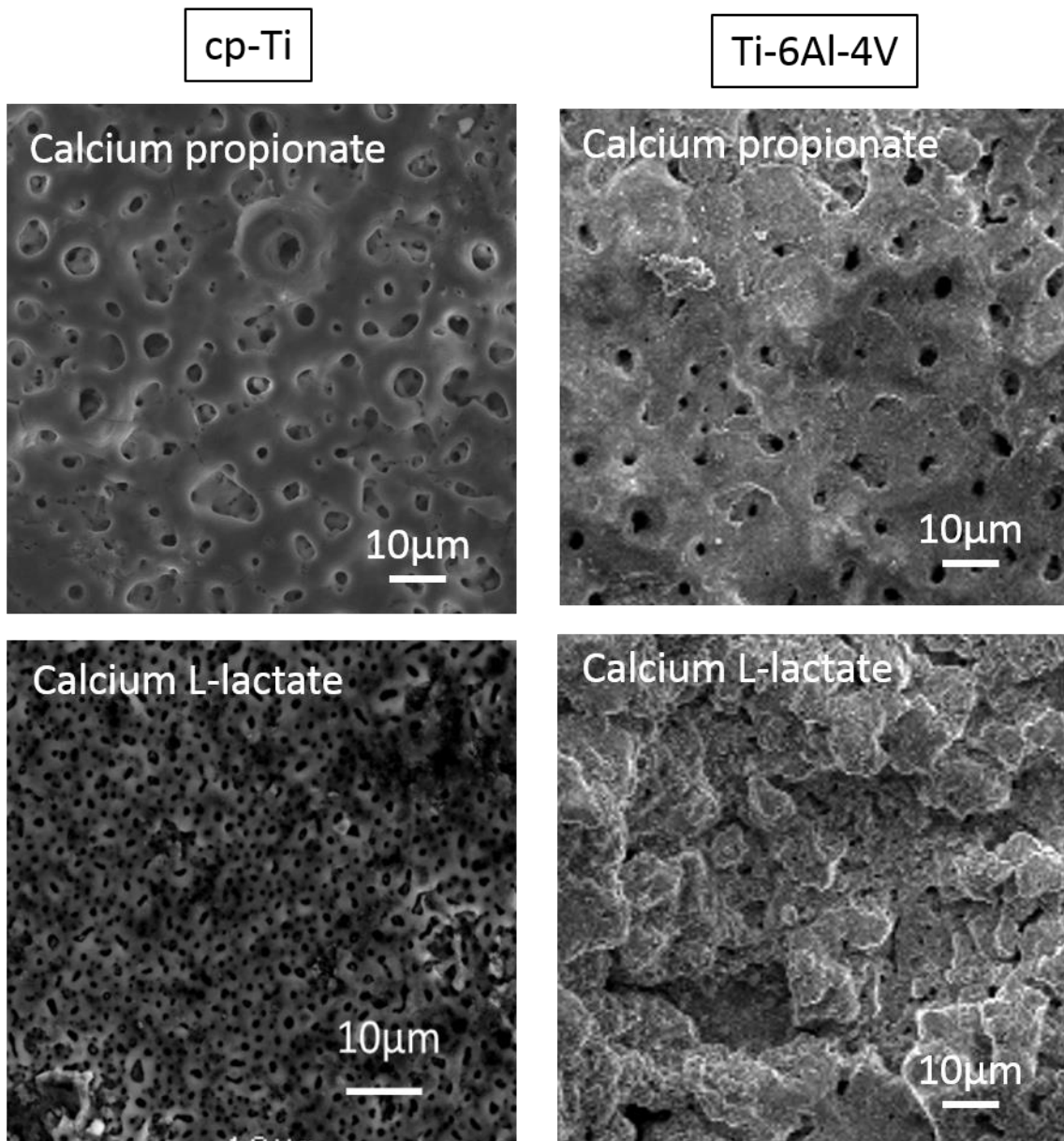


Figure 15 Surface morphology of coatings produced on cp-Ti and Ti-6Al-4V substrates in calcium propionate and L-lactate based electrolytes.

Table 4 Relative atomic percentages of elements on the surface of the coatings produced on (a) cp-Ti and (b) Ti-6Al-4V substrates.

a

| Elemental composition (at%) | Calcium formate | Calcium acetate | Calcium propionate | Calcium L-lactate |
|-----------------------------|-----------------|-----------------|--------------------|-------------------|
| Ca | 14 | 11 | 8 | 4 |
| P | 7 | 6 | 2 | 5 |
| Na | 1 | 1 | 1 | 1 |
| Ti | 6 | 8 | 17 | 18 |
| O | 63 | 64 | 68 | 66 |
| C | 9 | 10 | 4 | 6 |
| Ca/P | 2 | 1.8 | 4 | 0.8 |

b

| Elemental composition (at%) | Calcium formate | Calcium acetate | Calcium propionate | Calcium L-lactate |
|-----------------------------|-----------------|-----------------|--------------------|-------------------|
| Ca | 10 | 11 | 9 | 8 |
| P | 5 | 4 | 4 | 5 |
| Na | 1 | 1 | 1 | 1 |
| Ti | 10 | 10 | 11 | 16 |
| O | 63 | 64 | 66 | 69 |
| C | 10 | 8 | 7 | - |
| Al | 1 | 1 | 1 | - |
| V | - | 1 | 1 | 1 |
| Ca/P | 2 | 2.8 | 2.3 | 1.6 |

Table 4 presents the elemental composition of coatings produced using the CV technique on cp-Ti and Ti-6Al-4V substrates in the electrolytes with various calcium salts. The Ca/P ratio of the coatings produced using calcium formate based electrolyte on both alloys has shown to be similar and agrees well with the Ca/P ratio in the electrolyte, which was set at 2.

The calcium content in the coatings produced using calcium acetate based electrolyte on cp-Ti and Ti-6Al-4V substrates has also shown to be similar, but the reduction in the P content

in the latter substrate resulted in a higher Ca/P ratio in the coating. Similar behaviour is observed when calcium propionate based electrolyte was employed, where the Ca contents in the coatings on both alloys are similar, with the P content on the coating produced on the cp-Ti substrate being as low as 2 at%. This leads to a comparatively higher overall Ca/P ratio of the coating (Ca/P = 4). For the coatings produced using calcium L-lactate based electrolyte, the P content appears to be similar with a vast difference in the Ca content between the coatings produced on cp-Ti and Ti-6Al-4V substrates. This results in the overall Ca/P ratio of the coating formed using calcium L-lactate based electrolyte on the Ti-6Al-4V substrate to be doubled that in the coating produced on cp-Ti substrate. Although limitations of EDX analysis in quantitative detection of light elements such as O and C, must be born in mind, the data can provide an indication of possible burning occurring on the sample surface.

4.3 Discussion

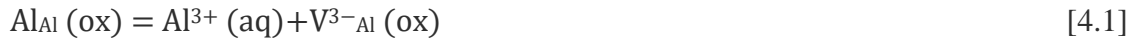
Results presented in the chapter have demonstrated the effect of alloying elements in the substrate on the electrochemical reactions occurring in the range of potentials used for PEO treatment. Furthermore, alternative to acetate calcium salts can also lead to theoretically positive outcome for production of bioactive coatings using PEO approach. The following sections discuss the results from an electrode kinetic aspect of the chemical reactions occurred during the range of potentials use for PEO treatment.

4.3.1 Influence of substrate alloying to the chemical reactions during the PEO treatment

The present results showed that the substrate alloying can lead to a considerable impact to the electrochemical behaviour over a wide range of voltages used for PEO treatment. It is accepted that the substrate Ti would undergo the electro-chemical reactions as mentioned in Equations [2.1] to [2.5] during the PEO treatment as discussed in Chapter 2. Soares *et al* [119] suggest the influence of substrate alloy composition is dominant during conventional anodising (approximately <135V), however above the dielectric breakdown voltage, the influence of alloying elements is suppressed by micro-arcing. However, the voltammogram behaviour observed in Figure 11 and Figure 12 suggests alloying elements in Ti substrate have a significant influence on their electrochemical behaviour in the whole range of studied potentials. Furthermore, the EDX results displayed in Table 4 indicate Al and V are present

at the surface of some coatings, which confirms the hypothesis that the alloying elements play a role in the coating formation.

Moon and Jeong [120] proposed that the oxide film formation on aluminium involves the following reactions;



Since $\text{Al}^{3+}(\text{aq})$ is not stable in alkaline solution it favours the reaction [4.3], which is consistent with the presence of a high intensity peak II on those recorded on Ti-6Al-4V substrate. Furthermore it is interesting to observe when both Al and V are detected on the surface of the coating produced in calcium acetate and propionate based electrolyte, a distinctive peak II can be observed in the voltammogram and followed by a depression. It can be assumed that dissolution of that oxide layer after formation to a certain thickness would occur. Furthermore, apart from the formation of Al_2O_3 , the presence of Al in the Ti-6Al-4V alloy could cause formation of Ti- Al_2O_5 crystals [121] which can be assumed to lead to differences in the coating formation mechanism compared to those produced on cp-Ti.

In higher voltage range where peak IV is observed in the voltammogram, it can be seen that the peak in the system with Ti-6Al-4V anode exhibits a sharper shape compared to that in the system with cp-Ti. The broader peaks in the latter imply more than one electrochemical process may be occurring at the anode at high voltage ranges [110]. This finding complies with the detection of higher intensity of crystalline phases in the coatings produced on cp-Ti than those on Ti-6Al-4V alloy.

Peak IV in the voltammogram marks the region of powerful arcing, the drop and disturbance in current density past peak IV in the forward scan could be attributed to the development of powerful arcing leading to intense rupture and spallation of the oxide film which would partly destroy the coating, exposing regions of bare substrate, wherein very high local current densities could trigger additional processes of electrolyte boiling and thermal decomposition of water;



Presence of aluminium in the substrate could potentially assist oxygen evolution [120], which is consistent with a more vigorous current response observed in the post-peak IV region of the forward scan in the CV curves obtained on the Ti-6Al-4V anode. It must also be noted that the differences in the electrolyte pH would also have a certain impact on the electrochemical response during the process. However, at this stage it is difficult to isolate the correlation between the solubility, pH and conductivity and their impact on the electrochemical behaviour at the range of voltages employed.

4.3.2 Anodic oxidation of various calcium salt solution during the PEO treatment

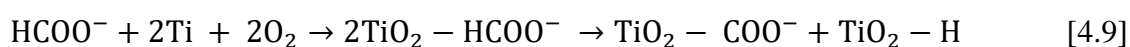
The relationship between the cyclic voltammetry behaviour and the electrochemical reaction of anodic oxidation of Ti in various calcium-containing electrolytes is not fully understood. It had been accepted that the effectiveness of an electrolyte for anodic oxidation is dependent on the function of the electrolyte ability to dissolve the anodic product. Various calcium salts were examined in the wide range of voltages commonly used for PEO treatment, and different types of behaviour have been observed.

The voltammograms of cp-Ti and Ti-6Al-4V substrates in the calcium formate electrolyte reveals a comparatively low stability of the anodic oxidation process with a sharp current increase to peak IV at a low voltage range. The vigorous reactions observed on both Ti alloys are consistent with the electrochemical behaviour of formic acid. The standard electrode potential of formic acid/CO₂ redox couple is -0.25 V [122], but the electro-oxidization takes place at potentials that are 0.6 V higher than the reversible thermodynamic potential of Pt [123]. It is important to emphasize in this study that sodium orthophosphate was also added to the electrolyte and the anode materials are cp-Ti or Ti-6Al-4V. Therefore it can be speculated that the combination of the differences in the anode material and electrolyte conductivity [124], and that formate is less readily oxidised on Ti compared to Pt would result in the shift in this behaviour to a higher range of potentials.

Cai *et al* [125] investigated the decomposition of formic acid on Pd and Pt surfaces and proposed that it can proceed via two routes [4.7] and [4.8a-c] ;



In relation to our work, TiO_2 is also a catalyst which could be used for decomposition of calcium formate. Therefore the highly reversible and high current wall observed in Figure 11 can be attributed to the decomposition of formate anions which generates H_2 and CO_2 .



Their work revealed a high current density peak in the forward and reverse scan, similar behaviour observed with our work. Although the potential range used is much lower (-0.4 to 1.4V) and the anode material is Pd, however it can be speculated that the behaviour observed in the CV curve when calcium formate was employed is also due to formate decomposition following a similar mechanism. The variation between current response observed in CV curves recorded on cp-Ti and Ti-6Al-4V anode for calcium formate based electrolyte can be explained by the influence of alloying elements in the substrate, possibly affecting the splitting potential in Equation [4.7].

This suggests that formate anion decomposes at the surface, where hydrogen and CO_2 are evolved [126]. Breiter [127] proposed anodic oxidation of formic acid leads to discharge of formate ions and produces an intermediate $\text{HCOO}\cdot$ radicals, as shown below.



The formate species is chemisorbed onto the surface, where the chemisorbed process is enhanced under polarisation [128]. This behaviour is similar to the Kolbe reaction which is referred to anodic oxidation of a carboxylate structure with subsequent de-carboxylation and coupling to produce a hydrocarbon or a substitute derivation corresponds to the alkyl function in the carboxylate reactant [129].

The most well-known example would be the reaction of acetate ions, where the overall process is suggested to be;



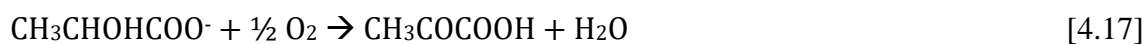
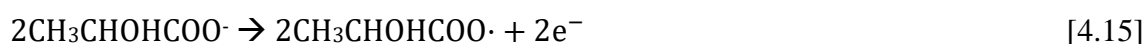
There are different mechanisms proposed for the Kolbe reactions, despite so, many theories are subjected to boundary conditions, therefore the details of the mechanisms are still controversial. It must be born in mind that the experimental conditions such as the electrolyte composition, anode material and the range of working potentials used are dissimilar and more complex to those used to examine the kinetic aspects of the carboxylic acid of Kolbe reactions. However the literature on such studies can aid the understanding of the formation of gaseous products and the electrolyte property.

The general form of Kolbe reaction is $2\text{RCOO}^- \rightarrow \text{R-R} + 2\text{CO}_2 + \text{e}^-$. Therefore it can be speculated that anodic oxidation of propionate anions will involve the following steps;



The equations [4.12] and [4.14] suggest the formation of ethyl and propoxy radicals is possible, furthermore it can be assumed that decomposition according to reaction [4.13] would result in further formation of gaseous products. On the other hand, formation of ethane from radical reaction shown in [4.14] is also feasible.

Vassilev [130] proposed that the increase in the alkyl length and side groups can influence the chemisoption rate. In this study, the calcium formate, acetate and propionate are all calcium salts of carboxylic acid with increasing carbon atoms. Meanwhile, calcium L-lactate has an -OH group when compared to the structure of calcium propionate, the data from the voltammograms proposed reversible behaviour for the former, and irreversible electrochemical behaviour for the latter. Compared to the proposed mechanism of anodic oxidation of propionate, the mechanism for lactate anion is more complex. Imprey [131] have proposed that it consists of the following steps;





It can be speculated that recombination and decomposition of the radicals and anions resulted in the complex reversible behaviour observed in the voltammogram. Equations [4.15] to [4.19] suggest that large quantity of gaseous products would be liberated during the anodic oxidation process. Furthermore, protons released at the anode (shown in Equation [4.18]) can react with pyruvate ion to form pyruvic acid, which in turn is oxidised to acetic acid. From that, it can be assumed that the anion decomposition mechanism and the interactions between the radicals result in the specific fingerprint in the CV curve observed in Figure 11 and 12.

Furthermore, Kolbe reactions proposed the liberation of gaseous products, such as CO_2 and protons such as H^+ during the reactions, which suggests that electrolyte pH should become comparatively lower throughout the experiment. This is discussed in more details for individual electrolytes in subsequent Chapters.

It must be noted that the calcium phosphate system is very complex, the range of surface morphology and phase composition observed in this study could be related to the calcium salt solubility, molecular weight and the overall electrolyte pH which could lead to various first phase precipitation and different chemical reaction in the formation of calcium phosphate phases.

The molar concentration of these salts is fixed at 2 M, therefore the weight concentration of calcium L-lactate in the electrolyte is approximately 1.6X higher than that of calcium formate. The increase in ion quantity in the electrolyte enhances solid phase precipitation and undergo transformation into phases of higher stability such as HA and OCP [132, 133]. Furthermore, Eliaz [134] have proposed when the concentration of calcium ion is higher than those of H ion in the solution, it promotes the precipitation of CaP. This could explain the presence of the set of high intensity peaks which corresponds to HA on the spectra of the coating produced in calcium L-lactate based electrolyte on both cp-Ti and Ti-6Al-4V anode (Figure 13).

Eliaz and Sridhar [135] have demonstrate that the pH = 6 favours formation of well-crystalline HA structure. Lower pH (pH = 4) would result in less crystallised and thicker structure. In PEO treatment, the electrolytes are alkaline based, and in those reactions which

does not favour production of H^+ ions during the treatment appears to promote HA precipitation by chemical mechanism.

4.4 Summary

This chapter has demonstrated the usefulness of the cyclic voltammetry method in understanding the electrochemical behaviour of Ti alloys during PEO treatments and the importance of the substrate composition for the electrochemical response of the system. In such, the CV method can be used to identify potential ranges where various anodic processes such as dissolution, oxide film formation, oxidation of electrolyte anions and precipitation of solid products, occur. Therefore it provides a quick and useful tool to obtain information on the suitability of various electrolytes and electrical control modes (galvanostatic or potentiostatic) as well as voltage/current ranges favourable for PEO treatments avoiding powerful arcing.

It is also shown that for the treatments in the calcium acetate based electrolyte which is commonly used in PEO related research, the influence of substrate appears to be complex which has been largely overlooked previously. Moreover the current/voltage diagram provides comparatively narrow voltage range for successful processing. This results in difficulties in optimising processing parameters to form HA coating using the calcium acetate based electrolyte. Meanwhile the analysis of Ti alloy behaviour in the electrolytes containing various calcium salts has opened up a new range of electrolyte compositions potentially suitable for PEO treatments. In particular, the findings in this chapter have demonstrated that calcium propionate and L-lactate can be considered promising sources of calcium in the PEO treatment to form bioactive coatings.

Chapter 5: PEO treatments of Ti alloys in the calcium propionate containing electrolytes and resulting coatings

5.1 Introduction

Chapter 4 has demonstrated that calcium propionate is a promising source of calcium in the PEO treatment to form bioactive coatings due to the stable electrochemical behaviour of Ti alloy substrates in corresponding electrolytes. However, calcium propionate has not yet been used in relation to the PEO treatment, therefore little information is available on the reactivity of propionate salts under high voltages. Therefore the present study is the first to examine in detail the electrochemical behaviour of Ti alloys in the calcium propionate based electrolytes under PEO conditions. In particular, the study aims at gaining a better understanding of the influence of the electrolyte concentration and the electrical parameters of the process to the electrochemical growth behaviour and characteristic of PEO coatings. The coatings are characterised in terms of microstructure, elemental and phase compositions. Finally, selected coatings undergo further examinations to reveal their biological response.

5.2 Results and Discussion

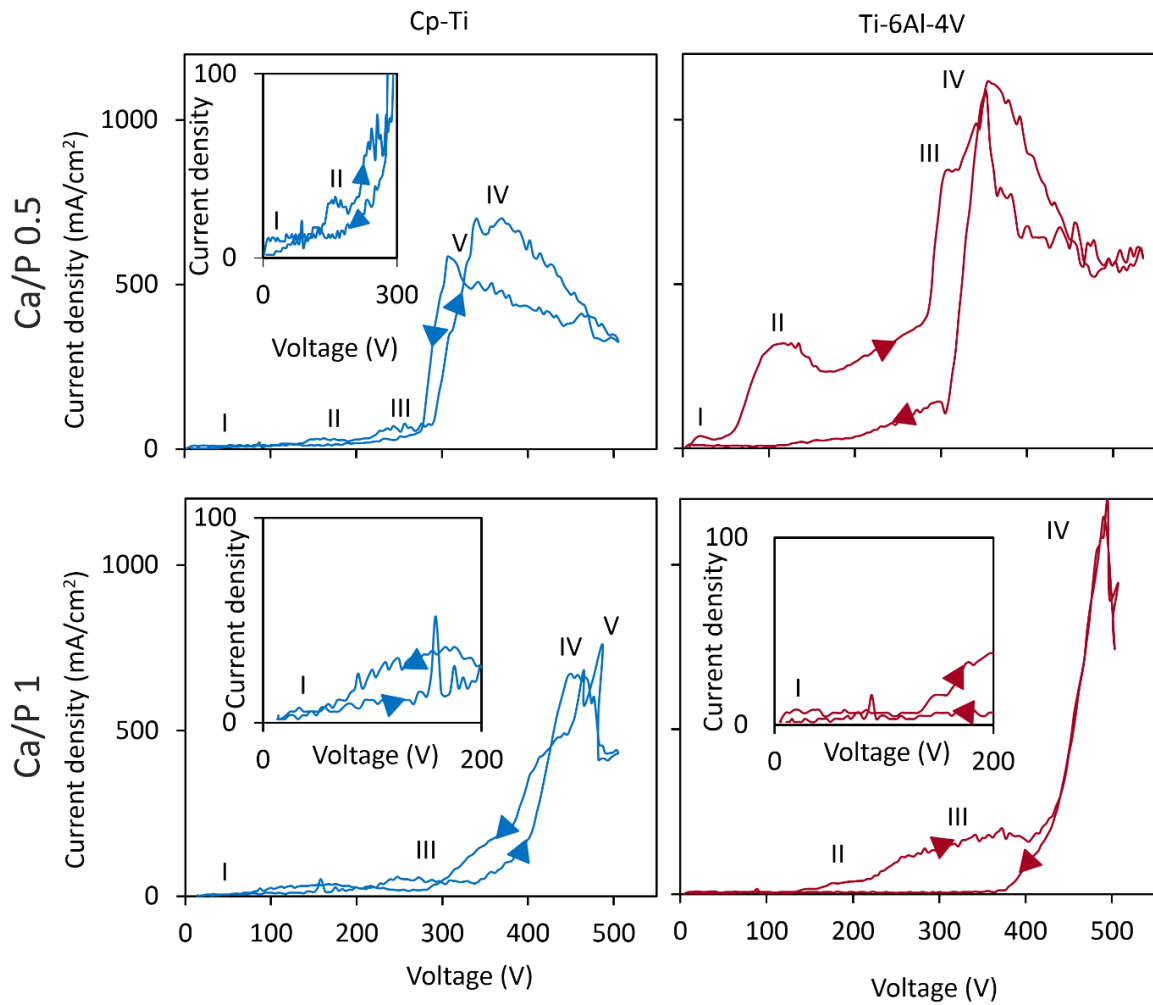
5.2.1 Influence of calcium propionate concentration to electrolyte characteristics and cyclic voltammetry behaviour of Ti anodes

Table 5 Effects of calcium propionate concentration to electrolyte properties.

| Electrolyte composition | | Electrolyte property | |
|-------------------------|---------------------------|----------------------|----------------------|
| Calcium propionate (M) | Sodium orthophosphate (M) | pH | Conductivity (mS/cm) |
| 0.5 | 0.1 | 11.9±0.1 | 25.6±2.9 |
| 1.0 | | 11.7±0.1 | 23.7±3.4 |
| 1.67 | | 8.3±0.1 | 23.6±2.6 |
| 2.0 | | 7.6±0.1 | 26.0±2.0 |

Table 5 displays the influence of calcium propionate concentration to the pH and conductivity in the temperature range from 15 to 30°C. All the electrolyte solutions prepared by dissolving calcium propionate and sodium orthophosphate in distilled water with the concentrations of sodium orthophosphate set at 0.1 M and the calcium salt at 0.5, 1.0, 1.67 and 2 M. Different calcium propionate concentrations were examined as it had been

suggested that the Ca salt content in the electrolyte has stronger influence to the coating formation process than that of phosphate. It can be seen that increasing the calcium propionate content significantly reduces the alkalinity of the electrolyte, and when the Ca/P ratio increased to 2, the electrolyte become nearly neutral. However, the increase in the calcium salt content does not appear to have a significant influence on the electrolyte conductivity.



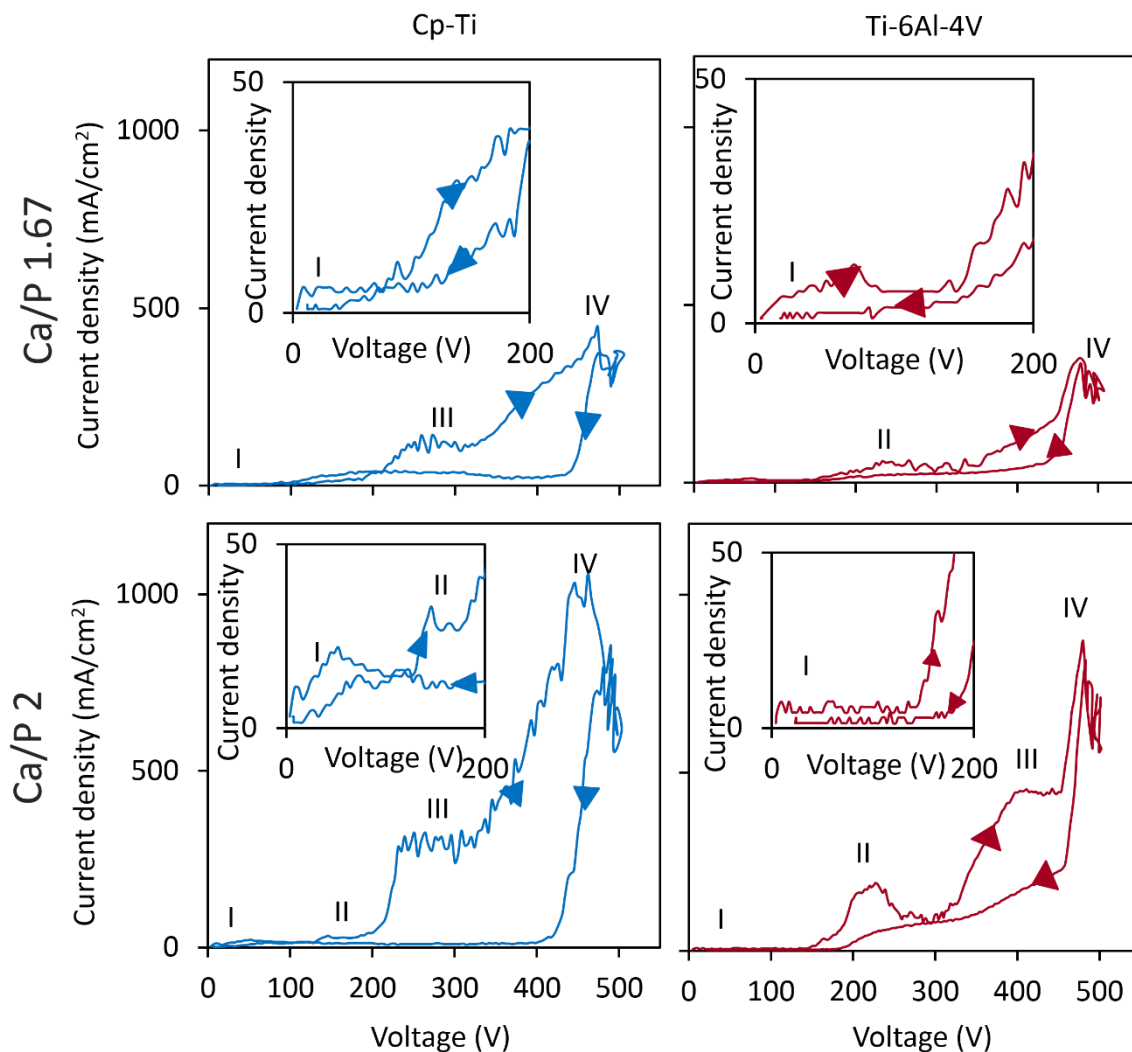


Figure 16 Cyclic voltammogram of cp-Ti and Ti-6Al-4V anodes in the sodium orthophosphate electrolyte with various calcium propionate content, directions of arrows represent the direction of scan.

Figure 16 reveals the current response to the voltage sweep of the two commonly used clinical Ti alloys in electrolytes with different Ca/P ratio. The direction of arrows represents the direction of the scan and the peaks I to V are labelled similar to those in Figure 11 and Figure 12 in Chapter 4. The shape of the voltammogram is much more complex than those observed in conventional CV studies [136, 137], indicating multiple reactions occurred at the surface over the range of voltages. Cyclic voltammetry method have not yet been used for PEO treatment, therefore there is limited data reported on this matter, but the influence of Ca content in the electrolyte and substrate alloying to the current response shown in Figure 16 has demonstrated the sensitivity of the electrochemical system to the conditions of CV scan.

Table 6 The peak locations deduced from the cyclic voltammogram of cp-Ti and Ti-6Al-4V anodes in Figure 1 with different Ca/P ratios in the electrolyte.

| Peak (Voltage) | Electrochemical behaviour | | | | | | | |
|-------------------|---------------------------|-----|------|-----|-----------|-----|------|-----|
| | Cp-Ti | | | | Ti-6Al-4V | | | |
| | 0.5 | 1 | 1.67 | 2 | 0.5 | 1 | 1.67 | 2 |
| I | 32 | 24 | 12 | 16 | 13 | 14 | 23 | 20 |
| II | 158 | - | - | 142 | 105 | 147 | 75 | 221 |
| III | 263 | 239 | 247 | 243 | 313 | 279 | 221 | 390 |
| IV | 340 | 450 | 474 | 446 | 354 | 495 | 478 | 477 |
| V | 316 | 487 | - | - | - | - | - | - |

A small peak I in the forward scan can be observed in all curves, as discussed in Chapter 4. Peak II is observed in the voltammogram for the cp-Ti anode in the Ca/P 0.5 at approximately 158 V, but becomes barely defined as the Ca/P ratio in the electrolyte increased. When the Ca/P ratio of the electrolyte increased to 2, peak II can be observed. It is interesting to note that peak II can be observed in all the curves on Ti-6Al-4V anode, with peak intensities exhibiting a similar trend.

It can be speculated that when the Ca/P ratio of the electrolyte is low, accompanied with high pH value it would lead to defects formation in the surface layer. The intensity of peak II is higher on Ti-6Al-4V anode than on cp-Ti, which could be explained by the influence of aluminium in the substrate to the oxide film formation (Equation [4.1] to [4,4]). When the Ca content in the electrolyte increased, it results in an increase in the electrolyte conductivity, which reduces the energy required to break down the dielectric barrier and enhance the change of CaP phase nucleate near the metal electrode.

The cyclic voltammograms of cp-Ti anodes in Figure 16 show that as the Ca/P ratio in the electrolyte increases, the intensity and the location of peak V shift to a lower voltage and current range. This suggests that the electrochemical behaviour of the anode surface becomes more irreversible. When comparing characteristics of peak IV between the voltammograms, the increase in the Ca/P ratio in the electrolyte appears to shift it to a higher voltage and

current range. This suggests the electrochemical reactions occurring at lower voltage ranges are less vigorous, which are favourable for PEO applications. When the Ca/P ratio in the electrolyte reaches 2, the voltammogram does not display a peak in the reverse scan, suggesting the system became electrochemically irreversible.

Results in this study are consistent with other work employing traditional CV method to study reactions involving various chemical compounds [117, 138, 139], where a decrease in electrolyte pH would increase the voltage and current range of peaks present in the voltammogram. It had been further proposed this is a result of an increase in the electrolyte pH, leading to more vigorous reactions at the surface. [18]. These findings comply with the dramatic increase in current response observed in the voltage range of 300-320 V, when the electrolyte is strongly alkaline (Ca/P 0.5). Another explanation could be a combination of lower electrolyte pH and increase the chance of CaP nucleation in the electrolyte would promote formation of insoluble products during the forward scan.

The cyclic voltammogram of the Ti-6Al-4V anode shows different current response behaviour than that observed when cp-Ti anode was used. This could be attributed to the presence of Al and V in the substrate affecting the electrochemical behaviour during the treatment. The difference in the location and intensity of peaks II when Ti-6Al-4V anode is used indicates the influence of substrate composition to the electrochemical behaviour of the studied system. The strong peak intensity is possibly due to the formation of highly defective TiO₂ structures under the high electric field. A similar current-voltage behaviour of the system during the forward and reverse scans is not favourable for the PEO process and it indicates the ease of shifting the type of reactions occurring at the substrate surface. Iknopisov [140] have proposed the increase in electrolyte conductivity, which can be a result of increasing in electrolyte concentration would reduce the breakdown as discussed in Chapter 2. Interestingly, in this study, the increase in Ca/P ratio of the electrolyte appears to lead to a more apparent peak II in the voltammogram when Ti-6Al-4V anode is used.

The findings in this section have demonstrated the dominating influence of substrate alloying on the electrochemical behaviour of the anodes over the range of potentials in calcium propionate based electrolyte. Further, it shows the increase in calcium propionate content in the electrolyte enhances the stability of the electrochemical system which is reflected by the plateau III in the voltammogram. This could be explained by a combination of pH influencing the dissociation of calcium propionate in the electrolyte, therefore affecting the

chemisorption of the propionate ions during the treatment and/or the influence of Ca content at the surface of the anode which modifies the electrical profile of the system.

5.2.2 Influence of calcium propionate concentration in the electrolyte to the coating phase composition and surface morphology.

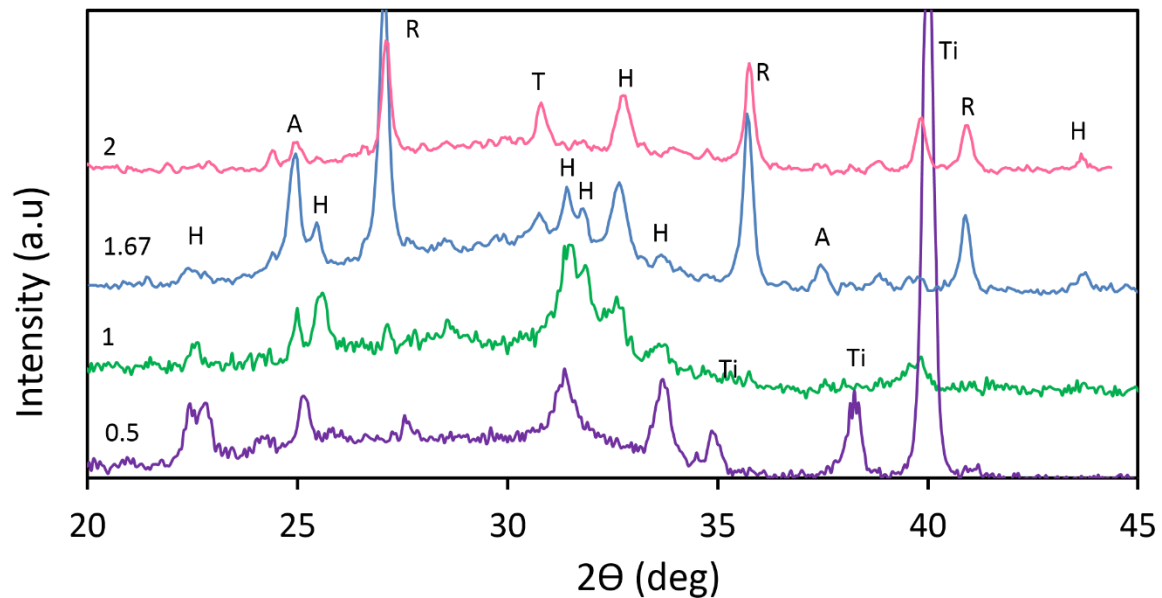


Figure 17 XRD spectra of coatings formed on cp-Ti substrate in calcium propionate containing electrolytes with different Ca/P ratios; (a) 0.5, (b) 1, (c) 1.67 and (d) 2. (A is anatase; R is rutile; Ti is titanium; H is hydroxyapatite; T is tri-calcium phosphate)

Figure 17 shows the phase composition of coatings produced on cp-Ti anode using calcium propionate electrolytes with various Ca/P ratios. The increase in the Ca/P ratio electrolyte appears to promote formation of rutile phase.

Peaks corresponding to HA, anatase and substrate were observed on the pattern of the coating produced in the electrolyte with Ca/P = 0.5. The pattern has a relatively broad scattering hump in the range of 20° to 35° 2θ indicating presence of amorphous constituent in the coating. A set of peaks corresponding to HA can be observed in the coating produced using electrolyte with Ca/P=1; the increase in the Ca content in the electrolyte appears to promote the crystallisation of HA in the coating. When the Ca/P ratio increased to 1.67, set of peaks that matches rutile can be observed in the pattern; this is systematically higher than anatase, indicating that rutile becomes more abundant in the coating. Peaks corresponding to tri-

calcium phosphate as well as HA, anatase and rutile can be observed in the coating produced using electrolyte with Ca/P ratio of 2. It is interesting to note that the increase in the electrolyte Ca/P ratio from 1.67 to 2 did not favour formation of crystalline HA in the coating, instead peaks that correspond to tri-calcium phosphate are observed in the pattern.

The pattern of the sample treated in the electrolyte with Ca/P ratio of 0.5 contains peaks corresponding anatase, rutile and titanium substrate. The peaks of anatase are systematically higher than those of rutile, suggesting that anatase is more abundant in the coating. This complies with Figure 16 where the location of peak IV appears at a comparatively lower potential range (340V). XRD patterns of the PEO samples produced using Ca/P ratio of 1.67 and 2 exhibited peaks corresponding to rutile, anatase, HA and titanium substrate. Rutile is the stable TiO_2 phase which is transformed from anatase under sufficient pressure and temperature. The peaks of rutile are systemically higher than those of anatase, which suggests rutile is more abundant in both coatings. This implies as the Ca/P ratio increased to 1.67, the coating is formed at a higher pressure and temperature than those formed with Ca/P ratio of 0.5 and 1. From our results, the presence of rutile phase appears to be associated with the current growth rate of the voltammogram towards peak IV in the forward scan (Figure 16). This complies with previous discussion where the region between peaks III and IV is related to sparking, and the slow increase in current growth rate over the voltage range observed in the voltammogram promotes the anatase to rutile phase transformation.

These findings are consistent with the cyclic behaviour where the increase in Ca content in the electrolyte tends to stabilise the electrochemical behaviour of the system, which is reflected by the slower increase of current towards peak IV as observed in Figure 16. In particular, when the Ca/P ratio in the electrolyte is low, a reversible behaviour is observed. This complies with the broad regions of amorphous scattering under the peaks for patterns of the coatings produced using electrolytes with Ca/P ratios of 0.5 and 1.

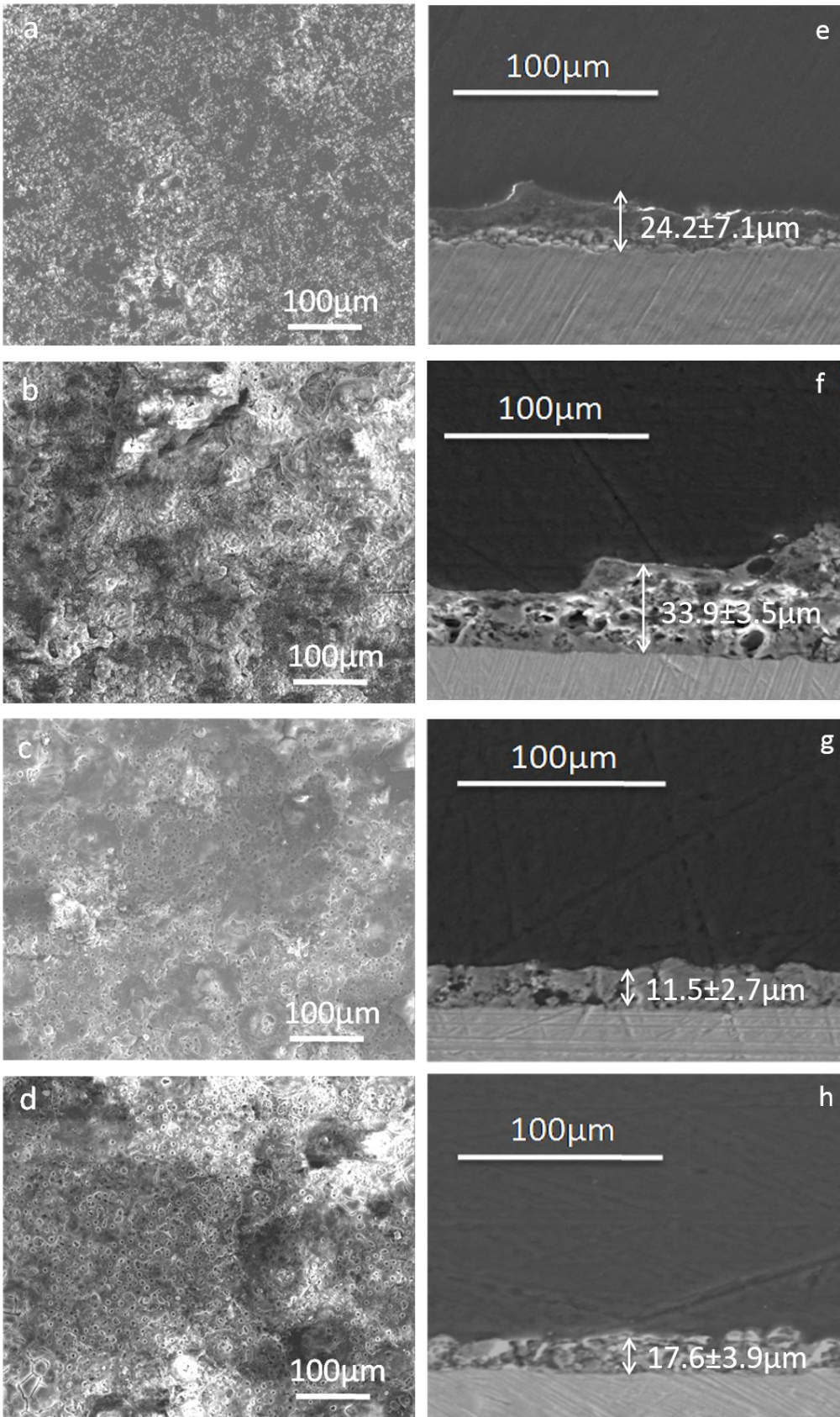


Figure 18 Surface and cross-sectional morphology of coatings produced on cp-Ti substrate using calcium propionate electrolytes with Ca/P ratios of (a, e) 0.5, (b, f) 1, (c, g) 1.67 and (d, h) 2.

Figure 18 reveals the surface morphologies of coatings produced on cp-Ti substrate using electrolytes with various Ca/P ratios. Figure 18a reveals that the surfaces of coatings produced in electrolytes with Ca/P ratio of 0.5 contain a mixture of micro sized islet features on a dense matrix with no evidence of porous morphology. This can be correlated with the result of CV analysis (Figure 16), where a rapid increase in the current towards peak IV is associated to vigorous gaseous product formation at low voltage range. This results in the thickening of the passive film instead of entering into the micro-arcing stage as reflected by the dense outer region of the coating observed in Figure 18e.

Surface morphological features such as globular matrix formation can be observed for the coating produced in the electrolyte with Ca/P ratio of 1 (Figure 18b). Compared to those produced using Ca/P ratio of 0.5, the surface structure reveals compact coral like structure. This could be a combination of increase the chance of CaP nucleation in the electrolyte and attract to the surface and/or oxide product in the discharge channels spray out during powerful arcing. The cross sectional SEM image shows large porous structure within the coating, suggesting high energy discharge during the treatment producing excessive oxygen. The highly uneven surface thickness observed in Figure 18f indicates vigorous reactions occur at the surface.

The dense inner layer and highly porous middle region observed on the coating produced in the electrolyte with Ca/P ratio of 1 aids the understanding of the current behaviour observed in Figure 16. It can be speculated that a thick barrier layer inhibits formation of electron conduction path across, which results in a long region of low current response to the potential increase in the voltammogram. As the voltage reaches approximately 400 V, the occurrence of sparking, caused by dielectric breakdown of the barrier oxide immediately undergoes the chain reactions of repassivation, oxidation, and as a side-product, excessive oxygen evolution due to a combination of anodic reactions of propionate and Ti oxidation described by Equations [4.15] to [4.19] and [2.1] to [2.5].

Figure 18c and d reveal the surface morphologies of coatings produced in electrolytes with Ca/P of 1.67 and 2, respectively. Porous morphologies can be observed in the coatings, along with doughnut like features; this is associated with micro-arcing and powerful arcing during the treatment. The micrographs displayed in Figure 18g and h reveal relatively uniform surfaces, whereas the crest-like features, similar to those present in the coating produced in the electrolyte with Ca/P=1, cannot be observed. It can be speculated that the porous

morphology of the coatings produced in electrolytes with Ca/P ratios of 1.67 and 2, with features associated with controlled sparking, is related to the plateau peak III and irreversible electrochemical behaviour observed in Figure 16.

Table 7 Relative atomic percentages of elements in the surface of the PEO coatings produced using electrolytes with various Ca/P ratios.

| Element (at%) | Processing variable | | | |
|------------------|---------------------------|------|------|------|
| | Ca/P ratio of electrolyte | | | |
| | 0.5 | 1 | 1.67 | 2 |
| Ca | 10.0 | 10.6 | 7.4 | 11.4 |
| P | 9.9 | 8.5 | 3.9 | 6.2 |
| Na | 4.8 | 2.5 | 0.8 | 0.6 |
| O | 63.2 | 63.0 | 65.3 | 62.0 |
| Ti | 4.0 | 5.0 | 13.2 | 5.8 |
| C | 8.1 | 10.5 | 9.4 | 14.0 |
| Ca/P ratio | 1.0 | 1.2 | 1.8 | 1.8 |

Table 7 displays relative atomic percentages of elements in the coatings formed in the electrolytes with different Ca/P ratios. Results show that the Ca/P ratio in the coating tends to increase with increasing of that in the electrolyte, but the addition of Ca propionate above Ca/P=1.67, does not affect the overall Ca/P ratio in the coating.

5.2.3 Summary

Results from this section of the study demonstrate the utility of cyclic voltammetry method and enhance the understanding of using this approach for investigation of PEO processes. In terms of PEO system selection, the voltammogram that exhibits;

- Stable and slow increase of current towards peak IV;
- Peak IV with high intensity located at a high voltage range;
- Absence of peak V in the reverse scan;

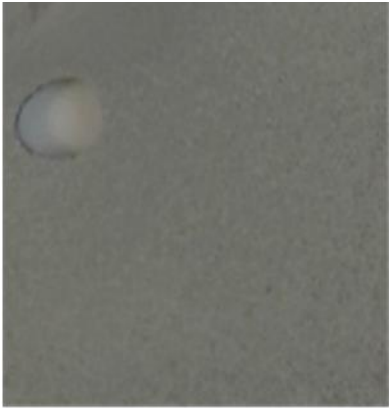
- Substantially lower current in the reverse scan;

appears to be favourable for single static control of electrical parameters, as it allows a large voltage range for stable and controllable sparking, moreover the anodising voltage would be sufficient to promote essential phase transformations, such as anatase-to-rutile, and crystallisation of HA. Out of all the concentrations tested, the electrolyte with Ca/P=1.67 exhibited the most favourable current-voltage behaviour in the forward and reverse scan. Therefore this electrolyte composition appears to be most suitable for further examination.

5.2.4 Application of CV method to understand the coating formation mechanism

Previous section discussed the use of CV method to examine the suitability of the PEO system and identified suitable ranges of electrical parameters for PEO treatment of cp-Ti in calcium propionate containing electrolytes. The purpose of this section is to study in more detail the coating formation process in characteristic voltage regions as outlined by the current-voltage diagram and corresponding coating microstructures developed during the PEO process. The surface and cross-sectional morphology, phase and chemical compositions of the coatings produced are also examined.

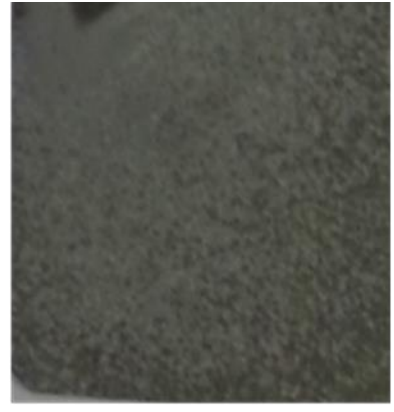
The voltammogram of the process carried out in the electrolyte with Ca/P=1.67 shown in Figure 16 suggests that stable micro-arcing should occur in the voltage range prior to peak IV. Therefore, appropriate voltages in the range from 440 to 460 V were applied to examine the coating formation process on the cp-Ti substrate. Figure 19 displays the optical microscopic images of the coatings produced for 3 min at 440, 450 and 460 V. It is interesting to note a colour variation on the coating surface as the applied voltage increased. The coatings produced at 400V have a comparatively uniform surface appearance, however as the applied voltage increased to 450V, white dots start appearing distributed on the surface, indicating non-uniform discharges. Coatings produced at 460V exhibit discolouration which is an indication of non-uniform coating process.



440V



450V



460V

1 cm

Figure 19 Visual inspection of coatings produced on cp-Ti substrate by 3 min PEO treatment in the calcium propionate electrolyte at 440, 450 and 460 V.

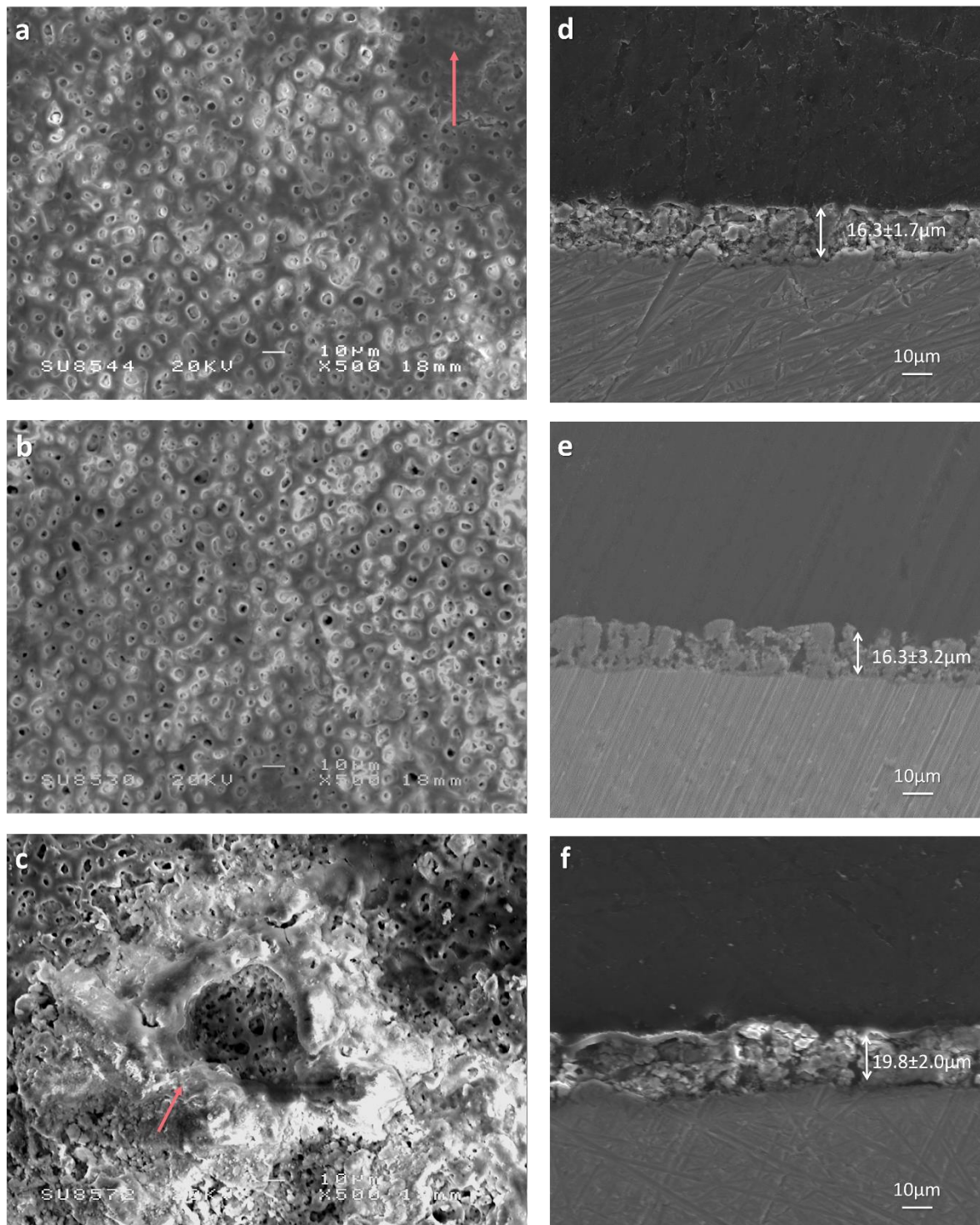


Figure 20 SEM micrograph of PEO coatings produced on cp-Ti substrate in calcium propionate based electrolyte with Ca/P ratio 1.67 at 440 V (a,d), 450 V (b,e) and 460 V (c,f) in Ca/P 1.67 for 3 mins.

SEM images in Figure 20 reveal surface and cross-sectional morphologies of the coatings produced for 3 min at 440, 450 and 460 V. Figure 20a which corresponds to the coating produced at 440 V reveals a region of dense matrix (indicated by the arrow in the image) and shows that the surface is dominated by filled pores. This suggests insufficient energy for sparking to commence throughout the dielectric film and results in features correlated to melted oxide products that solidify at the inner wall of a discharge channel. These features point to insufficient energy for evenly distributed discharges to occur at the surface. The surface is dominated by pores that are filled with matrix; this feature is correlated to melted oxide products that solidify at the inner wall of a discharge channel. This further indicates there was insufficient energy for evenly distributed uniform sparking to occur and for the melted oxide to spray out of the discharge channel. This complies with the presence of small granulated appearance of the coating matrix displayed in Figure 20d. When the applied voltage increased to 450 V, the number of open pores increases, with no apparent regions of dense matrix remaining. The increase in the number of open porous structures is associated with higher discharge energy at the local regions resulting in excessive gaseous product formation allowing the melted oxide to spray out of the discharge channel. Figure 20e presents the cross sectional morphology of the coating produced at 450 V. Distinctive traces of discharge channels penetrating throughout the surface can be observed; moreover small pores present in the bulk of the coating can also be observed, which is likely to be caused by gas entrapment in the matrix around the discharge channel.

Figure 20c reveals the surface morphology of the coating produced at 460 V. It corresponds to the region just before a sudden increase in current growth rate towards peak IV. Visual inspection (Figure 19) of the coating reveals features related to burning on the surface. The SEM images of the coating reveals severe ablation as indicated by the doughnut-like feature shown by the arrow.

Figure 20f reveals discharge channels penetrating throughout the coating and large globular features separated by cracks parallel to the surface throughout the coating. Small pores are observed in the bulk matrix which can be explained by high discharge energy resulting in gas entrapment in the matrix around the discharge channel. The surface shows evidence of discharge channels penetrating through the coating. These results indicate that applying DC potentiostatic mode at 460 V produces coatings under conditions of powerful discharge, which should be avoided as discussed in the previous section.

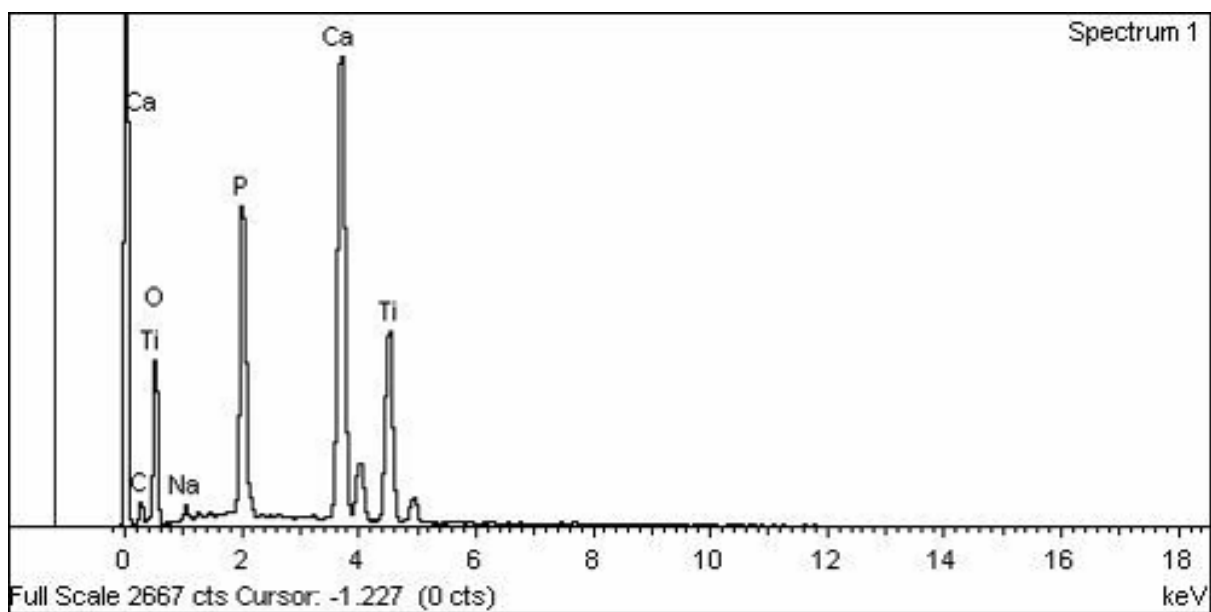


Figure 21 Surface EDX spectrum of the coating formed on cp-Ti substrate in the calcium propionate based electrolyte with Ca/P ratio of 1.67 at 450 V for 3min.

Table 8 Relative atomic percentages of elements in the surfaces of PEO coatings produced in the calcium propionate based electrolyte with Ca/P=1.67 at 440, 450 and 460 V for 3 min.

| Element (at%) | Processing variable | | |
|------------------|---------------------|------|------|
| | Applied voltage (V) | | |
| | 440 | 450 | 460 |
| Ca | 9.7 | 9.8 | 11.7 |
| P | 5.1 | 5.1 | 6.6 |
| Na | 1.1 | 0.7 | 1.0 |
| O | 69.4 | 69.7 | 64.5 |
| Ti | 14.7 | 12.5 | 6.3 |
| C | - | 2.2 | 9.9 |
| Ca/P | 1.9 | 1.9 | 1.8 |

The elemental composition of coatings produced at 440, 450 and 460 V is displayed in Table 8. Results suggest the applied voltage does not have significant influence on the overall Ca/P ratio in the coating. The ratio in the coating is higher than that in stoichiometric HA (Ca/P=1.67), tending towards tetra-calcium phosphate (Ca/P ~2) [141]. Nevertheless, the results show as the applied voltage increases, the calcium content in the coating also increases; this is especially noticeable when the voltage exceeds 450 V. Along with a sudden reduction in Ti and high C content, it can indicate that the increase in Ca content is due to Ca containing matrix splashing out during powerful arcing, forming a thick Ca rich layer on the surface. This is confirmed by the data from Figure 22 where the elemental composition of the doughnut feature is shown to have a particularly high level of Ca content.

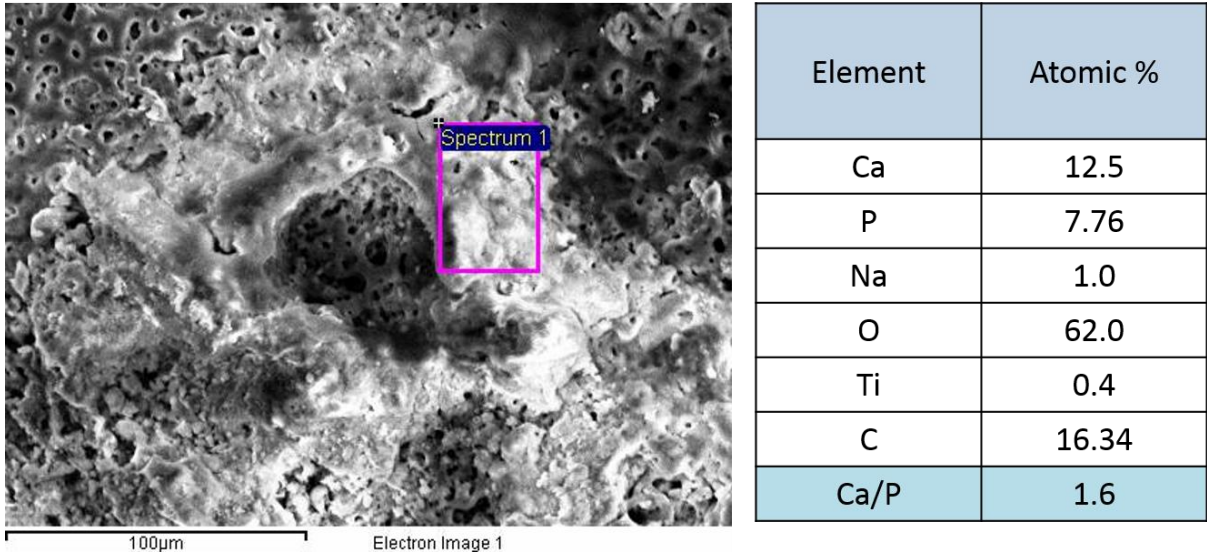


Figure 22 An SEM image of the coating produced in the calcium propionate based electrolyte with Ca/P=1.67 for 3 min and the elemental composition of the doughnut-like shape feature.

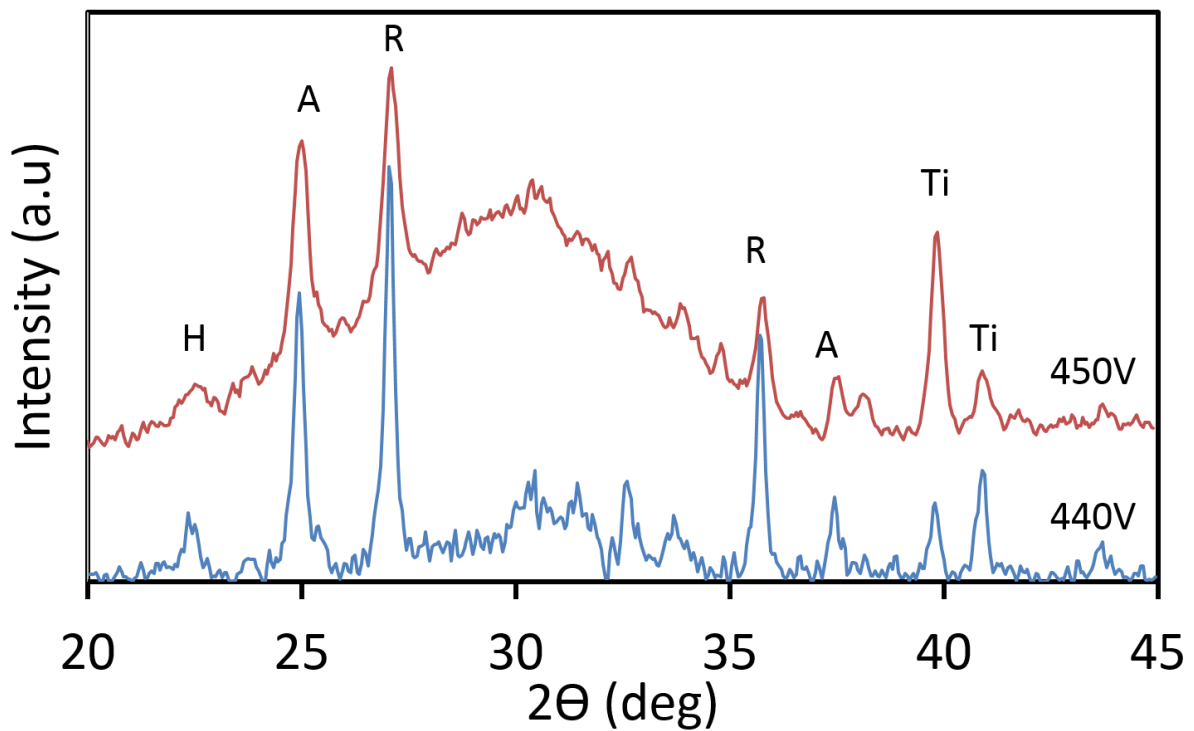


Figure 23 XRD spectra of coatings on cp-Ti substrate produced at 440 and 450V in the calcium propionate electrolyte with Ca/P ratio of 1.67 for 3 min. (A, anatase; R, rutile; Ti, titanium; H hydroxyapatite)

Figure 23 reveals the phase composition of the coatings produced on cp-Ti substrate at 440 and 450V for 3 min. The coating produced at 460 V was not inspected due to the high degree

of burning, suggesting the regime is not suitable for production of high-quality coatings. Peaks corresponding to anatase, rutile, HA and substrate can be observed on both patterns. When the applied voltage is low, the peaks that correspond to rutile are systematically higher than those of anatase, suggesting that rutile is more abundant in the coating. Interestingly, when the applied voltage increased to 450 V the peaks of rutile do not appear to be systematically higher. A small bump can be observed in the 2Θ ranging from 31 to 33° when the applied voltage is set at 440 V. However, when it increased to 450 V, the intensity of the bump increases significantly, indicating abundant precipitation of amorphous CaPs.

Overall, this section provided preliminary results correlating the system's current-voltage behaviour to the coating formation process. It showed that the CV method represents a useful means for rapid identification of suitability of an electrochemical system for PEO processing and determination of suitable voltage/current ranges. Coatings produced in the electrolyte with $\text{Ca/P}=1.67$ in this section showed features desirable for bioactive coatings, however visual inspections reveals presence of white dots which can be associated with traces of powerful arcing that may have occurred on the surface. Therefore further work to control the discharge during the treatment could potentially reduce the risk of appearing these adverse features.

5.2.5 Optimisation of electrical parameters using cp-Ti substrate

The findings from the previous section show that the CV method can provide a general range of working voltage/current conditions suitable for stable micro-arcing to occur. Despite so, further research is necessary to improve on the coating characteristics, such as the morphology and phase composition suitable for biomedical applications. As discussed in Chapter 2, pulsed unipolar modes allow a better control over the discharge behaviour by the introduction of the pause between current pulses. Compared to DC potentiostatic control, the 'off-time' can interrupt prolonged discharges, providing a better control over the microstructure and composition of the coating.

Results from the previous section have also shown the coating produced using the potentiostatic DC mode at 450 V have an overall Ca/P ratio at 2 which is higher than that in the stoichiometric HA ($\text{Ca/P}=1.67$), and when the applied voltage was increased to 460 V, morphological features associated with powerful arcing can be observed. Therefore, the aim of this section is to explore the use of a PUP mode with independent variation of pulse

duration and voltage amplitude for PEO treatments of cp-Ti in the calcium propionate electrolyte to adjust the Ca/P ratio and refine coating morphology.

The PEO treatments in this section were performed using the potentiostatic mode at 450V or 460 V in the electrolyte with Ca/P ratio of 1.67 for 3 min. The pulsed unipolar mode was employed with f of 600 Hz and duty cycle varied from 20 to 90%. Pulse frequency and duty cycle were defined as $f = 1/(t_{on} + t_{off})$ and $\delta = t_{on}/(t_{on} + t_{off})$, respectively. Typical oscillograms of electrical waveforms were recorded as discussed in Chapter 2 and the examples are shown in Figure 24. The waveform shows deviation from the ideal rectangular pulse shape with voltage reduce gradually during the off-time. Figure 24 showed when the duty cycle is set at 90 and 50%, the voltage does not decay to zero before the next pulse, this potentially increases the stress developed within the coating. Fluctuation in the voltage and current transient showing a sharp peak at the beginning of each pulse suggesting circuit overshoot at the start of each pulse on, Gao *et al* [92] suggests this is due to the pulses applied to capacitive loads, which is inevitable.

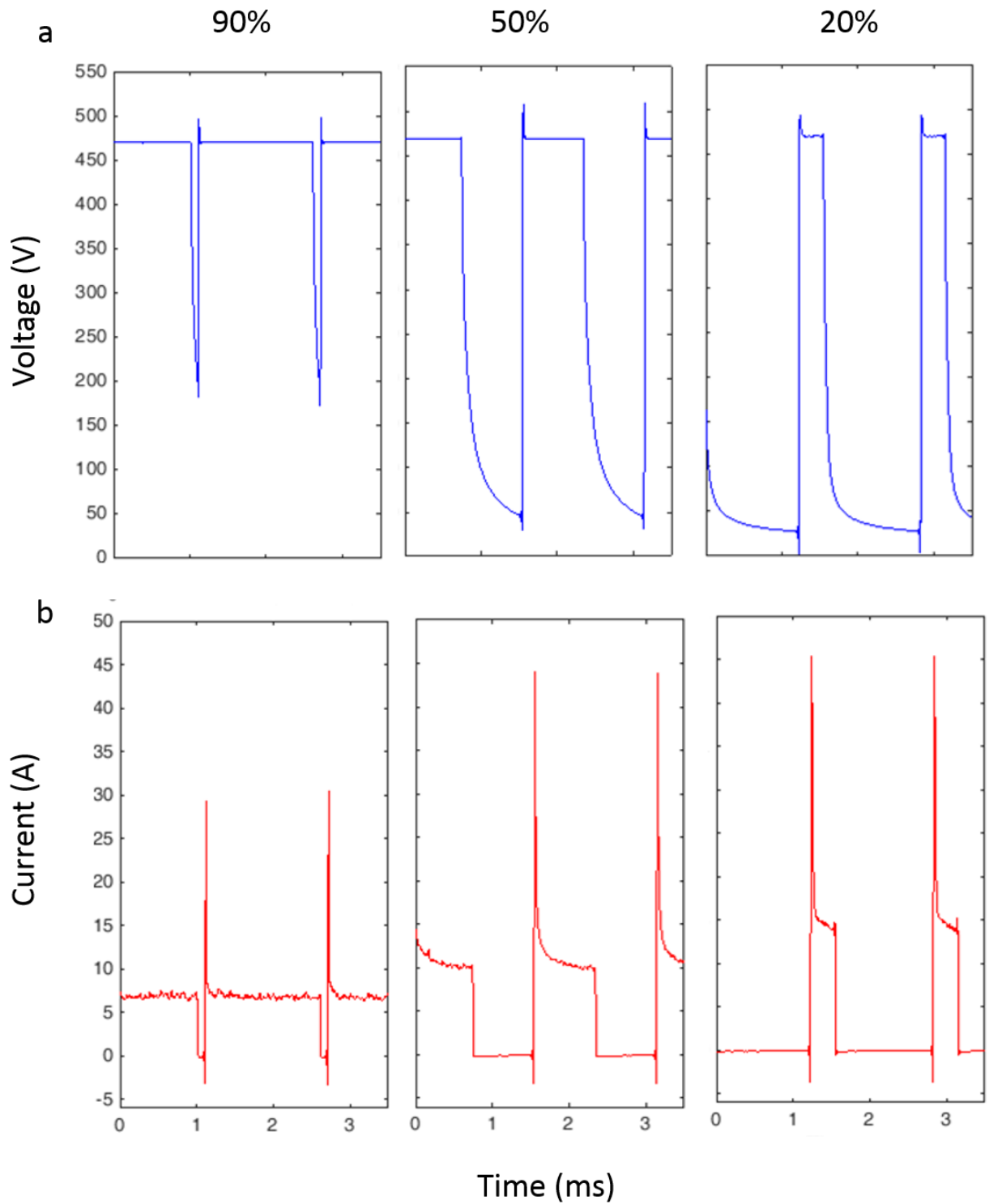


Figure 24 Typical examples of (a) pulsed unipolar voltage waveforms with duty cycles set at 90, 50 and 20% and corresponding current signals for voltage pulse magnitudes.

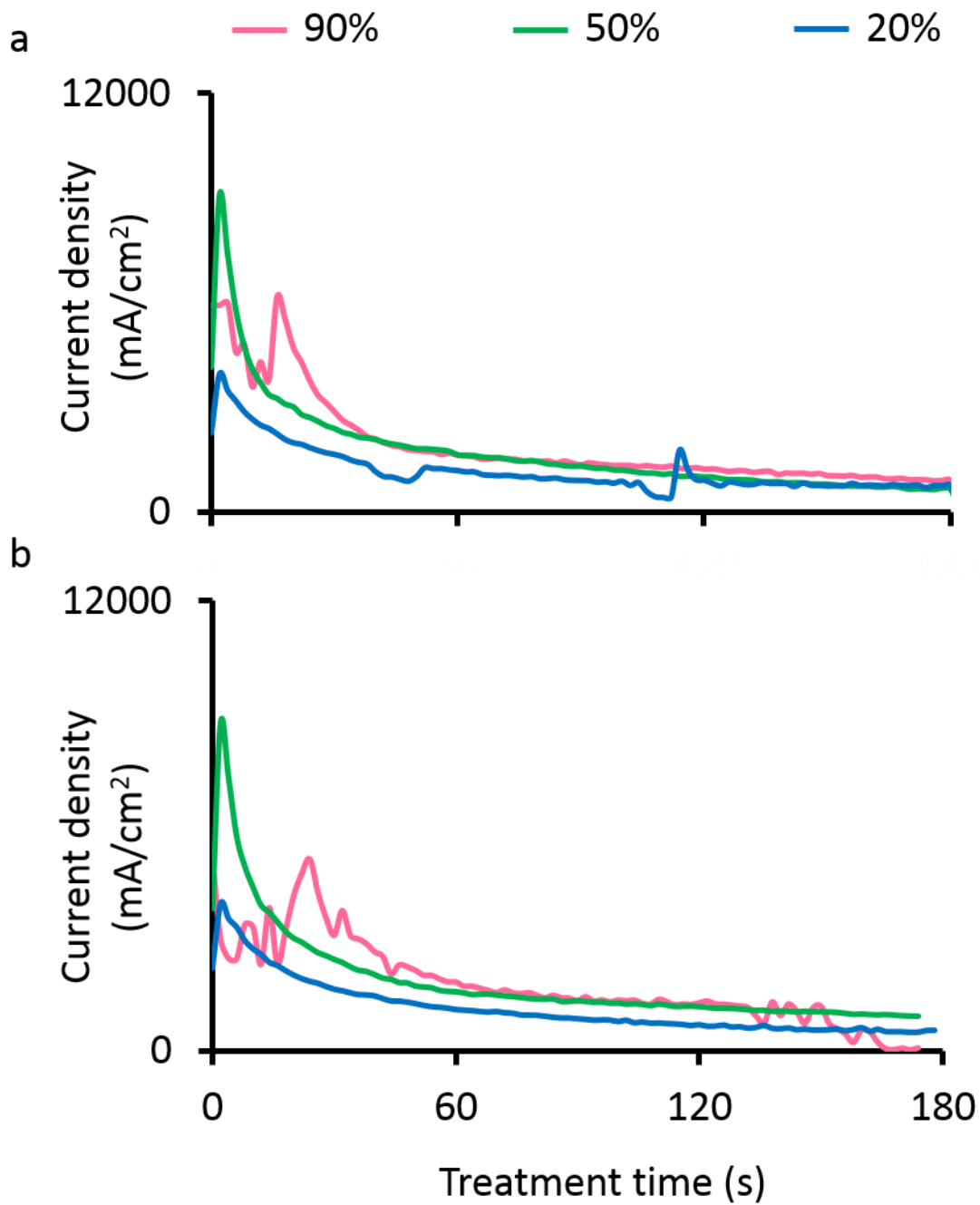


Figure 25 Current density transients recorded during PEO treatments of cp-Ti in the calcium propionate based electrolyte with Ca/P=1.67 using PUP voltage with various duty cycles and magnitude set at (a) 450V and (b) 460V.

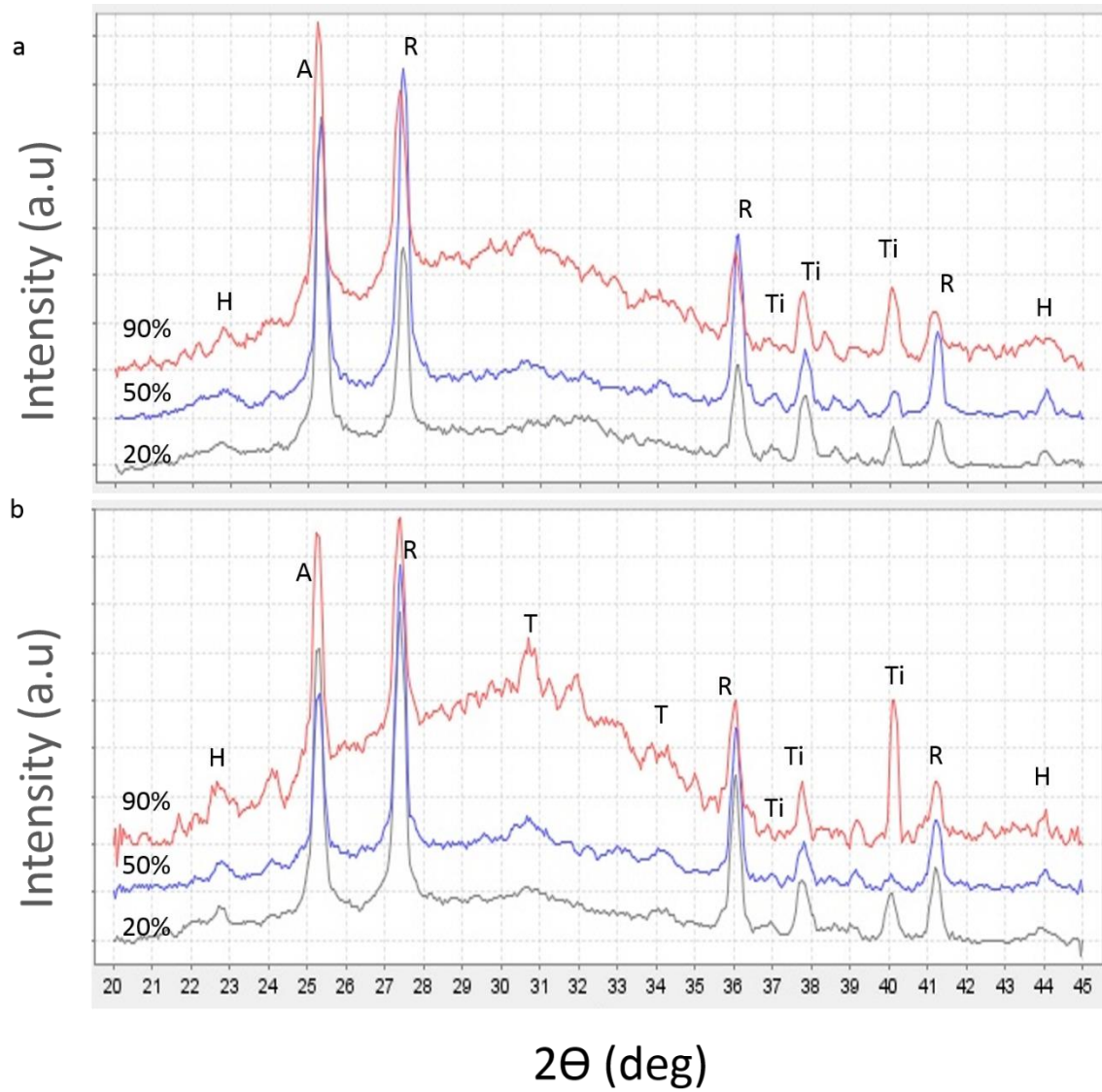


Figure 26 XRD spectra of coatings produced using pulsed unipolar mode (a) 450V and (b) 460V in calcium propionate electrolyte with Ca/P ratio set at 1.67 with various duty cycles. (A, anatase; R, rutile; Ti, titanium and alloy; H, hydroxyapatite; T, tricalcium phosphate)

The XRD patterns of coatings produced at different duty cycles with applied voltage of 450 and 460V are presented in Figure 26.

As shown in Figure 26a, anatase and rutile are the dominant crystalline phases in the coating produced at 450 V with duty cycles of 20 and 50%. The intensities of rutile peaks are systematically lower than those of anatase in the coating produced with 20% duty cycle, the peak intensities increase as the duty cycle increases. This is somewhat expected, as with the duty cycle increasing, the subsequent discharge duration becomes longer, leading to an increase in the temperature and pressure which enhances the anatase-to-rutile transformation. The XRD spectra of the coating produced with 90% duty cycle display a broad scattering hump between 28° and 32° 2θ , indicating the presence of amorphous CaP constituents. It is interesting to observe a reduction in the intensity of the set of peaks corresponding to rutile when the duty cycle increased to 90%, similar to those observed when DC mode was applied (Figure 23).

When the applied voltage increased to 460V, anatase and rutile remain dominant in the coating regardless of duty cycles (Figure 26b); the results are similar to those observed when the voltage was 450 V. When the duty cycle is set at 90%, a broad bump can be observed in the region of 28° and 32° 2θ , along with weak peaks corresponding to tri-calcium phosphate and HA. Moreover, the intensity of rutile peaks is systematically higher than those observed for the coating produced at 450V with the same duty cycle. This is due to the fact that the increase in applied voltage would increase the pulse energy which favours the anatase-to-rutile transformation. Accompanied with that, the increase in local discharge temperature appears to favour the reaction between Ca^{2+} and PO_4^{3-} ions resulting in formation of crystalline CaP phases such as TCP and HA [142]. It can be assumed that as the local temperature rises, dehydration is also promoted, which potentially enhances the formation of TCP phase in the coating.

Interestingly, for the coatings produced with 50% duty cycle at both voltages, rutile peaks are systematically higher than those of anatase. This could be a result of comparatively higher currents observed for both current transients in Figure 25.

5.2.6 Morphological analysis of coatings produced with different duty cycles

Surface morphologies of PEO coatings produced using PUP voltage mode at 450 and 460 V with various duty cycles are shown in Figure 27 and 28, respectively. It had been found that

in PEO coatings produced using galvanostatic mode, the average pore size and distribution are frequency dependent [92, 143]. Results from this study suggest the applied voltage also influences the pore size.

Image analysis based on Minkowski functionals is commonly used to study diffusion surface layers [144]. The SEM images were characterised in terms of surface coverage (C), the boundary length (L) and the Euler's number (E), which corresponds to the amount of pores (dark) and surface (bright), length of boundaries and the connectivity of the features, respectively. The variation in the curve shape and especially the C_{flex} , L_{max} and E_{min} points are used to analyse the coating characteristics.

Figure 27(a and d) reveals the surface morphology of the coating produced using $\delta = 90\%$ at 450 V. A combination of porous structure, such as pore-in-pore and pin-hole pores, is observed on the surface, with the average pore size in the coating being $2.75 \pm 1.26 \mu\text{m}$. This is consistent with the flex in the length (L) curve observed at low height threshold in the respective functional plot. When the duty cycle was set at 50%, a number of pin-hole pores becomes more apparent, with the average pore size of $3.11 \pm 0.92 \mu\text{m}$. The pin-hole pores are developed due to accumulation of excessive gaseous products evolved in discharge channels, leading to gas entrapment in the neighbouring region. When compared to coating formed with duty cycle of 90%, it is interesting to observe an increase in the number of open pores. These features indicate stronger discharge occurred when the duty cycle was set at 50%, which complies with the current peak observed in the current transient in Figure 25. For the coatings produced using $\delta = 50$ and 90%, cracks on the surface become more apparent than the coating produced using the potentiostatic DC mode (Figure 20). This could be a result of internal stress generated by a combination of electrostriction and double-layer charging at the beginning of each pulse [92]. This stress may be relaxed only partly due to thermal action of discharges during voltage pulses and dielectric relaxation of the coating material between them. Therefore, the complete relaxation would occur via crack formation.

When the duty cycle reduced to 20% the surface morphology (Figure 27c and f) reveals distinctive traces of discharge channels, which is consistent with the relatively high C_{flex} value in the corresponding Minkowski functional plot. This suggests the surface had enough time to cool down, and the subsequent sparking did not destroy the previous surface produced during the treatment. Analysis of the Minkowski functional plots for coatings produced with 90, 50 and 20% duty cycles shows the distance between E_{min} and the respective length (L)

measure reduces as the duty cycle decreases. This suggests the pores become more circular in shape, indicating that the subsequent discharge did not disrupt the previous coating structure. Furthermore, it suggests distances between individual discharges become relatively larger when the duty cycle is reduced. This could be explained by the fact that the decrease in duty cycle would result in decreases in both discharge duration and energy dissipated, leading to a stronger tendency for formation of a more dispersed porous structure. Figure 28 reveals the surface morphology of coatings produced using the PUP voltage mode at 460 V with various duty cycles. Results confirm the use of the PUP mode can significantly improve the surface morphology compared to that formed using the potentiostatic DC mode, wherein features consistent with appearance of powerful arcing can be observed Figure 28c. Trends in coating morphology similar to that shown in Figure 27 can be observed as the duty cycle increased. When the duty cycle is set at 90%, the surface morphology reveals a combination of pore-in-pore and closed pore structures. The pore shapes deviate from circular shape, which is reflected in the significant distortion of the L curve. The average pore size was found to be $2.59 \pm 1.23 \mu\text{m}$, the broad range is consistent with the width of L peak observed.

When the duty cycle reduced to 50%, the pore shape appears to be more circular which is consistent with the reduction in the distance between E_{min} and the corresponding value of L measure at that height threshold. When compared the coating produced at 450 V (Figure 27b,e), the number of pin-hole pores reduces, this is also shown by a reduction in the flex in the L curve at low height threshold. This could be explained by the higher discharge energy, so the subsequent discharge destroys the morphology created by the previous event, leading to surface re-melting. The average pore size observed in the coating is $3.11 \pm 1.11 \mu\text{m}$. The reduction of the duty cycle to 20% did not result in presence of distinctive discharge channels as those observed in the coating produced at 450 V. Instead, the surface appears to have undergone re-melting to produce a comparatively smooth topology. It is interesting to observe that the number of open pores increased with a reduction of duty cycle. This could be due to the fact that the increase in duty cycle would lead to stronger discharges on the surface at a lower spatial density.

This section has demonstrated that the PUP voltage mode can improve the surface morphology by interrupting the discharge and controlling energy dissipated in the coating.

Moreover the Minkowski functionals provide a useful tool with high sensitivity for the morphological analysis of PEO coatings.

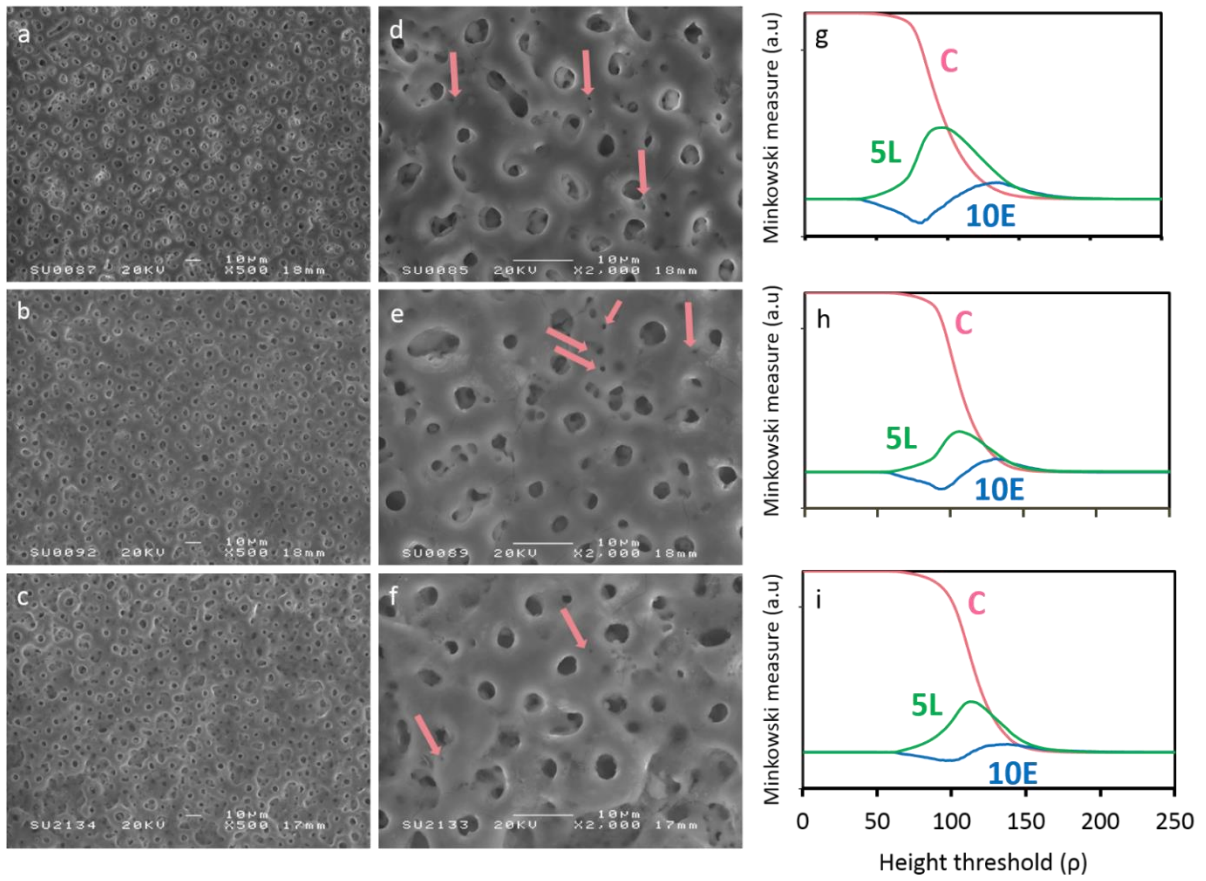


Figure 27 SEM micrographs of coatings produced using pulsed unipolar voltage mode ($V_{+}=450V$) with duty cycles of (a,d) 90, (b,e) 50 and (c,f) 20% and corresponding Minkowski functionals (g-i) $C(\rho)$, $L(\rho)X5$ and $E(\rho)X10$.

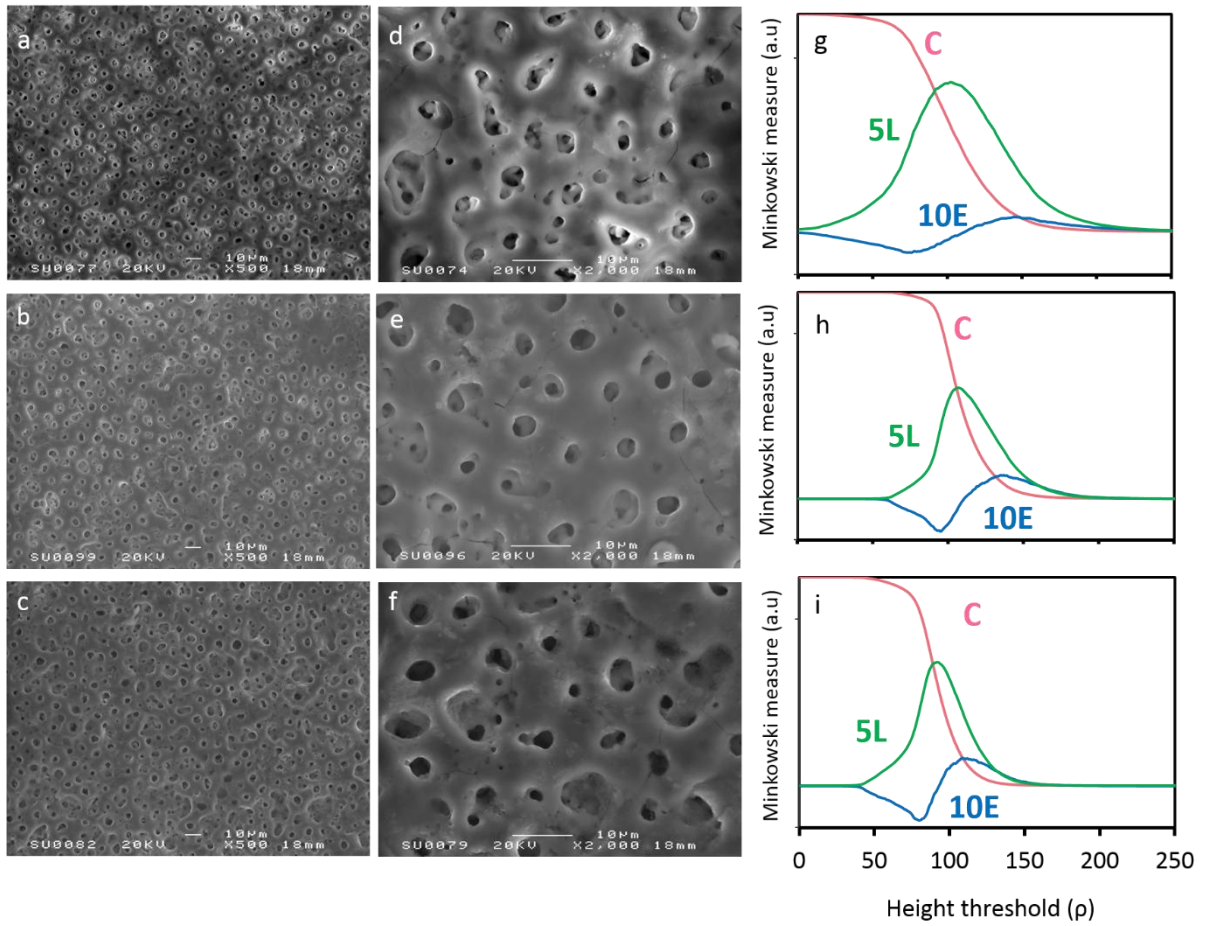


Figure 28 SEM micrographs of coatings produced using pulsed unipolar voltage mode ($V_{+}=460V$) with duty cycles of (a,d) 90, (b,e) 50 and (c,f) 20% and respective Minkowski functionals (g-i) $C(\rho)$, $L(\rho) \times 5$ and $10E(\rho) \times 10$.

Table 9 Chemical composition of PEO coatings produced at different duty cycles.

| Element (at%) | Processing variable | | | | | |
|------------------|---------------------|------|------|----------------|------|------|
| | V(+) = 450V | | | V(+) = 460V | | |
| | Duty cycle (%) | | | Duty cycle (%) | | |
| | 90 | 50 | 20 | 90 | 50 | 20 |
| Ca | 8.9 | 7.7 | 7.3 | 9.6 | 7.8 | 7.3 |
| P | 4.8 | 4.0 | 3.6 | 5.2 | 4.1 | 3.6 |
| Na | 0.6 | 0.5 | 0.5 | 0.6 | 0.6 | 0.5 |
| O | 66.7 | 67.2 | 63.9 | 66.1 | 67.3 | 68.0 |
| Ti | 13.0 | 14.6 | 13.9 | 11.7 | 15.2 | 15.1 |
| C | 6.0 | 6.0 | 10.8 | 6.8 | 5.0 | 5.5 |
| Ca/P | 1.9 | 1.9 | 2.0 | 1.85 | 1.9 | 2.0 |

The elemental composition of the coatings produced at different duty cycles and voltages is displayed in Table 9. Results show similar Ca/P ratio for all coatings, with a trend of Ca and P content to increase as the duty cycle increases. This can be explained by the increase in the attraction of the negatively charged phosphate anions by electrostatic forces as the duty cycle increases. PO_4^{3-} ions can be transported under the high electric field towards the positively charged substrate, moreover can transport through the discharge channel towards the inner layer as the treatment progress. It can be speculated that this condition favours the formation of CaP chemically in the electrolyte at approximate region and precipitate on the surface.

In essence, this section has demonstrated the use of PUP PEO mode can improve the surface morphology of the coatings produced by interrupting the discharge duration. However, formation of crystalline HA on the surface still remains an issue. Therefore further research exploring the effects of electrical parameters is required. Moreover, it has demonstrated the sensitivity of the Minkowski functional for analysis of PEO coatings, which ensure its potential use in this application.

5.2.7 Influence of negative bias to the coating characteristics

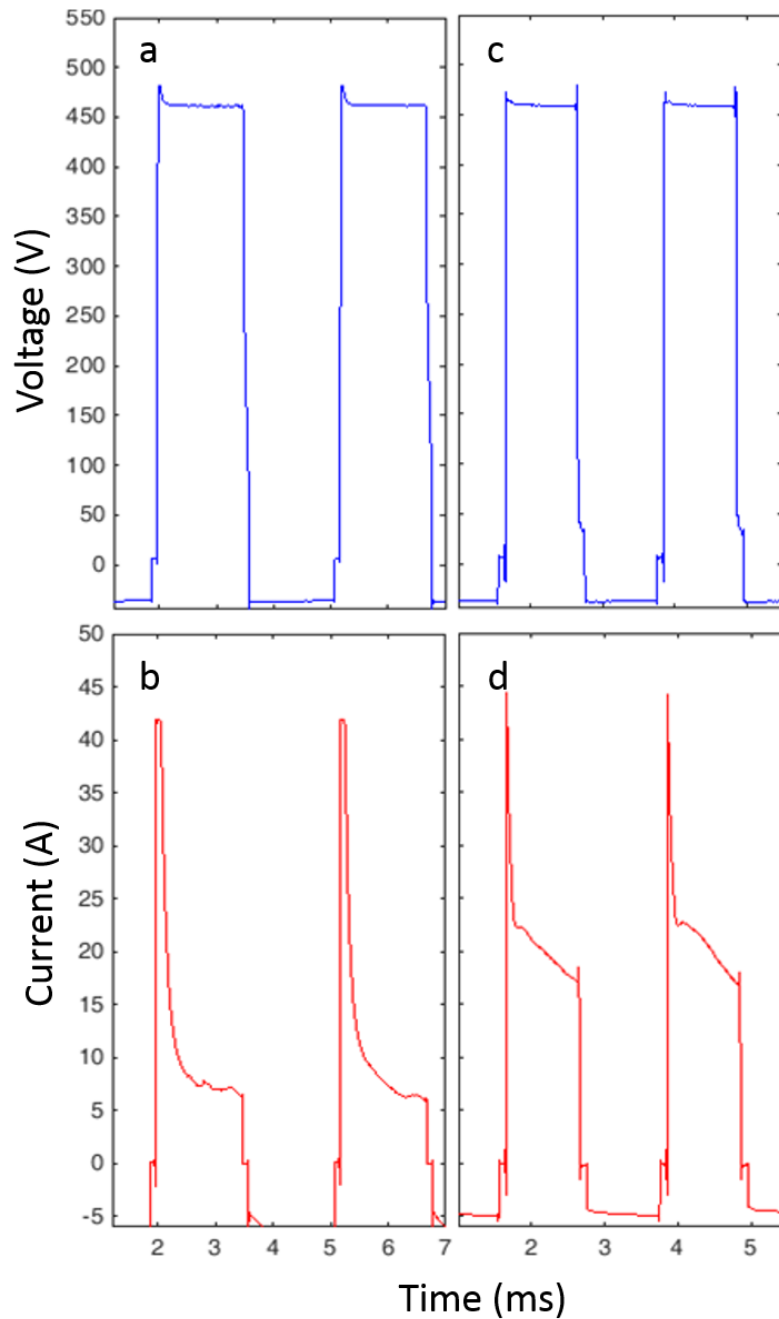


Figure 29 Typical examples of pulsed bipolar voltage waveform with frequency set at (a) 300 and (c) 450 Hz and corresponding current signals for voltage pulse magnitudes.

As discussed in Chapter 2, a novel bipolar pulse source which allows more controllable electrical regimes to be implemented has been recently developed. The main advantage of the PBP current mode is the control over the discharge characteristics as each parameter such as the pulse on, and off time can be altered independently. These advantages therefore enable a

large number of combinations of electrical parameters. As a result, over the past decade numerous of studies have investigated capabilities of pulsed current regimes to produce the coatings desired [11, 145-147].

Results from the previous section demonstrate that when PUP PEO mode was applied the coatings formed showed porous morphology with evidence of CaP precipitation. A limited formation of crystalline HA phases in the coating could be a result of the alkaline environment not favouring the nucleation process. The introduction of the negative bias can therefore not only interrupt the discharge duration, allow cooling of the surface, but also attract Ca^{2+} ions to the surface by electrostatic forces, providing a favourable condition for CaP nucleation. Furthermore, cathodic processes during the negative biasing can reduce the pH of the local region which had been suggested to enhance CaP nucleation [30].

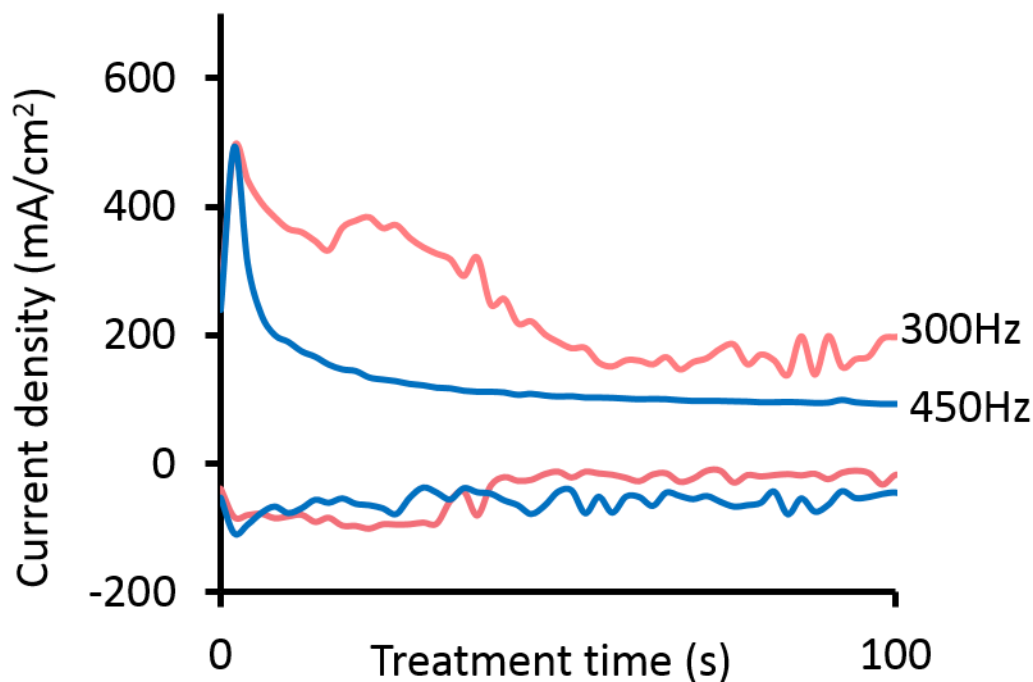


Figure 30 Current transients recorded during PEO treatments of cp-Ti substrate in the calcium propionate electrolyte with Ca/P ratio of 1.67 using the PBP voltage mode with pulse frequencies of 300 and 450Hz.

In this study, a pulsed bipolar (PBP) current mode was employed under potentiostatic control ($V(+) = 450\text{V}$, $V(-) = -40$) and f set at 300 and 450 Hz on cp-Ti substrate for 3 min, to investigate the influence of negative bias during the coating characteristics in the calcium propionate based electrolyte with Ca/P=1.67. The oscillograms of the electrical waveforms

and pulse average current transients during the treatments are displayed in Figure 29 and 30, respectively.

Figure 30 displays current transients recorded during the treatments carried out at 300 and 450 Hz, and both curves reveal the positive current increased rapidly to approximately 500 mA/cm² in the beginning of the treatment and then reduced rapidly, reflecting resistance increase due to the growth of the dielectric layer on the sample surface. Large disturbances in the current transient can be observed for the treatment at 300 Hz for both cathodic and anodic response. Meanwhile, when the frequency was set at 450 Hz, the current dropped in a steady manner.

The current transient recorded at 300 Hz indicates an unstable chain of reactions might have occurred at the surface, inducing gas evolution and/or generating defects in the dielectric layer.

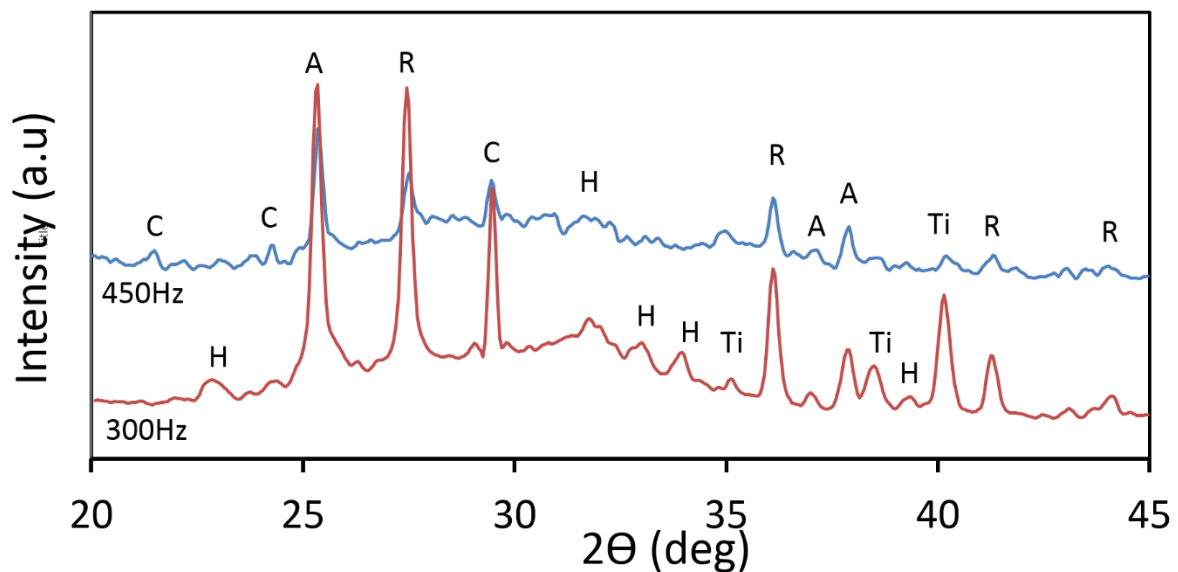


Figure 31 XRD spectra of coatings produced on cp-Ti substrate by PBP PEO treatments in the calcium propionate based electrolyte with Ca/P=1.67 at various pulse frequencies. (A, anatase; R, rutile; Ti, titanium; H, hydroxyapatite; C, calcium carbonate)

The phase composition of coatings produced on cp-Ti substrate at different frequencies in the electrolyte with Ca/P=1.67 is displayed in Figure 31. Peaks corresponding to anatase, rutile, calcium carbonate and Ti substrate can be observed on the patterns of both coatings.

The pattern of the coating produced at 450 Hz shows that the peaks of anatase are systematically higher than those of rutile, suggesting anatase is more abundant in the coating. Weak broad peak at 31 to 33° 2 θ can be observed indicating presence of a mixture of amorphous and crystalline CaP constituents on the surface. When the frequency decreased to 300 Hz, the intensity of rutile peaks becomes stronger. This coincides with the disturbance in the current transient (Figure 30), indicating the vigorous reactions occurred at the surface could promote anatase-to-rutile phase transformation.

It is interesting to observe a set of peaks that matches CaCO₃, with the peak at 29.2° 2 θ having the highest intensity. This could be a result of a combination dissolved CO₂ in the aerated alkaline electrolyte which lead to the adsorption of carbonate ions on the surface and the attraction of propionic ions to the discharge channels, leading formation of CaCO₃ phase. This could be promoted by the fluctuating current response observed for the treatment at 300 Hz (Figure 30), with associated reactions probably leading to high levels of carbon and calcium on the surface.

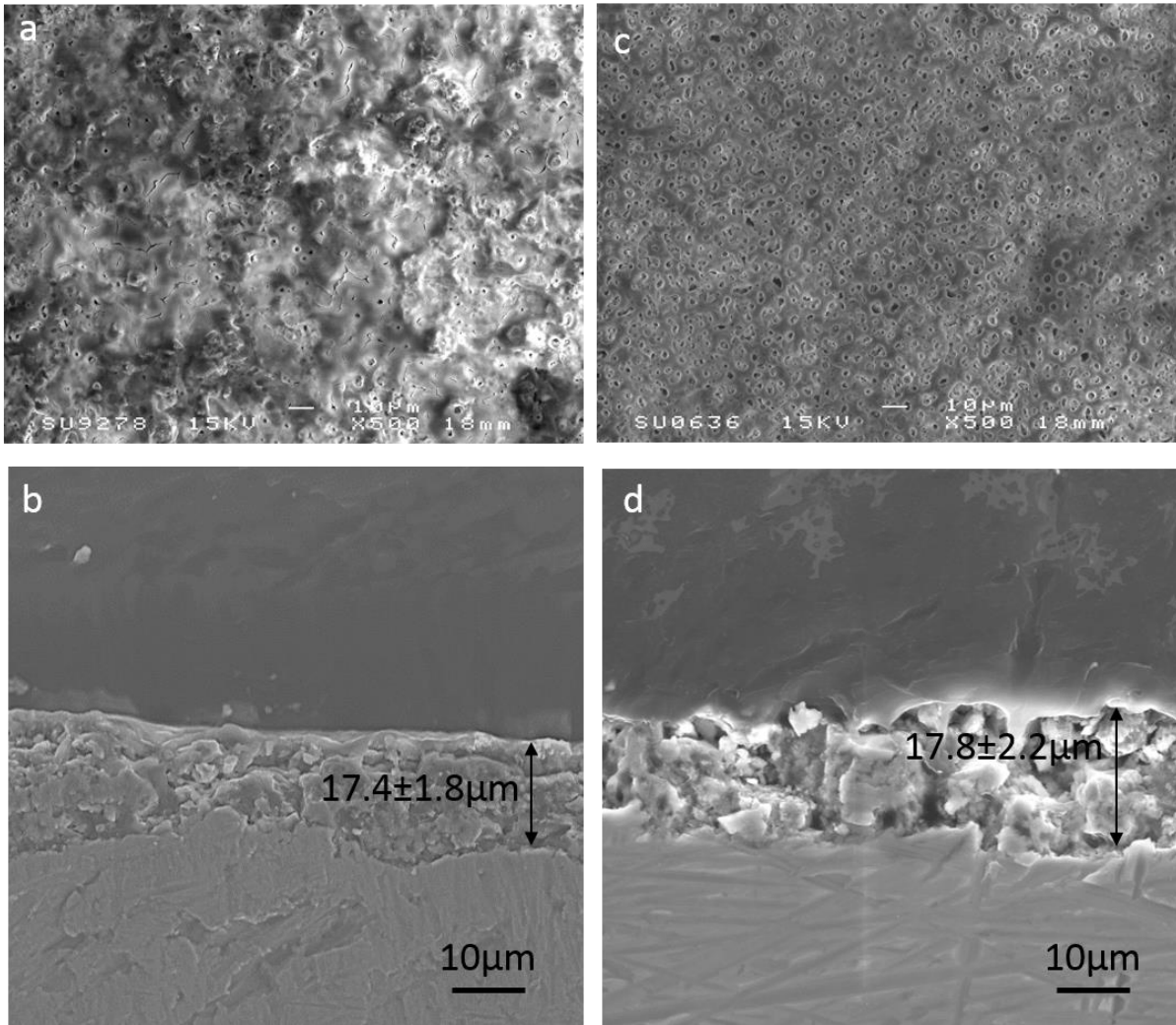


Figure 32 SEM micrographs of coatings produced on cp-Ti substrate by PBP PEO treatments in the calcium propionate based electrolyte with Ca/P=1.67 at voltage pulse frequencies of (a, b) 300Hz and (c,d) 450Hz.

Figure 32(a and c) reveals the surface morphology of coatings formed using potentiostatic PBP PEO currents. When the frequency is set at 300 Hz, a translucent layer with cracks propagating through the matrix can be observed. Results from Figure 32b suggest that the surface of the coating produced at 300 Hz is relatively smoother than that of the coating produced at 450 Hz (Figure 32d), which indicates the layer of translucent material is not a result of powerful arcing causing coating material to spray out of discharge channels, but surface re-melting. When the frequency is set at 450 Hz, elongated porous structures can be observed, with presence of pore-in-pore and pin-hole pores at the surface.

Table 10 Relative atomic percentages of elements in the surfaces of PEO coatings produced on cp-Ti substrate in the calcium propionate based electrolyte with Ca/P=1.67 at various frequencies.

| Element (at%) | Processing variable | |
|------------------|---------------------|-------------|
| | Frequency (f) | |
| | 300Hz | 450Hz |
| Ca | 12.0 | 10.9 |
| P | 6.8 | 6.5 |
| Na | 1.1 | 1.1 |
| O | 64.8 | 64.5 |
| Ti | 9.8 | 9.4 |
| C | 5.5 | 7.6 |
| Ca/P | 1.76 | 1.67 |

The elemental composition of the coatings produced at different frequency is displayed in Table 10. Results indicate the use of the PBP voltage mode increased the Ca and Na content in the coating compared to those produced using the PUP voltage mode. This is expected as the introduction of the negative bias would favour the electro-attraction of positively charged ions to the surface. When the frequency is lower, the Ca content in the coating is relatively higher than in that produced at $f = 450$ Hz. This can be explained by shorter time duration in the negative bias to allow transfer of Ca ions from the electrolyte. The comparatively higher C content on the surface of the PEO coatings complies with results from Figure 31, where peaks corresponding to CaCO_3 can be observed.

Although the use of PBP current mode enhances the Ca/P ratio on the surface of the PEO coatings towards 1.67, the resulting surface morphology reveal irregular porous structure on the coating produced with 300 Hz. Meanwhile the coating produced with 450 Hz provided good surface morphology with appropriate Ca/P ratio. However, the resulting phase composition of the coatings indicate presence of calcium carbonate at the surface.

Furthermore, the disturbance in the current transients, indicates difficulties in controlling the treatment process and the coating quality. Therefore further adjustments of the electrical mode are required to produce PEO coatings in the calcium propionate based electrolyte to maintain stabilised processing conditions throughout the treatment.

5.2.8 Understanding and exploring the application of the calcium propionate based electrolyte to the treatment of Ti-6Al-4V alloy

The cyclic voltammogram presented in Figure 16 implies calcium propionate electrolyte with is not suitable for PEO processing of Ti-6Al-4V alloy due to the absence of significant differences between forward and reverse scans, suggesting prevalence of reversible behaviour in the electrochemical system. From the range of calcium propionate based electrolyte with various Ca/P ratio electrolyte those with Ca/P ratio at 1.5 and 1.67 were selected to understand relationships between the current responses of the system and the resulting surface morphology.

In this section, the surface morphology of the coatings produced at various stages of the micro-arc region identified in the voltammogram will be examined to provide more information on the processes leading to the coating formation. When the Ca/P ratio is set at 1.5, the difference between the current flex in the forward curve and corresponding current density in the reverse scan at the same voltage is 30 mA/mm² (Figure 33a). Results from the previous sections using cp-Ti substrate have indicated the point of flex is associated with the commencement of powerful arcing.

Figure 33c reveals that, as the applied voltage increased to 450 V, the pores in the coating deviate from circular shape and become filled by oxide products, with regions of dense matrix observed on the surface. Appearance of dense matrix is commonly associated with development of energetic discharges, however the porous features observed are not consistent with such micro-discharge phenomena. Figure 33f displays the surface morphology of the coating produced at 450 V, featuring a mixture of open and closed pores as well as pin-holes. The pore shape does not deviate from a circular shape, similar to that observed in Figure 33c and large regions of dense matrix are absent.

PEO treatment involves a range of reactions occurring during the coating development process, results from Figure 33 suggest if the forward and reverse curves are located at similar current and voltage regions, the products formed during the forward scan would

readily dissolute in the reverse scan due to the cathodic reactions occurring. This could explain the appearance of a layer of matrix on the surface. These results indicates the single static mode to be not suitable for the PEO treatment of Ti-6Al-4V substrate using calcium propionate electrolyte.

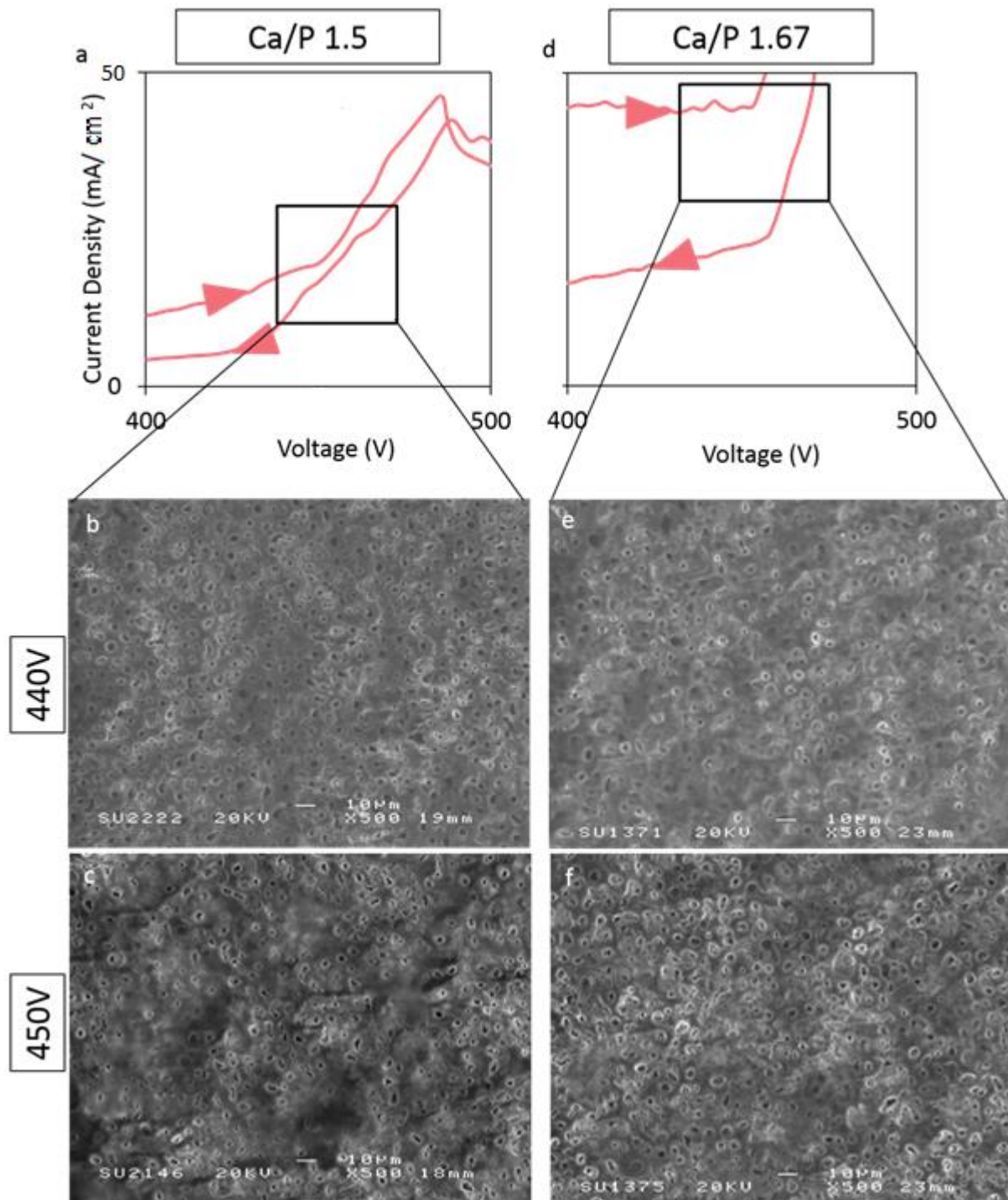


Figure 33 Cyclic voltammograms of Ti-6Al-4V anode in the calcium propionate based electrolytes with various Ca/P ratios and corresponding SEM images of coatings produced at different voltages.

5.2.9 Application of the two-step control PEO process

Previous section shows the use of the single-step potentiostatic PEO mode for the treatment of Ti-6Al-4V substrates is not suitable from a manufacturing perspective, as the resulting coatings show uneven appearance and disturbances in current transients recorded throughout the treatment suggest the reactions leading to the coating formation are not stable. The presence of high-intensity peak II in the CV curves indicates that relatively high current densities would be required for the single-step galvanostatic PEO mode to allow sparking to commence. Therefore a new control mode is developed to overcome these issues.

The two-step control method involves the application of a short-term (up to 30 s) potentiostatic polarisation at 250 V to provide the minimum energy required to overcome the energy barrier associated with peak II, this would facilitate the achievement of potentials sufficient for the sparking to commence. The second step can then be carried out with galvanostatic control at a current density lower than that required to overcome the peak II. In this study, the current density and the second step is set at 50 mA/cm², with various treatment times used to understand the coating formation process under such conditions. The aim of the two-step control method is to enhance the stability of the coating formation process during PEO treatments of heterogeneous substrates, e.g. α - β Ti-6Al-4V alloy.

Figure 34 displays the current and voltage transients recorded during the two-step control PEO treatment. Stage I corresponds to the treatment carried out under potentiostatic mode at 250 V. The treatment during Stage II was carried out under the galvanostatic control using current density at 50 mA/cm² at different times.

Compared to the transients recorded for the treatments conducted in the single step mode, the use of the two-step control method has shown to promote a more stable and controllable behaviour of electrical characteristics throughout the treatment. When the treatment enters stage II, the voltage increases within 2 min up to approximately 350 V, thereafter decreasing in growth rate, before being stabilised at around 410 V at 550 s into the treatment.

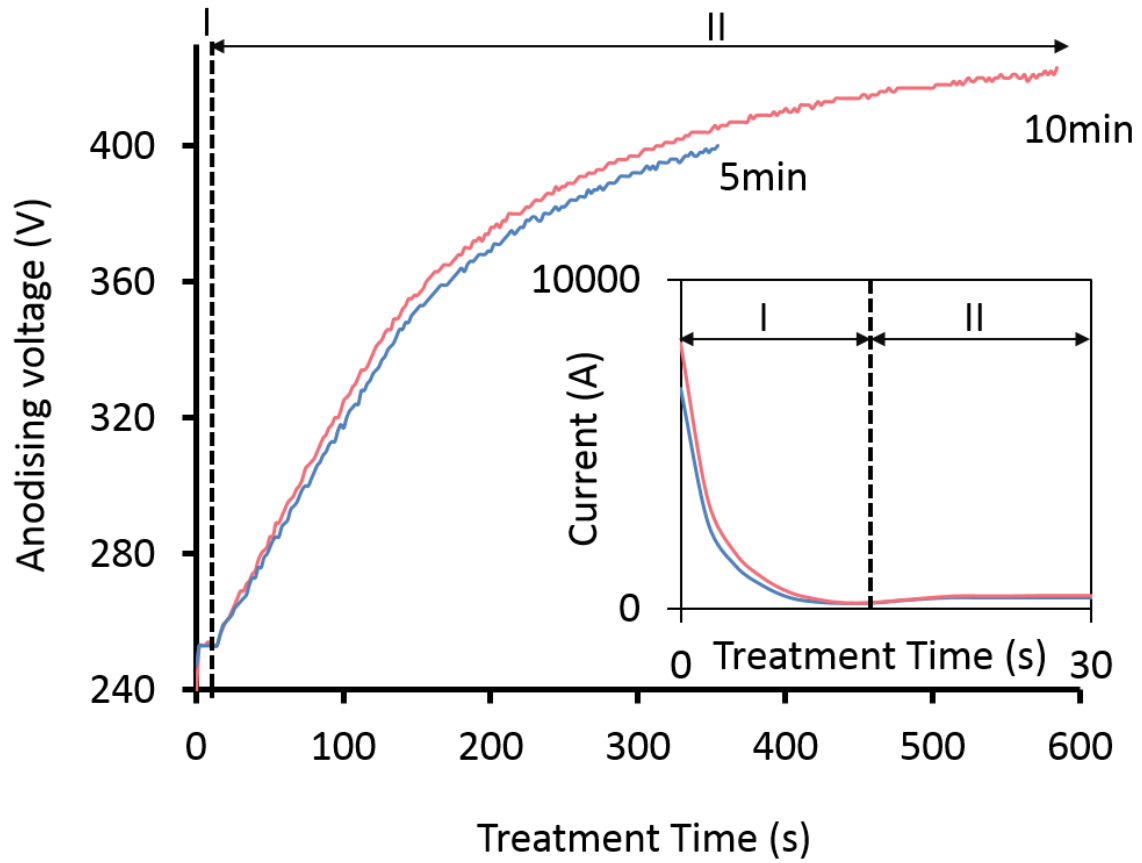


Figure 34 Current and voltage transients recorded during the two-step PEO treatment of Ti-6Al-4V substrate in the calcium propionate based electrolyte, with stage I carried out at 250V and stage II – at 50 mA/cm², for various times.

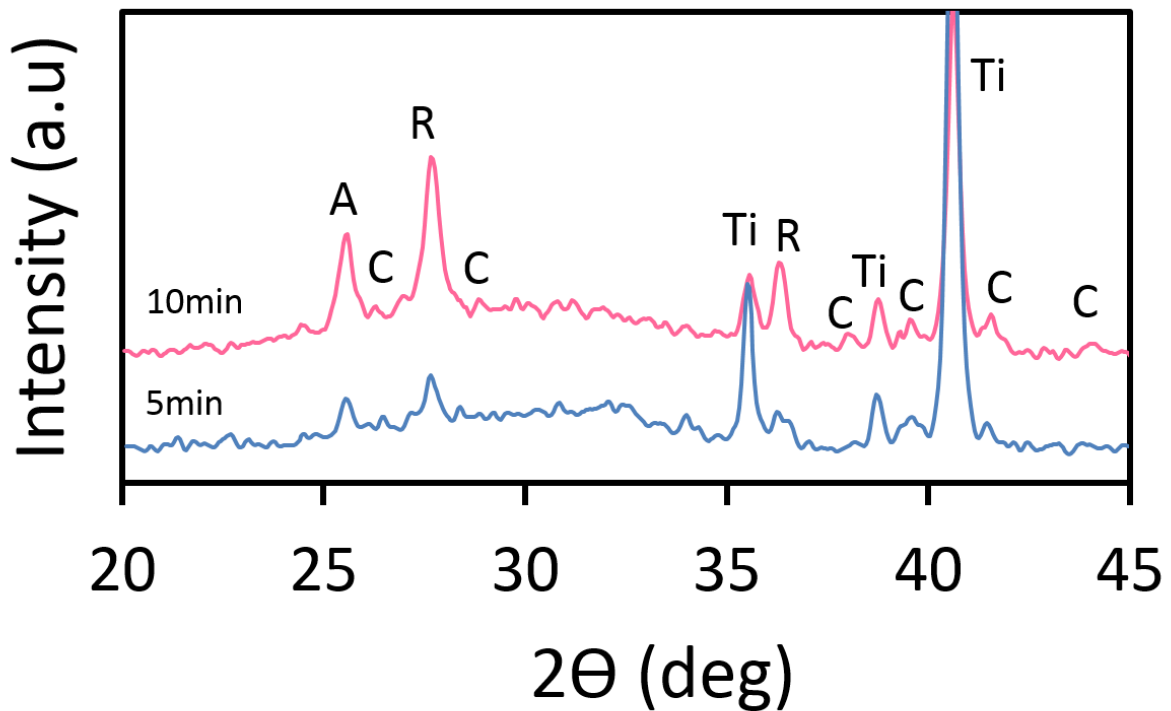


Figure 35 XRD spectra of coatings produced on Ti-6Al-4V substrate using the two-step control method in the calcium propionate electrolyte with Ca/P ratio of 1.67. (A is anatase, R is rutile, Ti is titanium alloy and C is calcium carbonate)

Figure 35 shows XRD spectra of coatings formed using Ti-6Al-4V substrate in the calcium propionate electrolyte using the two-step control method. Peaks corresponding to anatase, rutile and Ti substrate can be observed, interestingly the peaks of calcium carbonate can also be seen. This suggests that the calcium propionate based electrolyte favours formation of calcium carbonate at the surface of the coating. A scattering bump in the 2θ ranging from 31° to 33° detected on both spectra indicates precipitation of amorphous CaP compounds.

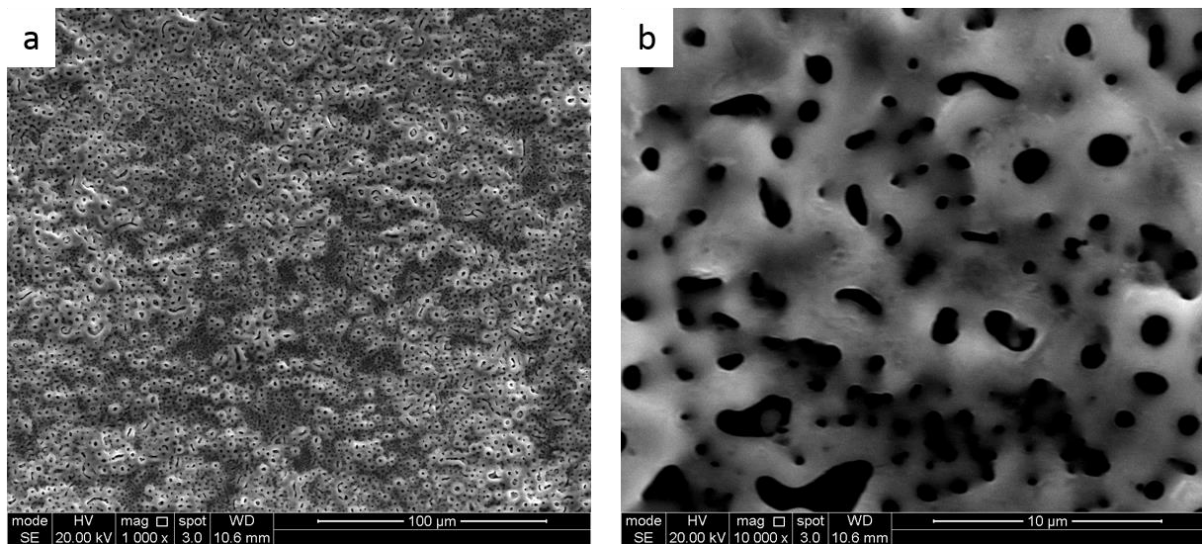


Figure 36 Surface plane SEM images of the PEO coating on Ti-6Al-4V substrate produced at 250V for 15s.

Figure 36 presents the surface morphology of Ti-6Al-4V substrate after 250V polarisation was applied for 15s. This corresponds to the beginning of sparking stage, when small sparks can be seen moving rapidly across the surface. A porous structure with the average pore size of $0.97 \pm 0.39 \mu\text{m}$ is formed on the surface. The raised large porous structure observed on the surface could be a result of gas evolution during the crystallisation of the amorphous and oxide film rupturing being healed by the subsequent discharges.

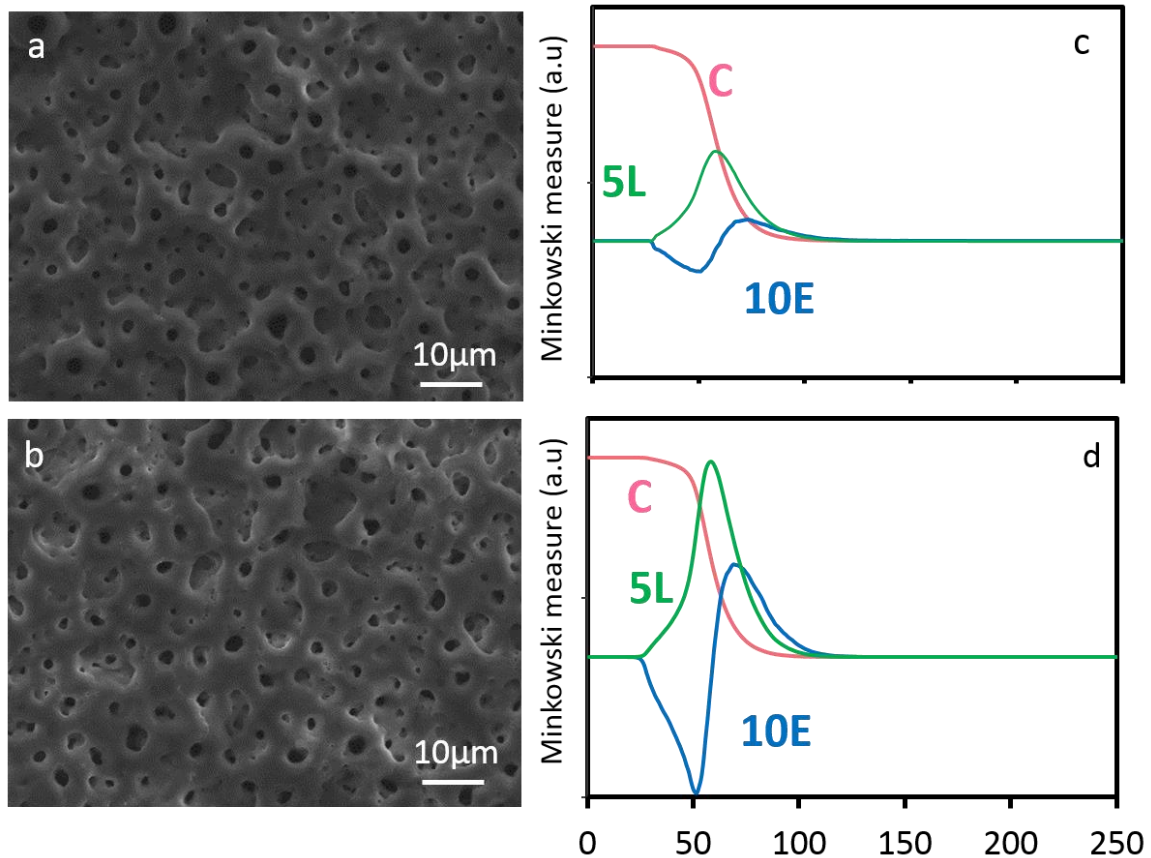


Figure 37 SEM micrographs of coatings produced on Ti-6Al-4V substrate using the two-step control method with treatment times set at 5(c) and 10 min (d), with respective Minkowski functionals (c,d) C(ρ), 5L(ρ) and 10E(ρ).

Figure 37 presents the surface morphologies and the corresponding Minkowski functionals of coatings produced using the two-step control method on Ti-6Al-4V substrates in the calcium propionate based electrolyte. A uniform porous structure can be observed on both coatings, which indicates the use of the two-step control mode can significantly improve the surface morphology compared to that formed using the potentiostatic DC mode. The increase in treatment time appears to enhance the connectivity between the pores and the matrix, this is reflected in a higher L_{\max} value in the Minkowski plot.

The use of the two-step control method has demonstrated a possibility to achieve more stable treatment conditions, which is reflected in absence of disturbances in the current and voltage transients. Further, the coatings produced possess uniform porous structures that are supposed to favour cellular attachment.

5.2.10 In vitro experiments for coatings produced using calcium propionate based electrolyte

Surface topology is usually regarded as one of the major factors influencing the cellular response to the surface. However, the direct correlation between the two is still unclear. In PEO research, the correlation between the individual morphological features such as pits, grooves and circular pore shapes are often analysed qualitatively. Therefore it is difficult to compare between published results of different works. The following section pursues a two-fold objective; first to evaluate the biological response of PEO coatings formed in the calcium propionate based electrolyte, secondly to study the influence of morphological features of the coatings produced to the osteoblastic response.

The details of processing parameters of Ti-6Al-4V substrate for further *in vitro* assessment are displayed in Table 11. For the remainder of this thesis, the samples will be referred to as CP 1, CP 2 and CP 3 coatings. MG-63s were seeded onto the surface at 75,000 cells/cm² and the cell viability were assessed as described in Chapter 3.

Table 11 Processing conditions of Ti-6Al-4V substrates selected for in vitro assessment.

| Sample label | PEO treatment conditions | | |
|--------------|--------------------------|------------------------------|----------------------|
| | Step 1 (V) | Step 2 (mA/cm ²) | Treatment time (min) |
| CP 1 | 250 | 50 | 5 |
| CP 2 | | 50 | 10 |
| CP 3 | 450, $\delta = 50$ | - | 5 |

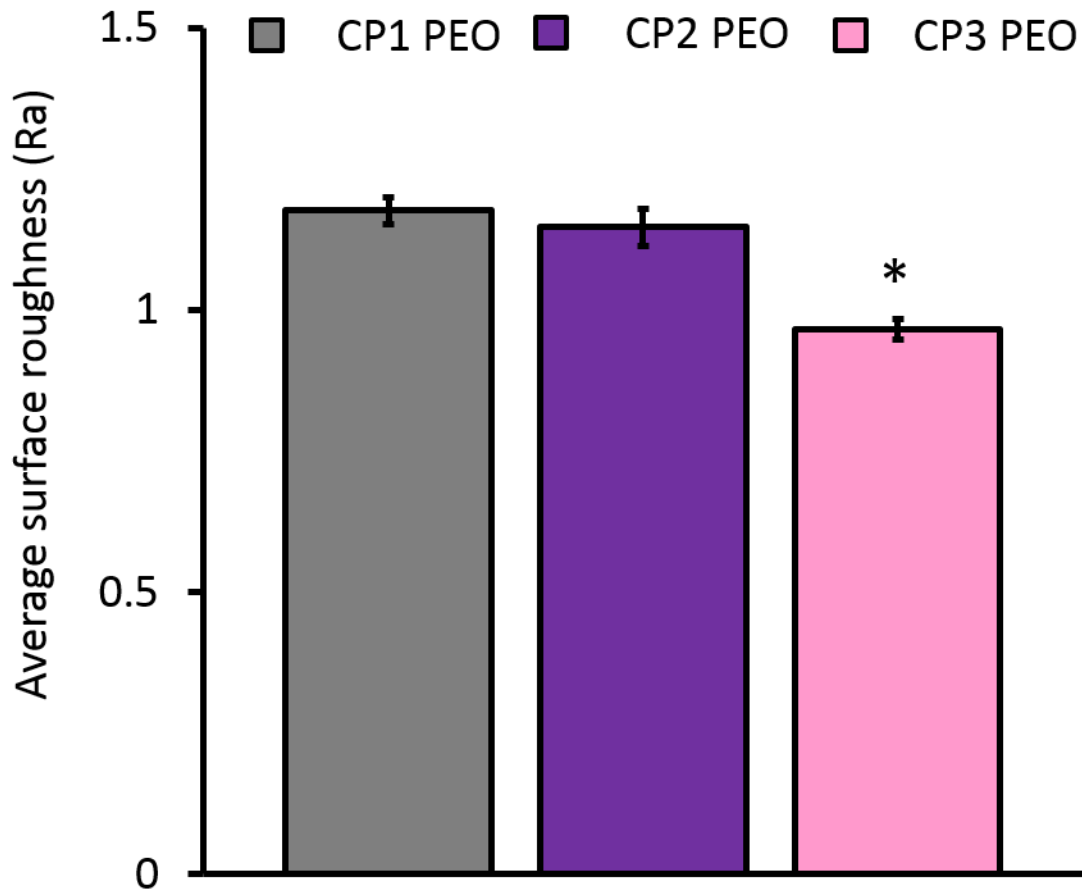


Figure 38 The mean average surface roughness of PEO coatings produced for biological examination (* $p > 0.005$, indicating statistically significant difference from both CP1 and CP2, $n=3$)

The average surface roughness of the coatings produced in the calcium propionate based electrolyte on the Ti-6Al-4V substrate is displayed in Figure 38. The average roughness of the surfaces lies between 1.0 and 1.4 μm and is significantly lower for the CP 3 coating than for the CP 1 and CP 2. At the same time, there are no significant differences between the latter two coatings.

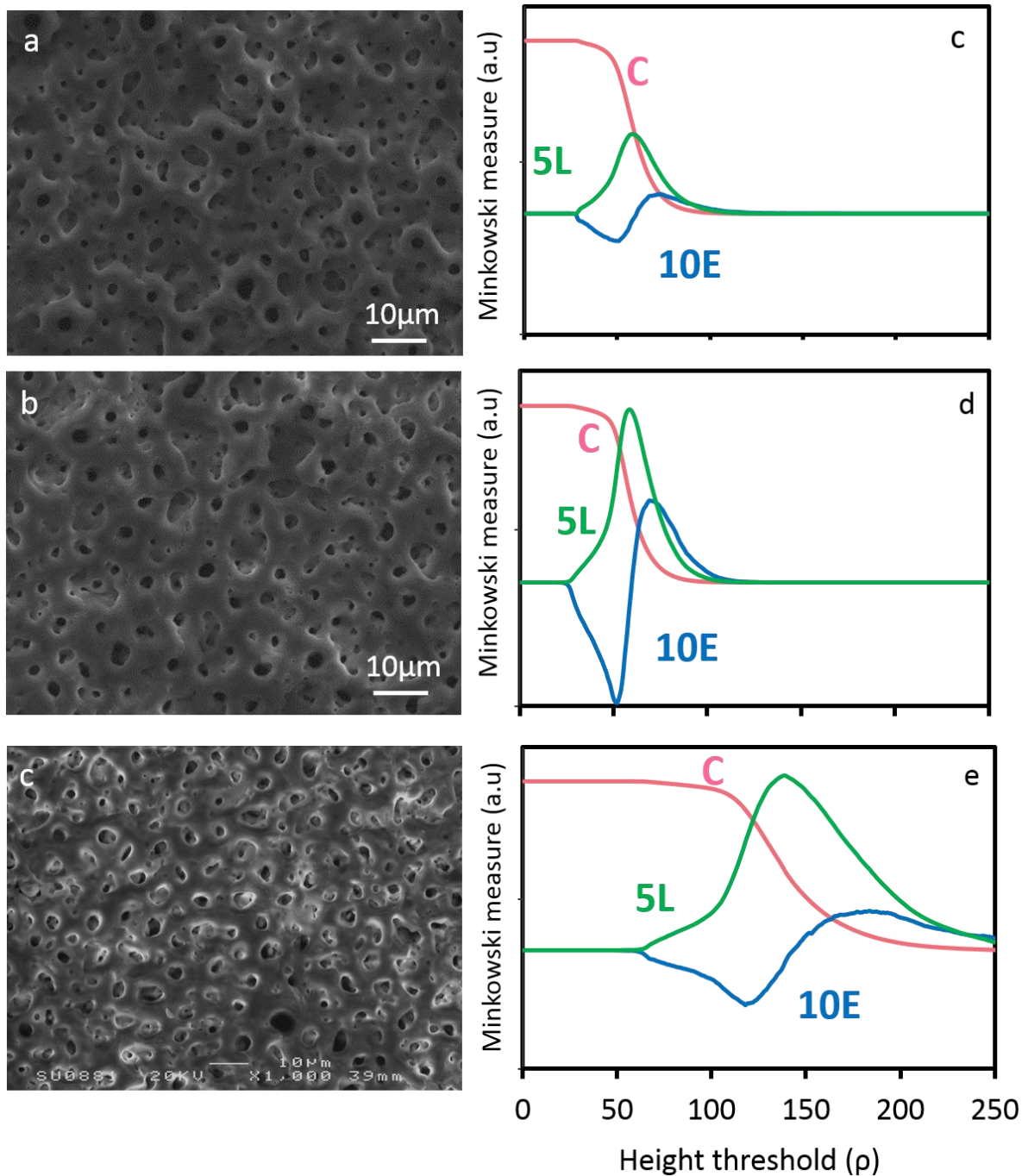


Figure 39 SEM micrographs of coatings produced on cp-Ti substrate in calcium propionate electrolyte selected for in vitro assays with respective Minkowski functionals $C(\rho)$, $L(\rho) \times 5$ and $E(\rho) \times 10$.

The surface morphologies and the respective Minkowski functional plots of the PEO coatings selected for biological assessment are presented in Figure 39. Uniform porous morphologies can be observed for all processing parameters. When compared the Minkowski plots, the shape of the surface coverage C curves shown similar characteristics for the CP 1 and CP 2 coatings, which reflected by the similar average surface roughness in Figure 38. The

comparatively higher threshold range for the curve inflection for the CP 3 coating implies some pores are partly filled, which is consistent with the corresponding SEM image.

The boundary length L curves for both CP 1 and CP 2 show symmetrical maxima, suggesting a presence of certain regularities in the pore size and shape distributions for the two coatings. A higher L_{max} value for the latter coating implies a more developed interconnectivity between the pores and the matrix. The L curve of the CP 3 coating features distortions, this suggests the surface morphology is more irregular and some pores shown deviation from circular shape.

5.2.11 *In vitro* biological response of coatings produced using calcium propionate based electrolyte

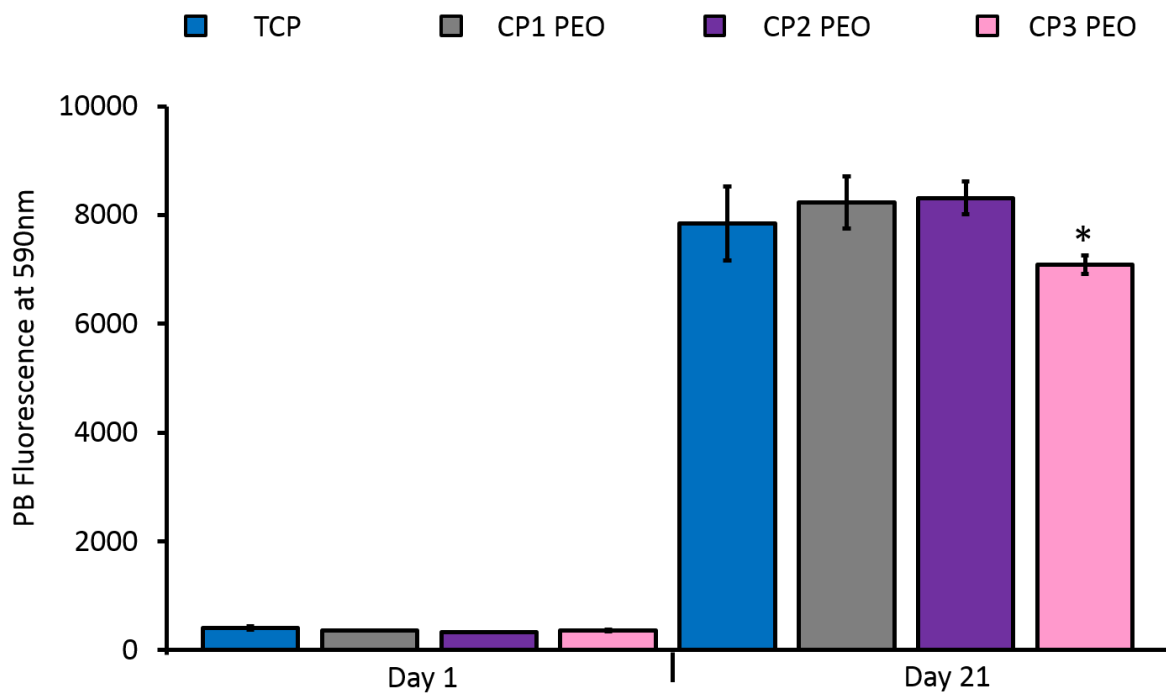


Figure 40 Viability of MG63 cells on the PEO coatings assessed using PrestoBlue assay at days 1 and 21. The resulting PrestoBlue stain was measured at 590nm. * indicates statistically significant difference ($p < 0.05$) from CP 1, CP 2 and tissue culture plastic control. (n=3)

The cell viability is displayed in Figure 40 and after 24 h of seeding, the viability of the cells was examined using PrestoBlue assay and found the cells to be attached to the PEO coatings and tissue culture plastic controls, without significant differences. At 21 days after seeding, there was no significant difference between cell viability on CP 1, CP 2 and tissue culture

plastic control. This indicates over a longer period of time, there is an increase in the cell viability on the CP 1 and CP 2, which is comparable to the TCP control.

5.3 Conclusion

This work has investigated the prospects of using novel calcium propionate based electrolytes in PEO treatments of Ti alloys. The use of the CV method have aid the identification of the potential ranges favourable for PEO treatments using calcium propionate based electrolyte. In this study, it has shown that with the Ca/P ratio in the range of 1.67 and 2 is suitable for PEO treatment in such a plateau peak III and a lack of peak V in the reverse scan in observed in the voltammogram.

Furthermore, it has explored into the influence of different electrical modes to the coating property, such as the phase composition and surface morphologies. The development of the two-step control method has provided the capability to reduce disturbances in current and voltage transients and obtain uniformly porous PEO coatings. The use of the two-step control method has opened up a new direction of research into more controllable PEO processing of heterogeneous Ti alloy substrates and further investigations into such electrical mode can allow refinement of the coating characteristics.

Coatings produced in the calcium propionate based electrolyte showed good biocompatibility *in vitro*. The MG-63 osteosarcoma cells have shown high proliferation rate on the examined coatings, which is comparable with that on the tissue culture plastic control. This concludes the surface features regularity as presented in CP1 and CP2 are favourable for cell proliferation, while the interconnectivity between the pores and matrix does not appear to show significant influences. Meanwhile, the reduction in surface regularity (CP 3) shown to reduce the cell viability on the surface, which can be speculated as not favourable for cell proliferation.

Chapter 6: PEO treatments of Ti alloys in the calcium L-lactate containing electrolyte and resulting coatings

6.1 Introduction

In Chapter 4, it has been demonstrated that calcium L-lactate can be considered a promising source of calcium in the PEO treatment to form bioactive coatings. However it had also been shown that the electrochemical behaviour of both cp-Ti and Ti-6Al-4V alloy substrates in solutions containing carboxylate ions is rather complex. This Chapter investigates the effect of calcium L-lactate in the electrolyte for PEO treatment by examining the electrochemical behaviour of Ti substrates in it. The obtained results are used to optimise the processing parameters of PEO treatments aiming to produce bioactive coatings with controllable phase composition and morphology. The coatings produced are characterised in by XRD and SEM methods, and selected coatings will undergo *in vitro* assessment of biological response.

6.2 Results and Discussion

6.2.1 Influence of calcium L-lactate concentration to electrolyte characteristics and cyclic voltammetry behaviour of Ti anodes

Table 12 Effects of calcium L-lactate concentration to the electrolyte properties.

| Electrolyte composition | | Electrolyte property | |
|-------------------------|---------------------------|----------------------|----------------------|
| Calcium L-lactate (M) | Sodium orthophosphate (M) | pH | Conductivity (mS/cm) |
| 1.5 | 0.1 | 9.2±0.2 | 16.25±2.3 |
| 1.67 | | 9.2±0.1 | 18.9±2.5 |
| 2.0 | | 10.79±0.8 | 18.8±0.8 |

The electrolyte solutions were prepared by dissolving calcium L-lactate and sodium orthophosphate in distilled water, similar to those described in Chapter 5. Table 12 displays the influence of calcium L-lactate concentration to the electro-physical and chemical properties of the electrolyte in the temperature range from 15 to 30 °C. The electrolytes are mild-to-strong alkaline with alkalinity increased as the concentration of the calcium salt increases above 1.67 M. Meanwhile, the conductivity of the electrolyte does not appear to be influenced by lactate concentration.

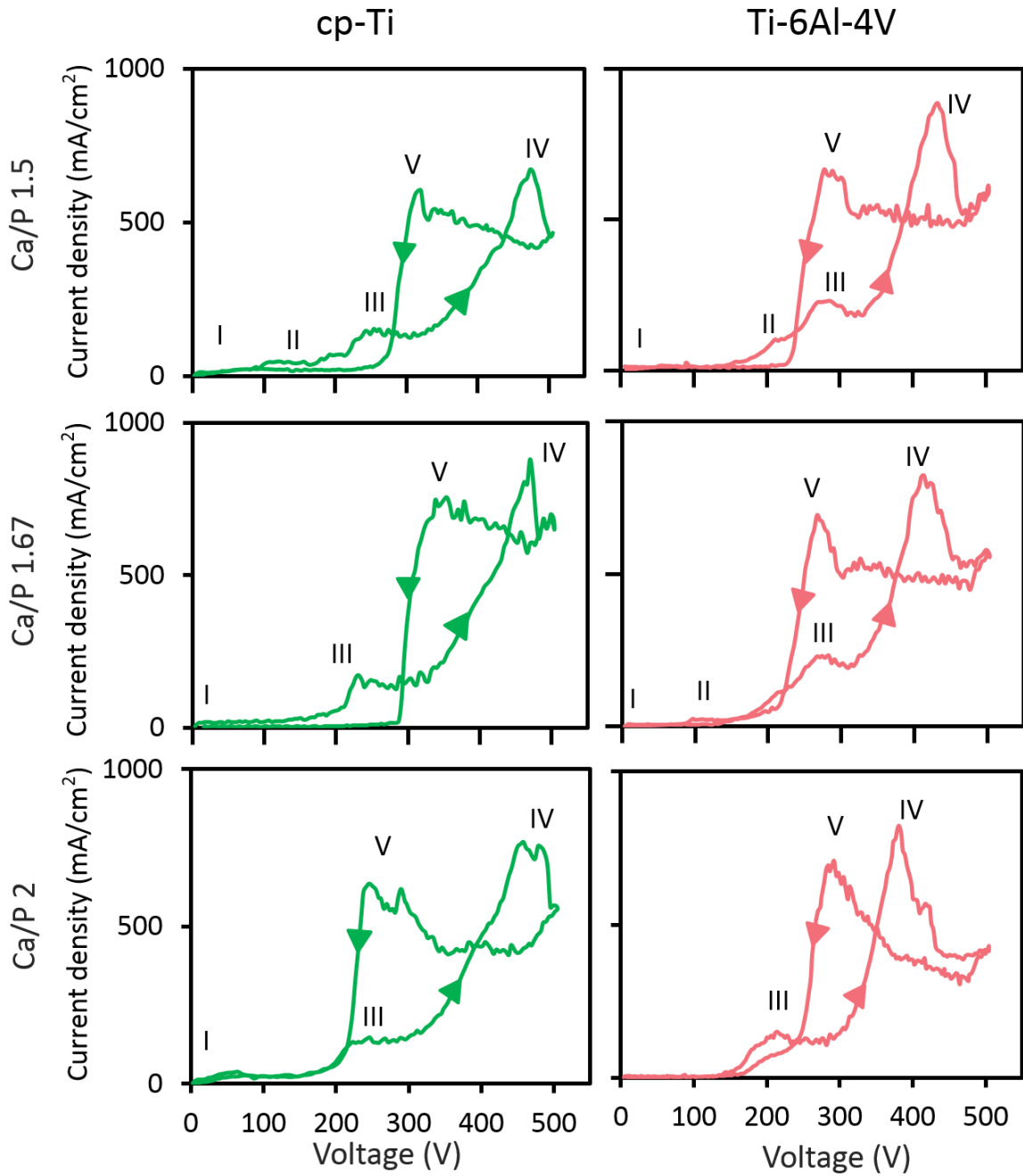


Figure 41 Cyclic voltammogram of cp-Ti and Ti-6Al-4V anodes in sodium phosphate electrolyte with varied calcium L-lactate content. The direction of arrows represent the direction of scan.

Table 13 Peak locations deduced from the cyclic voltammogram of cp-Ti and Ti-6Al-4V anodes in Figure 41 with various Ca/P ratio in the electrolyte.

| Peak (Voltage) | Electrochemical behaviour | | | | | |
|-------------------|---------------------------|------|---------|-----------|------|-----|
| | Cp-Ti | | | Ti-6Al-4V | | |
| | 1.5 | 1.67 | 2 | 1.5 | 1.67 | 2 |
| I | 11 | 8 | 12 | 20 | 15 | 12 |
| II | 104 | - | - | 216 | 96 | - |
| III | 246 | 227 | 215 | 262 | 255 | 210 |
| IV | 473 | 470 | 457-486 | 430 | 418 | 384 |
| V | 316 | 346 | 290-251 | 306 | 278 | 286 |

Figure 41 shows the current response to the voltage sweep for the two commonly used clinical Ti alloys in electrolytes with different Ca/P ratio. The peaks I to V are labelled similar to those in Figure 11 and Figure 12 in Chapter 4. The voltage ranges corresponding to the peaks located in the voltammograms are displayed in Table 13.

In the forward scan, a small peak I is observed in all curves, as discussed in Chapter 4. Peak II is observed in the voltammogram of the cp-Ti anode in Ca/P 1.5 at approximately 104 V, however as the Ca/P ratio increased, peak II becomes barely defined. When Ti-6Al-4V anode was employed in the electrolyte with Ca/P=1.5, peak II is detected at a higher voltage range (216 V) and as the Ca/P ratio in the electrolyte increased, peak II is shifted to a lower voltage range (96 V) with a lower peak intensity. Comparatively depressed peaks II in the voltammograms for both anodes in the calcium L-lactate electrolyte suggest multiple reactions occurring at the surface suppress the reaction of anodic dissolution.

Peak III marks the initiation of micro-arcing and corresponds to surface re-passivation **due** to competing chemisorption of hydroxyl and PO_4^{3-} ions. As the Ca/P ratio in the electrolyte increases, the location of peak III is shifted to a lower voltage range, as summarised in Table 13. This is consistent with literature data where the increase in electrolyte conductivity would lower the breakdown voltage [14, 140]. Post-peak III depressions can be observed on the voltammograms for both anodes, but the rate of current reduction in that region appears to decrease with an increase in Ca/P ratio in the electrolyte. This could be attributed to the fact that the increase in calcium content would enhance attraction of CaP compounds precipitated near the electrode and/or facilitate anodic decomposition of lactate anion as described in Equation [4.15] to [4.19], liberating a large quantity of gaseous products during the process, which interferes with the local resistance in the system.

When comparing the post-peak III regions in the voltammograms of cp-Ti and Ti-6Al-4V anodes, the drop in current is much more noticeable in the latter. This could be explained by the presence of aluminium in the alloy leading to the formation of Al_2O_3 as discussed in Chapter 4. Furthermore, the addition of OH^- ions from calcium L-lactate contributes to the adsorption onto the anode surface, in particular on the sites where alloying elements such as Al are present [148, 149]. Regardless of the mechanism, it appears that in the post-peak III region, generation of free electrons is accelerated, leading to the development of stronger electron avalanches, which result in the transition of sparking to arcing, as manifested in the high current rise towards peak IV.

The peaks IV in the systems involving both anodes reveal similar shapes when the Ca/P ratio in the electrolyte is set at 1.5 and 1.67. The shape of peak IV in the voltammogram of cp-Ti anode in Ca/P=2 electrolyte transformed from one sharper shape to broader doublet peaks, this suggests more than one oxidation process occurring at the anode surface [110]. In Chapter 4, the anodic oxidation mechanism of lactate proposed by Impey was discussed, Zhai *et al* [150] have further analysed the selectivity of the oxidation and decomposition of lactate ions depending on their concentration. It was proposed that the increase in lactate ion concentration would decrease the selectivity of propionic acid and acetic acid on aluminium sulphate catalyst [151]. It can therefore be speculated that the increase in Ca content in the electrolyte in this study would also initiate different ratio of propionic and acetic acid formation, but due to the vast number of variables present further investigation is required to understand the conversion process in a PEO system.

During the initial stage of the reverse scan (500 to 450 V), the response current continues to reduce at a slower rate on all curves. In the voltage range of 450 to 300 V, when the Ca/P ratio in electrolyte is set at 1.5 and 1.67, the current begins to increase at a similar pace. However when the Ca/P ratio is set at 2, the current is stabilised at $\sim 430 \text{ mA/cm}^2$, before increasing to 620 mA/cm^2 . The stabilised current observed in the reverse scan when Ca/P ratio increased to 2 suggests that insoluble products formed during the forward scan become more abundant in the coating than those formed in electrolyte with lower Ca/P ratios.

A well-defined peak V in the range of 200 to 350 V can be observed in all voltammograms pointing to the reversibility of the anodic process. This suggests a possibility of unstable behaviour of the system and a risk of shifting in the type of reaction that would occur at the surface when using a single static control mode, regardless whether it is potentiostatic or galvanostatic. However, due to the high current growth rate in the voltage range 300 to 450 V associated with micro-arc stage in the PEO treatment, it can be assumed that the galvanostatic mode is comparatively more suitable for this electrochemical system.

The use of potentiostatic mode would allow the voltage to become stable in that voltage range, however the current and voltage transients recorded in Chapter 5 (Figure 16) demonstrated the limitation over the control in surface discharge characteristic. Moreover, the application of potentiostatic control restricts process up-scaling and transfer to different equipment. These disadvantages could be avoided if galvanostatic control was possible. Therefore, the galvanostatic mode would be preferred, and corresponding research is discussed in the following sections.

6.2.2 Application of galvanostatic mode to PEO treatments of cp-Ti substrate in calcium L-lactate electrolyte

The following section examines the possibility of using galvanostatic control mode for PEO treatments of cp-Ti in the electrolyte with Ca/P ratio of 2. The inset in Figure 42 highlights the investigated region of applied current density and its effect on the voltage transient behaviour. This region is selected to understand the characteristics of the oxide film growth under the galvanostatic conditions.

Three stages can be resolved in the voltage transients in Figure 42. At the beginning, for all conditions the anodising voltage increased linearly with the time in the range of 10s to approximately 170 V. The voltage growth rate then decreased gradually and depending on

the applied current density, the extent of this decrease appeared to be different. Interestingly, the final anodic voltage recorded during the treatment is approximately 390 V.

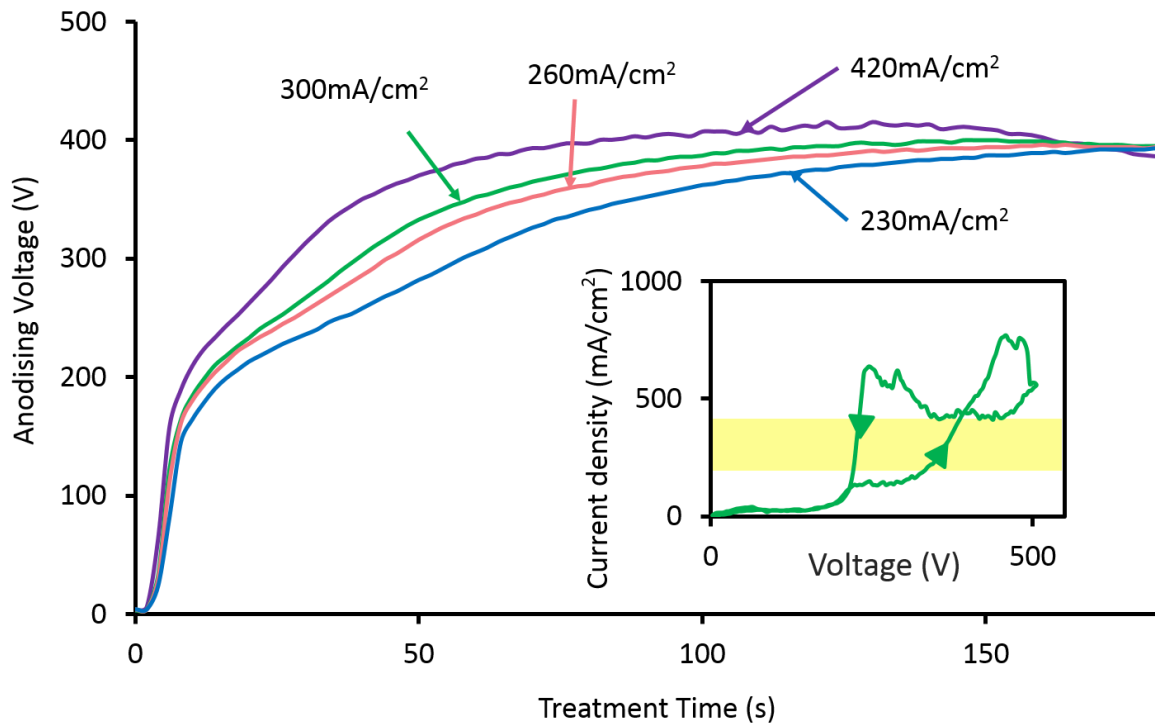


Figure 42 Voltage transient recorded during galvanostatic treatments of cp-Ti substrate in calcium L-lactate electrolyte with Ca/P ratio of 2 with different current densities. The inset shows a part of the cyclic voltammogram highlighting the corresponding region examined.

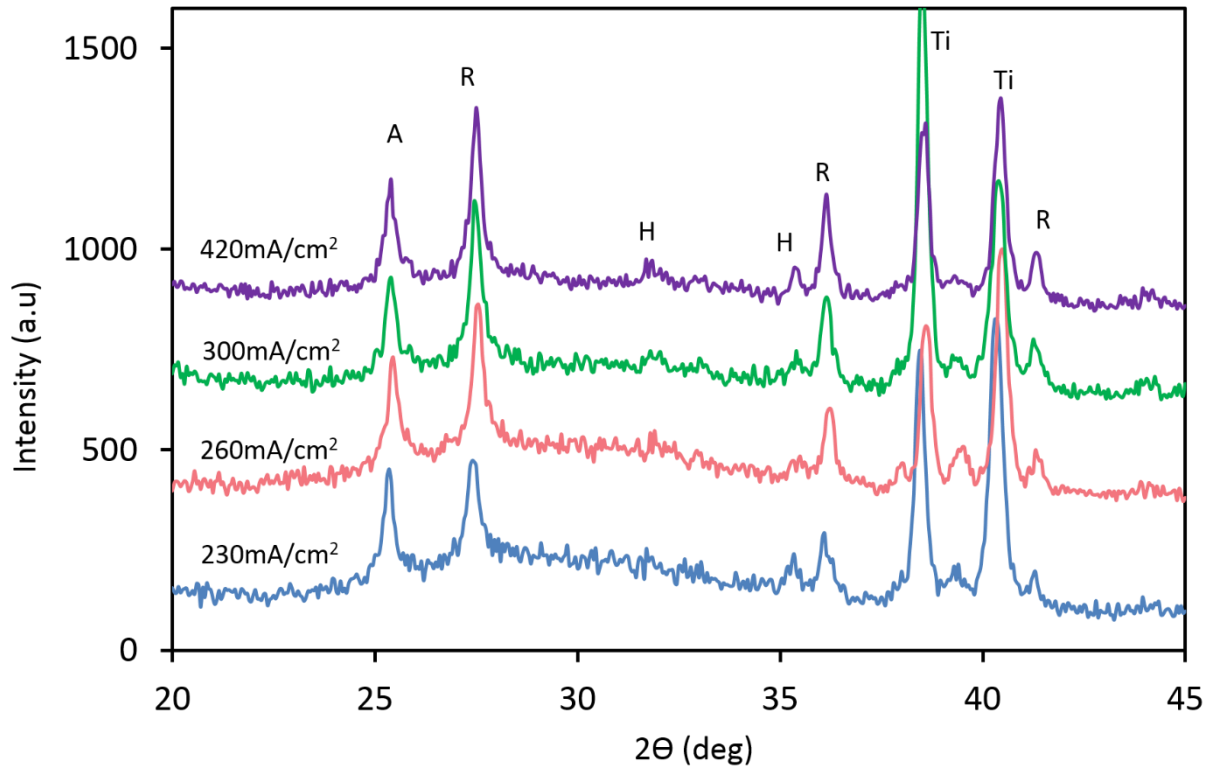


Figure 43 XRD spectra of PEO coatings produced on cp-Ti substrates for 3min in the calcium L-lactate electrolyte with Ca/P ratio of 2 using a galvanostatic DC mode with different current densities. (A, anatase; R, rutile; Ti, titanium and alloy; H, hydroxyapatite)

Figure 43 reveals the phase composition of the coatings produced on cp-Ti at different current densities in the electrolyte with Ca/P 2. Anatase and rutile are the dominant phases for these coatings. The set of peaks corresponding to rutile appears to increase with the increase in applied current density, these peaks are also systematically higher compared to those of rutile in the coating produced above 260 mA/cm². This can be explained by a tendency to develop more powerful discharges at the surface and/or comparatively longer micro-arc stages as shown by the longer stabilised voltage transients at a higher voltage region in Figure 42, which provides favourable conditions for repeated powerful discharge events, promoting the transformation of metastable anatase to stable rutile phase. It is interesting to note that the intensity of anatase peaks does not reduce despite that of rutile increasing with current density. This suggests that the formation of titanium dioxide continues to occur along with the anatase-to-rutile phase transformation.

In essence, galvanostatic mode does not appear to be particularly suitable for PEO treatment in calcium L-lactate electrolyte from the commercial manufacturing viewpoint. Throughout

the treatment, vigorous gas evolution occurred and resulted in electrolyte bubbling and boiling after 3min. This complies with the hypothesis put forward in the previous section suggesting that the reactions at the surface may shift as reflected in the current-voltage behaviour in the region corresponding to micro-arcing (Figure 42). Despite the peaks present in the coating matching HA, from the manufacturing viewpoint this behaviour is not feasible, as bubbling has many adverse effects on the PEO process. Gaseous product formation is commonly associated with the amorphous-to-crystalline transformation at the initial stages of the treatment, moreover during the PEO treatment, gas generated within the coating is released to the electrolyte forming pores on the surface.

These gaseous products, rise to the surface of the electrolyte and enter into the atmosphere. However, in this study vigorous bubbling occurred leading to a foam formed at the electrolyte surface. This foam-like substance formed during PEO treatment would restrict the heat dissipation from the electrolyte and possibly alter its pH. This would subsequently lead to an increase in the electrolyte temperature, affecting the melting-solidification process occurring at the surface which would alter the phase composition and surface morphology of the coating and ultimately lead to inconsistency between batches. Therefore, a method which allows the reactions occurring during the PEO treatment to be stabilised in a more controllable process would be more viable in manufacturing of bioactive coatings for orthodontic and orthopaedic applications.

6.2.3 PEO process and coating optimisation

6.2.3.1 The characteristics of coating growth behaviour under the two-step control method

The reversible behaviour of the electrochemical system makes calcium L-lactate not suitable for the single static control mode. In Chapter 5, a two-step control method was employed to enhance the stability of the coating formation process during PEO treatment. Therefore this section explores the coating formation behaviour under the two-step control mode in the calcium L-lactate based electrolyte in aim to stabilise the reactions that occur during the treatment and to reduce electrolyte boiling.

Similar to the approach explored in Chapter 5, the two-step control method can be categorised into two stages. Stage I here corresponds to the treatment carried out under the

potentiostatic mode at 250V. The treatment during Stage II was carried out under the galvanostatic control using current density at 100 mA/cm² under different treatment times.

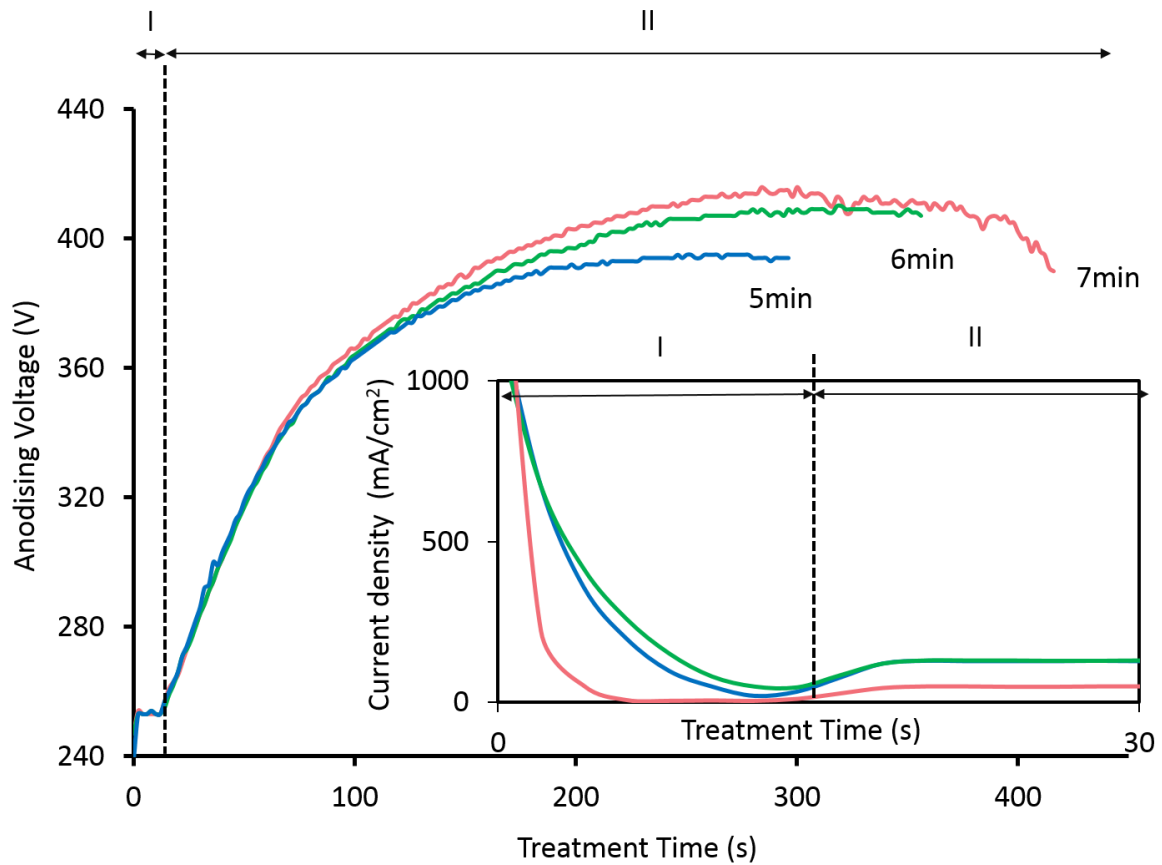


Figure 44 Voltage and current transients recorded during PEO treatments of cp-Ti using the two-step control method in the calcium L-lactate electrolyte with Ca/P 1.67 at the current density of 100 mA/cm² during Stage II with various treatment time.

Figure 44 reveals voltage and current transients recorded during PEO treatments of cp-Ti in the electrolyte with Ca/P=1.67 using the two-step control method. Stage I corresponds to the potentiostatic step at 250 V. The treatment during Stage II was carried out under the galvanostatic control at current density of 100 mA/cm² for different treatment times, similar to the treatments discussed in Chapter 5.

Compared to Figure 42, the use of the two-step control method has shown to allow a more controllable and stabilised voltage growth rate at the initial stages of the treatment. The voltage continues to grow up to approximately 356 V before it starts decreasing. The

anodising voltage appears to stabilise at 5min and as the treatment continues, disturbances can be observed in the voltage transient which begins to reduce at ~ 400 s into the treatment. The variation in the final anodising voltage from 350 V to 410 V recorded for different treatment times despite the same electrochemical parameters, suggests presence of instabilities in electrochemical reactions occurring at the surface. This could be explained by the current-voltage behaviour at low current density depicted in Figure 41. Visual inspection of the samples revealed evidence of inhomogeneous coating with white dots located at the surface and localised burning.

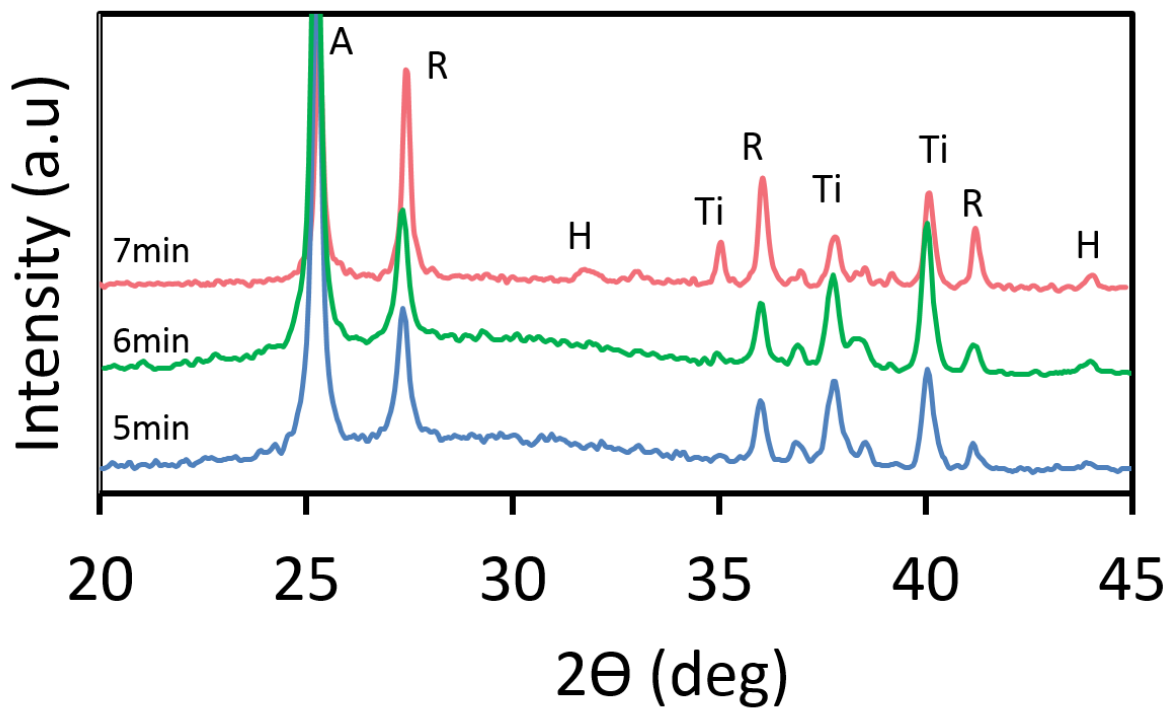


Figure 45 XRD spectra of coatings produced in two-step control method on cp-Ti substrate in the calcium L-lactate electrolyte with Ca/P=1.67 at current density of 100 mA/cm^2 during Stage II of the treatment with different treatment times. (A, anatase; R, rutile; Ti, titanium and alloy; H, hydroxyapatite)

XRD patterns of coating produced on cp-Ti using Ca/P 1.67 electrolyte are shown in Figure 45. Peaks that correspond to anatase, rutile and Ti substrate can be observed. In the coating produced for 5 min, the set of peaks that correspond to anatase are systematically higher than those of rutile, suggesting that anatase is the dominant phase in the coating. As the treatment time increases, the intensities of rutile peak increase. Similar trend indicating development of

anatase-to-rutile phase transformation with increasing treatment time is observed in Figure 54.

Figure 47 shows the surface morphology of coatings produced in the electrolyte with Ca/P=1.67 at different treatment times. In the coating produced for 5 min, evenly distributed pores with average pore size of $2.42 \pm 1.6 \mu\text{m}$ can be observed. Cracks running between the pores are seen, which could be attributed to thermal and growth stress in the coating during the treatment. As the treatment time increased to 6 min, distinctive traces of discharge channels are observed on the coating surface, which is reflected in the sigmoidal flex in the coverage (C) curve (Figure 47). The average pore size of the coating produced for 6 min is $2.49 \pm 0.88 \mu\text{m}$; the small variation in pore size observed is in complimentary of the narrow peak present in the corresponding Minkowski functional (L). The small flex observed in the L curve at low binarization threshold also complies with the presence of large quantity of pin-hole pores on the coating surface. When the treatment time increased to 7 min, the pore shape begins to deviate from circular shape, which is reflected by the reduction in the curve inflection in the corresponding Minkowski plots. The observation of the granular features on the coating produced at 7 min is consistent with the presence of disturbance in the voltage transient in Figure 42, which is an indicator for powerful arcing.

Visual inspection of the coatings shows evidence of burned morphology and white dots on the coating produced for 7 min. Further increase in treatment time (Figure 46) reveals discolouration of the coating, which could be related to dissolution of the coating material.



1 cm



Figure 46 Typical surface appearance of cp-Ti sample PEO treated in the calcium L-lactate electrolyte with Ca/P = 1.67 for over 7 min

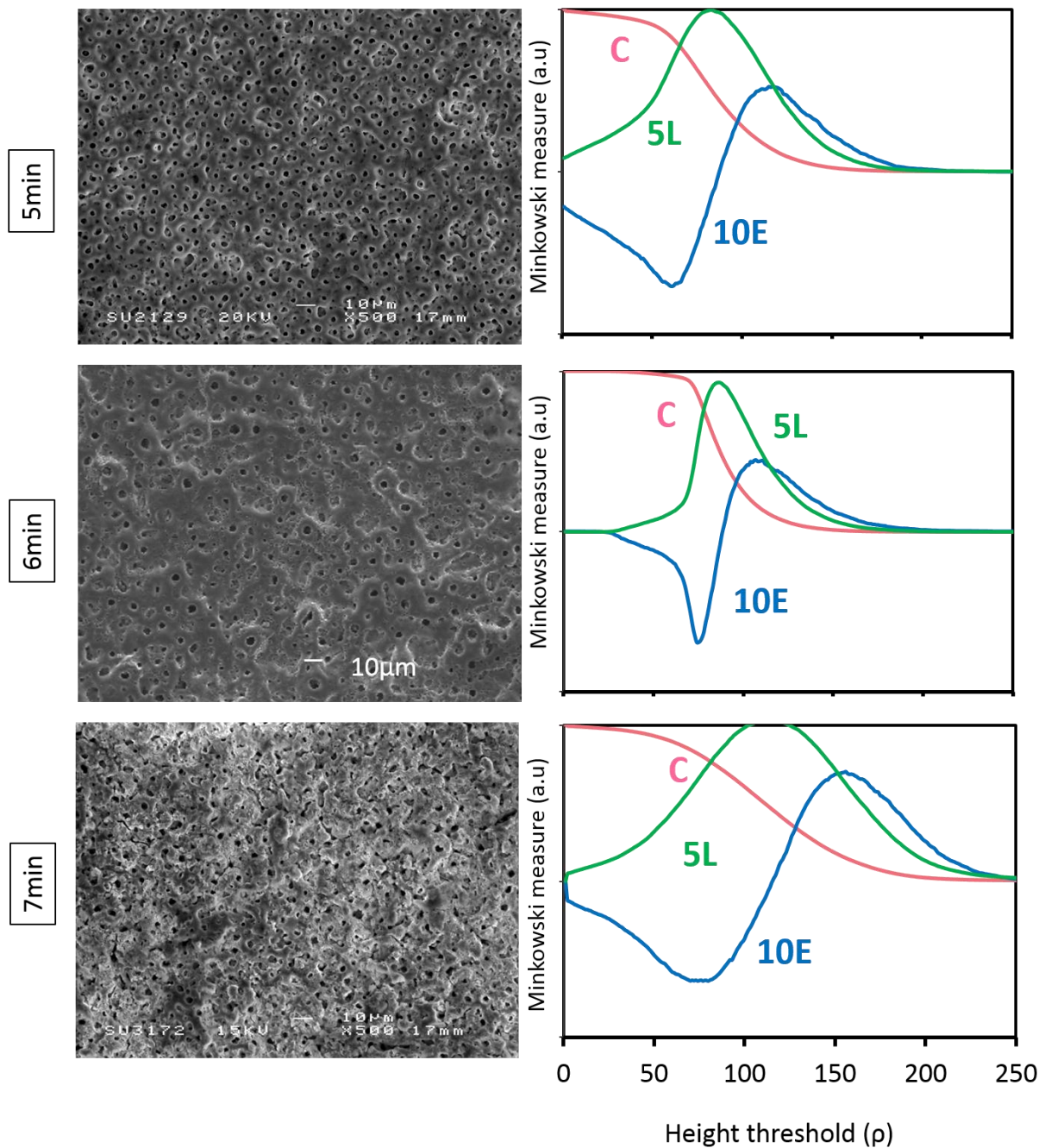


Figure 47 SEM micrographs of coatings produced using two-step control method on cp-Ti substrate in the calcium L-lactate electrolyte with Ca/P ratio of 1.67 at the current density of $100\text{mA}/\text{cm}^2$ during Stage II at different treatment times and respective Minkowski functionals $C(\rho)$, $L(\rho)\times 5$ and $E(\rho)\times 10$.

6.2.3.2 Effects of current density to the coating morphology and phase composition

The previous section demonstrated that the two-step control method can be applied to the PEO treatment in the calcium L-lactate based electrolyte and the results are promising. From the voltage and transient recorded in Figure 44 in previous section, the disturbance in the

voltage behaviour at high potentials is correlated to powerful arcing, which results in appearance of granular features in the surface morphology observed in Figure 47 . Therefore, this section investigates the effect of applied current density on the voltage growth behaviour in the aim to reduce powerful arcing which occurs as the treatment time increases.

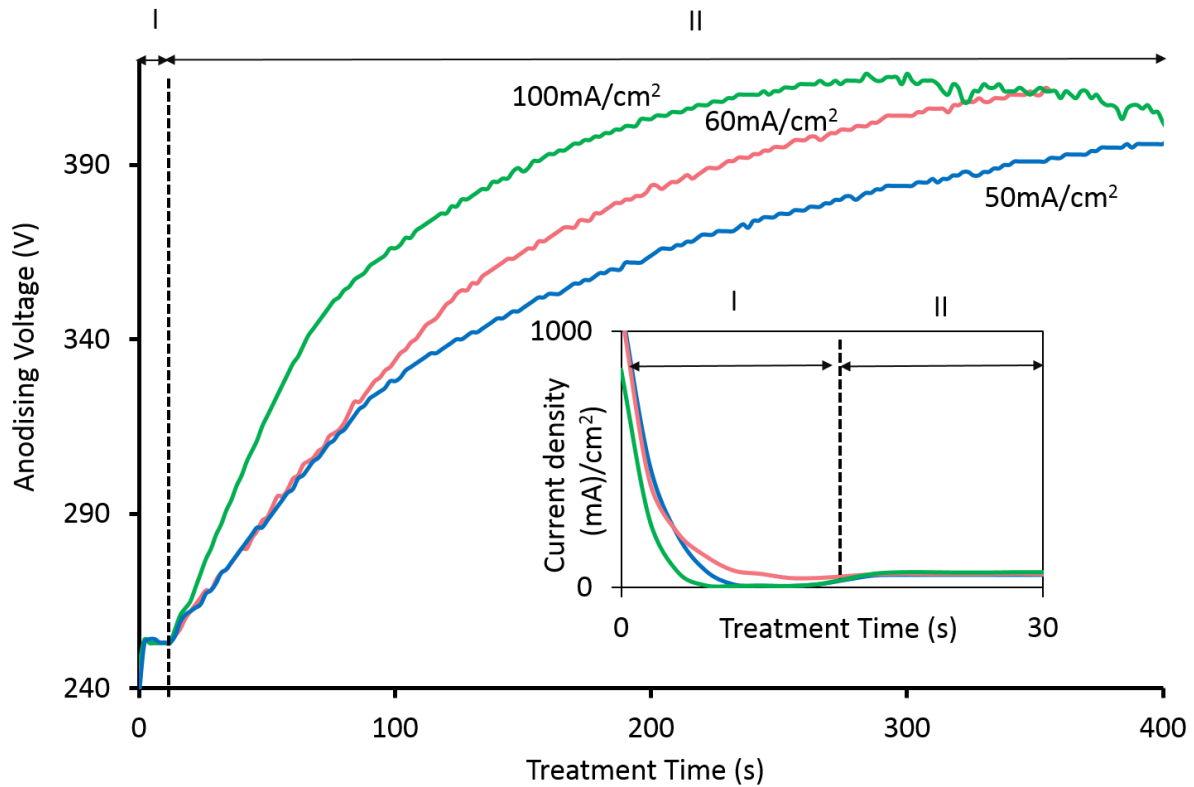


Figure 48 Voltage and current transients recorded during PEO treatments of cp-Ti using the two-step control method in the calcium L-lactate electrolyte with Ca/P=1.67 for 7 min at various current densities during Stage II of the treatment.

Figure 48 reveals voltage and current transients recorded during PEO treatment of cp-Ti substrate in calcium L-lactate electrolyte at different current density during Stage II of the treatment. Stage I was carried out in the potentiostatic step at 250 V. Stage II here corresponds to the treatments carried out under galvanostatic control using various current densities, similar to those discussed previously.

The voltage transient recorded for of the process carried out at 50 mA/cm² is shown to increase to approximately 320 V, after which the voltage retains a similar growth rate until reaching the final value of 395V. A similar behaviour is observed when the current density is set at 60 mA/cm², where the voltage increased to approximately 350 V before retaining a

stable growth rate, leading to the final voltage of 395 V. The growth rate observed at the beginning of Stage II for the treatments performed at 50 and 60 mA/cm² is constant (0.97 V/s). As the applied current density increased to 100 mA/cm², it increases to approximately 1.67 V/s. The non-linear increase in voltage growth rate with applied current density agrees with the results of Sul *et al* [14] showing that higher current densities may cause gas bubble entrapment on the anode surface which reduces the area available for electrochemical reactions, forcing the anodic voltage to increase. This also leads to the disturbance in the voltage transient observed at an earlier stage of the treatment when applied current density is higher.

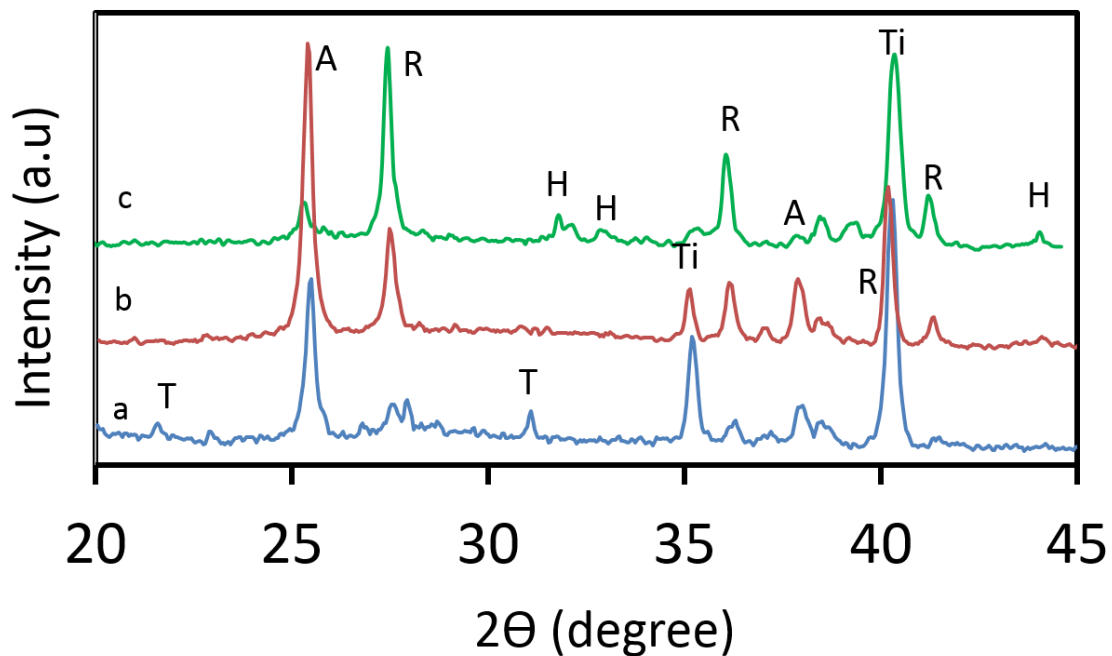


Figure 49 XRD spectra of cp-Ti with PEO coatings produced in two-step control method in the calcium L-lactate electrolyte with Ca/P=1.67 for 7 min at the current density of (a) 50, (b) 60 and (c) 100 mA/cm² during Stage II of the treatment. (A, anatase; R, rutile; Ti, titanium and alloy; H, hydroxyapatite; T, tricalcium phosphate)

Figure 49 shows the XRD patterns of the coated samples produced at different current densities during the Stage II of the treatment. The XRD spectrum of the coating produced at the lowest current density (50 mA/cm²) shows peaks corresponds to anatase, rutile, tricalcium phosphate and Ti substrate. Peaks corresponding to anatase are systematically higher than those of rutile, suggesting the former is more abundant in the coating. The

coating phase composition agrees well with the voltage transient behaviour observed in Figure 48, where the voltage growth rate and its final value are comparatively low.

The spectra of the coating produced at 60 mA/cm² reveal intensities of rutile peaks began to increase when compared to those at 50 mA/cm². At 100 mA/cm², the set of peaks corresponding to rutile becomes to be systematically higher than that of anatase, suggesting that increases in applied current density promote the anatase-to-rutile transformation.

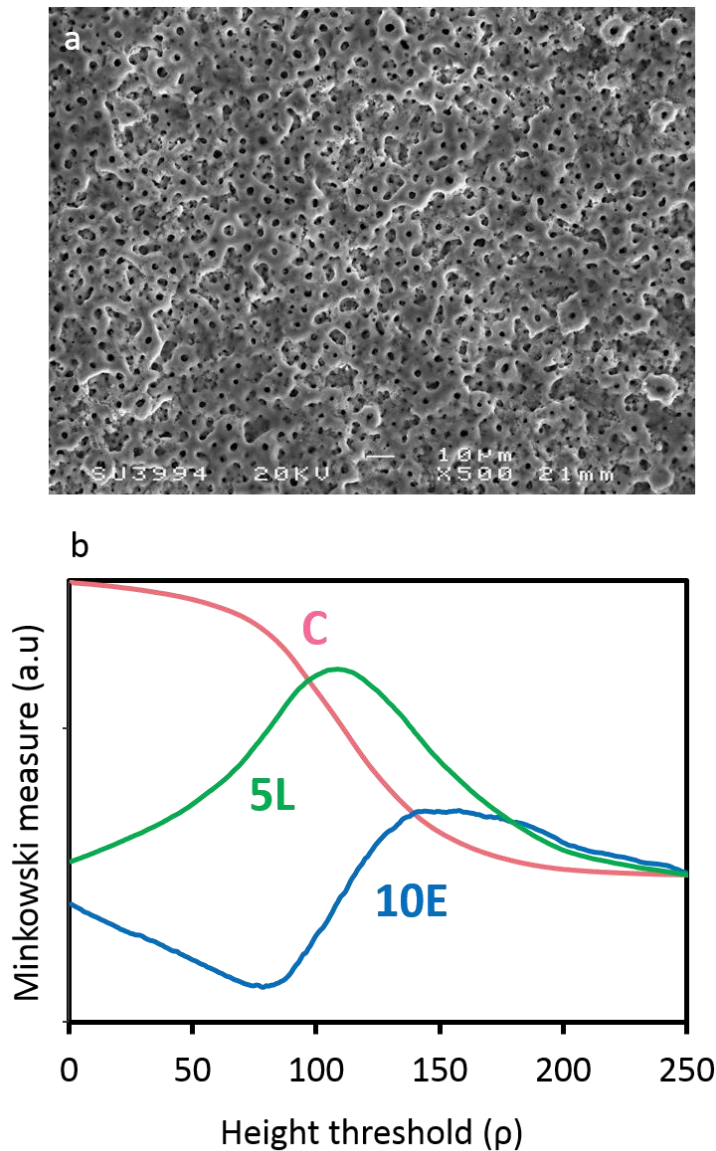


Figure 50 An SEM micrograph of the coating produced using the two-step control method on cp-Tii substrate in the calcium L-lactate electrolyte with Ca/P ratio of 1.67 at current density of 60 mA/cm² and respective Minkowski functionals C(ρ), L(ρ)X5 and E(ρ)x10.

Figure 50 presents the surface morphology and corresponding Minkowski plots of the coating produced using galvanostatic control at 60 mA/cm^2 in the Stage II. Features of porous morphology can be observed in the coating, with presence of pin-hole pores distributed throughout the surface. Compared to the coating produced at 100 mA/cm^2 (Figure 47), the coverage (C) curve reveals a pronounced sigmoidal flex, which suggests features associated with discharge channels are more pronounced, whereas the features related inhomogeneous morphology such as surface deposits, are reduced.

This observation agrees with corresponding Minkowski functionals where the presence of flex at low height threshold in the length (L) curve can be observed. Similar to the coating produced at current density of 100 mA/cm^2 , deviations of the pore shape from circular can be observed on this coating and the average pore size is estimated at $2.33 \pm 1.1 \text{ }\mu\text{m}$. However by comparing the length (L) and Euler (E) curves, it can be seen that with the current density reduced, the pore shape becomes comparatively more circular.

6.2.3.3 Effect of Ca/P ratio in the electrolyte to the coating growth behaviour

In the following section, the electrolyte concentration was increased, so that to shift Ca/P ratio from 1.67 to 2. Despite Figure 41 showing the increase in Ca/P ratio in the electrolyte does not influence the overall electrochemical behaviour of the system, it also shows features characteristic of a highly reversible process. However the differences in peak shapes between voltammograms corresponding to polarisation of cp-Ti in electrolytes with different Ca/P ratio suggest differences in the anodic process. As such, when the Ca/P ratio in the electrolyte was set at 1.67, the current increase towards peak III in the forward scan is higher and peak III is located at a higher potential range compared to corresponding features observed in the electrolyte with Ca/P = 2. Furthermore, from the cyclic voltammograms in Figure 41, it is clear that when the Ca/P ratio increased to 2, the peaks IV and V in the forward and reverse scan of cp-Ti exhibit a double peak shape which suggests multiple reactions occurring as discussed in Chapter 4.

Figure 51 shows the surface morphology of the coating produced at the end of Stage I. Pores with average diameter of $1.15 \pm 0.68 \text{ }\mu\text{m}$ can be observed. This appears to provide significantly larger range of pore size when compared to those produced in the calcium propionate based electrolytes (Chapter 5, Figure 15). Moreover, dispersed discharge

channels are observed at scattered locations on the coating. This could be explained by the location and intensity of peaks in the voltammogram. In this study, applying initial voltage of 250 V would not only overcome the energy barrier imposed by peak II in the cyclic voltammogram but also brings the surface to a voltage range where local instabilities commonly known as sparking stages occur. As a result, the pore size observed on the surface will be considerably larger.

The voltage and current transients recorded during the two-step PEO treatment are shown in Figure 52. Compared to Figure 44, increasing the Ca/P ratio in the electrolyte results in a more stable voltage growth throughout the treatment. This could be attributed to the increase in ion content in the electrolyte, which leads to formation of a Ca containing sheath on the surface. The anions participate in a series of reactions with Ti substrate and recombination and decomposition of radicals as described in Equation [4.15] – [4.19], maintaining a relatively more stable plasma discharge environment [15]. Further, more readily formed Ca phosphate compounds can fill in the cracks and maintain a sufficient electric field, therefore resulting in a more stable voltage growth rate compared to that in the electrolyte with Ca/P ratio 1.67.

When the treatment enters Stage II, the voltage transient increased up to about 300V, then exhibited a decreasing growth rate after 3 min. The anodising voltage continues to increase at a lower rate, and begins to stabilise at around 410 V after 6 min into the treatment. As the treatment continues, the anodising voltage was nearly constant until 8.5 min where a disturbance in the curve can be observed along with a slight decrease in the anodising voltage. This could be a result of powerful arcing leading to the disturbance in the electrical response of the system.

The final anodic voltage of the process carried out in the electrolyte with Ca/P=2 is similar to that with Ca/P=1.67, which disagrees with the common understanding that an increase in electrolyte conductivity decreases the anodic forming voltage [14, 19]. This could be attributed to the use of the two-step control method, where during Stage I the surface of the anode is brought to the same surface condition.

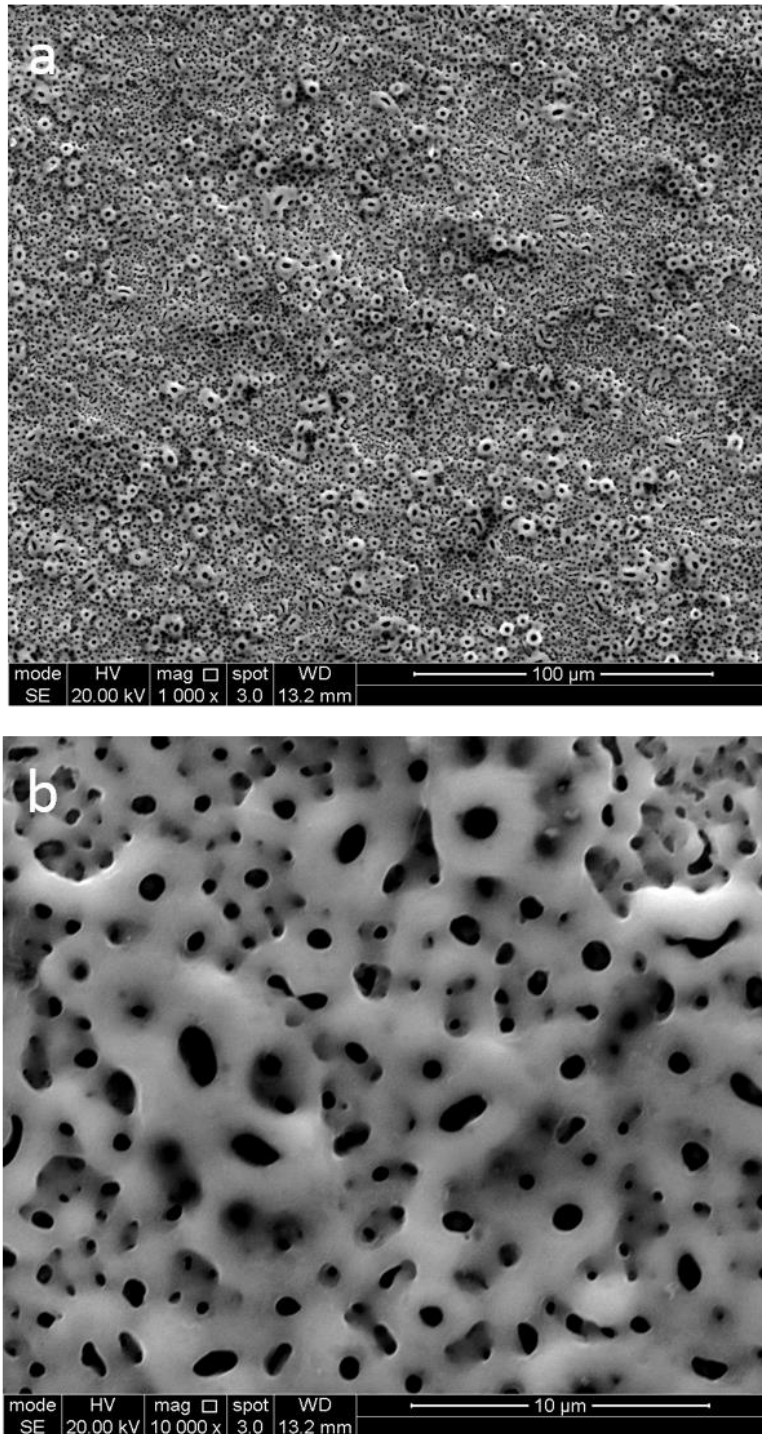


Figure 51 SEM micrographs of coatings produced in the calcium L-lactate electrolyte on the cp-Ti substrate at stage I using DC potentiostatic mode at 250V for 15s.

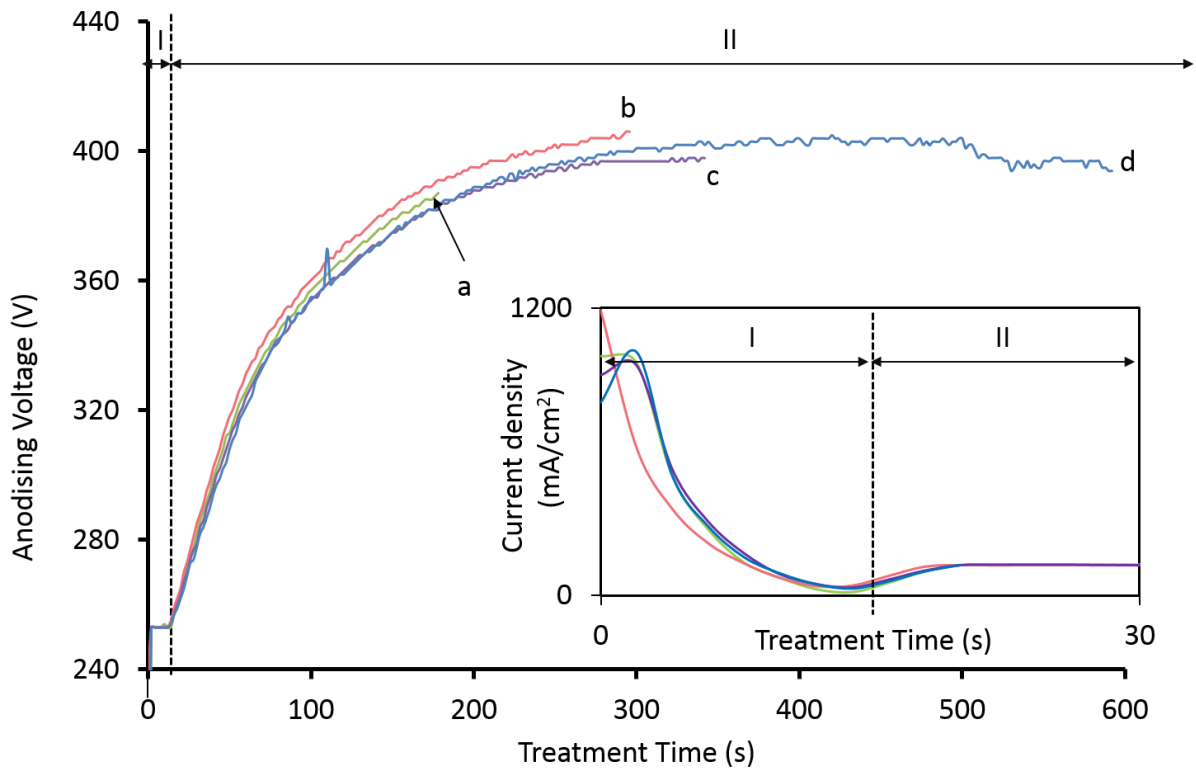


Figure 52 Voltage and current transients recorded during PEO treatments using the two-step control method on cp-Ti substrate in the calcium L-lactate electrolytes with Ca/P ratio 2 at current density of 100 mA/cm² during Stage II carried out for (a) 3, (b) 5 (c) 6 and (d) 10 min.

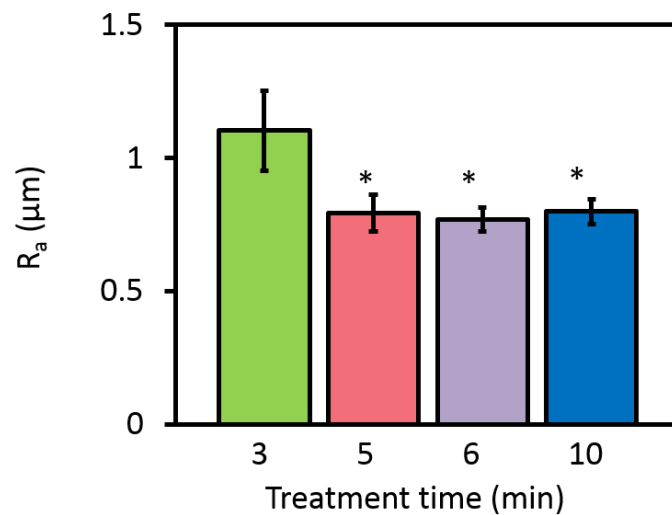


Figure 53 The mean average value of surface roughness of PEO coatings produced with various treatment time. (* $p < 0.05$, indicating statistically difference from coating produced in 3 min)

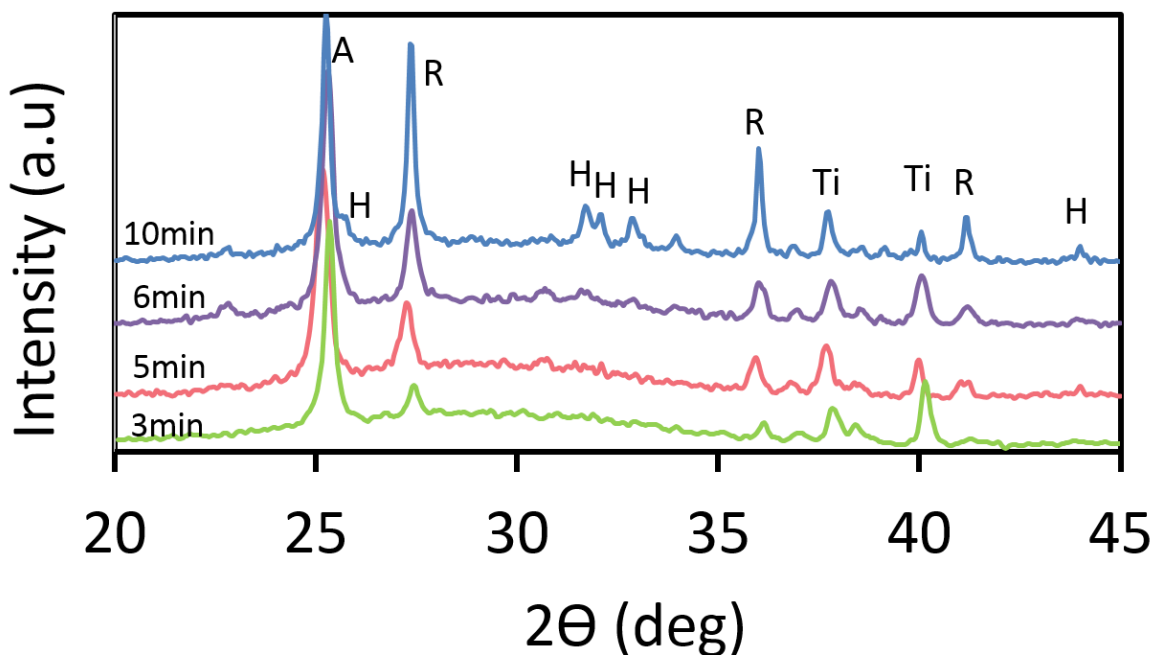


Figure 54 XRD spectra of PEO coatings produced on cp-Ti substrate using the two-step control method in the calcium L-lactate electrolyte with Ca/P ratio 2 at the current density of 100 mA/cm² during Stage II for different treatment times. (A, anatase; R, rutile; Ti, titanium H, hydroxyapatite)

Figure 54 reveals the phase composition of coatings produced on cp-Ti in calcium L-lactate electrolyte at different treatment times. Peaks that correspond to anatase, rutile and cp-Ti substrate are observed in all coatings. Results suggest at the beginning of the second step of the two-step treatment (3 min), anatase phase was the dominant. As the treatment progresses, the intensity of rutile peak begins to increase. With treatment time increasing to 10 min, peaks corresponding to HA can be observed. The repeated melting-re-solidification process at the coating surface enhances formation of complex oxide phases such as HA. This is consistent with the disturbance observed in the voltage transient curve (Figure 52), where the formation of HA phases would alter the local resistivity at the surface.

It is interesting to observe that the intensity of anatase peaks does not reduce as the treatment continues while the peaks of other phases become more noticeable. As mentioned in Chapter 2, anatase is the metastable phase of TiO₂ while rutile is the more stable one. During the treatment, Ti would undergo chemical reactions described in Equations [2.1] – [2.5] to form TiO₂. Data from the XRD spectrum suggest that at the beginning of the two-step treatment, anatase phase dominates the coating. As treatment continues, the coating grows both inward

and outward from the original substrate surface which provides sufficient thermal energy and time for the rearrangement of atoms to transform from anatase to rutile in the inner region, while the formation of new anatase phases continues in the outer region.

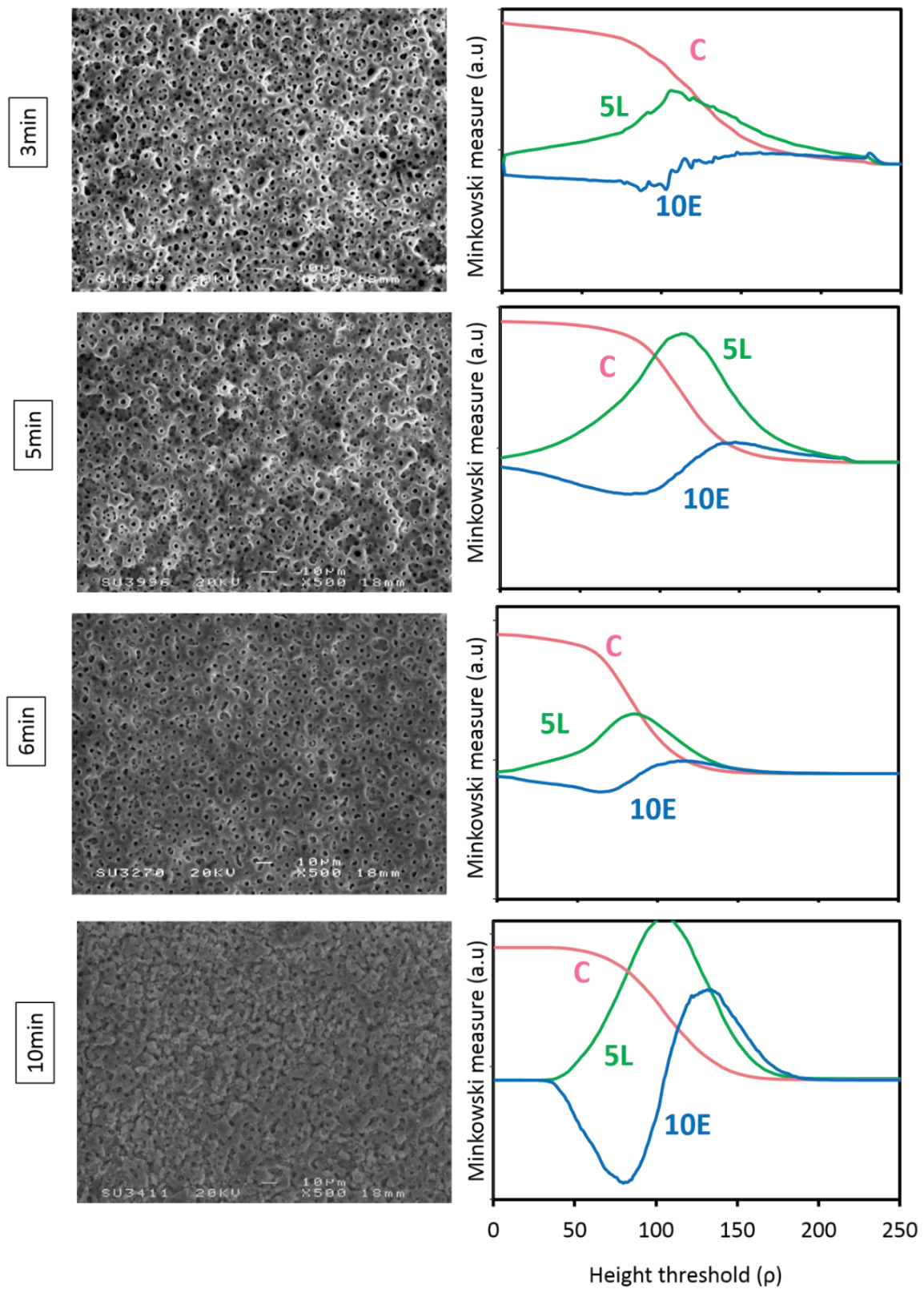


Figure 55 SEM micrographs of PEO coatings on cp-Ti substrate produced using the two-step control method in the calcium L-lactate electrolyte with Ca/P ratio 2 at the current density of 100

mA/cm^2 during Stage II for various treatment times and respective Minkowski functionals $C(\rho)$, $L(\rho)X5$ and $E(\rho) \times 10$.

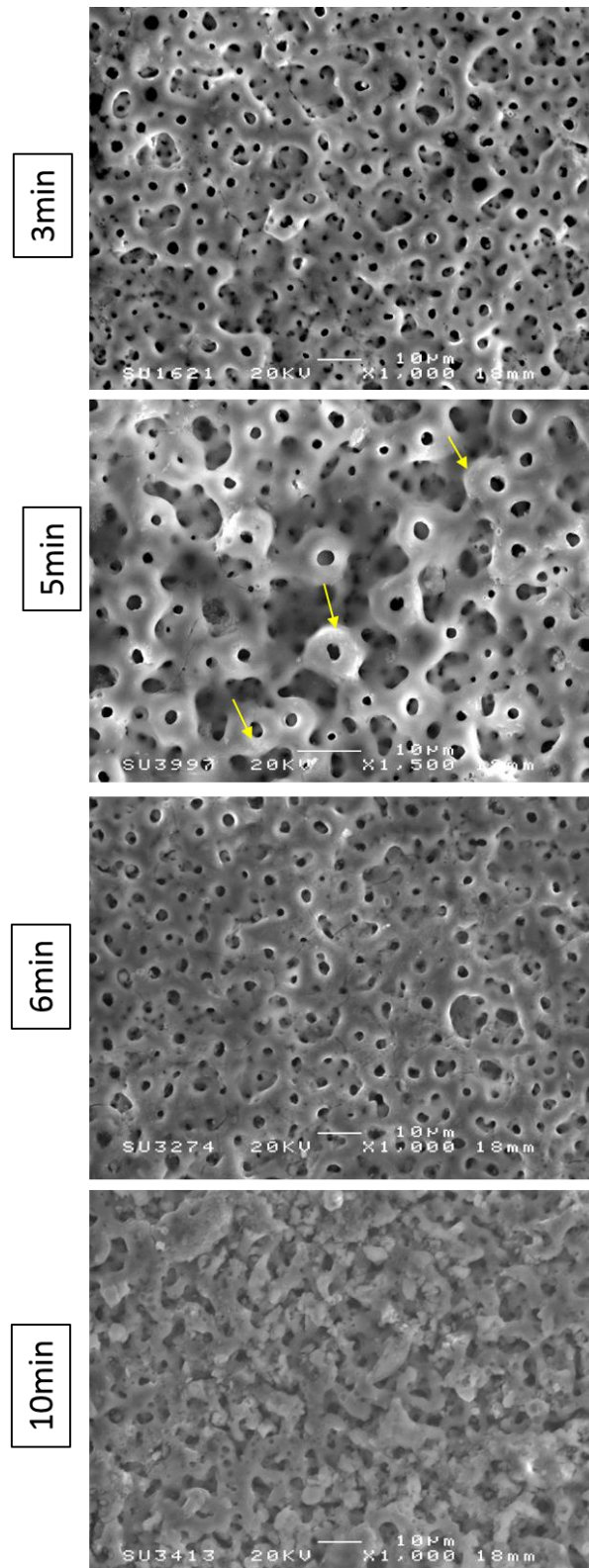


Figure 56 Higher-magnification surface-plane images of coatings shown in Figure 55.

Figure 55 presents surface morphologies and the corresponding Minkowski functional plots of PEO coatings produced for different times using the two-step control method. During the sparking stage (3 min) the coating surface appears to be rugged, discharge channels are observed at sparsely located locations on the coating. The corresponding Minkowski plot (Figure 55) reveals the curves have inflection at similar threshold ranges $\rho = 50-100$ but the curves' shapes are different, indicating corresponding coatings have dissimilar porous features. The average surface roughness value is $1.07 \pm 0.14 \mu\text{m}$, with the average pore diameter of $2.45 \pm 1.1 \mu\text{m}$. Cracks are observed in the coating around discharge channels possibly due to the initial breakdown of the coating, leading to increases in thermal and structural stresses in the adjacent regions [152].

In the coating produced for 5 min, distinctive traces of discharge channels are observed throughout the surface. At this stage of PEO pretreatment, the pores are formed due to micro-discharges and it can be assumed that the large number of discharge channels observed are a result of pores not being destroyed by the subsequent micro-discharges in the short period of time. The presence of discharge channels is reflected in the shape of flex in the surface coverage C curve. The matrix around the discharge channel shows a lighter region in the darker matrix (as indicated by arrows) this suggests the coating material in that area has inhomogeneous chemistry. This could be attributed to the high temperature at which the molten matrix material is ejected from the discharge channel to the neighbouring region, and the cooler electrolyte rapidly cools the matrix. The difference in cooling rate and the oxide matrix composition could lead to variations in matrix appearance. A low E_{min} value with a corresponding high L value observed in the Minkowski functional, which is commonly an indicator of characteristic features in the porous structures deviating from circular shape. This work shows the variation in the focal distance caused by the fact that the protruding discharge channel can form a shadowing effect, which can be miscalculated as a pore in the Minkowski analysis.

As the treatment time increased to 6 min, the surface becomes less rugged, showing evidence of repeated melting-solidification processes taking place, leading to a comparatively smoother surface with porous structure. This complies with the voltage transient behaviour observed in Figure 52, where the voltage begins to stabilise indicating the commencement of the micro-arc stage.

A grooved morphology with globular features is observed on the coating when the treatment time increased to 10 min. This complies with the large variance between the E_{\min} value and the corresponding threshold L value. Furthermore, the L_{\max} is observed near the threshold range $\rho = 127$, where the corresponding Euler value is at zero crossing, suggesting the topology is closed to a turbulent pattern structure [144].

The formation of the globular features on the surface correlates with the disturbance in the voltage transient observed in Figure 52. Due to the repeated melting-solidification process as treatment time increases, high temperature and pressure are developed within the discharge channel, which promotes crystallisation of complex oxide compounds such as HA. The oxide products are likely to be ejected from the discharge channel resulting in deposits observed [40]. Surface morphological features similar to those observed in Figure 47 for the coating produced on cp-Ti in the electrolyte with Ca/P=1.67 for 7 min could be found on the coating produced for 10 min here, comparison of the corresponding Minkowski functionals reveals similar characteristics of length (L) and Euler (E) curves.

This section of the study demonstrated the success in using the two-step control method for PEO treatment of cp-Ti in the calcium L-lactate based electrolyte to form porous coatings with a comparatively lower applied current density. Analysis of the coating morphology and phase composition provides information of the coating forming mechanism during the two-step treatment which is shown to be similar to that of DC PEO treatments with a single static control mode but offering more stability. Most importantly, the use of the two-step control method mitigates the issues associated with electrolyte boiling and foam formation. This increases the potential of calcium L-lactate electrolyte for PEO treatments of Ti alloy for biomedical applications.

6.2.4 Formation of HA containing PEO coating

Research discussed in the previous section has demonstrated the ability to form HA containing coating from the calcium L-lactate electrolyte using the two-step control of electrical parameters of the PEO process. However, the surface layer displayed a grooved morphology and visual inspection of the coating showed signs of inhomogeneous coating with white dots and localised burning located at the surface. It had been shown that lower applied current densities in Stage II lead to a reduction in voltage growth rate which results in formation of a porous PEO coating with less features attributed to the powerful arcing.

However, the decrease in voltage growth rate has a significant influence to the phase composition of the coating. From discussion in previous sections, it can be deduced that;

1. The two-step control method provides a more stable conditions for PEO treatment, eliminating electrolyte foaming and bubbling.
2. Reversible behaviour observed in the voltammogram indicates reactions occurring at the surface shift from formation to dissolution, which is likely to be related to the recombination and decomposition of carboxylate anions and corresponding radicals.
3. Formation of crystalline HA phase affects the surface morphology of the coating, and commonly results in formation of a deposited material on the coating surface.
4. Calcium L-lactate based electrolyte with Ca/P ratio of 2 provides more suitable electrochemical conditions than that with Ca/P=1.67 for the two-step control PEO process, possibly due to the increase in Ca content.
5. Increasing treatment time enhances the formation of HA phase on the surface, however prolonged treatments lead to inhomogeneous coating appearance (e.g. white dots on the surface)

Based on these inferences, this section presents and discussed results of the studies on formation and characterisation of HA containing coatings with porous PEO morphology.

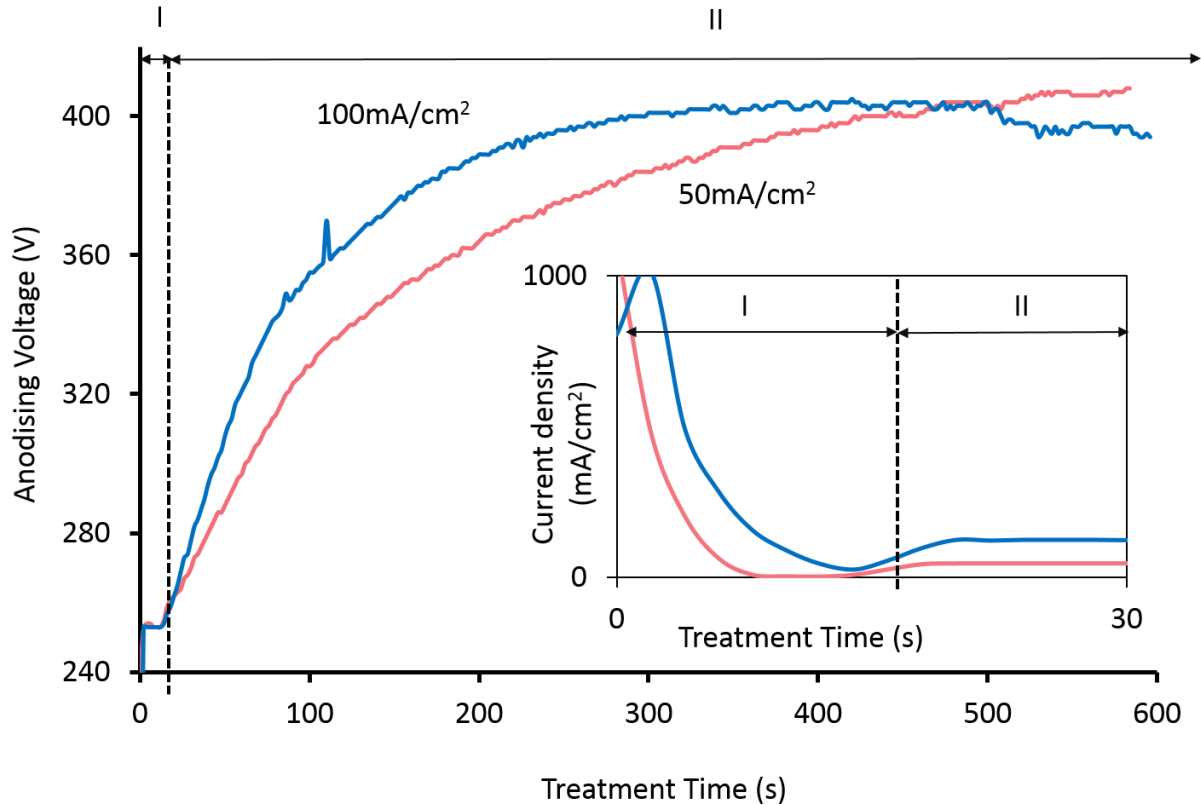


Figure 57 Voltage and current transients recorded during 10 min PEO treatments of cp-Ti with the two-step control method in the calcium L-lactate electrolyte with Ca/P=2 at the current densities of 50 and 100 mA/cm² during Stage II of the treatment.

Figure 57 displays the voltage and current transients recorded during PEO treatments with various current densities at Stage II for 10 min. Stage I corresponds to the treatment that was carried out in the potentiostatic mode, with 250 V. The treatment during Stage II was carried out under the galvanostatic control using 50 or 100 mA/cm². The voltage transient of the treatment performed at 50 mA/cm² shows a faster increase in voltage during Stage II until 320 V, therefore it retains a low growth rate until approximately 410 V. The voltage continues to grow at the end of the treatment, meanwhile the voltage transient recorded of the treatment produced at 100 mA/cm² has shown to stabilise and display features related to electrical disturbance.

The average surface roughness of the coating produced at 50 mA/cm² is $R_a = 0.92 \pm 0.03 \mu\text{m}$, which is significantly higher than that of the coating formed at 100 mA/cm². This agrees with common understanding of PEO coating formation mechanism, indicating that at the

stage when voltage is stabilised, repeated melting-solidification occurs, smoothing the surface.

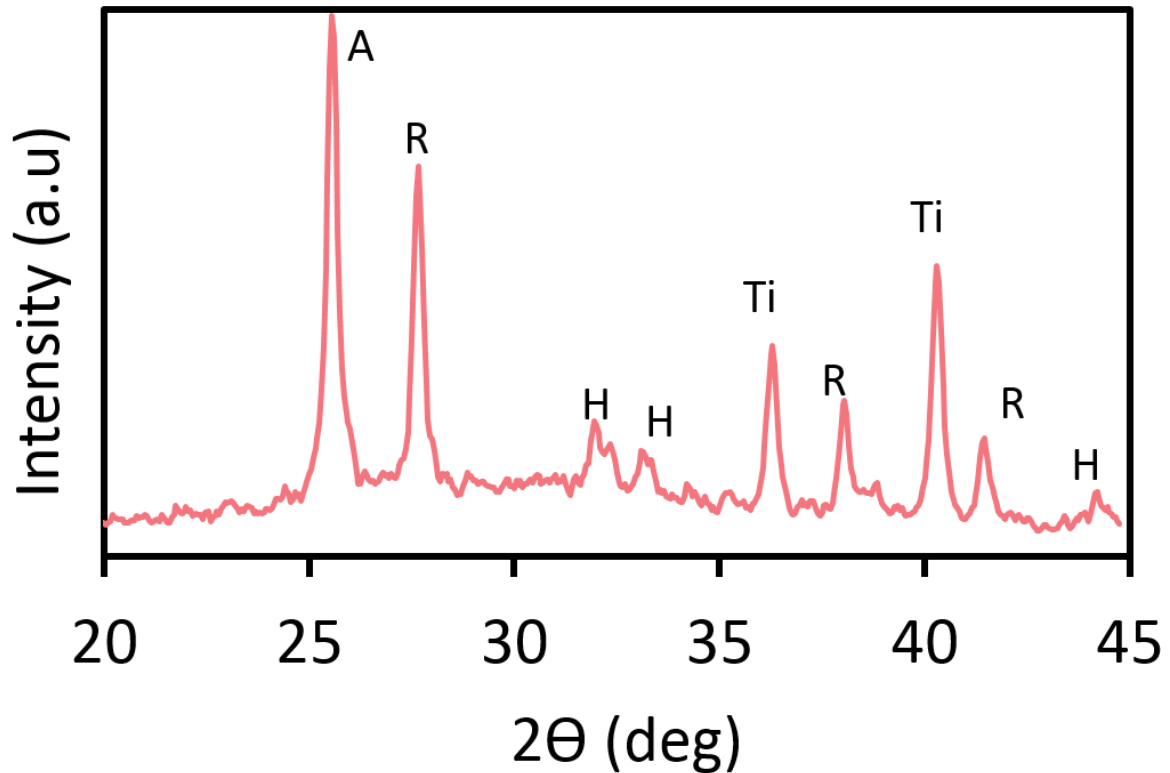


Figure 58 XRD spectra of coating produced on cp-Ti substrate using the two-step control PEO treatment for 10 min in the calcium L-lactate electrolyte with Ca/P=2 at the current density of 50 mA/cm². (A, anatase; R, rutile; Ti, titanium and alloy; H, hydroxyapatite)

Figure 58 reveals the XRD pattern of cp-Ti sample with PEO coatings produced at current density of 50 mA/cm² for 10 min in the electrolyte with Ca/P ratio of 2. The pattern exhibits peaks corresponding to anatase, rutile, HA and Ti substrate. The set of peaks corresponding to anatase is systematically higher than that of rutile, suggesting anatase is more abundant in the coating. Compared to the XRD spectrum of coatings produced at the current density of 100 mA/cm² (Figure 54), it can be concluded that the peak intensity of rutile increases when the current density is higher. This is consistent with the comparatively longer voltage stabilisation period observed in Figure 57 when the current density is set at 100 mA/cm². Moreover, the XRD pattern displays a slight bump under the peaks, suggesting amorphous phases are present in the coating produced at the lower current density.

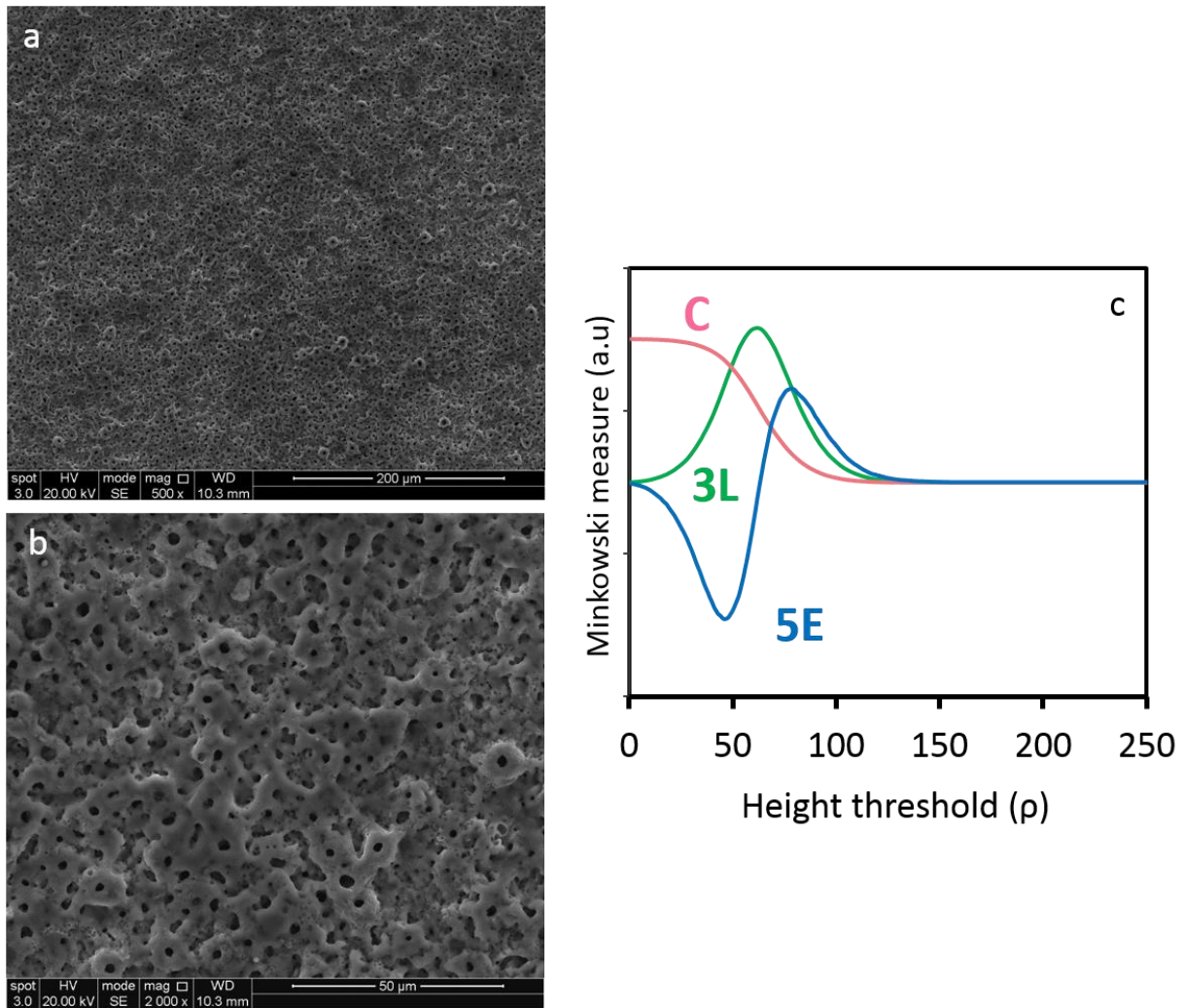


Figure 59 SEM micrographs of coatings produced using two-step control method of cp-Ti substrate in the calcium L-lactate electrolyte with Ca/P ratio 2 for 10 min at the current density of 50 mA/cm² during Stage II and respective Minkowski functionals C(ρ), L(ρ)X3 and E(ρ)x5.

Figure 59 presents the surface morphology of the coating produced at the current density of 50 mA/cm² and corresponding Minkowski functional plots. Porous features are observed on the coating, with presence of fine pin-hole pores. This is reflected in the flex in the length (L) curve at low threshold value in Figure 59c. A high peak intensity is observed at low threshold range, suggesting preferred pore perimeter, which complies with results of morphological analysis using ImageJ software showing the average pores size of 2.8±0.88 μm. The small difference between L_{max} and corresponding E value suggests pores are mainly circular in shape. The zero crossing value of Euler (E) curve is at a low threshold (ρ), suggesting the pores are evenly distributed in the coating.

Due to the combination of a uniform porous morphology and peaks of crystalline HA in the XRD pattern, this coating is selected for further biological studies.

6.2.5 Understanding substrate effects and exploring the application of calcium L-lactate electrolyte for PEO treatment of Ti-6Al-4V alloy

Results of the studies discussed in the previous section suggest that the system with the voltage-current behaviour featuring closely located forward and reverse curves at approximate voltage range is not particularly suitable for PEO treatments as such systems are prone instabilities in chemical reactions occurring at the surface. Despite so, the work discussed in this section explores the use of the two-step control method for the treatment on Ti-6Al-4V substrate.

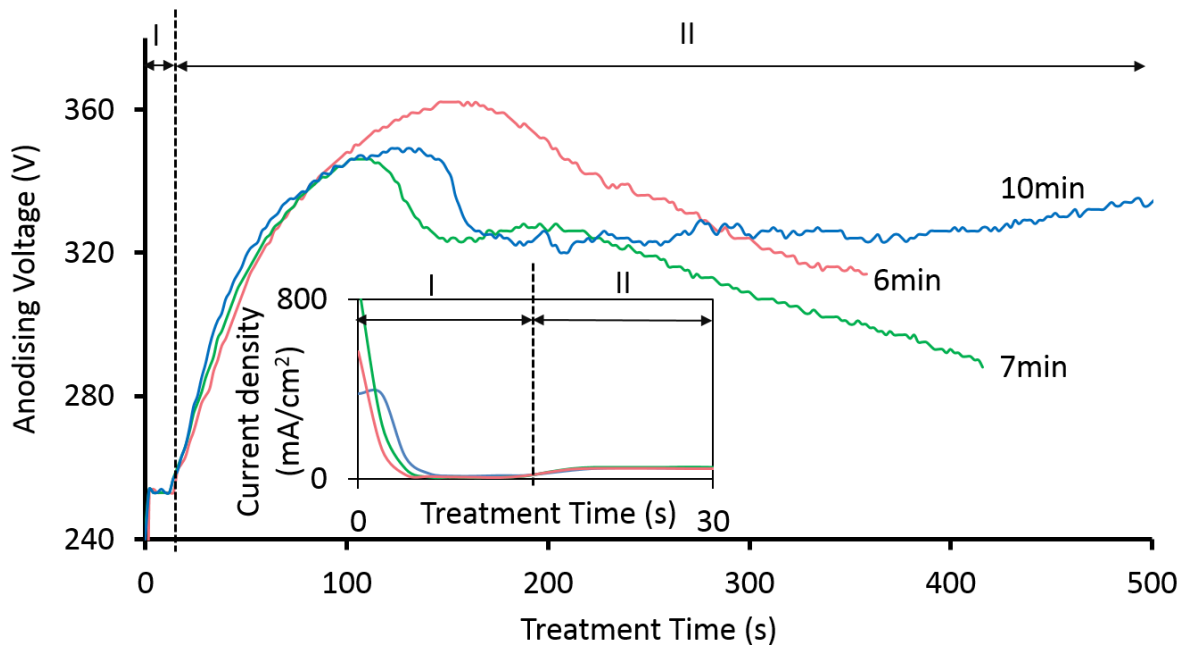


Figure 60 Voltage and current transients recorded during PEO treatments of the Ti-6Al-4V substrate using the two-step control method in the calcium L-lactate electrolyte with Ca/P=2 at the current density of 100 mA/cm² during Stage II for different durations.

Voltage and current transients recorded during the PEO treatments of Ti-6Al-4V substrate are shown in Figure 60. Stage I corresponds to the potentiostatic treatment at 250V. The treatment during Stage II was carried out under the galvanostatic control using 100 mA/cm² under different treatment time, similar to those discussed in Chapter 5.

Inconsistencies in the voltage transients observed despite the same electrical parameters applied indicate the instability of the electrochemical system in the high voltage range (>340V). This is consistent with the reversible behaviour of corresponding voltammogram in the low current density region observed in Figure 41, which could trigger instabilities in the reactions occurring at the surface. When cross-referencing the anodising voltage recorded in Figure 60 to the voltammogram of the process in the electrolyte with Ca/P =1.67 (Figure 41), it can be observed that this corresponds to the region where a rapid current rise from peak III to IV occurs, suggesting that vigorous reactions take place in a short period of time. Voltage transients recorded for all treatments using Ti-6Al-4V substrate display significant drops in voltage after the transient flex at 360, 347, 346 V in treatments carried out for 6, 7 and 10 min, respectively. This could be a result of crack formation in the coating, leading to disturbances in its electrical resistance.

From ~400 s into the treatment, the voltage starts to increase at a slow rate. This could be a result of sparking occurring preferentially in the weak regions of the coating and densifying its morphology. Nevertheless, inconsistencies in the voltage transients comply with previous speculations regarding instabilities of the electrochemical reactions occurring at the surface.

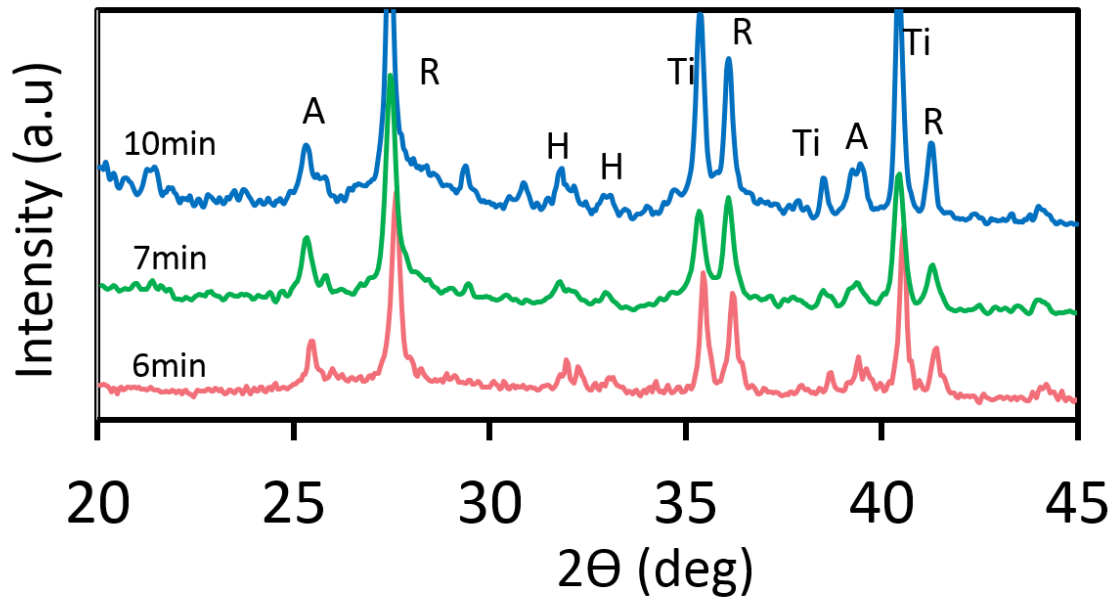


Figure 61 XRD spectra of Ti-6Al-4V samples with PEO coatings produced using the two-step control method in the calcium L-lactate electrolyte with Ca/P=2 at current density of 100mA/cm² for various times. (A, anatase; R, rutile; Ti, titanium and alloy; H, hydroxyapatite)

Figure 61 displays the phase composition of coatings produced on Ti-6Al-4V substrate. Despite the low anodising voltage compared to the similar treatments of cp-Ti, the set of peaks that matches rutile is systematically higher than that of anatase, suggesting the former is more abundant in the coating. This could be explained by the influence of substrate alloying element as discussed in Chapter 4, which leads to a dramatic increase in current from peak III to IV, the increase in oxygen production also promotes the anatase-to-rutile phase transformation and formation of crystalline HA.

Figure 62 presents the surface morphology of the coatings produced with increasing treatment time. Dense regions can be observed on the coating produced for 6 min. Pores are present on the surface with features correlated to severe surface re-melting, the secondary destruction of the layer disrupt the previous formed porous features.

As the treatment time increases, deposits are observed on the coating with cracks linking between the globular deposits. This could be explained by the thermal and structural stress during the coating material being ejected from the discharge channel, redeposited and solidified on the surface. At 10 min, prominent re-melting features are also observed, with presence of distorted pores distributed evenly throughout the coating.

The presence of cracks and deposits observed on the coating explains the disturbance in the voltage transient presented in Figure 60. It is interesting that despite the relatively low anodising voltage all coatings display features associated with powerful arcing. Therefore it can be assumed that the dramatic increase in current between peaks III and IV resulted in vigorous reactions at the surface accompanied with high energy discharge. Although this aids to the anatase-to-rutile transformation and HA formation, the resulting coating undergoes severe re-melting. Visual inspection of coatings has shown evidence of discolouration and white dots which may be associated with coating burning.

It is interesting to observe such great differences in the surface morphology and phase composition between the coatings produced on the cp-Ti and the Ti-6Al-4V substrates. This behaviour can be explained by the different phases present in the alloy that provide different oxide growth rates. Soares *et al* [119] suggests the oxide layer grows faster on the beta-phase than on the alpha-phase of the Ti-6Al-4V alloy substrate. Although their work suggests that above the dielectric breakdown, the resultant coating would mask the influence of the substrate and the coating growth rate would be less dependent on the crystal structure, our work shows the influence of substrate extends into the sparking and micro-arc stages of the PEO process. This could be explained by the combination of the high concentration of oxygen formed on the surface from the beta-phase in the Ti-6Al-4V alloy, which provides suitable conditions for nucleation of anatase and rutile and possible incorporation of Al and V into the discharge channel altering the electrical profile of the local region. Results in this section indicate that Ti-6Al-4V substrate might not be suitable for the two-step PEO treatment in the calcium-L lactate based electrolyte.

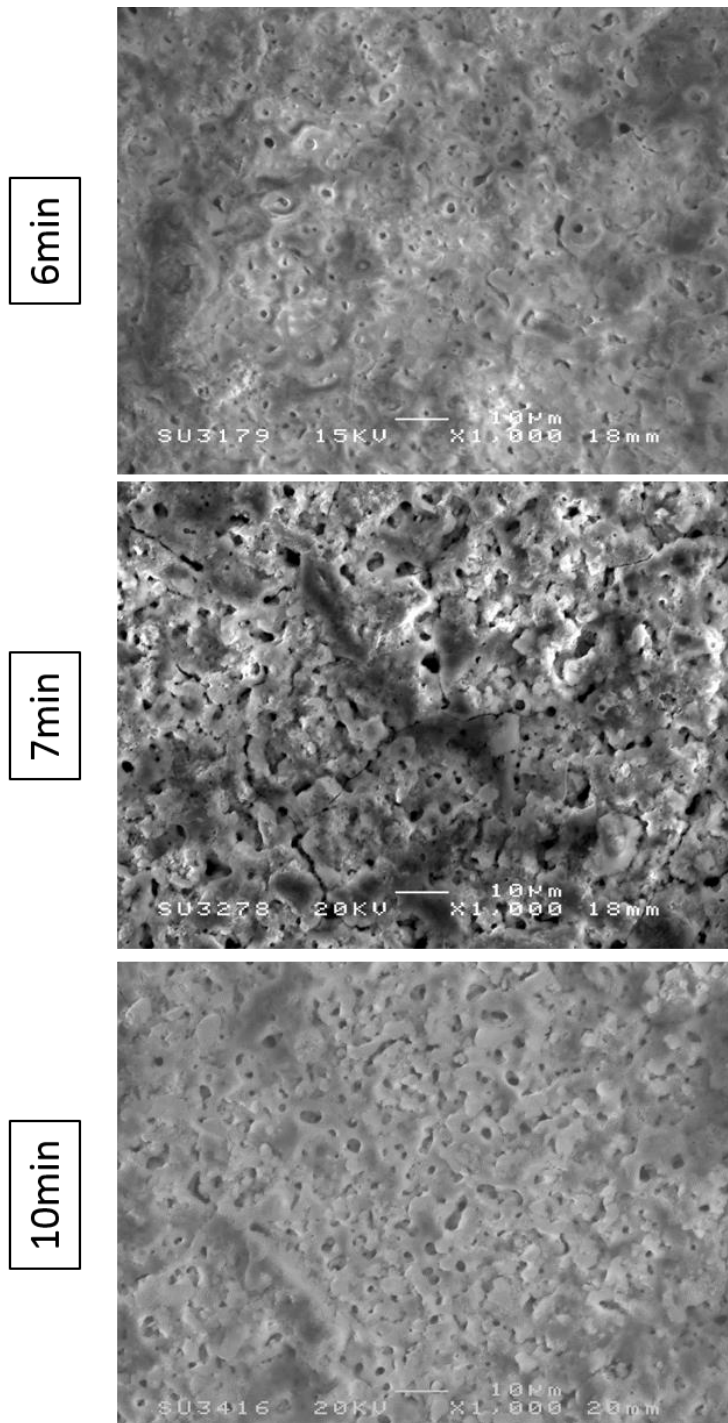


Figure 62 SEM micrographs of PEO coatings produced on Ti-6Al-4V using the two-step control method in the calcium L-lactate electrolyte with Ca/P=2 at the current density of 100 mA/cm² for various times.

6.2.6 In vitro experiments for coatings produced using calcium L-lactate based electrolyte

The details of processing parameters employed for the treatment of cp-Ti substrate that are selected for further *in vitro* assessment are displayed in Table 14. For the remainder of this thesis, the coatings will be referred to as A-TiO₂, R-TiO₂ and CaP PEO coatings. Osteoblast cells MG-63s were seeded onto the surface at 75,000 cells/cm² and the cell viability was assessed as described in Chapter 3.

Table 14 The processing conditions selected for *in vitro* assessment.

| Sample label | PEO treatment conditions | | |
|--------------------|--------------------------|------------------------------|----------------------|
| | Step 1 (V) | Step 2 (mA/cm ²) | Treatment time (min) |
| A-TiO ₂ | 250 | 100 | 3 |
| B-TiO ₂ | | 100 | 5 |
| CaP | | 50 | 10 |

Individual coating microstructure, phase composition and average surface roughness were discussed in the previous sections. In essence, the A-TiO₂ and B-TiO₂ PEO coatings are both TiO₂ based coatings, with the former possessing a higher surface roughness than the latter. The CaP PEO coating contains calcium phosphate phases and has shown similar average surface roughness as the B-TiO₂ PEO coating. This section focuses on the comparison between the selected coatings. Figure 63 reveals the image of the sample used for *in vitro* experiments and shown to eliminate the problems of inhomogeneous coating appearance and edge effects.



15mm

Figure 63 Visual inspection of coating produced on cp-Ti substrate in the calcium L-lactate electrolyte used for biological assessment.

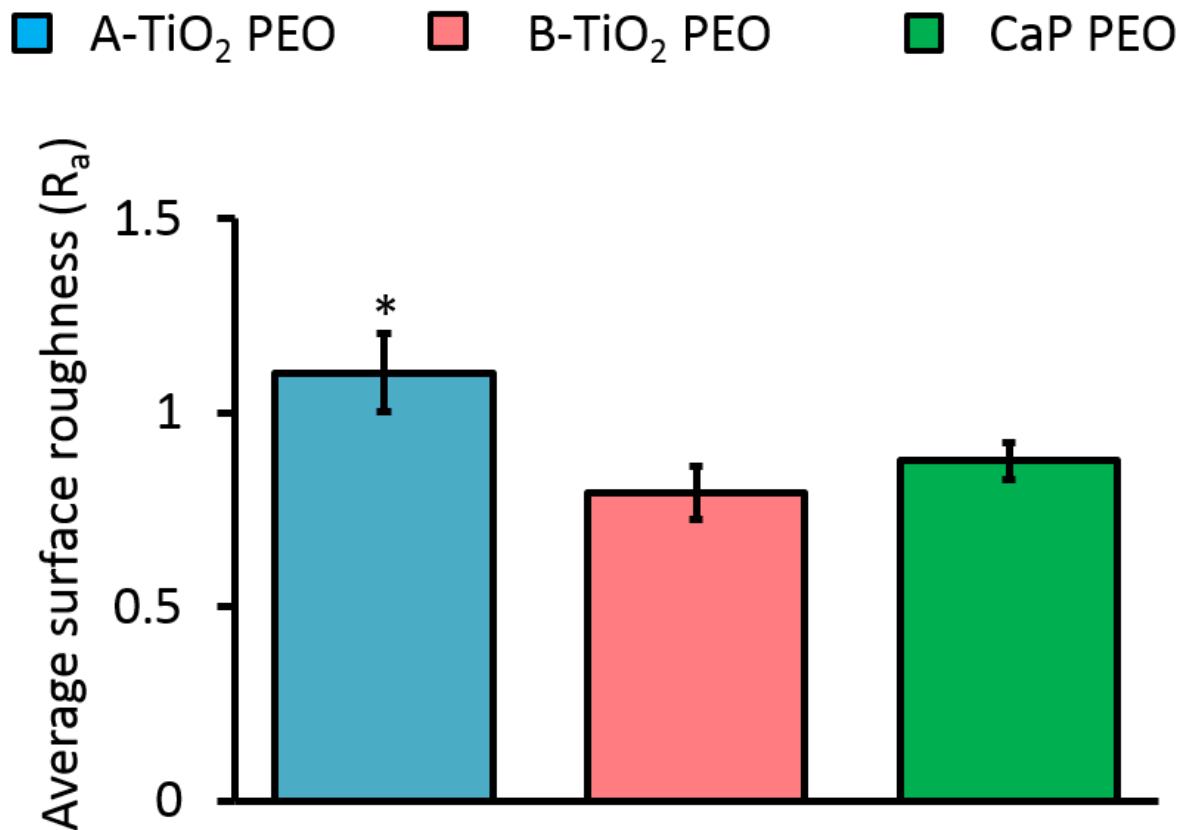


Figure 64 The mean average surface roughness of the A-TiO₂, B-TiO₂ and CaP PEO coatings. (* $p < 0.05$, indicating statistically difference from the B-TiO₂ and CaP PEO coating, $n=3$)

The average surface roughness for the A-TiO₂, B-TiO₂ and CaP PEO coatings is displayed in Figure 64. Results shown the average roughness of the B-TiO₂ and CaP PEO coating are statistically lower than that of A-TiO₂ PEO coating. No statistically significant differences ($p < 0.05$) were found between the B-TiO₂ and the CaP PEO coatings.

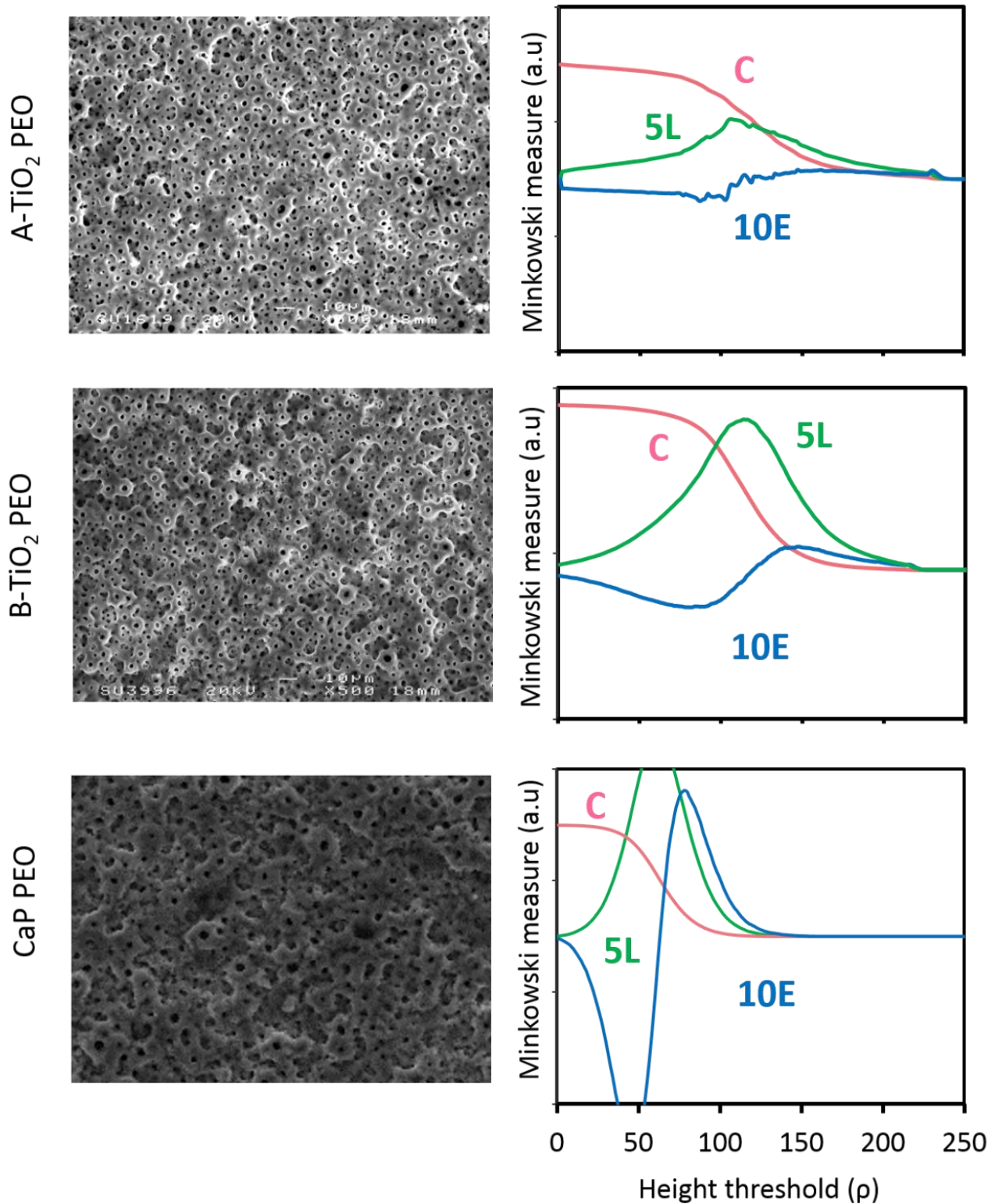


Figure 65 SEM micrographs of coatings produced on cp-Ti substrate in calcium L-lactate electrolyte selected for *in vitro* assays with respective Minkowski functionals $C(\rho)$, $L(\rho) \times 5$ and $E(\rho) \times 10$.

Figure 65 displays the surface morphologies and the respective Minkowski functionals of the PEO coatings selected for biological assessment. When compared the Minkowski plots of the

A-TiO₂ and B-TiO₂ coatings, the shape of the curves is not significantly different and show features such as curve inflection (surface coverage C curve), L_{\max} and E_{\min} at similar threshold range, indicating they have similar porous features. The CaP PEO coating exhibits different porous features when compared to the A-TiO₂ and B-TiO₂ coatings, and is reflected in the corresponding Minkowski plots.

In essence, it can be stated that the characteristics of interconnectivity between pores and matrix as well as phase compositions of A-TiO₂ and B-TiO₂ coatings are very similar, but the average surface roughness of A-TiO₂ coating is significantly higher than that of the B-TiO₂ PEO coating. Meanwhile, the average surface roughness of the CaP PEO coating is not significantly different from that of the B-TiO₂ PEO coating, but the latter exhibits different morphological features and crystalline HA in the structure.

This work examines the biocompatibility of the coatings produced using calcium L-lactate based electrolyte with understanding of the influence of the average surface roughness and the morphological features with phase compositions to the osteoblastic behaviour.

6.2.7 *In vitro* biological response of coatings produced using calcium L-lactate based electrolyte

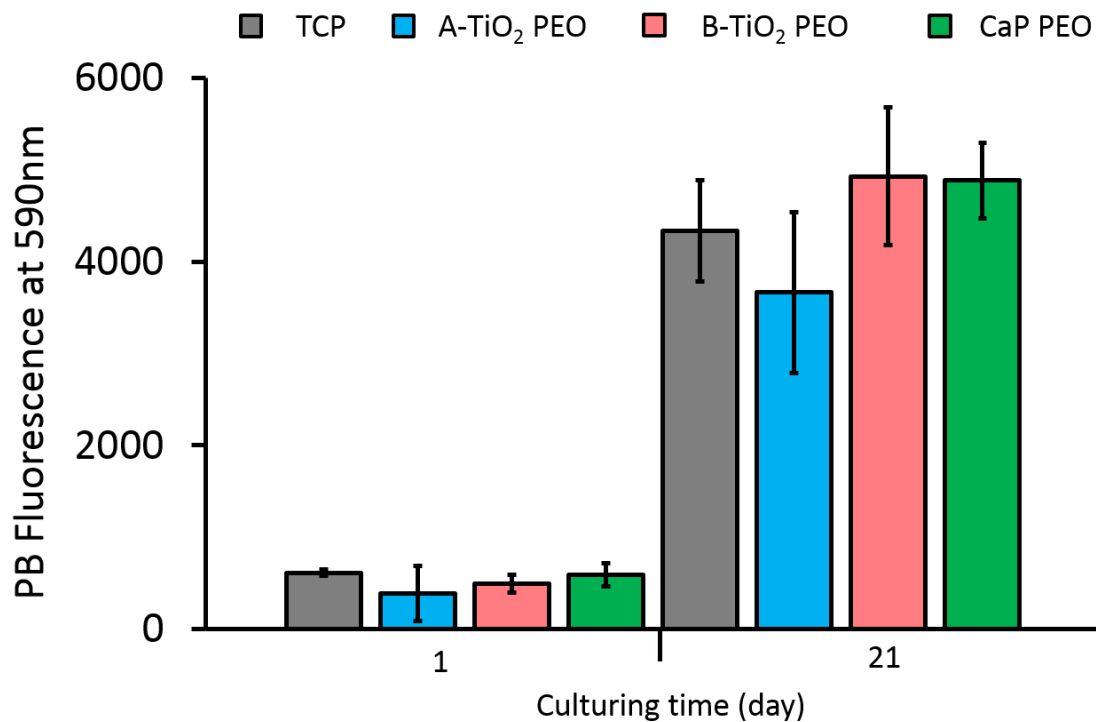


Figure 66 Cell viability on coatings and tissue culture plastic (TCP) control at day 1 and 21 using PrestoBlue, measuring at 590nm. (n = 3)

The MG-63 cells were seeded on the sample surfaces with 75,000 cells per surface, and were incubated for 24 hrs before assessed using PrestoBlue assay to examine the biocompatibility of the coatings, the mean average fluorescent results are displayed in Figure 66. At 24h after seeding, there were no significant differences ($p < 0.05$) between the viability of those on coated samples and tissue culture plastic (TCP). However, the results indicate the cell viability on the A-TiO₂ PEO coated samples has a larger deviation than that on the B-TiO₂ and CaP PEO coatings. This is interesting, as the increase in the average surface roughness is commonly associated with enhanced cell attachment. The wettability of all coatings has shown to be $< 60^\circ$ (50.67 ± 5 , 45.3 ± 2.5 and $46.3 \pm 1.5^\circ$ for the A-TiO₂, B-TiO₂ and CaP PEO coating, respectively), therefore they all are classed as hydrophilic, favouring to cell attachment. This suggests other factors are influencing the attachment process for the cells on the coatings produced in the calcium L-lactate electrolyte. At 21 days after seeding, the cell viability results from the PEO coatings do not show significant differences compared to

those found on the tissue culture plastic. However, the trend of a lower fluorescence value was found on the A-TiO₂ PEO coating.

6.3 Conclusions

This part of the work has investigated the use of calcium L-lactate based electrolyte in the PEO treatments of Ti with the two-step control of electrical parameters and corresponding effects on the coating characteristics and biological properties. It has been shown that it is possible to successfully produce homogeneously porous PEO coatings with crystalline HA incorporation. Preliminary investigation into the biocompatibility of coatings produced using calcium L-based electrolyte showed that the cell response on the coatings was comparable to that on tissue culture plastic. Thus, the work in this chapter has demonstrated the utility of the calcium L-lactate based electrolyte as a promising source of calcium and the two-step control method as a prospective PEO treatment to produce uniformly porous HA coatings on cp-Ti.

Chapter 7: PEO treatment of Ti alloys in HA containing electrolyte

7.1 Introduction

The use of calcium and HA containing colloid and slurry electrolytes had been discussed in Chapter 2. There had been issues with HA agglomerates incorporated on Ti surfaces and the use of chemical additives that might react with the HA particles and cause their decomposition are still unsolved. Therefore the aim of this chapter is to explore the use of two-step control method for PEO treatments carried out in HA micro- and nano-powder containing electrolytes. The influence of electrical control mode, electro-physical behaviour and particle size to the voltage growth rate and resulting coating microstructure is discussed. Based on the results of these studies, selected coatings undergo *in vitro* assessment.

7.2 Results

7.2.1 Understanding the use of disodium phosphate based electrolyte to cyclic voltammetry behaviour of Ti-6Al-4V anode

Figure 67 reveals the cyclic voltammetry response of a Ti-6Al-4V substrate to an anodic sweep between 0 and 500V at a rate of 2V/s. The direction of arrows represents the direction of the scan, and the peaks I to V are labelled similar to those in Figure 11 and 12 in Chapter 4.

Peaks at low voltage range exhibit similar behaviour to those observed in previous Chapters, where a small peak I at approximately 20 V corresponds to oxygen generation during the anodisation of titanium. A sharp peak II at around 210 V can be observed, at a similar voltage range as those observed in previous Chapters investigating anodic behaviour of Ti-6Al-4V alloy in calcium propionate and L-lactate based electrolytes. This confirms that the presence of peak II is strongly correlated to the dissolution of the passive film formed during conventional anodising, therefore it is highly dependent on substrate alloying. The plateau peak III suggests PEO treatment occurs at around 340 to 450 V. A large current rise at the end of the forward scan towards peak IV can be observed; this indicates development of large discharges and/or unstable sparking leading up to powerful arcing. Compared to the cyclic voltammograms observed in Figure 11 and 12 in Chapter 4, there is an absence in a disturbance of the current at around 500 V in the forward and reverse scan. This complies with the discussion of CaP production undergoes possible amorphous-to-crystalline transition, melting and/or dissolution occurring at the surface at high temperature, which

affects coating resistance, contributing to the disturbance in the electrical response. In the reverse scan, a broad peak V can be observed at a low current density range, but the lack of overshooting indicates the system can be assumed to be electrochemically irreversible for PEO treatment.

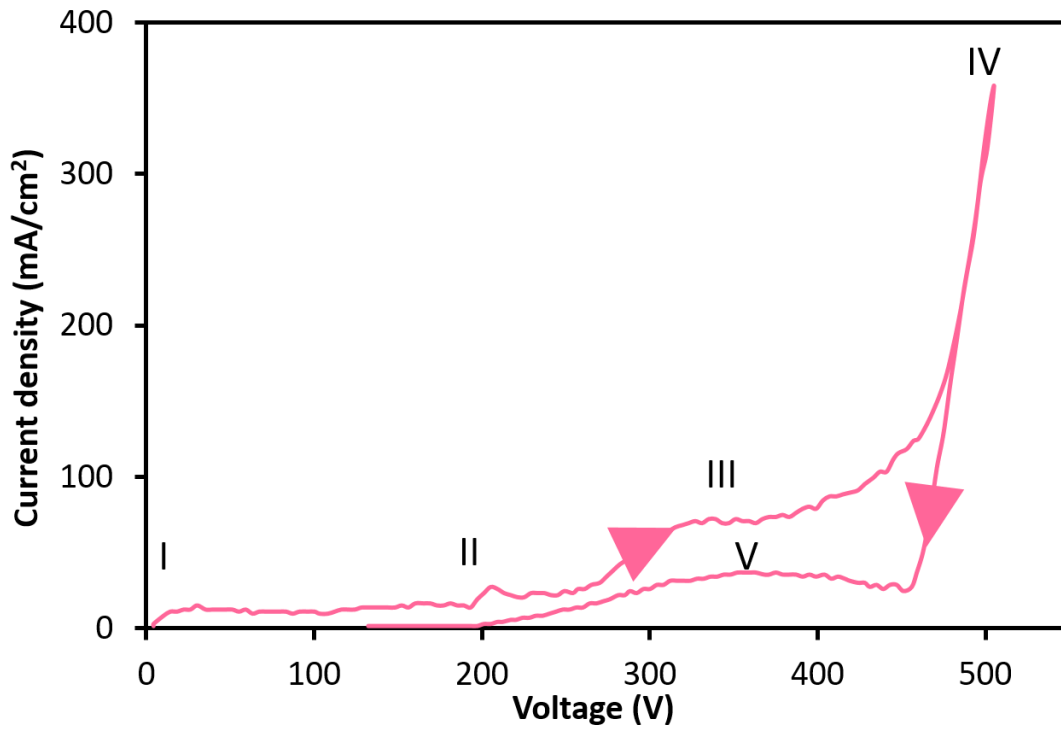


Figure 67 Cyclic voltammogram of Ti-6Al-4V anode in 6g/L Na₂HPO₄ electrolyte, the directions of arrows represent the direction of scan.

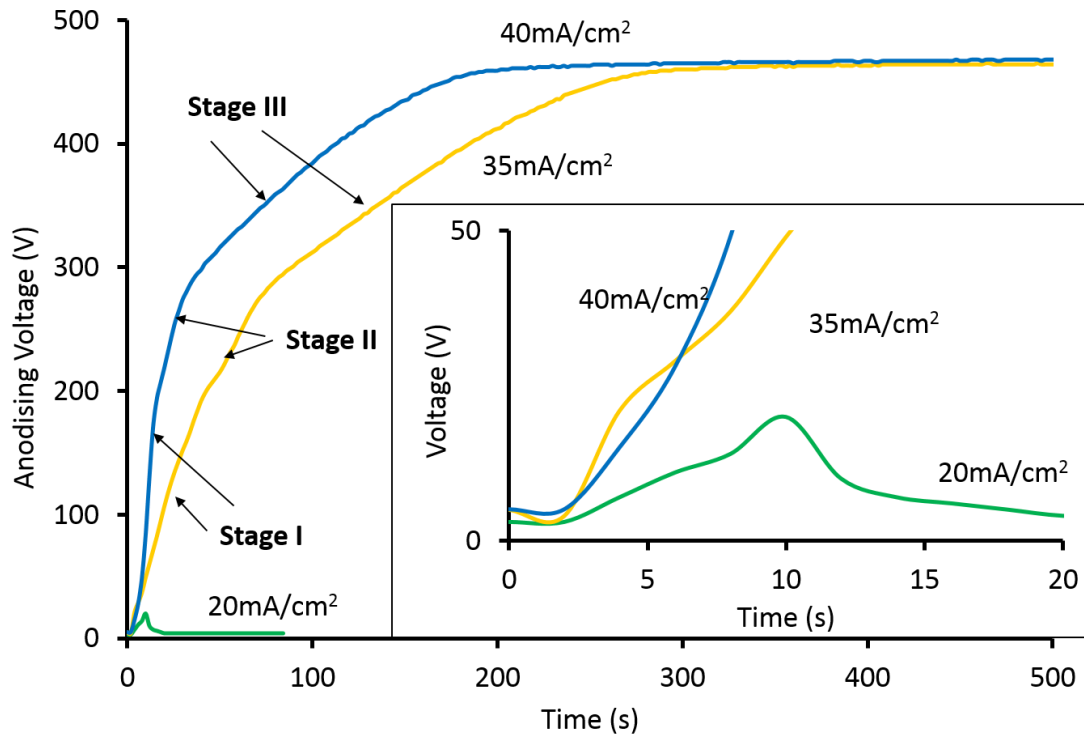


Figure 68 Voltage transients recorded during DC PEO treatments of Ti-6Al-4V alloy in 6g/L Na_2HPO_4 electrolyte at different current densities.

Figure 68 presents the voltage response of a Ti-6Al-4V substrate to single-step galvanostatic polarisation with various current density. The analysis of the voltage transient recorded during the treatment and are labelled similar to those in Chapter 2 to describe the discharge phenomena during PEO treatment. The minimum applied current density must be over 20 mA/cm^2 to achieve the sparking stage, this complies with the discussion of peak II in Figure 67, where the peak intensity shown to be 25 mA/cm^2 . Therefore it confirms the need to apply sufficient energy to the surface to overcome the peak II barrier which has been associated to dissolution of passive film formation for further coating growth mechanisms such as sparking to occur.

Stage I in Figure 68 is characterised by a rapid increase in voltage with time up to approximately 200 V, which corresponds to conventional anodic oxidation of the substrate surface. Thereafter, 200 V a flex in the voltage transient can be observed and followed by a slower voltage growth rate up to 280 V, this is marked as Stage II which corresponds to the commencement of sparking. It has been suggested to be attributed to the competition of coating growth and dissolution process. Stage III occurs at around 300 to 450 V, where the voltage increase rapidly to exceed the threshold value for dielectric breakdown, this is in

consistence with the broad plateau peak III observed in Figure 67, this section corresponds to micro-regional instability caused by electron avalanche. The voltage becomes stable at around 470V which corresponds to micro-discharging activity being more vigorous compared to Stage II; such behaviour corresponds to the final region limited by peak IV in Figure 67. Visual inspection of the coating shows signs of a burned morphology due to the powerful arcing. Interestingly, the insert of the insert of Figure 68 emphasises a small bump in the voltage transient that occurs at around 10s for the process carried out at 20 mA/cm². This further propose the oxygen production during the anodization of titanium during the initial anodising phase of PEO process and complies with the discussion of Peak I.

Due to the behaviour of the voltammogram which indicates the need of a high applied current density to achieve sparking, two-step control method as described previously is used in the following section in aim to reduce signs of burned morphology and ensure the voltage can reach a threshold value for the PEO process to commence.

7.2.2 Effect of control modes on the PEO process

The use of PEO treatment in combination with electrophoretic deposition relies on the electrostatic forces between the negatively charged HA and the positively charged substrate. The isoelectric point of HA is approximately pH = 7, therefore it can be assumed that in the alkaline electrolyte, the HA particles attain a negative charge.

In this section, pulsed unipolar and bipolar current modes are applied to understand the influence of electrical regime of the PEO process on Ti-6Al-4V substrate. Typical oscillograms of voltage and current waveforms used in this study are shown in Figure 69 and the voltage and current transients recorded during PEO treatments are presented in Figure 70. Stage I corresponds to the treatment carried out in the potentiostatic mode, at 250V. Stage II was carried out under the galvanostatic control at a current density of $i(+)=35$ mA/cm², $i(-)=0$ mA/cm² (PUP mode); 11.7 mA/cm² (PBP mode) with total treatment time of 10 min.

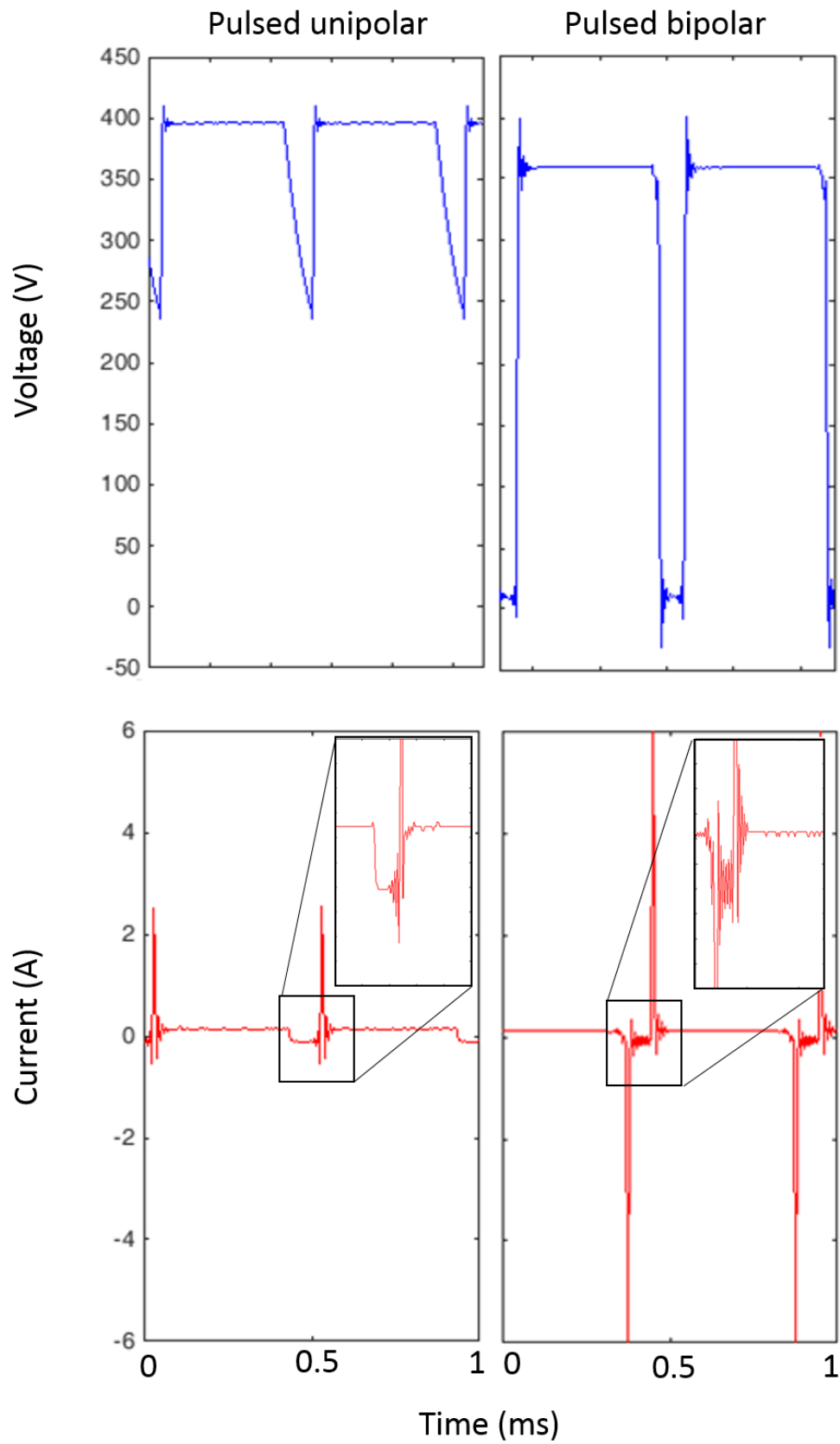


Figure 69 Oscillograms of pulsed unipolar and pulsed bipolar current output used in PEO treatment.

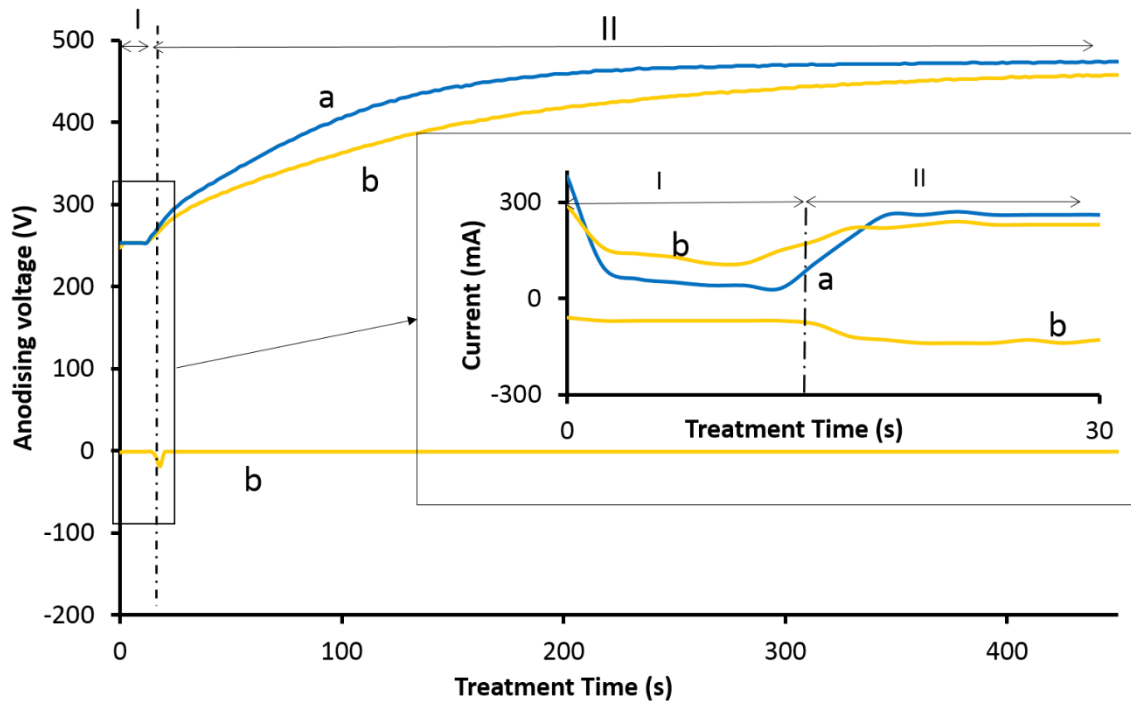


Figure 70 Voltage and current transients recorded during pulsed current PEO treatments of Ti-6Al-4V in 6g/L Na_2HPO_4 electrolyte containing 10g/L of HA micro-powder, with anodic current density set at 35 mA/cm^2 (a) pulsed unipolar mode and (b) pulsed bipolar mode with cathodic current density of 11.7 mA/cm^2 .

Figure 70 reveals that using the two-step treatment allows a more controllable and stabilised voltage growth rate compared to the single-step treatments under galvanostatic control (Figure 68). When the PUP mode was applied, the voltage transient demonstrated the comparatively higher growth rate at the beginning of Stage II and reached the steady state value at approximately at 470 V at $t = 150\text{s}$, which is stabilised at a much shorter treatment time and does not have such noticeable reduction in the growth rate in different stages as transients shown in Figure 68. When the PBP mode has been applied, the voltage growth rate was approximately halved to that observed in the PUP mode. This can be explained by the fact that introduction of a cathodic polarisation (apart from interrupting discharges and reducing accumulation of heat in the local regions) reduces space charge build up in the surface layer. The final anodic forming voltages for the processes carried out in the PUP and PBP modes with cathodic current densities of 11.7 mA/cm^2 are 473 and 458 V, respectively.

The negative voltage magnitude increases when the galvanostatic mode was initially applied (Stage II), then reverts back from -19V to -1 V at 22 s into the treatment and remained in the

steady stage until the end of the treatment, suggesting the negative component did not have a significant influence on the overall surface polarisation in this study.

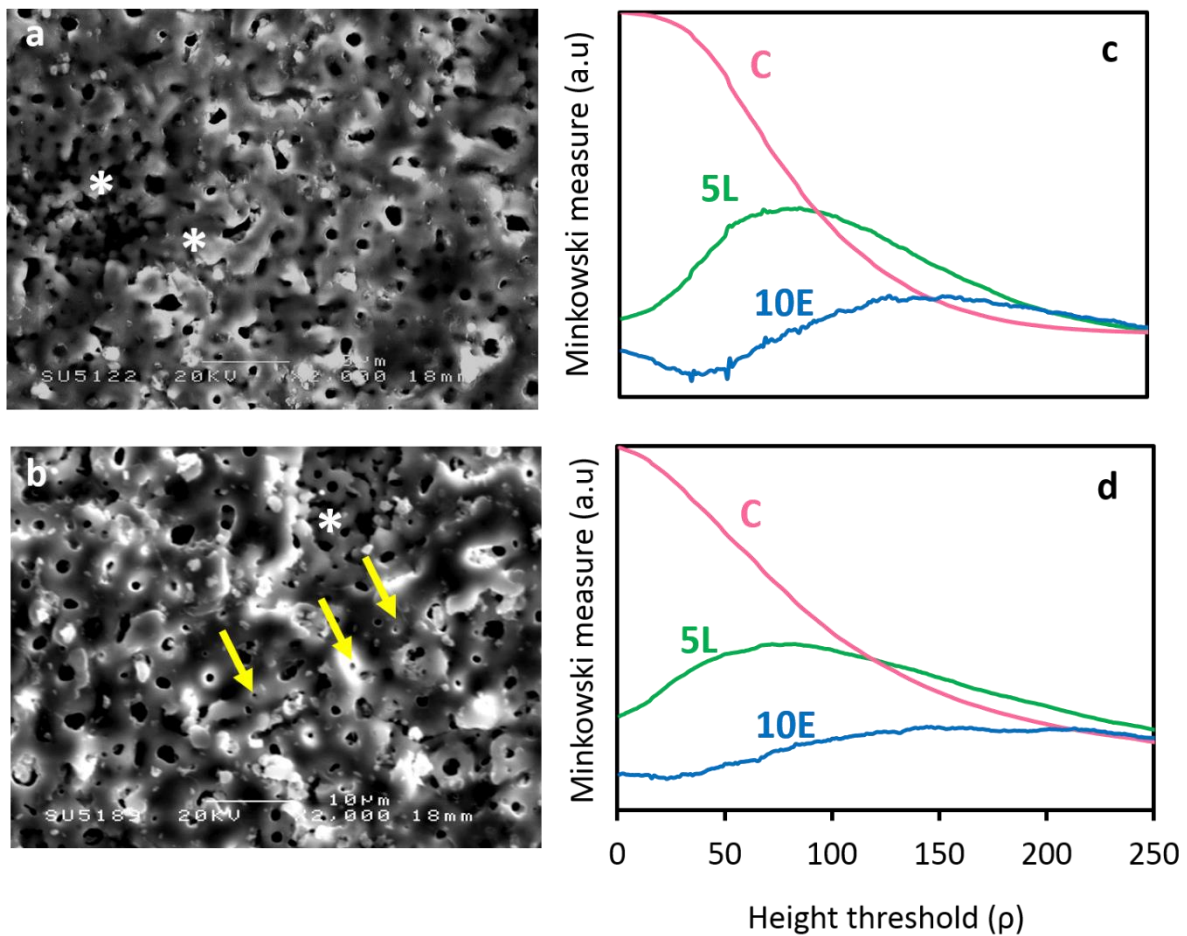


Figure 71 SEM micrographs of coatings produced by pulsed current PEO treatments with anodic current density of 35 mA/cm^2 : (a) – pulsed unipolar mode; (b) – pulsed bipolar mode with cathodic current density of 11.7 mA/cm^2 ; (c,d) – respective Minkowski functionals (c,d) $C(\rho)$, $L(\rho) \times 5$ and $E(\rho) \times 10$.

The surface morphologies of the PEO coatings produced using PUP and PBP current mode are shown on Figure 71. A typical porous morphology can be observed on all coatings, with features associated with high temperature surface re-melting, as denoted by asterisks in Figure 71a and b. Traces of discharge channels are present on the coating produced using the PUP current mode, this feature is reflected in the shape of the C curve in Figure 71c. The coating produced using the PBP current mode reveals features associated with powerful arc discharge causing coating destruction and re-melting of the surface. Moreover, the presence

of particles at the surface could also contribute to the lack of curve inflection in the coverage C curve.

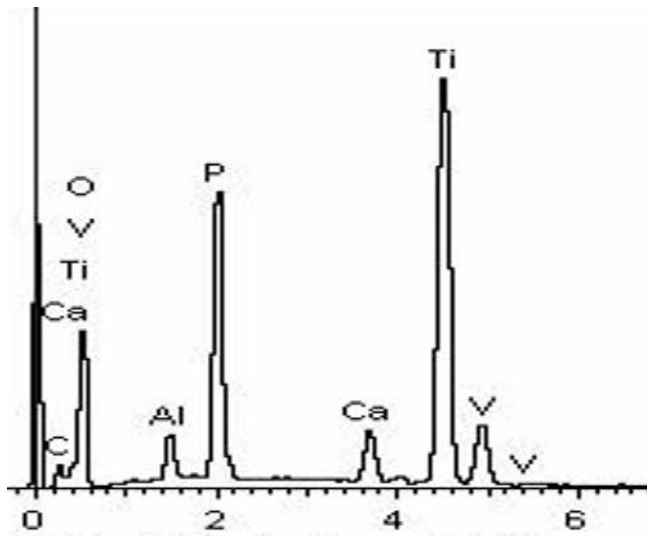


Figure 72 A typical EDX spectrum of the studied PEO coatings.

Table 15 The chemical composition of PEO coatings produced with different electrical modes.

| Element (at%) | $\frac{i^-}{i^+}$ ratio | |
|------------------|-------------------------|---------------|
| | 0 | $\frac{1}{3}$ |
| Ca | 3.0 | 2.0 |
| P | 8.0 | 8.1 |
| Ti | 14.0 | 14.3 |
| Al | 1.5 | 1.5 |
| V | 0.5 | 0.5 |
| O | 73.0 | 73.2 |
| Na | - | 0.4 |
| Ca/P | 0.4 | 0.2 |

The coatings' elemental composition derived from corresponding EDX spectra (Figure 72) is shown in Table 15. Results show the coating produced using the PUP current mode has a higher Ca/P ratio than those produced with the PBP current mode. However, the Ca/P ratio in the coating is still lower than that in the stoichiometric HA (Ca/P ~1.67). This could be a combined result of large particle size influencing the migration of HA micro-particles and the low concentration of HA micro-particle addition in the electrolyte. When the PBP mode was applied, the Ca/P ratio was comparatively lower than that of PUP mode, this can be assumed to be related to the fact that during negative biasing, HA micro-particles would be moving in the opposite direction to the substrate.

This section of the study demonstrates the importance of electrical parameters to the elemental composition of the coating. The HA particles readily migrate to the substrate during the positive bias due to electrophoresis, however the overall Ca/P value is low. This could be attributed to the low concentration of HA micro-powder addition in the electrolyte and/or large particle size influencing particle movement in the electrolyte. Compared to literature [62], the use of the two-step control method with HA containing slurry electrolyte appears to reduce signs of HA agglomeration on the surface.

7.2.3 Influence of HA micro-powder addition to the coating characteristics

Previous section showed the influence of electrical parameters on the elemental composition of the coating produced using the two-step control PEO method. The use of PBP current mode in the step II reduced features associated to powerful arcing, but the average Ca/P ratio on the coating surface also went down. In aim to enhance the Ca/P ratio in the coating, this section investigates the influence of HA micro-powder addition concentration in the electrolyte on the characteristics of coating growth and composition under the two-step polarisation conditions.

In this section of the study, the pulsed bipolar current mode with $i(+)=35 \text{ mA/cm}^2$, $i(-)=11.7 \text{ mA/cm}^2$) and pulse times of $t_{\text{on}}^+ = 400$, $t_{\text{off}}^+ = 25$, $t_{\text{on}}^- = 50$, $t_{\text{off}}^- = 25 \mu\text{s}$ were selected for the step II of the treatment. Typical oscillograms of electrical waveforms used in this section are similar to those shown in Figure 69.

Table 16 The effect of HA micro-powder concentration in the electrolyte to the electrolyte properties in the temperature range from 15 to 30°C.

| Electrolyte composition | | Electrolyte property | |
|-------------------------|--------------------------------|----------------------|----------------------|
| HA micro-powder (g/L) | Sodium phosphate dibasic (g/L) | pH | Conductivity (mS/cm) |
| 10 | 6 | 9.1 | 6.69 |
| 20 | | 9.0 | 6.53 |
| 30 | | 8.9 | 6.26 |

The PEO treatments were carried out in a 6g/l Na₂HPO₄ (Fisher Scientific) based electrolyte with 10 to 30g/l additions of HA micro-powder with the mean average particle size of 2.5 µm (Fluidinova). Table 16 displays the influence of HA micro-powder concentration to the electro-physical and chemical properties of the electrolyte. A small decrease in pH and the conductivity value of the electrolyte can be detected as the HA micro-powder addition increased. This could be explained by Equation [2.10];



From this equation, it follows that a part of OH⁻ ions associated with HA particles of low mobility would cause the solution pH and conductivity to be reduced. Research suggests addition of soluble salts, such as calcium acetate, would increase solution conductivity and reduce the anodic forming voltage [14, 19]. The current and voltage transients for PEO processes in electrolytes with various concentrations of HA micro-powder additions are displayed in Figure 73 which reveals additions do not have significant influence to the voltage and current behaviour when the two-step control mode is employed. The final values of anodic voltages for the process carried out in electrolytes with HA micro-powder concentrations of 10, 20 and 30 g/L are 456 V, 460 V and 465 V, respectively. This indicates the behaviour is different from that found in electrolytes containing soluble Ca and phosphate compounds, moreover the increase in HA micro-powder addition appears to decrease the electrolyte conductivity and increase final anodic voltage. The reduction in pH value coincides with conductivity reduction explained by Equation [2.10], therefore the pH and voltage drop in the electrolyte will be higher for higher HA concentration.

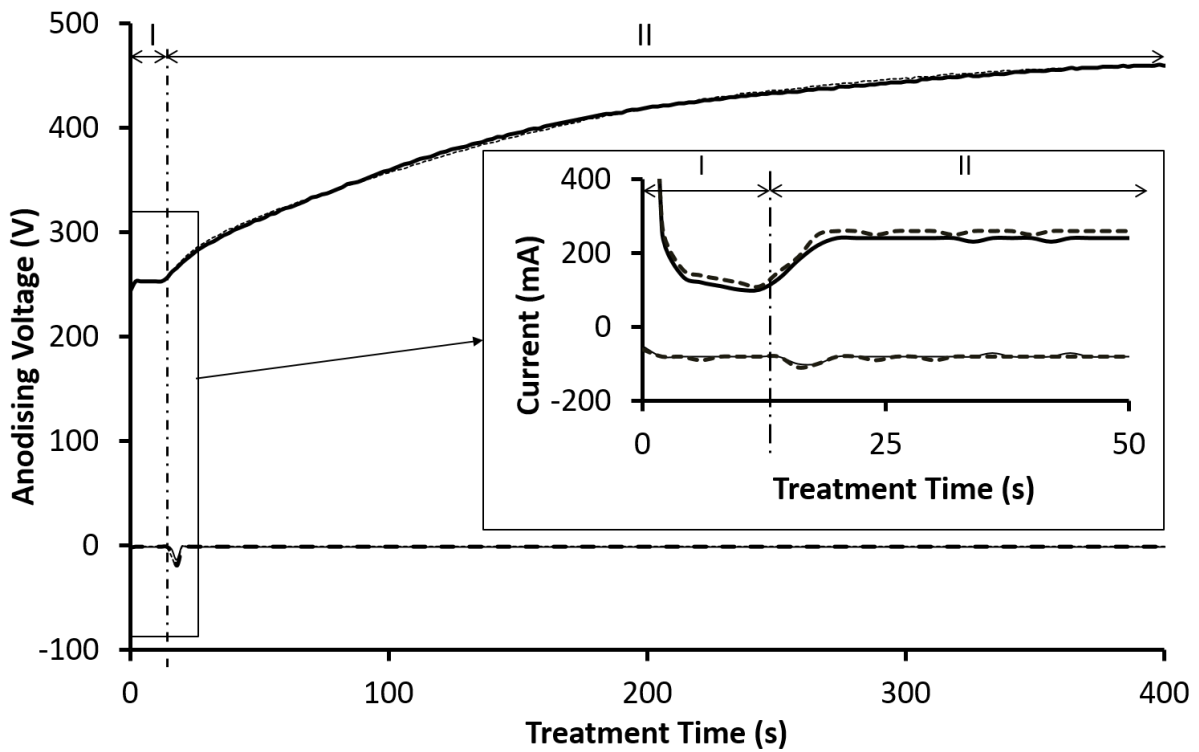


Figure 73 Voltage and current transients recorded during PEO treatments of Ti-6Al-4V alloy using pulsed bipolar current treatment in the 6g/L Na_2HPO_4 electrolyte containing 10g/L (solid line), 20g/L (dotted line) and 30g/L (broken line) of HA.

Figure 74 shows the mean average value of thickness and surface roughness of PEO coatings produced using in electrolytes with various concentrations of HA micro-powder addition. The coating thickness is maintained within 5-7 μm range which is consistent with similar voltage behaviour during treatments carried out in electrolytes with various concentrations of HA micro-powder addition (Figure 73). Figure 74b reveals the average surface roughness of the coating produced in the electrolyte with 20 g/L HA micro-powder addition to be significantly lower than those with 10 g/L.

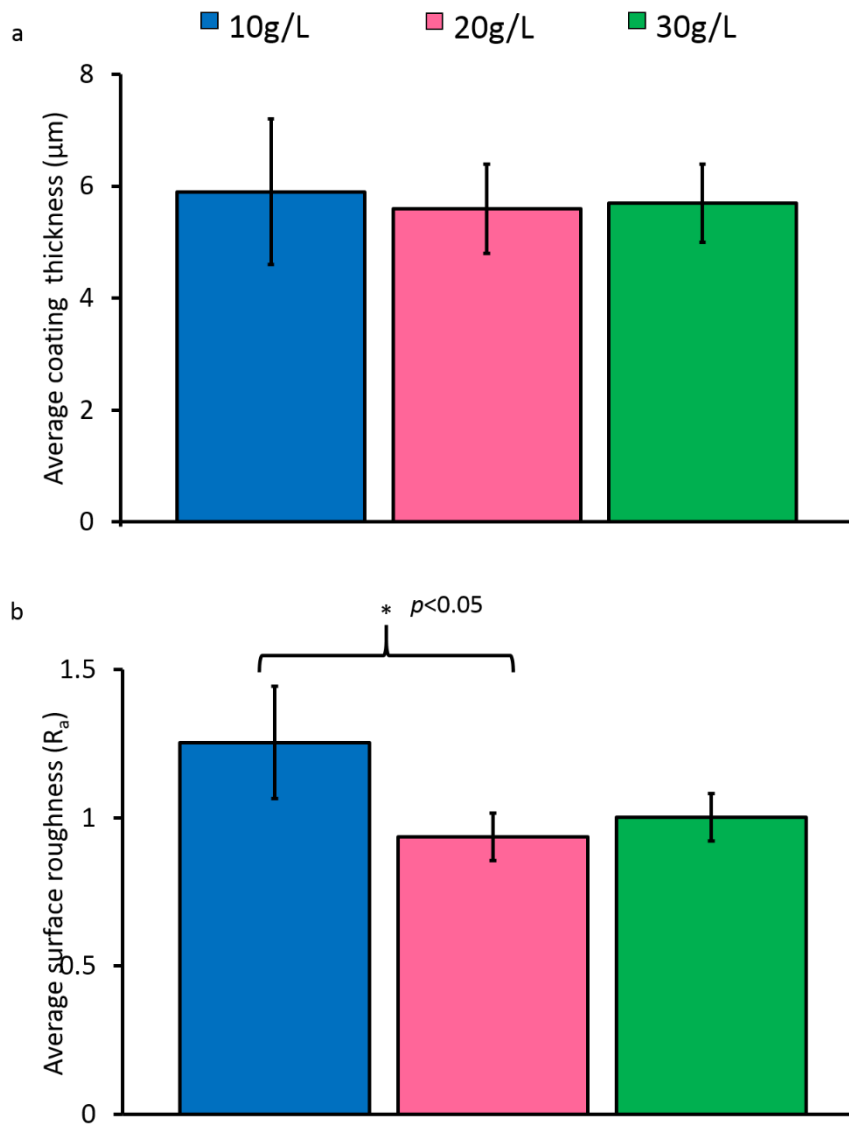


Figure 74 The mean average values of thickness (a) and surface roughness (b) for PEO coatings produced in electrolytes with 10g/L, 20g/L and 30g/L HA micro-powder addition. (* $p < 0.05$)

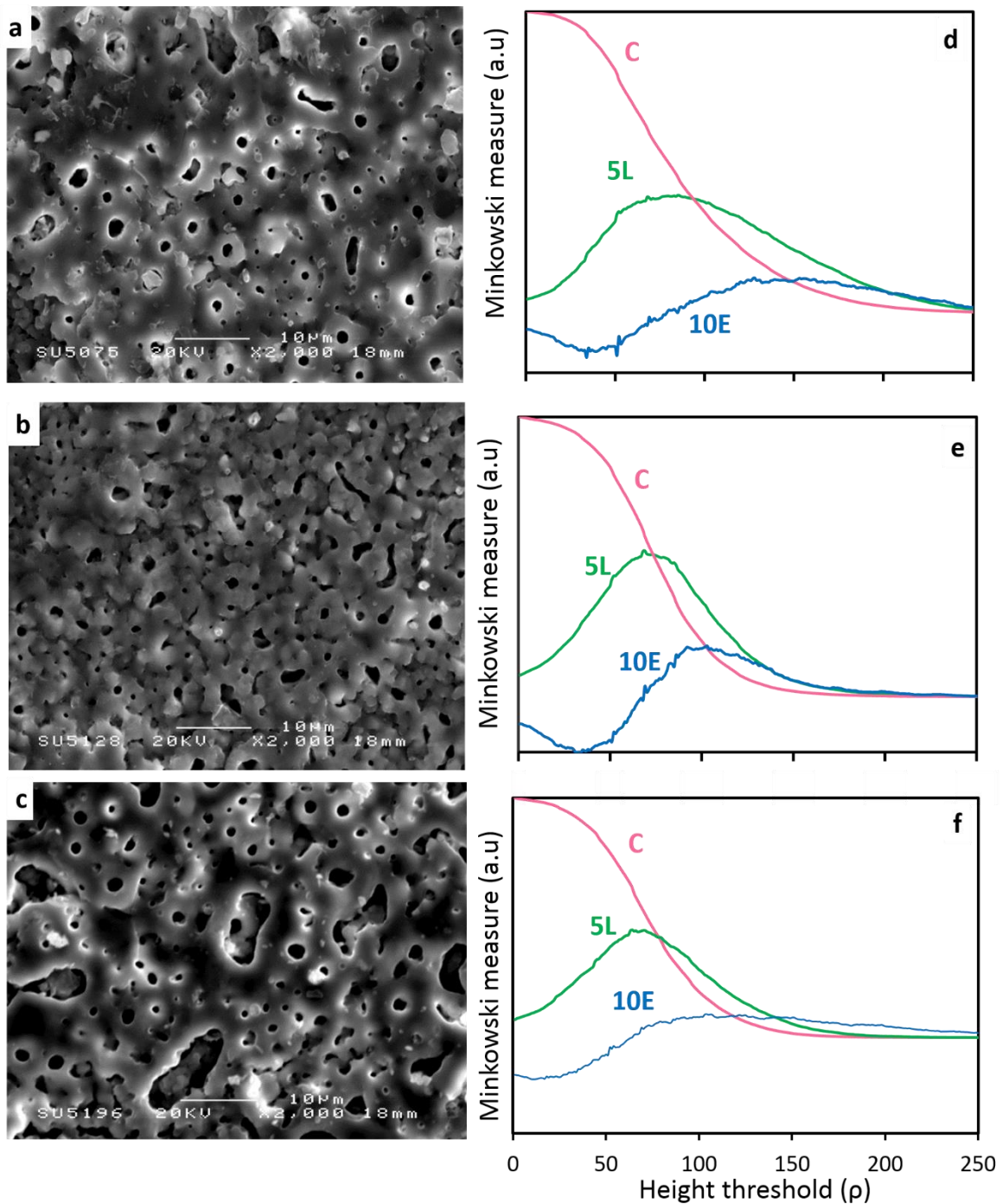


Figure 75 SEM micrographs of PEO coatings produced in 6g/L Na_2HPO_4 electrolyte with (a) 10g/L (b) 20g/L and (c) 30g/L addition of HA micro-powder and the respective Minkowski functionals (d-f) $C(\rho)$, $5L(\rho)$ and $10E(\rho)$.

Figure 75 (a-c) reveals the SEM images of PEO coatings produced in the electrolytes with 10, 20 and 30 g/L addition of HA micro-powders; the corresponding image analysis results in the form of Minkowski functional plots are shown in Figure 75(d-f). Large elongated and fine circular pin-hole pores are observed on all coatings, which has been suggested to be

beneficial for cell attachment [153]. As the concentration of HA micro-powder increased, the number of elongated pores increases, resulting in the average pore size of $0.24 \pm 0.4 \mu\text{m}$ and $0.38 \pm 1.3 \mu\text{m}$ for the coatings produced in the electrolytes with 20 g/L and 30 g/L HA micro-powder addition, respectively [154]. When the concentration of HA micro-powder is 10g/L (Figure 75a), a denser morphology is observed which is associated with high discharge energy, leading to oxide products deposited around the discharge channel fusing together [155]. When the HA micro-powder addition increased to 30 g/L (Figure 75c), elongated pores evolved into pore-in-pore features, which is often correlated with high forming voltages producing stronger electron avalanches [84]; as a result, comparatively larger discharge channels are formed. Electrolyte entering those large channels promotes development of dielectrically weaker spots on the surface, which facilitates further localised discharges to be constrained within the larger pores.

It is interesting to observe the range of surface morphologies of the coatings exhibiting features correlating to an increase in discharge intensity/applied voltage with an increase in HA micro-powder addition, while the voltage growth rate recorded in Figure 73 exhibits highly similar behaviour. This indicates that other factors, such as the incorporation of HA micro-particles in the surface layer, might be influencing local electrical profiles during sparking.

We attempted to investigate the influence of HA particles in the PEO coating to the current density distribution in the coating during the PEO process using a finite element modelling (FEM) approach. In this study, the electrical field at the surface was calculated and analysed using ELCer in-house software package [156], similar to [157] based on solving Maxwell's equation in time and space into the following'

$$\frac{\partial \rho}{\partial t} + \nabla \cdot \bar{j} = 0 \quad [7.1]$$

$$\nabla \cdot \bar{j}(r, t) = -\nabla \cdot (\sigma(r)\nabla\phi(r, t) + \varepsilon(r) \frac{\partial}{\partial t} \nabla\phi(r, t)) = 0 \quad [7.2]$$

where ρ is the charge density, j is the current density, ϕ is the electric potential, ε is the permittivity of free space, which allow the approximation of the electric potential $\phi(r, t)$ as a function of time and space [156]. A layered 3D model microstructure of the surface layer with an HA particle incorporated into TiO_2 matrix adopted for calculation is shown in Figure 76a. The HA particle is modelled by a cube with a lateral dimension of $2\mu\text{m}$, conductivity of

$\sigma=1 \times 10^{-8} \text{ Sm}^{-1}$ and relative permittivity of $\epsilon_r=50$ [158, 159], positioned in the outer region of the coating. The material properties set as $\sigma=0.63 \text{ Sm}^{-1}$, $\epsilon_r=80$ for the electrolyte; $\sigma=1 \times 10^{-10} \text{ Sm}^{-1}$, $\epsilon_r=150$ for TiO_2 and $\sigma=1 \times 10^8 \text{ Sm}^{-1}$ and $\epsilon_r=0$ for the Ti substrate. The structure was discretized using a tetrahedron mesh with over 330,000 elements to provide detailed resolution of the solved system.

Figure 76b reveals a typical pattern of electric field distribution in the studied metal-oxide-electrolyte system, highlighting the influence of dielectric properties of HA particles incorporated in titanium dioxide matrix to the electric field in it. Results indicate that the incorporation of HA particle at the surface can lead to the local distortion to the electric field in the outer region of the coating, moreover, it leads to a shielding effect, causing a comparatively lower electric field present below the particle. This is consistent with results in Figure 75, where an increase in HA micro-powder addition concentration results in appearance of morphological features usually formed under more energy intense current regimes.

Figure 76c shows the effect of frequency on the heterogeneity of current distribution at the electrolyte-oxide interface (expressed as the ratio of maximum to minimum current density), with corresponding 2D diagrams of current distribution in the studied metal-oxide electrolyte system shown in Figure 76d. It can be seen that the presence of HA particle at the interface causes micro-heterogeneities in the primary current density distribution in the electrolyte, at the interface with Ti electrode, and it exhibits complex dependence on frequency. On one hand, the maximum current density in the system increases with frequency, which reflects capacitive behaviour of the dielectric surface layer. On the other hand, when the frequency approaches DC, the heterogeneity could be as high as a factor of 10, but it would decrease rapidly to about 2.3 when the frequency increased to 2 Hz. This can be explained by the presence of a shielded region with reduced electric field in the electrolyte just above the HA particle, which descends into the surface layer when frequency increases. Once the centre of this shadow cloud passes the interface, the heterogeneity in the current density distribution is quickly regained before dropping to about a factor of 4.5 in the range of higher frequencies ($>10^4 \text{ Hz}$) corresponding to the absence of any shielding effects caused by the HA particle. This implies that below certain critical frequency (which depends upon the size of HA particles), the PEO process may tend to experience instabilities due to highly heterogeneous

distribution of local current densities that could potentially cause destruction of HA particles incorporated in TiO₂ matrix.

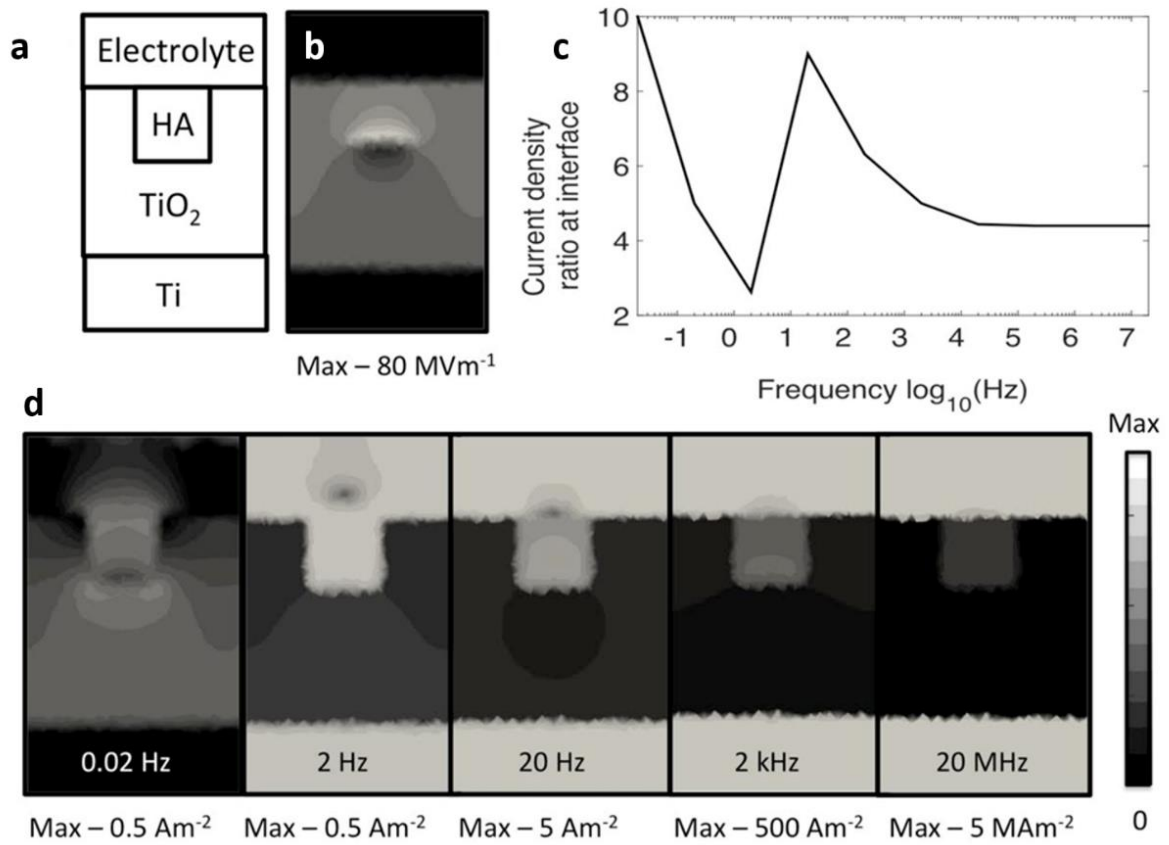


Figure 76 (a) Schematic representation of the FEM model of the metal-oxide electrolyte system, (b) typical electric field distribution at 2 kHz, (c) frequency dependence of the ratio of minimum to maximum current density at the electrolyte-oxide interface and (d) current density distributions in the surface layer at different frequencies.

Table 17 Chemical composition of PEO coatings produced using difference HA micro-powder addition.

| Element (at%) | Processing variable | | |
|------------------|--|------|------|
| | HA micro-powder addition concentration (g/L) | | |
| | 10 | 20 | 30 |
| Ca | 1.7 | 1.4 | 2.2 |
| P | 7.8 | 7.8 | 8.4 |
| Ti | 14.8 | 15.1 | 14.5 |
| Al | 1.6 | 1.7 | 1.6 |
| V | 0.4 | 0.4 | 0.5 |
| O | 73.7 | 73.6 | 72.8 |
| Ca/P | 0.22 | 0.18 | 0.26 |

Table 17 reveals the elemental composition of coatings produced with various concentrations of HA micro-powder addition in the electrolyte. Results suggest HA micro-powder concentration did not significantly influence the Ca/P ratio in the coating.

Result suggest HA micro-powder concentration did not significantly influence the Ca/P ratio in the coating, although displayed a slight increase in the individual Ca and P content for the coating produced in the electrolyte containing 30 g/L HA micro-powder.

7.2.4 Effects of the negative bias on the coating characteristics

The use of PBP mode allows parameters such as applied voltage (or current), duty cycle and frequency to be adjusted independently for both positive and negative bias. It is known that each of these parameters may have a significant influence to the characteristics of discharge. Previous section has demonstrated the possibility to incorporate HA micro-powder into the coating from slurry electrolytes. However, visual inspection outlined issues with coating morphology, which is associated with powerful arcing. This section investigates into the use

of negative pulses with various duty cycle in aim to reduce the powerful arcing on the surface. The negative bias has been suggested to provide a means to interrupt discharge and allow the surface to be cooled by electrolyte. However, in the HA slurry electrolyte, it may also lead to HA powder moving away from the substrate due to electrostatic forces.

In the following section, PEO treatments of Ti-6Al-4V alloy are carried out in the electrolyte with 30 g/L HA micro-powder addition using the two-step control method wherein a pulsed bipolar current mode ($i(+)$ = 35 mA/cm², $i(-)$ = 17.5 mA/cm²) with the negative pulse duty cycle varied from 4% to 16% is employed during step II. The voltage transients recorded during the treatment are displayed in Figure 77. Transient behaviour can be categorised into regions I, II and III. Region I corresponds to Stage I, the potentiostatic step at 250 V in the two-step control treatment. Regions II and III correspond to the treatment carried out under galvanostatic control mode with different frequencies; here region III describes a region where there is a drop in the voltage transient for some treatments.

The increase in negative duty cycle does not appear to have significant influence to the positive voltage up to region II, suggesting the negative pulse duty cycle does not influence the initial coating growth behaviour. The voltage begins to stabilise at around 200 s into the treatment at around 410 – 420 V, varying slightly for different treatments. It is interesting to observe that the coating produced with the negative duty cycle of 10% has a higher final anodic voltage than that produced at 6%. This could be explained by the higher voltage magnitude of the negative voltage transient observed, where the short negative pulse will result in the current being forced into the negative region in a short time.

When the negative duty cycle increased to 16%, a voltage drop can be observed at $t \sim 350$ s. This could be a result of the resistive-capacitive type of behaviour which can be observed for oxide films on metal surfaces.

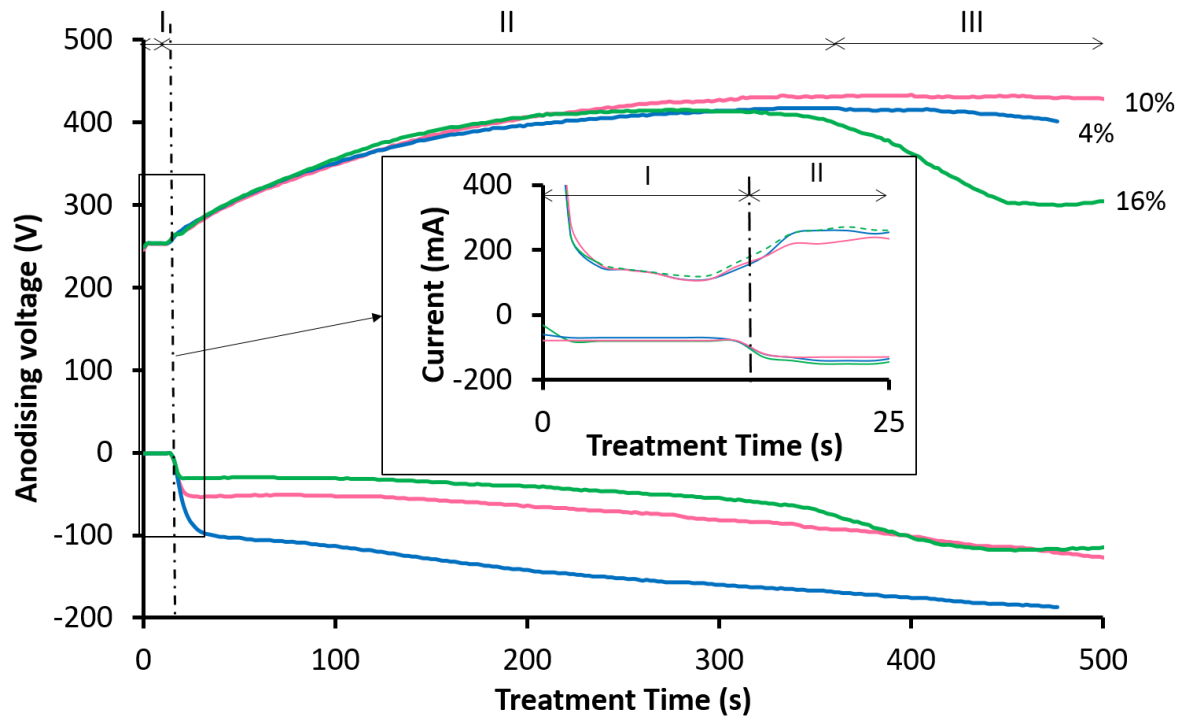


Figure 77 Voltage and current transients recorded during PEO treatments of Ti-6Al-4V alloy in the 6g/L Na_2HPO_4 electrolyte containing 30g/L HA micro-powder addition using pulsed bipolar current treatment with various negative duty cycles at step II.

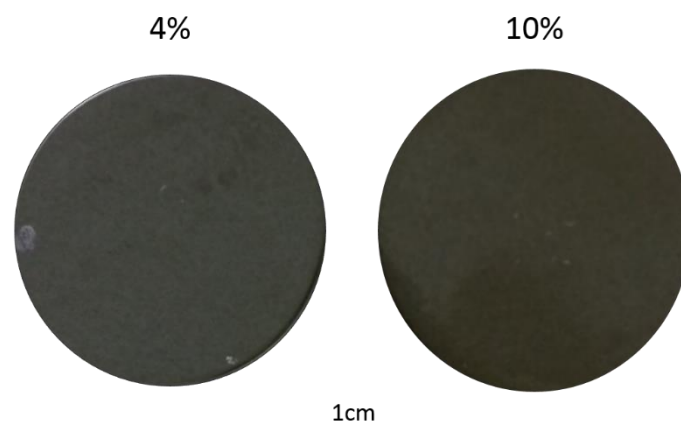


Figure 78 Images of coating produced using PBP PEO treatments with negative duty cycles of 4% and 10%.

Visual inspection of coating displayed in Figure 78 shows when the negative duty cycle is low, white dots and non-uniform colouring appear on the surface which suggests local powerful arcing occurred during the treatment. The presence of white dots is not found on

the coating produced with 10% negative duty cycle, shows the increase in the negative duty cycles can reduce features associated with powerful arcing. However, variance in coating colour between the edge and the inner region can be noted.

Figure 80(a-c) displays the surface morphologies of coatings produced using the two step control mode in which a PBP current with various negative duty cycles was employed in step II; the corresponding functional plots are shown in Figure 80(d-f). When compared to the surface morphologies observed in coatings produced with various concentrations of HA micro-powder addition shown in Figure 75, presence of globular or precipitates can be observed in all presently discussed coatings. Jiang and Wang [9] proposed that the negative pulse does not play a crucial role in the formation of the coating microstructure because it only intersperses with the spark discharges at the surface. This work shows the increase in the negative duty cycle not only allows the surface to cool, but also enhances the HA particle incorporations. Pin-hole pores are observed in all coatings, which is considered to be a result of gas evolution [160], moreover the number of pin-hole and smaller pores increased as the negative duty cycle increases. This is due to the increase in the negative pulse duration during the treatment, leading to a higher rate of gaseous production, e.g. due to decomposition of water.



As the hydrogen gas escapes from the coating it forms small pores on the surface. The average pore size is 0.27, 0.22 and 0.35 μm for the coatings produced with negative duty cycles of 4%, 10% and 16%, respectively. Signs of re-melting can be observed on the coating surface as shown in Figure 80a; which correlates to higher energy discharges during the treatment when the negative duty cycle is low. As the negative duty cycle increases, discharge channels become more distinct. This complies with results from Figure 79, where the average surface roughness of coating produced at 16% negative duty cycle is significantly higher than that at 4%.

When comparing the Minkowski plots (Figure 80d-f), the shape of surface coverage C curve is shown to have a less apparent inflection on the coating produced using negative duty cycle at 16% than those of 4 and 10%. It can be speculated the presence of HA micro-particles on the surface leads to the appearance of shaded regions on the surface, resulting in misperception during the Minkowski analysis. The boundary length L and the Euler curve

(E) behaviour of all coatings display similar characteristics. In which, a higher L_{\max} value for the coating produced at 10% negative duty cycle suggests a more developed interconnectivity between pores and matrix.

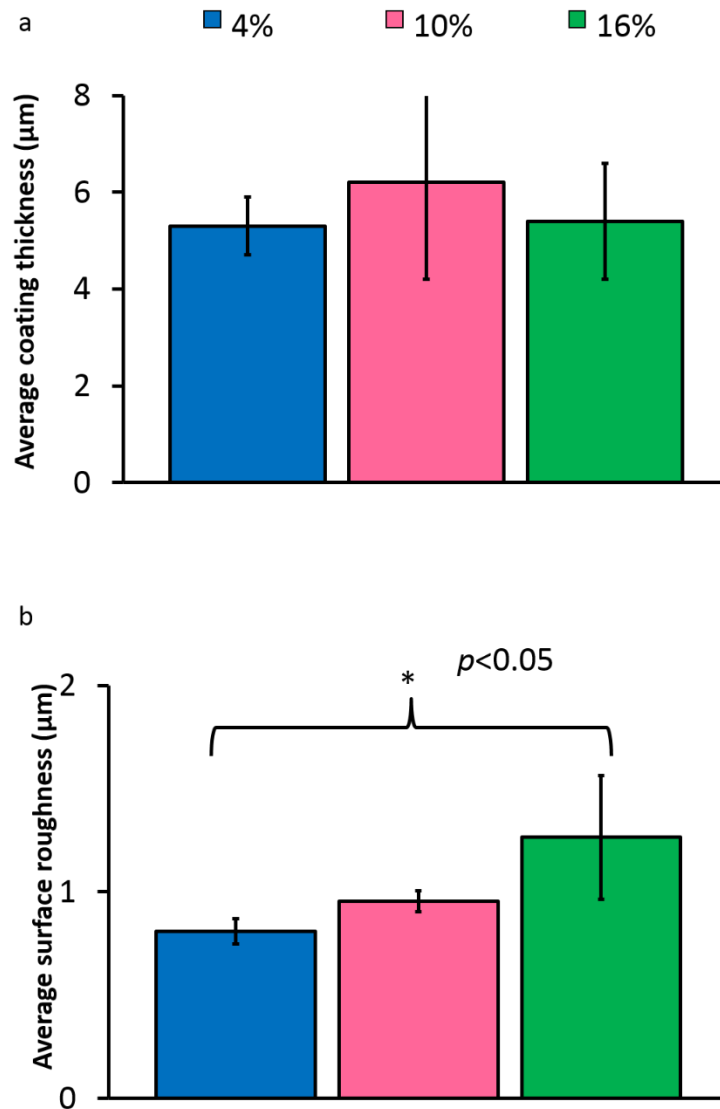


Figure 79 The mean average value of thickness (a) and surface roughness (b) of PEO coatings produced on Ti-6Al-4V substrate using the two-step control method, with the negative duty cycle set at 4%, 10% and 16% during step II. (* $p < 0.05$).

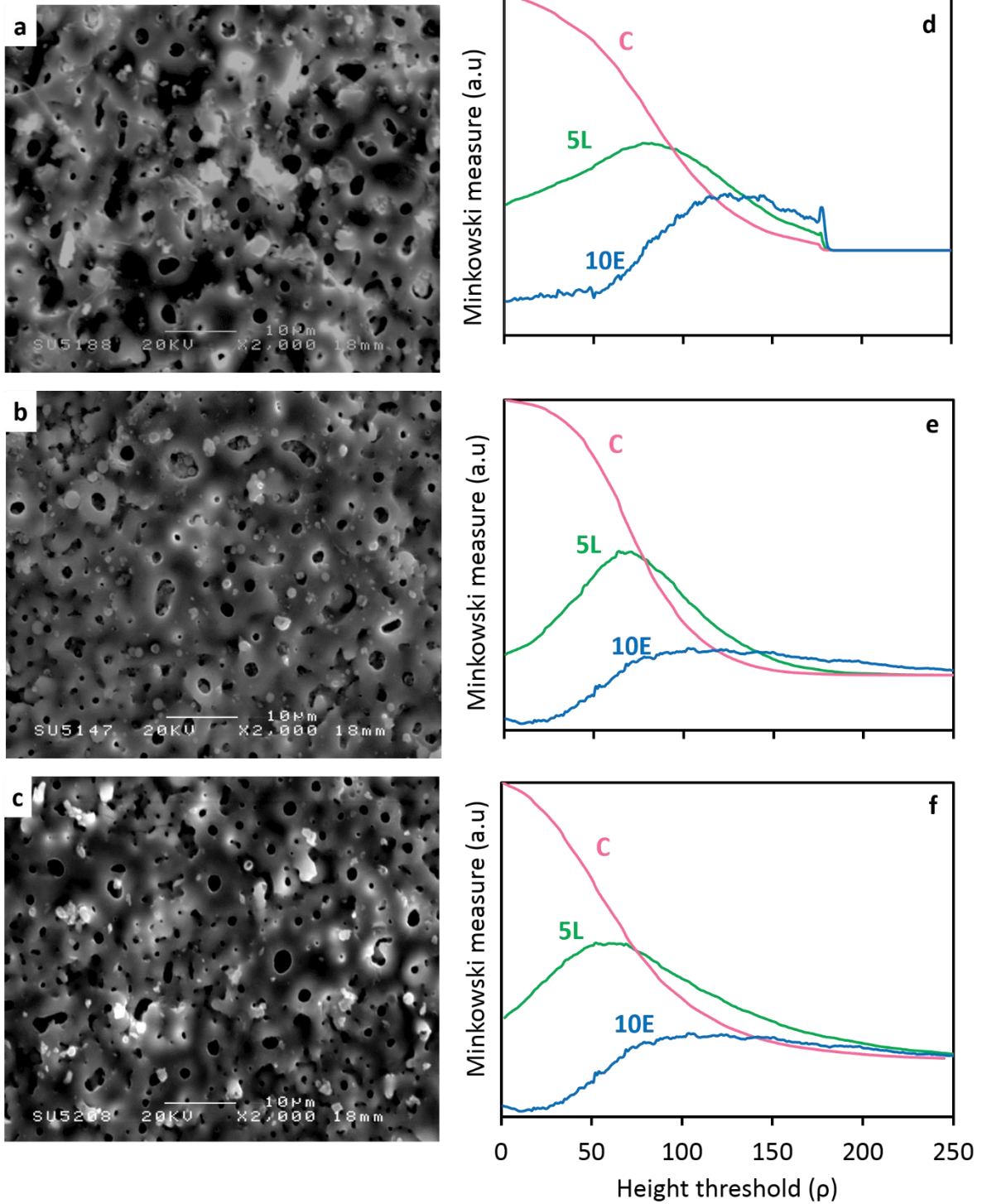


Figure 80 SEM micrographs of coatings produced on Ti-6Al-4V substrate in the electrolyte with 30g/L HA micro-powder addition using the two-step control method, with the negative duty cycle set at (a) 4%, (b) 10% and (c) 16% during the step II, with respective Minkowski functions (d-f) C(ρ), 5L(ρ) and 10E(ρ).

Table 18 Chemical composition of PEO coatings produced using Ti-6Al-4V substrate with 30g/L HA micro-powder addition electrolyte using the two-step control method, with various negative duty cycles during the Step II.

| Element (at%) | Processing variable | | |
|------------------|-------------------------|------|------|
| | Negative duty cycle (%) | | |
| | 4 | 10 | 16 |
| Ca | 2.9 | 1.6 | 1.9 |
| P | 8.4 | 8.1 | 7.8 |
| Ti | 13.3 | 14.8 | 15.3 |
| Al | 1.4 | 1.6 | 1.6 |
| V | 0.4 | 0.4 | 0.4 |
| O | 73 | 72.8 | 72.2 |
| Na | 0.7 | 0.7 | 0.8 |
| Ca/P | 0.35 | 0.20 | 0.24 |

The elemental composition of coatings produced with different negative cycles is shown in Table 18. The Ca/P ratio in the coating is lower than the desired value of 1.67, this is consistent with the previous discussion pointing out to the fact that the negatively charged HA micro-particles will tend to be repelled away from the substrate during the negative bias due to electrostatic forces. The examination of the Ca content on the surface of the coating appears to be correlated to the features associated with powerful arcing, this agrees with discussion of the FEM analysis (Figure 76) concerning the influence of HA particles incorporation to the electric field distribution on the surface.

In essence, the increase in the negative duty cycle can reduce microstructural heterogeneity associated with powerful arcing, which is not favourable for reproducibility of the coating. Meanwhile, the increase in the negative duty cycle also leads to the coatings becoming more prone to internal stress and cracking.

7.3 Summary

This section has demonstrated successful formation on titanium substrates of porous coatings incorporating chemical compounds from electrolyte suspensions using the two-step control method. The elimination of the need for use of organic chelating agents and stabilisers in the electrolyte is highly preferable for biomedical applications.

The use of FEM approach to model electric field distribution in the metal-oxide-electrolyte system increased the understanding of current density distribution and the influence of HA micro-powder embedded in the coating to the plasma discharge behaviour during the PEO treatment. As a result, despite similar voltage growth behaviours observed with various HA micro-powder additions in the electrolyte, the surface morphologies exhibit features usually correlated to treatments in different voltage ranges. The use of pulsed bipolar current has shown to reduce features related to powerful arcing, and increase the mean average surface roughness. This could be attributed to the increase in amount of gaseous products formed with introduction of the negative bias.

The incorporation of HA micro-powder in the coating shown to be significantly lower than the stoichiometric HA ($\text{Ca/P} = 1.67$). This indicates insufficient incorporation of HA in the micro-powder form. This could be attributed to the large particle size which results in low HA mobility in the electrolyte. Therefore, the use of nano-particles should be investigated in aim to enhance the particle uptake on the surface.

7.4 The effect of HA nano-powder addition in the electrolyte to the coating characteristics

Previous section has demonstrated a possibility to form porous PEO coatings with incorporation of HA particles from slurry electrolytes. It was suggested the comparatively large HA micro-powder size would result in shielding effect on the coating, leading to heterogeneity of current density at the surface. Furthermore, the overall Ca/P ratio on the surfaces of coatings produced in the electrolytes with HA micro-powder additions is low and it is supposed to be a result of insufficient mobility of large size particles.

This section explores the use of HA nano-particles in the electrolyte in aim to reduce heterogeneity of current density distribution at the surface and increase the concentration of HA in the coating. The use of HA nano-particles had been of great interest in biomedical

field as it is shown when used as scaffolds or doped coatings to enhance their biocompatibility due to their structural similarity with apatite, high surface to volume ratio and surface activity [161-164]. Furthermore, incorporation of HA nano-particles has been suggested to be more beneficial for osteoblastic proliferation when compared to HA micro-particles [165] as they are more readily absorbed into cells [166].

Numerous research studied synthesis, structure and properties of HA nano-powder, and showed formation of uniform size particles to be difficult. Moreover the size effect and the subsequent biological effects of HA nano-particles is still not yet understood. [61, 167]. Due to the large amount of variables involved with formation of HA nano-particles, this study used commercially available HA nano-powder (nanoXIM-Hap303, Moreira da Maia, Portugal) to investigate the effect of particle size to the coating growth behaviour and resulting morphology.

7.4.1 Results and discussion

Table 19 The effect of HA nano-powder concentration in the electrolyte to the electrolyte properties.

| Electrolyte composition | | Electrolyte property | |
|-------------------------|--------------------------------|----------------------|----------------------|
| HA nano-powder (g/L) | Sodium phosphate dibasic (g/L) | pH | Conductivity (mS/cm) |
| 10 | 6 | 9 | 5.88 |
| 15 | | 8.9 | 7.70 |

Table 19 displays the influence of HA nano-powder to the electro-physical properties of electrolytes. The increase in HA nano-powder content increased the electrolyte conductivity; such behaviour was not observed when HA micro-powder was used, this could be attributed to the increase in HA solubility when nano-particles are used [14, 168].

In this section of the study, two-step control PEO treatment is also employed with stage I corresponding to the treatment carried out under potentiostatic control at 250V. The treatment during Stage II was carried out under galvanostatic control using PBP current mode ($i(+)=35 \text{ mA/cm}^2$, $i(-)=17.5 \text{ mA/cm}^2$) with pulse times set at $t_{on}^+ = 400$, $t_{off}^+ = 25$, $t_{on}^- = 50$, $t_{off}^- = 25 \mu\text{s}$. Similar processing parameters have been applied previously in experiments with HA micro-powder in order to understand the influence of particle size to the electrical transient behaviour and the subsequent coating morphology. Previous results indicated that

the addition of HA micro-powder does not influence the voltage and current transients during the two-step control PEO treatment, therefore similar investigation is conducted here with addition of HA nano-powder in order to gain a better understanding of the effect of particle size.

The voltage and current transients recorded during the treatment are displayed in Figure 81. Stages I and II are labelled according to the discussion earlier.

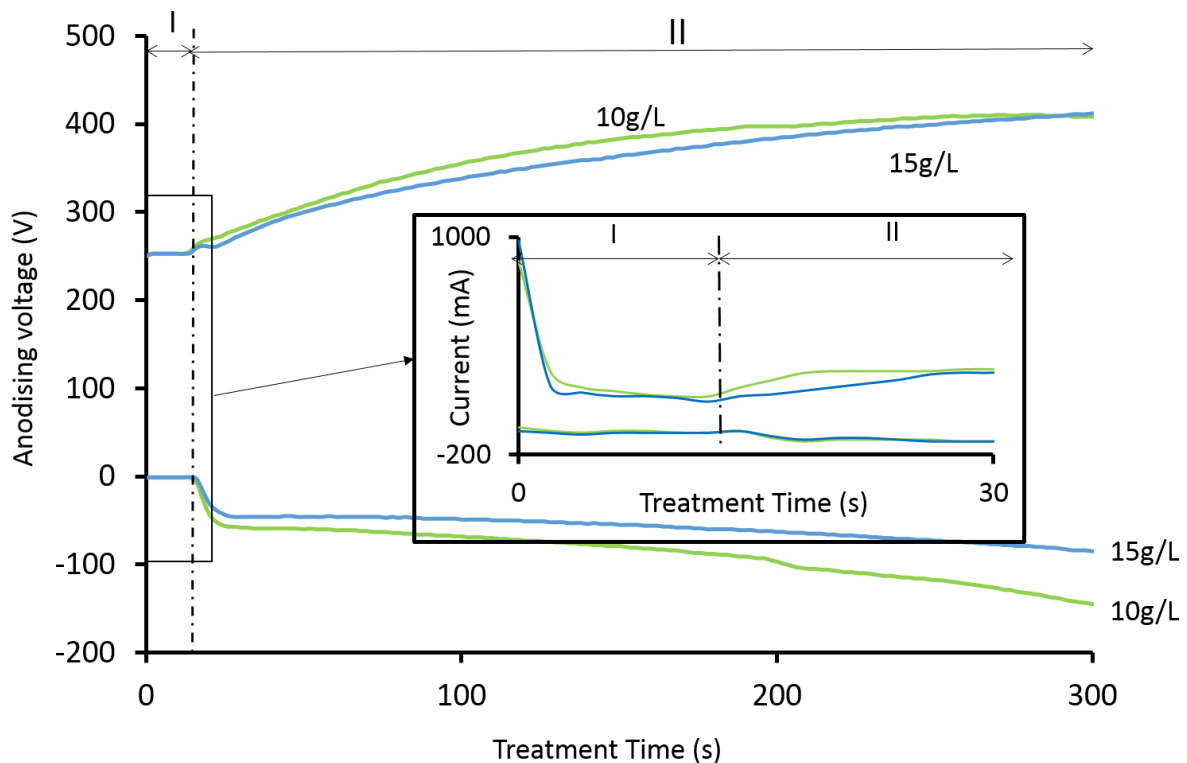


Figure 81 Voltage and current transients recorded during PEO treatments of Ti-6Al-4V alloy using the pulsed bipolar current mode in the 6g/L Na_2HPO_4 electrolyte containing 10 and 15 g/L HA nano-powder additions.

The addition of HA nano-powder in the electrolyte has shown to influence the anodic and cathodic voltage growth behaviour during the treatment. At the beginning of the stage II, the positive voltage growth rate for the treatment in the electrolyte with 10 g/L HA nano-powder is slightly higher than that with 15 g/L, but both treatments resulted in similar final anodic voltage at approximately 412 V. This is consistent with the earlier discussion on the influence of HA micro-powder, where the increase in HA powder does not influence the forming voltage.

It is interesting to observe an increase in the concentration of HA nano-powder addition leads to a decrease in the negative voltage growth rate. Similar behaviour is observed when the negative duty cycle increased in Figure 77 when HA micro-powder was employed.

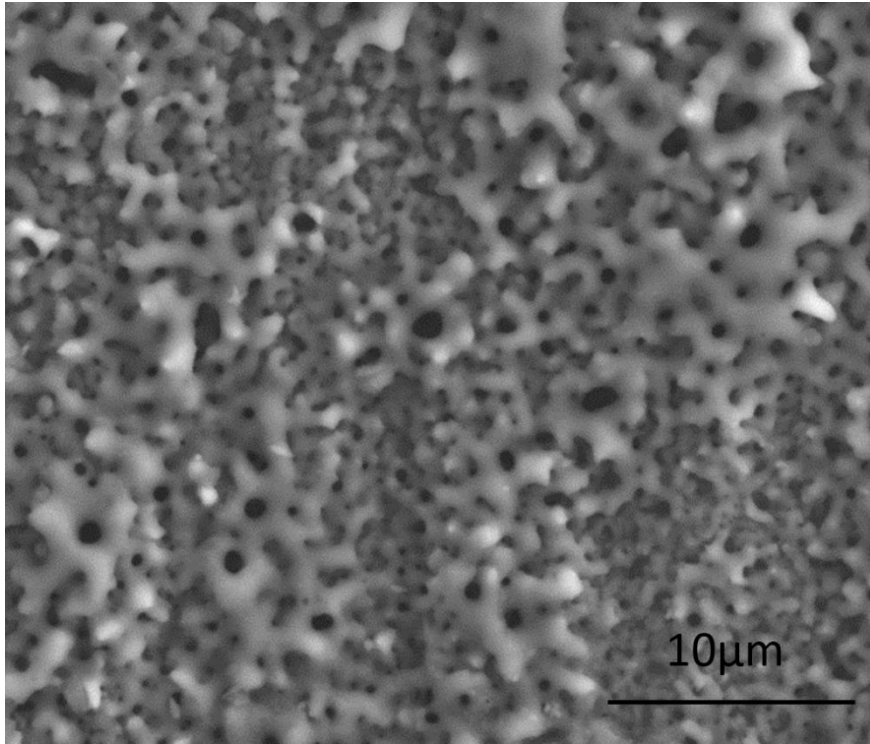


Figure 82 Surface morphology of coatings produced on Ti-6Al-4V substrate using the two-step control PEO mode in the electrolyte with 10g/L HA nano-powder addition.

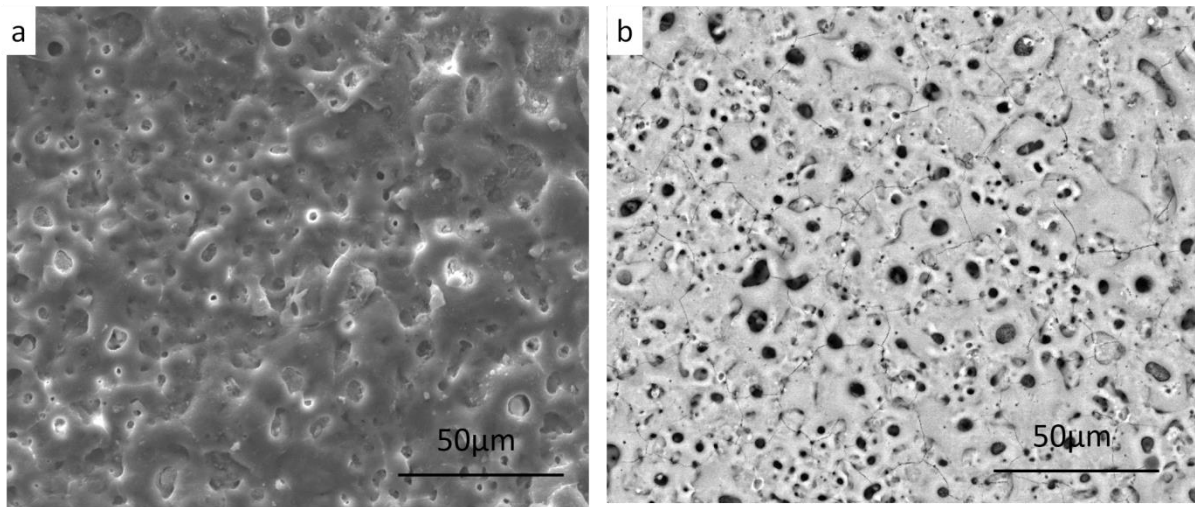


Figure 83 Secondary (a) and backscattered (b) SEM micrographs of the coating produced on Ti-6Al-4V substrate using the two-step control PEO mode in the electrolyte with 15g/L HA nano-powder addition.

The surface morphologies of coatings produced using 10 g/L and 15 g/L HA nano-particles are presented in Figure 82 and

Figure 83. It had been proposed the need for chemical additives [62], especially when using HA nano-powders to prevent HA agglomerates deposited onto the coating. Results in this study suggest the application of the two-step control PEO mode can reduce agglomerate features on the surface without the need for additives even if HA nano-powder additions are used.

It is interesting to observe the differences in the surface morphology as the concentration of HA nano-powder addition increases, this could be explained by the voltage transient shown in Figure 81, where the positive voltage enters a stable stage earlier during the treatment in the electrolyte with 10 g/L of HA nano-powder than that with 15 g/L of HA nano-powder. The stable voltage corresponds to the micro-arc stage where sparking spreads over the surface resulting in the porous morphology and repeated in sparking enhances the overall uniform coating thickness. The average surface thickness of the coating produced in the electrolyte containing 10g/L HA nano-powder addition is 9.1 ± 0.7 μm with the mean average pore size of 1 ± 0.75 μm .

An increase in the concentration of HA nano-powder in the electrolyte increases the chance of its deposition on the surface via electrophoretic mechanisms. The average coating thickness and pore size of the coating produced in the electrolyte with 15 g/L HA nano-powder addition is 9.4 ± 1.8 and 3.85 ± 1.5 μm , respectively. Despite the lower voltage growth rate observed in the voltage transient curve in Figure 81, the increase in HA nano-powder concentration (which increased the electrolyte conductivity) would also result in features related to higher energy arcing, moreover a comparatively higher conductivity of HA also leads to a higher local current density in the proximity of incorporated particle, as discussed in Figure 76. The combination of these affects results in stronger electric avalanches and discharges. Moreover, the porous structure observed in

Figure 83a appears to be filled by deposits. SEM imaging in backscattered electron mode (

Figure 83b) suggests the chemical composition of material deposited in the pores is different from that of the coating surface, therefore it can assumed that the pores comprise of compact HA nano-particles, which may undergo melting and quenching while forming a deposit within the pore.

The coating produced in the electrolyte with 10 g/L HA nano-powder addition did not reveal cracks on the surface. Cracks are commonly observed when HA micro-powder has been

used due to the differences in thermal expansion, when the particle size reduced, therefore the thermal expansion would also reduce during deposition and cooling. However, fine cracks between discharge channels and deposits in the pores can be observed in the coating produced in the electrolyte containing 15 g/L of HA nano-powder. This could be attributed to the large amount of HA nano-powder located at the discharge channel which undergoes repeated decomposition or re-crystallisation causing cracks formation.

This section of the study has demonstrated the importance of the particle size in the slurry electrolyte for the PEO treatment. Addition of HA nano-powder in the electrolyte has shown similar effect to those with soluble components, where the conductivity of the electrolyte increased. This could be explained by the smaller particle size which enhances their mobility in the electrolyte and also the conductivity. Besides, partial dissolution of poorly crystalline HA nano-particles may also take place. Results have indicated the use of HA nano-powder enhances the particle movement in the electrolyte, resulting in their facilitated incorporation into the porous morphology. Further investigation of the coatings is required to understand the *in vitro* response of the HA nano-powder incorporated coatings.

7.4.2 Influence of HA particle size to the biological properties of PEO coatings

The ability to *in-situ* incorporation of HA micro- and nano- particles from the electrolyte into the coating using the two-step control PEO process is particularly favourable for biomedical applications. It had been suggested that the porous PEO coating can provide a favourable structure for cell adhesion and proliferation [30] and therefore it was proposed that further enhancement of bioactivity can be achieved by incorporation of HA particles into the coating. However there is limited research associated with comparing the bioactivity of PEO coatings. Previous sections have demonstrated a possibility of HA particles incorporation in porous PEO coatings, the following work focuses on comparing the surface morphology and osteoblastic response of such coatings.

For the remainder of this chapter, the coatings produced in 6 g/L Na_2HPO_4 , with various HA micro-powder addition or HA nano-powder addition will be referred to as TiO_2 , $\text{TiO}_2+\mu\text{HA}$ and TiO_2+nHA coatings, respectively. Details of the PEO treatment conditions used for the following section are presented in Table 20.

Table 20 The processing conditions on Ti-6Al-4V substrate selected for in vitro assessment.

| Sample label | PEO treatment conditions | | | | | |
|------------------------|--------------------------|----------------|-------------------------|--------------------------|-------------------------|--------------------------|
| | Step 1 (V) | Step 2 (i-/i+) | t(+) _{on} (μs) | t(+) _{off} (μs) | t(-) _{on} (μs) | t(-) _{off} (μs) |
| TiO ₂ | 250 | 0 | 400 | 100 | - | - |
| TiO ₂ + μHA | | 1/3 | 400 | 25 | 50 | 25 |
| TiO ₂ + nHA | | 1/2 | 400 | 25 | 50 | 25 |

Figure 84 presents the surface morphologies of the TiO₂, TiO₂ + μHA and TiO₂ + nHA coatings and the corresponding Minkowski functional plots (Figure 84 (d-f)). A highly porous surface morphology can be observed for the TiO₂ coating with an average pore size of 0.53±0.26 μm. This can be explained by the long-life sparks during the treatment, resulting in repeated discharge at the surface. The TiO₂ + μHA coating exhibits features of a porous morphology with translucent deposition as shown in Figure 84b, the pore size is approximately 0.24±0.07 μm. These surface features observed on the TiO₂ + μHA coating could be attributed to the comparatively large HA micro-powder being unable to enter into the discharge channels during the treatment, forming a layer at the surface. The TiO₂ + nHA coating shows a porous morphology with pore size of 1±0.75 μm. Deposits correlates to matrix splashed out from the discharge channels can be observed, forming a volcano-hole structure on the coating. There are no features correlated to powerful arcing present in the micrograph. Therefore, it can be speculated that the coating did not experience secondary destructive formation resulting in a smoother surface appearance.

When comparing the Minkowski functionals of the TiO₂ and TiO₂ + nHA coating in Figure 84(d and f), similar surface coverage curve C is observed, which indicates they have similar porous features. Furthermore similar locations of threshold ranges and shapes of the boundary length (L) and Euler (E) curves for the two coatings suggest them exhibiting similar structure.

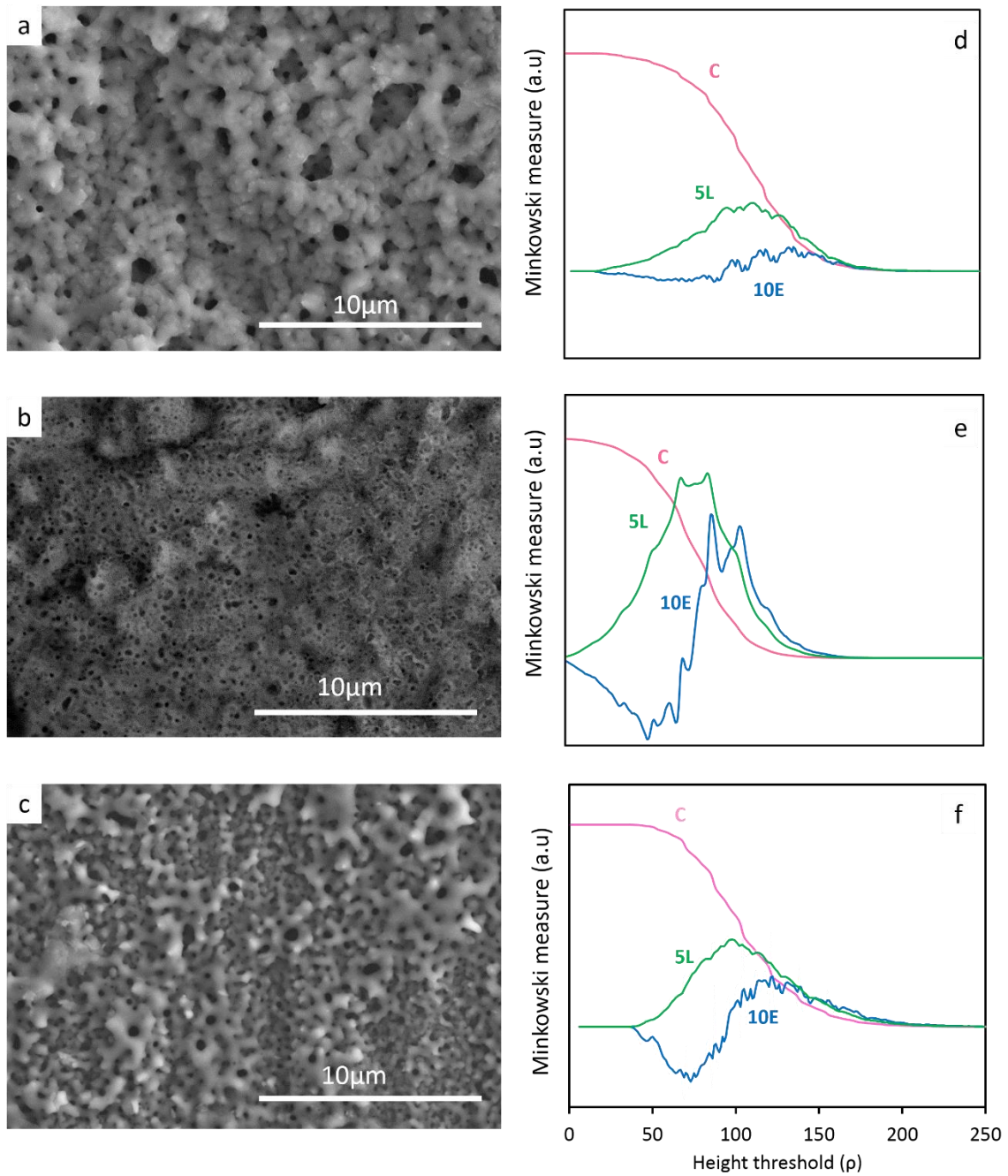


Figure 84 SEM micrographs of (a) TiO_2 (b) $\text{TiO}_2 + \mu\text{HA}$ and (c) $\text{TiO}_2 + \text{nHA}$ PEO coatings with respective Minkowski functionals $C(\rho)$, $5L(\rho)$ and $10E(\rho)$.

Figure 85 presents the average surface roughness of the TiO_2 , $\text{TiO}_2 + \mu\text{HA}$ and $\text{TiO}_2 + \text{nHA}$ coating. The average roughness value for the $\text{TiO}_2 + \text{nHA}$ coating is significantly higher than those for the TiO_2 and $\text{TiO}_2 + \mu\text{HA}$ coatings. It is interesting to observe the $\text{TiO}_2 + \mu\text{HA}$ coating to have a significantly lower average surface roughness, this could be explained by

the blockage of pore opening by the relatively large HA particles as displayed in Figure 84c. Although results show the coating produced in this section are significantly different, however it must be noted that all the values are within the 'micro-sized topology' category [169], which defines surface roughness in the range of 1-10 μm . Moreover, the average surface roughness value variation is within 0.1 μm , therefore the variance is attributed to the low standard deviation.

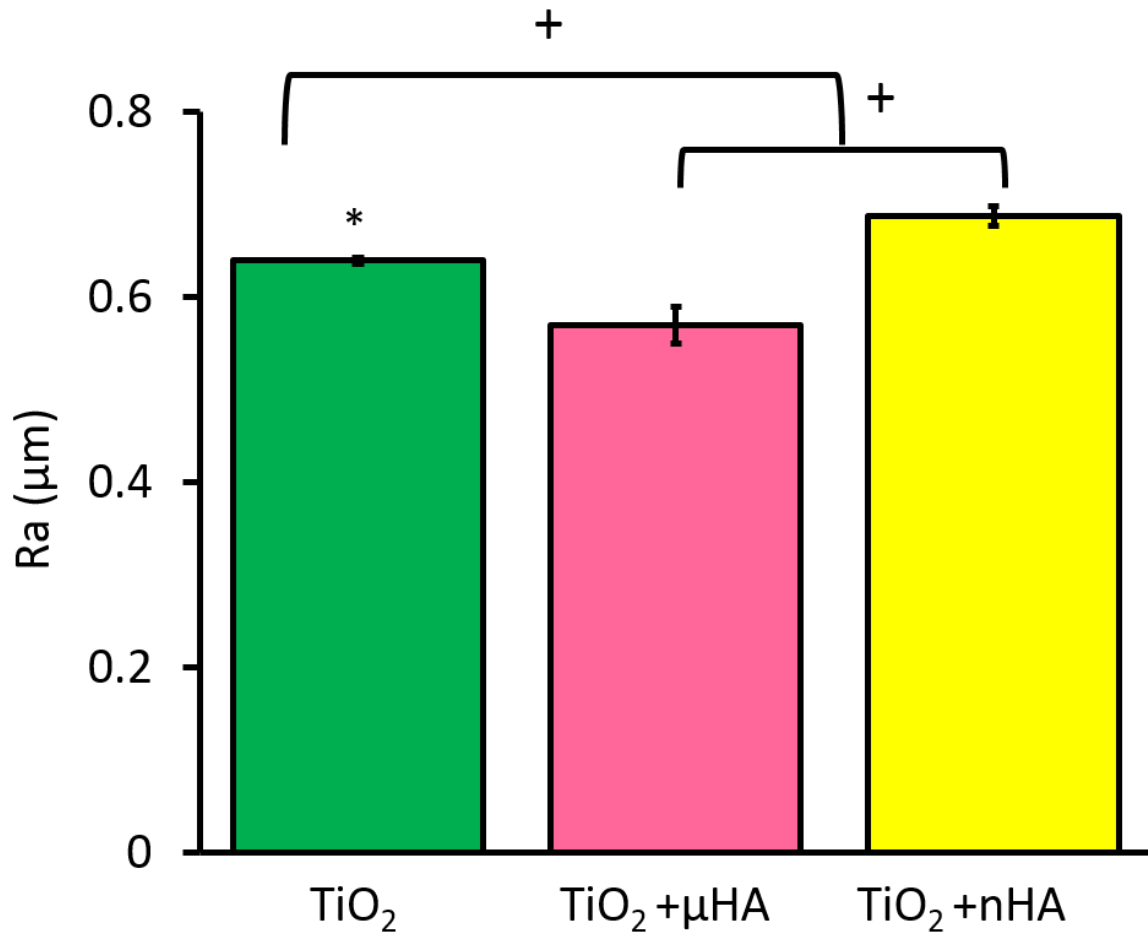


Figure 85 The mean average values of surface roughness of TiO₂, TiO₂ + μHA and TiO₂ + nHA coatings. * means comparison with TiO₂ + μHA coatings and showed $p < 0.05$; + means comparison to TiO₂+nHA showed $p < 0.05$. (Data is mean \pm SD, n=3)

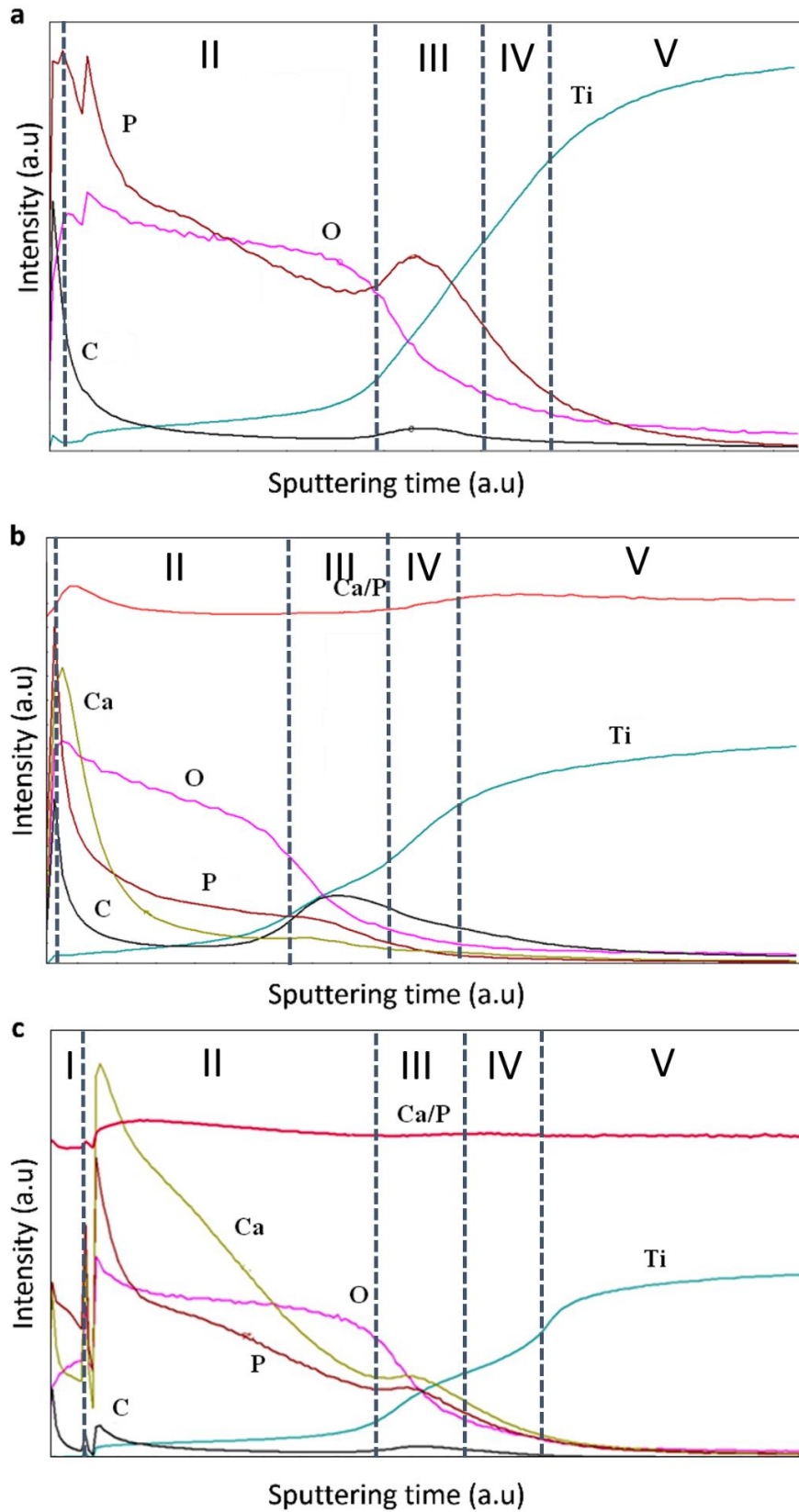


Figure 86 GDOES profiles of selected elements in the (a) TiO_2 (b) $\text{TiO}_2+\mu\text{HA}$, and (c) TiO_2+nHA coatings.

Glow discharge optical emission spectroscopy (GDOES) method is used to determine the elemental composition of the coating. This method had been used to examine the express control of metallurgical products and had recently shown to be used to investigate diffusion in coatings and bulk materials.

Figure 86 reveals the elemental distribution profiles over the thickness of the TiO_2 , $\text{TiO}_2 + \mu\text{HA}$ and $\text{TiO}_2 + \text{nHA}$ coatings and five zones can be identified in the profiles. The first zone is featured by an elevated carbon content. This had been suggested to be related a combination of the dissolved CO_2 in the aerated alkaline electrolyte, which would result in adsorption of carbonated anions in the porous surface structure during the PEO treatment [170]. A comparatively large disturbance in Zone I can be observed for the elemental profiles of the $\text{TiO}_2 + \text{nHA}$ coating. This complies with the comparatively higher surface roughness observed in Figure 85. Kirkyukhantsev-Korneev [171] proposed that surface roughness influences the penetration of air into the discharge gap, therefore often leads to disturbance at the beginning of the analysis.

Zone II is characterised by a gradual reduction of P and O in the coating and increase in Ti content, which correlates to the outer and middle regions of the coating. A phosphorous rich region is observed at the outer region of the coating, where Ti appears to be depleted, outlining a similar behaviour as observed in previous work [30]. For the $\text{TiO}_2 + \mu\text{HA}$ and $\text{TiO}_2 + \text{nHA}$ coatings, Ca are observed on the coating, confirming the incorporation of HA into the PEO coating. The elevated P content at the outer region of the $\text{TiO}_2 + \mu\text{HA}$ coating could thus be a combination of phosphate adsorption and HA incorporation [30]. A dramatic reduction in Ca content is observed as the profile continues into the coating, however the P content did not show similar reduction rate. This could be explained by the comparatively larger HA micro- particle size to the pore structure, therefore it cannot penetrate through the structure during the treatment, as a result forming a layer of Ca enriched layer at the surface. This complies with the layer of matrix observed in Figure 84b. The content of P did not appear to reduce at the same rate as Ca, suggesting some HA particles could decompose and react with phosphate ions.

An outer region enriched with Ca and P is also observed in Figure 86c, but Ca could be detected throughout the coating. This suggests HA nano-powder was incorporated throughout the coating. Therefore the use of nano-powder can enhance the incorporation of HA into the PEO coating as it can penetrate through the porous structure.

Zone III is characterised by a large reduction in the O and a small peak in the P profile, which is associated with the inner barrier region of the coating. Previous work has proposed that phosphate anions are attracted to the positive bias, which leads to a P enriched region at the metal/oxide interface [30]. This is particularly noticeable for the TiO₂ coating, which was produced in the PUP mode, where the TiO₂+ μ HA and TiO₂+nHA coating, which were produced using the PBP mode revealed a proportionally lower P content in the inner region. Relatively high P than Ca contents in Zone III in the TiO₂+ μ HA coating could be explained by a comparatively lower HA content at the surface therefore phosphate groups from the electrolyte were incorporated while forming TiO₂ coating matrix. Figure 86c reveals that the profiles of Ca and P in Zone III of the TiO₂+nHA coating altered in a proportional manner, which suggests HA nano-powder reached the inner region of the coating. It can be assumed that during the treatment, negatively charged HA particles would be attracted to the positively biased metal substrate. The small particles would attain a higher charge and have a higher mobility in the electrolyte, therefore they could more readily migrate to the substrate, which complies with the Ca and P peak observed. This further marks the importance of particle size to the particle movement in the electrolyte, which has shown to influence the coating growth. The carbon content increased noticeably in the inner region, indicating similarities in behaviour of carbonate and phosphate anions during PEO process. Zone IV corresponds to the interfacial region which is characterised by an increase in Ti content, and Zone V is referred to the Ti substrate.

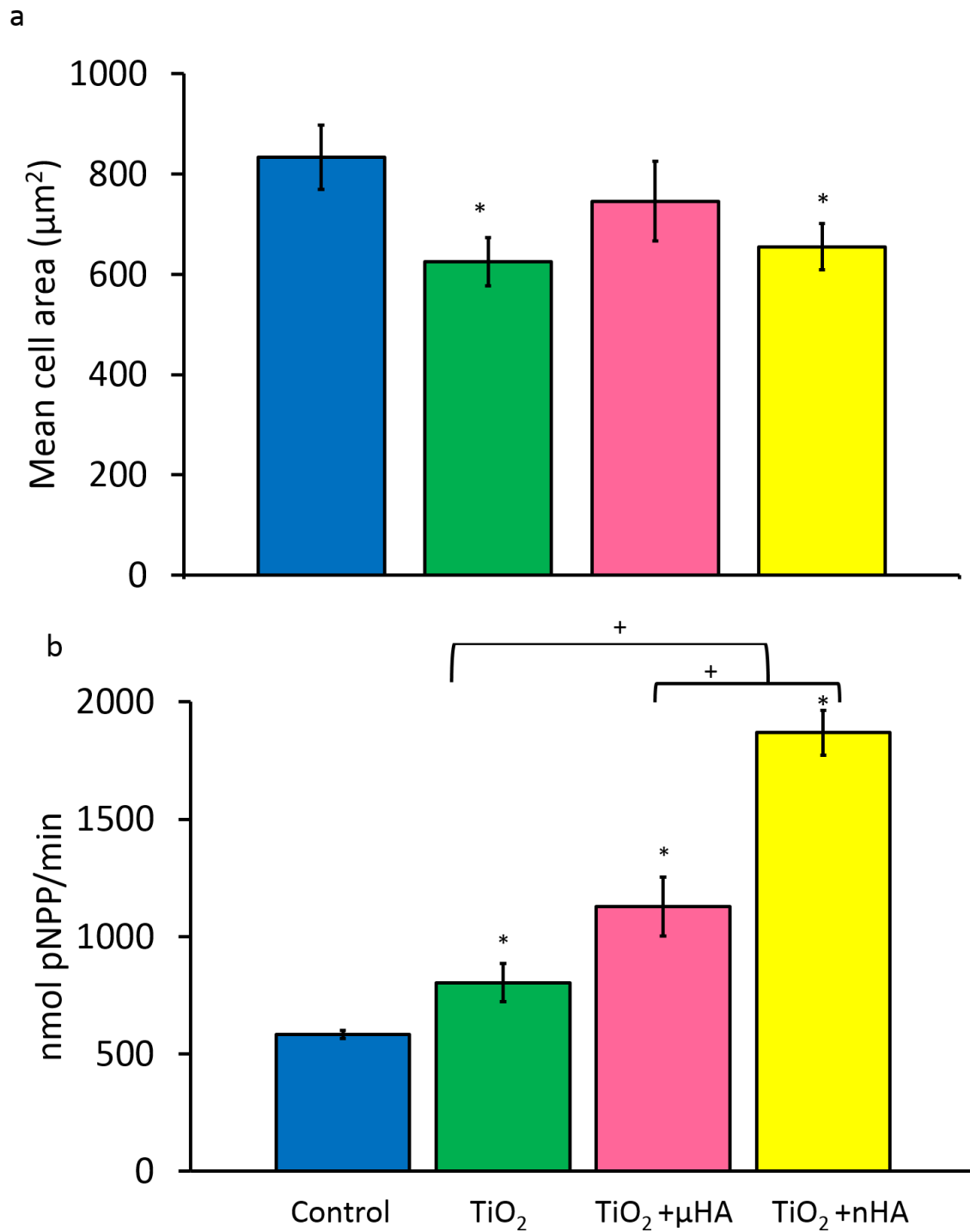


Figure 87 Biocompatibility of coatings (a) Morphometric analysis of MC3T3-E1 cells after 24h in culture on control and PEO coated surfaces. Projected mean cell area from 30 cells on random fields. (b) ALP activity of cells cultured for 14 days on surfaces of TiO₂, TiO₂ + µHA and TiO₂ + nHA. * means comparison with control and shown p<0.05; + means comparison to TiO₂+nHA and shown p<0.05.

Figure 87a reveals the mean projected areas of cells cultivated on the surface of samples after 24h. The cell attachment and spreading behaviour had been proposed to be influenced by the surface features and average roughness [172]. The mean areas of cells on the TiO₂ and TiO₂+nHA coating are significantly lower than that on the control ($p<0.05$), however the latter is not significantly different from that on the TiO₂+ μ HA coating. In this study, the overall average roughness range between all coatings produced was very narrow, therefore it is unlikely to influence the cell spreading. Sjostrom *et al* [153] proposed that nano-pillar features on the surface reduces cell spreading, as the cells may not conform. This complies with Figure 84a and c, the deposits around the discharge channels form a nano-scale network type morphology. Moreover, Minkowski analysis in Figure 84d and f, further shows the similar surface features between the two coatings. At the same time, it is possible that the comparatively smaller pore size would aid the cell spreading on the surface.

ALP is an early marker for osteoblast differentiation and plays a role in mineralization. Figure 87b displays the ALP activity after culturing for 14 days on the surface of the TiO₂, TiO₂+ μ HA and TiO₂+nHA coatings. The ALP activities of cells on the PEO coatings are significantly higher than that on the tissue culture plastic control, indicating PEO coatings are beneficial for osteoblast differentiation. HA had been proposed to enhance expression of cell differentiation markers [173], which could be attributed to the release of calcium [174]. Results in this study also showed similar behaviour. Furthermore, the ALP activity of cells on the TiO₂+nHA coating is significantly higher than those on the TiO₂+ μ HA coating ($p<0.05$), suggesting the use of nano-powder can significantly increase the ALP activity of cells, as the smaller particles are likely to be more readily dissolved from the coating. Moreover, despite the similarity in surface features of TiO₂ and TiO₂+nHA coatings, the ALP activity of cells on the TiO₂+nHA is significantly higher than that on the TiO₂ coating, confirming that ALP activity is highly sensitive to the surface chemistry and is enhanced by HA nano-powder incorporation.

7.5 Conclusion

Coatings containing HA micro- and nano-powders on Ti-6Al-4V substrate were successfully produced without the need for additives using the two-step control PEO mode. Furthermore the influence of electrical parameters, particle size and concentration on the coating characteristics and biological properties was examined. The addition of HA micro-powder to the electrolyte does not influence the overall voltage transient, however due to the large

particle size, it leads to inhomogeneous distribution of electrical current across the surface, resulting in irregular morphological features usually related to higher forming voltages. The use of HA nano-powder in the electrolyte for the PEO treatment has shown positive results. The comparatively smaller particles may be able to migrate more readily towards the surface and penetrate into the coating without altering the porous structure favourable for biological response.

All coatings examined in this study showed good biocompatibility and bioactivity *in vitro*. The ALP activity of the cells on the TiO₂+nHA coating was significantly higher than those on TiO₂ and TiO₂+μHA coatings. This suggests the combination of HA nano-particles on the surface and porous TiO₂ morphology provides a synergic effect on the osteoblastic differentiation.

Chapter 8: Conclusions and future work

8.1 Conclusions

The study has substantially expanded the understanding of electrochemical processes that occur during the PEO treatment of Ti and broadened the range of electrolytes for production of HA containing PEO coatings for orthopaedic and orthodontic implant applications. In particular, the cyclic voltammetry method which had previously been scarcely used in PEO research has shown to be useful to understand the electrochemical behaviour of Ti alloys at the potentials of PEO processing. This approach has been instrumental in development and optimisation of several new electrolyte systems containing sources of Ca and phosphate, both in ionic and nano-particulate form, to produce hybrid CaP-TiO₂ PEO coatings with controllable morphology. Furthermore coatings with comparable biological response to those on tissue culture plastic control have been successfully produced on both cp-Ti and Ti-6Al-4V alloys. Specific findings of this project can be summarised as follows;

1. Characteristic regions corresponding to dissolution of the previously formed passive film, decomposition of carboxylate anions as well as regions of micro-arcing and powerful arcing occurring at high potentials have been identified in voltage-current diagrams of cp-Ti and Ti-6Al-4V anodes in solutions of trisodium orthophosphate with Ca salts of various carboxylic acids. These diagrams have been used to categorise electrolyte systems and determine ranges of electrical parameters favourable for PEO treatments. For the first time, calcium propionate and calcium L-lactate based electrolytes have been proposed and examined extensively for PEO applications.
2. Direct comparison of the electrochemical processes occurring on cp-Ti and Ti-6Al-4V substrate over a wide range of anodic potentials, including the high-voltage domain, which had not been done before, has revealed that the presence of Al in the Ti-6Al-4V substrate causes potential required for micro-arcing to commence to be higher than that on cp-Ti.
3. Minkowski functional approach used extensively to compare quantities describing morphological features of different PEO coatings have shown to provide a sensitive tool analyse morphological features of PEO coatings. These Minkowski functional provide a useful tool to reveal differences in morphological features and additional information when analysing the osteoblastic response of surface morphology

4. Calcium propionate based electrolytes with the Ca/P ratio = 1.67 or 2 have shown to be suitable for production on Ti alloys of porous PEO coatings incorporated with significant amounts of Ca and P. The coatings produced on cp-Ti under pulsed unipolar current conditions possessed a uniform porous structure and introduction of negative biasing enhanced the overall Ca/P ratio on the coating surface. However, instabilities in current response have rendered the PEO processing with a single-step control of electrical parameters not suitable for the present system.
5. The highly reversible electrochemical behaviour of Ti alloys in the calcium L-lactate based electrolytes has also restricted the use of single-step galvanostatic or potentiostatic PEO treatments. The two-step control method was therefore developed to overcome these issues. This method involves application of 250V potentiostatic polarisation to overcome the energy barrier provided by peak II followed by galvanostatic polarisation at a current density lower than those commonly used for PEO treatment. Such treatment has proven capable to improve the process stability for production of PEO coatings on Ti alloys in the electrolytes providing highly reversible behaviour. For the treatments in the calcium L-lactate based solutions, this yielded several significant practical benefits:
 - a. Reduced energy consumption by enabling processing at comparatively lower current densities (below that required to achieve breakdown voltage in the single-step galvanostatic process), alleviating limitations in power supplies and commercial upscaling of the process;
 - b. Refined surface morphology of PEO coatings on cp-Ti substrates, providing more homogenous porous structures compared with those produced by single-step galvanostatic PEO treatments;
 - c. Ensured *in situ* synthesis of crystalline HA within the uniformly porous structure of PEO coatings produced on cp-Ti substrates.
6. A broader significance of the two-step control method has been demonstrated by PEO treatments in electrolytes containing HA micro- and nano- particulate additives. These treatments succeeded in reproducible formation of HA containing TiO₂ coatings on Ti-6Al-4V substrates without the need for organic stabilisers. The nanoparticles exhibited a stronger tendency for migration towards the metal surface and deposition within the porous titania matrix, resulting in formation of PEO coatings with porous morphology and HA nano-particles distributed throughout the coating thickness.

7. *In vitro* testing of the coatings produced on cp-Ti in calcium propionate and L-lactate based electrolytes revealed cell attachments comparable to that on tissue plastic control at 24 h after seeding. It was therefore concluded the coatings produced are biocompatible.
8. Biological examinations of PEO coatings on Ti-6Al-4V alloy produced in electrolytes with HA micro- and nano particle additives have shown good biocompatibility and bioactivity *in vitro*. The cells exhibited a high proliferation rate compared to that on tissue culture plastic control. The cell's ALP activity after 14 days was significantly higher on the Ti + nHA coating than on both TiO₂ and TiO₂+ μ HA coatings. It was concluded the combination of HA nano-particles on the surface with the porous morphology provides a synergic effect on the osteoblastic differentiation.

8.2 Future work

This work is amongst the first to examine various calcium based electrolytes for PEO processing of Ti alloys. It has proven the possibility of using these electrolytes with the novel single-stage PEO process with a two-step control of electrical parameters. The current study has optimised and provided a base understanding of the properties and reactions of these novel electrolytes for PEO processes on Ti alloys and the corresponding *in vitro* biological response. The expansion of this understanding the following aspects would be particularly beneficial;

1. Investigation of the mechanism by which calcium salts of carboxylic acids influence the coating formation mechanism and osteoblastic response. This could include, e.g. *in situ* mass-spectrometry of gaseous products and comparison with TiO₂ PEO coatings of similar structure.
2. Examination of the *in vitro* cell response to the coatings produced with other cell lines including hESMPs at extended incubation times, including further analysis of cell differentiation and function.
3. Detailed investigation of the mechanical properties of these coatings to determinate parameters, such as wear resistance, cohesive and adhesive strengths that are important for load bearing and dental implants.
4. Investigation of the *in vivo* biological response of the coatings produced and their influence to bone responses.

5. Investigation into anionic and/or cationic substitution in the calcium apatite formed by PEO process. This can improve the coatings' resemblance to the biological apatite and enhance biocompatibility.
6. Examination into incorporation of Ag, chitosan and other bactericidal agents into the PEO coatings to produce multifunctional coatings, combining osseointegrative ability with anti-bacterial or anti-microbial activity. These studies may also include optimisation of electrolyte compositions based on the systems developed in this work, investigation of their electrochemical response at high potentials, as well as studies into effects of processing parameters on the coating composition, morphology and biological properties.
7. Expansion of the developed methods of cyclic voltammetry, multistep process control and semi-quantitative morphological analysis to other electrochemical systems, PEO processes and coatings, to evaluate their broader significance and capabilities and limitations.

Reference

1. Van Noort, R., *Introduction to dental materials*. Edinburgh 1994: Mosby.
2. Buckwalter, J.A., *J Bone Joint Surg Am.* 1995;77:1256-1275.
3. Buckwalter, J.A., M.J. Glimcher, R.R. Cooper and R. Recker, *Bone Biology*. 2009: p. 1276-1289.
4. De Groot, K., J.G.C. Wolke and J.A. Jansen, *Calcium phosphate coatings for medical implants*. Proceedings of the Institution of Mechanical Engineers, Part H: Journal of Engineering in Medicine, 1998. **212**(2): p. 137-147.
5. Odekerken, J.C., T.J. Welting, J.J. Arts, G. Walenkamp and P.J. Emans, *Modern orthopaedic implant coatings—their pro's, con's and evaluation methods*. Modern surface engineering treatments. New York: InTech, 2013: p. 45-73.
6. Güntherschulze, A. and H. Betz, *Die Bewegung der Ionengitter von Isolatoren bei extremen elektrischen Feldstärken*. Zeitschrift für Physik. **92**(5): p. 367-374.
7. F, N.G. and W. Mcneill, *Method of making cadmium niobate*, 1958, Google Patents.
8. Yerokhin, A.L., X. Nie, A. Leyland, A. Matthews and S.J. Dowey, *Plasma electrolysis for surface engineering*. Surface and Coatings Technology, 1999. **122**: p. 73-93.
9. Wang, Y., *Plasma electrolytic oxidation treatment of aluminium and titanium alloys*. Surface Engineering of Light Alloys: Aluminium, Magnesium and Titanium Alloys, 2010: p. 110.
10. Hussein, R., X. Nie, D. Northwood, A. Yerokhin and A. Matthews, *Spectroscopic study of electrolytic plasma and discharging behaviour during the plasma electrolytic oxidation (PEO) process*. Journal of Physics D: Applied Physics, 2010. **43**(10): p. 105203.
11. Hussein, R.O., D.O. Northwood and X. Nie, *The effect of processing parameters and substrate composition on the corrosion resistance of plasma electrolytic oxidation (PEO) coated magnesium alloys*. Surface and Coatings Technology, 2013. **237**: p. 357-368.
12. Matykina, E., A. Berkani, P. Skeldon and G.E. Thompson, *Real-time imaging of coating growth during plasma electrolytic oxidation of titanium*. Electrochimica Acta, 2007. **53**(4): p. 1987-1994.
13. Matykina, E., Skeldon, P. and Thompson, G.E., 2007. *Fundamental and practical evaluation of plasma electrolytic oxidation coatings of titanium*. Surface Engineering, **23**(6), pp.412-418.
14. Sul, Y.T., C.B. Johansson, Y. Jeong and T. Albrektsson, *The electrochemical oxide growth behaviour on titanium in acid and alkaline electrolytes*. Medical engineering & physics, 2001. **23**(5): p. 329-46.

15. Yerokhin, A., L. Snizhko, N. Gurevina, A. Leyland, A. Pilkington, and A. Matthews, *Discharge characterization in plasma electrolytic oxidation of aluminium*. Journal of Physics D: Applied Physics, 2003. **36**(17): p. 2110.
16. Matykina, E., A. Berkani, P. Skeldon and G. Thompson, *Real-time imaging of coating growth during plasma electrolytic oxidation of titanium*. Electrochimica Acta, 2007. **53**(4): p. 1987-1994.
17. Diamanti, M. and M. Pedferri, *Effect of anodic oxidation parameters on the titanium oxides formation*. Corrosion Science, 2007. **49**(2): p. 939-948.
18. Neupane, M.P., *Effect of Electrolyte pH on the Structure and in vitro Osteoblasts Response to Anodic Titanium Oxide*. Metals and Materials International, 2008. **14**(5): p. 607-613.
19. Shi, X., *Effects of electrolytic concentration on properties of micro-arc film on Ti6Al4V alloy*. Mining Science and Technology (China), 2009. **19**(2): p. 220-224.
20. Becker, W., P. Hujoel, B.E. Becker and P. Wohrle, *Survival Rates and Bone Level Changes around Porous Oxide-Coated Implants (TiUnite™)*. Clinical implant dentistry and related research, 2013. **15**(5): p. 654-660.
21. Lee, K., H.-C. Choe, B.-H. Kim and Y.-M. Ko, *The biocompatibility of HA thin films deposition on anodized titanium alloys*. Surface and Coatings Technology, 2010. **205**: p. S267-S270.
22. Sul, Y., *The significance of the surface properties of oxidized titanium to the bone response: special emphasis on potential biochemical bonding of oxidized titanium implant*. Biomaterials, 2003. **24**(22): p. 3893-3907.
23. Sul, Y.-T., C.B. Johansson, K. Röser and T. Albrektsson, *Qualitative and quantitative observations of bone tissue reactions to anodised implants*. Biomaterials, 2002. **23**(8): p. 1809-17.
24. Sul, Y.-T., C. Johansson, E. Byon and T. Albrektsson, *The bone response of oxidized bioactive and non-bioactive titanium implants*. Biomaterials, 2005. **26**(33): p. 6720-6730.
25. Sul, Y.-T., C.B. Johansson, S. Petronis, A. Krozer, Y. Jeong, A. Wennerberg, and T. Albrektsson, *Characteristics of the surface oxides on turned and electrochemically oxidized pure titanium implants up to dielectric breakdown:: the oxide thickness, micropore configurations, surface roughness, crystal structure and chemical composition*. Biomaterials, 2002. **23**(2): p. 491-501.
26. Narayanan, R., S.K. Seshadri, T.Y. Kwon and K.H. Kim, *Calcium phosphate-based coatings on titanium and its alloys*. Journal of biomedical materials research. Part B, Applied biomaterials, 2008. **85**(1): p. 279-99.
27. Siebers, M.C., P.J. Ter Brugge, X.F. Walboomers and J.A. Jansen, *Integrins as linker proteins between osteoblasts and bone replacing materials. A critical review*. Biomaterials, 2005. **26**(2): p. 137-46.

28. Anselme, K., *Osteoblast adhesion on biomaterials*. Biomaterials, 2000. **21**(7): p. 667-81.
29. Boyan, B.D., T.W. Hummert, D.D. Dean and Z. Schwartz, *Role of material surfaces in regulating bone and cartilage cell response*. Biomaterials, 1996. **17**(2): p. 137-46.
30. Yeung, W.K., G.C. Reilly, A. Matthews and A. Yerokhin, *In vitro biological response of plasma electrolytically oxidized and plasma-sprayed hydroxyapatite coatings on Ti-6Al-4V alloy*. Journal of Biomedical Materials Research Part B: Applied Biomaterials, 2013. **101B**(6): p. 939-949.
31. Liu, X., P. Chu and C. Ding, *Surface modification of titanium, titanium alloys, and related materials for biomedical applications*. Materials Science and Engineering: R: Reports, 2004. **47**(3-4): p. 49-121.
32. Liang, B., S. Fujibayashi, M. Neo, J. Tamura, H.-M. Kim, M. Uchida, T. Kokubo, and T. Nakamura, *Histological and mechanical investigation of the bone-bonding ability of anodically oxidized titanium in rabbits*. Biomaterials, 2003. **24**(27): p. 4959-4966.
33. Chen, Y., *Plasma Electrolytic Oxidation (PEO) Coatings on a Zirconium Alloy for Improved Wear and Corrosion Resistance Plasma Electrolytic Oxidation (PEO) Coatings*, Electronic Thesis And Dissertation, 2010.
34. Robinson, H.J., A.E. Markaki, C.A. Collier and T.W. Clyne, *Cell adhesion to plasma electrolytic oxidation (PEO) titania coatings, assessed using a centrifuging technique*. Journal of the Mechanical Behavior of Biomedical Materials, 2011. **4**(8): p. 2103-12.
35. Yang, B., *Preparation of bioactive titanium metal via anodic oxidation treatment*. Biomaterials, 2004. **25**(6): p. 1003-1010.
36. Kossenko, A., S. Lugovskoy, B. Kazanski, N. Astashina and A. Lugovskoy, *Investigation of hydroxyapatite on Ti-6Al-4V alloy prepared by plasma electrolytic oxidation*. In Proceedings of the 7th International Conference on Materials Technology, Modelling (MMT-2012), Ariel, Isreal (pp. 295-301).
37. Shozui, T., K. Tsuru, S. Hayakawa, Y. Shirosaki and A. Osaka, *XPS study on potential suppression factors of suppressing in vitro apatite formation on anatase films prepared on various substrates*. Surface and Coatings Technology, 2009. **203**(16): p. 2181-2185.
38. Wei, D., Y. Zhou, D. Jia and Y. Wang, *Biomimetic apatite deposited on microarc oxidized anatase-based ceramic coating*. Ceramics International, 2008. **34**(5): p. 1139-1144.
39. Vallés, G., P. González-Melendi, J.L. González-Carrasco, L. Saldaña, E. Sánchez-Sabaté, L. Munuera, and N. Vilaboa, *Differential inflammatory macrophage response to rutile and titanium particles*. Biomaterials, 2006. **27**(30): p. 5199-211.
40. Han, Y., J. Sun and X. Huang, *Formation mechanism of HA-based coatings by micro-arc oxidation*. Electrochemistry Communications, 2008. **10**(4): p. 510-513.

41. Song, W.-H., Y.-K. Jun, Y. Han and S.-H. Hong, *Biomimetic apatite coatings on micro-arc oxidized titania*. *Biomaterials*, 2004. **25**(17): p. 3341-9.
42. Wu, S.-D., H. Zhang, X.-D. Dong, C.-Y. Ning, A.S.L. Fok, and Y. Wang, *Physicochemical properties and in vitro cytocompatibility of modified titanium surfaces prepared via micro-arc oxidation with different calcium concentrations*. *Applied Surface Science*, 2015. **329**(0): p. 347-355.
43. Aliasghari, S., P. Skeldon and G.E. Thompson, *Plasma electrolytic oxidation of titanium in a phosphate/silicate electrolyte and tribological performance of the coatings*. *Applied Surface Science*, 2014. **316**: p. 463-476.
44. Terleeva, O.P., Y.P. Sharkeev, A.I. Slonova, I.V. Mironov, E.V. Legostaeva, I.A. Khlusov, E. Matykina, P. Skeldon, and G.E. Thompson, *Effect of microplasma modes and electrolyte composition on micro-arc oxidation coatings on titanium for medical applications*. *Surface and Coatings Technology*, 2010. **205**(6): p. 1723-1729.
45. Terleeva, O.P., Y.P. Sharkeev, A.I. Slonova, I.V. Mironov, E.V. Legostaeva, I.A. Khlusov, E. Matykina, P. Skeldon, and G.E. Thompson, *Surface & Coatings Technology Effect of microplasma modes and electrolyte composition on micro-arc oxidation coatings on titanium for medical applications*. *Surface & Coatings Technology*, 2010. **205**(6): p. 1723-1729.
46. Wei, D. and Y. Zhou, *Characteristic and biocompatibility of the TiO₂-based coatings containing amorphous calcium phosphate before and after heat treatment*. *Applied Surface Science*, 2009. **255**(12): p. 6232-6239.
47. Ni, J., Y. Shi, F. Yan, J. Chen and L. Wang, *Preparation of hydroxyapatite-containing titania coating on titanium substrate by micro-arc oxidation*. *Materials Research Bulletin*, 2008. **43**(1): p. 45-53.
48. Kang, B.-S., Y.-T. Sul, S.-J. Oh, H.-J. Lee and T. Albrektsson, *XPS, AES and SEM analysis of recent dental implants*. *Acta Biomaterialia*, 2009. **5**(6): p. 2222-2229.
49. Sun, J., Y. Han and X. Huang, *Hydroxyapatite coatings prepared by micro-arc oxidation in Ca- and P-containing electrolyte*. *Surface and Coatings Technology*, 2007. **201**(9-11): p. 5655-5658.
50. Faghihi-Sani, M.-A., A. Arbabi and A. Mehdinezhad-Roshan, *Crystallization of hydroxyapatite during hydrothermal treatment on amorphous calcium phosphate layer coated by PEO technique*. *Ceramics International*, 2012.
51. Sun, J., Y. Han and X. Huang, *Hydroxyapatite coatings prepared by micro-arc oxidation in Ca- and P-containing electrolyte*. *Surface and Coatings Technology*, 2007. **201**(9-11): p. 5655-5658.
52. Ni, J.-H., Y.-L. Shi, F.-Y. Yan, J.-Z. Chen and L. Wang, *Preparation of hydroxyapatite-containing titania coating on titanium substrate by micro-arc oxidation*. *Materials Research Bulletin*, 2008. **43**(1): p. 45-53.

53. Maïmoun, L., T.C. Brennan, I. Badoud, V. Dubois-Ferriere, R. Rizzoli, and P. Ammann, *Strontium ranelate improves implant osseointegration*. Bone, 2010. **46**(5): p. 1436-41.
54. Marie, P.J., P. Ammann, G. Boivin and C. Rey, *Mechanisms of Action and Therapeutic Potential of Strontium in Bone*. Calcified Tissue International, 2001. **69**(3): p. 121-129.
55. Kung, K.-C., T.-M. Lee and T.-S. Lui, *Bioactivity and corrosion properties of novel coatings containing strontium by micro-arc oxidation*. Journal of Alloys and Compounds, 2010. **508**(2): p. 384-390.
56. Nan, K., T. Wu, J. Chen, S. Jiang, Y. Huang, and G. Pei, *Strontium doped hydroxyapatite film formed by micro-arc oxidation*. Materials Science and Engineering: C, 2009. **29**(5): p. 1554-1558.
57. Chung, C.-J. and H.-Y. Long, *Systematic strontium substitution in hydroxyapatite coatings on titanium via micro-arc treatment and their osteoblast/osteoclast responses*. Acta Biomaterialia, 2011. **7**(11): p. 4081-4087.
58. Nie, X., A. Leyland, A. Matthews, J. Jiang and E. Meletis, *Effects of solution pH and electrical parameters on hydroxyapatite coatings deposited by a plasma-assisted electrophoresis technique*. Journal of Biomedical Materials Research, 2001. **57**(4): p. 612-618.
59. Kim, D.-Y., M. Kim, H.-E. Kim, Y.-H. Koh, H.-W. Kim, and J.-H. Jang, *Formation of hydroxyapatite within porous TiO₂ layer by micro-arc oxidation coupled with electrophoretic deposition*. Acta Biomaterialia, 2009. **5**(6): p. 2196-2205.
60. Lebrette, S., C. Pagnoux and P. Abélard, *Stability of aqueous TiO₂ suspensions: influence of ethanol*. Journal of colloid and interface science, 2004. **280**(2): p. 400-408.
61. Bai, Y., I.S. Park, S.J. Lee, T.S. Bae, W. Duncan, M. Swain, and M.H. Lee, *One-step approach for hydroxyapatite-incorporated TiO₂ coating on titanium via a combined technique of micro-arc oxidation and electrophoretic deposition*. Applied Surface Science, 2011. **257**(15): p. 7010-7018.
62. Shin, K.R., S.I. Yoon, Y.G. Ko and D.H. Shin, *Deposition of hydroxyl-apatite on titanium subjected to electrochemical plasma coating*. Electrochimica Acta, 2013. **109**(0): p. 173-180.
63. Zhitomirsky, I. and A. Petric, *Electrolytic deposition of zirconia and zirconia organoceramic composites*. Materials Letters, 2000. **46**(1): p. 1-6.
64. Besra, L. and M. Liu, *A review on fundamentals and applications of electrophoretic deposition (EPD)*. Progress in Materials Science, 2007. **52**(1): p. 1-61.
65. Corni, I., M.P. Ryan and A.R. Boccaccini, *Electrophoretic deposition: From traditional ceramics to nanotechnology*. Journal of the European Ceramic Society, 2008. **28**: p. 1353-1367.

66. Wei, D., Y. Zhou, D. Jia and Y. Wang, *Chemical treatment of TiO₂-based coatings formed by plasma electrolytic oxidation in electrolyte containing nano-HA, calcium salts and phosphates for biomedical applications*. Applied Surface Science, 2008. **254**(6): p. 1775-1782.
67. Yu, H., S. Chen and P. Cao, *Synergistic bactericidal effects and mechanisms of low intensity ultrasound and antibiotics against bacteria: A review*. Ultrasonics sonochemistry, 2012. **19**(3): p. 377-82.
68. Chen, W., Y. Liu, H. Courtney, M. Bettenga, C. Agrawal, J. Bumgardner, and J. Ong, *In vitro anti-bacterial and biological properties of magnetron co-sputtered silver-containing hydroxyapatite coating*. Biomaterials, 2006. **27**(32): p. 5512-5517.
69. Necula, B.S., L.E. Fratila-Apachitei, A. Berkani, I. Apachitei and J. Duszczak, *Enrichment of anodic MgO layers with Ag nanoparticles for biomedical applications*. Journal of materials science. Materials in medicine, 2009. **20**(1): p. 339-45.
70. Necula, B.S., L.E. Fratila-Apachitei, S.a.J. Zaat, I. Apachitei and J. Duszczak, *In vitro antibacterial activity of porous TiO₂-Ag composite layers against methicillin-resistant Staphylococcus aureus*. Acta Biomaterialia, 2009. **5**(9): p. 3573-80.
71. Venkateswarlu, K., N. Rameshbabu, A.C. Bose, V. Muthupandi, S. Subramanian, D. Mubarakali, and N. Thajuddin, *Fabrication of corrosion resistant, bioactive and antibacterial silver substituted hydroxyapatite/titania composite coating on Cp Ti*. Ceramics International, 2012. **38**(1): p. 731-740.
72. Jovović, J., S. Stojadinović, N.M. Šišović and N. Konjević, *Spectroscopic characterization of plasma during electrolytic oxidation (PEO) of aluminium*. Surface and Coatings Technology, 2011. **206**(1): p. 24-28.
73. Jovović, J., S. Stojadinović, N. Šišović and N. Konjević, *Spectroscopic study of plasma during electrolytic oxidation of magnesium-and aluminium-alloy*. Journal of Quantitative Spectroscopy and Radiative Transfer, 2012. **113**(15): p. 1928-1937.
74. Vermesse, E., C. Mabru and L. Arurault, *Surface integrity after pickling and anodization of Ti-6Al-4V titanium alloy*. Applied Surface Science, 2013. **285**, Part B(0): p. 629-637.
75. Duan, H., C. Yan and F. Wang, *Growth process of plasma electrolytic oxidation films formed on magnesium alloy AZ91D in silicate solution*. Electrochimica Acta, 2007. **52**(15): p. 5002-5009.
76. Ma, Y., X. Nie, D.O. Northwood and H. Hu, *Corrosion and erosion properties of silicate and phosphate coatings on magnesium*. Thin Solid Films, 2004. **469-470**: p. 472-477.
77. Cai, Q., L. Wang, B. Wei and Q. Liu, *Electrochemical performance of microarc oxidation films formed on AZ91D magnesium alloy in silicate and phosphate electrolytes*. Surface and Coatings Technology, 2006. **200**(12-13): p. 3727-3733.
78. Sharma, A., A.J. Mcquillan, L. A Sharma, J. Waddell, Y. Shibata, and W. Duncan, *Spark anodization of titanium-zirconium alloy: surface characterization and*

- bioactivity assessment*. Journal of Materials Science: Materials in Medicine, 2015. **26**(8): p. 1-11.
79. Metikoš-Huković, M., A. Kwokal and J. Piljac, *The influence of niobium and vanadium on passivity of titanium-based implants in physiological solution*. Biomaterials, 2003. **24**(21): p. 3765-3775.
 80. Blackwood, D.J. and L.M. Peter, *The influence of growth rate on the properties of anodic oxide films on titanium*. Electrochimica Acta, 1989. **34**(11): p. 1505-1511.
 81. Sato, N., *A theory for breakdown of anodic oxide films on metals*. Electrochimica Acta, 1971. **16**(10): p. 1683-1692.
 82. Shin, K.R., Y.S. Kim, H.W. Yang, Y.G. Ko and D.H. Shin, *In vitro biological response to the oxide layer in pure titanium formed at different current densities by plasma electrolytic oxidation*. Applied Surface Science, 2014. **314**(0): p. 221-227.
 83. Snizhko, L., A. Yerokhin, N. Gurevina, D. Misnyankin, A. Pilkington, A. Leyland, and A. Matthews, *A model for galvanostatic anodising of Al in alkaline solutions*. Electrochimica Acta, 2005. **50**(27): p. 5458-5464.
 84. Dehnavi, V., B.L. Luan, D.W. Shoesmith, X.Y. Liu and S. Rohani, *Effect of duty cycle and applied current frequency on plasma electrolytic oxidation (PEO) coating growth behavior*. Surface and Coatings Technology, 2013. **226**: p. 100-107.
 85. Sah, S.P., E. Tsuji, Y. Aoki and H. Habazaki, *Cathodic pulse breakdown of anodic films on aluminium in alkaline silicate electrolyte – Understanding the role of cathodic half-cycle in AC plasma electrolytic oxidation*. Corrosion Science, 2012. **55**: p. 90-96.
 86. Arrabal, R., E. Matykina, F. Viejo, P. Skeldon, G.E. Thompson, and M.C. Merino, *AC plasma electrolytic oxidation of magnesium with zirconia nanoparticles*. Applied Surface Science, 2008. **254**(21): p. 6937-6942.
 87. Yerokhin, A., A. Shatrov, V. Samsonov, P. Shashkov, A. Leyland, and A. Matthews, *Fatigue properties of Keronite® coatings on a magnesium alloy*. Surface and Coatings Technology, 2004. **182**(1): p. 78-84.
 88. Sun, C., R. Hui, W. Qu, S. Yick, C. Sun, and W. Qian, *Effects of processing parameters on microstructures of TiO₂ coatings formed on titanium by plasma electrolytic oxidation*. Journal of Materials Science Letters', 2010. **45**(22): p. 6235-6241.
 89. Kim, K., A. Yeatts, D. Dean and J.P. Fisher, *Stereolithographic bone scaffold design parameters: osteogenic differentiation and signal expression*. Tissue Engineering Part B: Reviews, 2010. **16**(5): p. 523-539.
 90. Shin, K.R., Y.G. Ko and D.H. Shin, *Effect of electrolyte on surface properties of pure titanium coated by plasma electrolytic oxidation*. Journal of Alloys and Compounds, 2011. **509**: p. S478-S481.

91. Teixeira, L.N., G.E. Crippa, L.P. Lefebvre, P.T. De Oliveira, A.L. Rosa, and M.M. Beloti, *The influence of pore size on osteoblast phenotype expression in cultures grown on porous titanium*. International Journal of Oral and Maxillofacial Surgery, 2012. **41**(9): p. 1097-1101.
92. Gao, Y., A. Yerokhin, E. Parfenov and A. Matthews, *Application of Voltage Pulse Transient Analysis during Plasma Electrolytic Oxidation for Assessment of Characteristics and Corrosion Behaviour of Ca- and P-containing Coatings on Magnesium*. Electrochimica Acta, 2014. **149**(0): p. 218-230.
93. Mannelquist, A., N. Almqvist and S. Fredriksson, *Influence of tip geometry on fractal analysis of atomic force microscopy images*. Applied Physics A: Materials Science & Processing, 1998. **66**: p. S891-S895.
94. Rožić, L., S. Petrović, N. Radić, S. Stojadinović, R. Vasilić, P. Stefanov, and B. Grbić, *Fractal approach to surface roughness of TiO₂/WO₃ coatings formed by plasma electrolytic oxidation process*. Thin Solid Films, 2013. **539**: p. 112-116.
95. Jiang, C., R. Pitt, J. Bertram and D. Aneshansley, *Fractal-based image texture analysis of trabecular bone architecture*. Medical & biological engineering & computing, 1999. **37**(4): p. 413-418.
96. Medina, W., O. Skurtys and J.M. Aguilera, *Study on image analysis application for identification Quinoa seeds (Chenopodium quinoa Willd) geographical provenance*. LWT - Food Science and Technology, 2010. **43**(2): p. 238-246.
97. Smith Jr, T.G., G.D. Lange and W.B. Marks, *Fractal methods and results in cellular morphology — dimensions, lacunarity and multifractals*. Journal of Neuroscience Methods, 1996. **69**(2): p. 123-136.
98. Salerno, M. and M. Banzato, *Minkowski measures for image analysis in scanning probe microscopy*. Microscopy and Analysis, 2005. **19**(13-15): p. 18-28.
99. Sittichokechaiwut, A., A.M. Scutt, A.J. Ryan, L.F. Bonewald and G.C. Reilly, *Use of rapidly mineralising osteoblasts and short periods of mechanical loading to accelerate matrix maturation in 3D scaffolds*. Bone, 2009. **44**(5): p. 822-9.
100. Huang, Y., Y. Wang, C. Ning, K. Nan and Y. Han, *Hydroxyapatite coatings produced on commercially pure titanium by micro-arc oxidation*. Biomedical materials (Bristol, England), 2007. **2**(3): p. 196-201.
101. Tetteh, G., A. Khan, R. Delaine-Smith, G. Reilly and I. Rehman, *Electrospun polyurethane/hydroxyapatite bioactive Scaffolds for bone tissue engineering: The role of solvent and hydroxyapatite particles*. Journal of the Mechanical Behavior of Biomedical Materials, 2014. **39**: p. 95-110.
102. Altaweel, M.M., R.P. Hanzlik, J.N. Ver Hoeve, J. Eells and B. Zhang, *Ocular and systemic safety evaluation of calcium formate as a dietary supplement*. Journal of Ocular Pharmacology and Therapeutics, 2009. **25**(3): p. 223-230.
103. Pohl, S.A., D.J. Caldwell, J.T. Lee, J.R. Coppedge, S.L. Dunn-Horrocks, K.D. Stringfellow, K. Jessen, and M.B. Farnell, *Effects of dietary calcium formate*

- inclusion on broiler performance, skeletal development, and gut maturation.* The Journal of Applied Poultry Research, 2012. **21**(2): p. 311-317.
104. Vavrusova, M., M.B. Munk and L.H. Skibsted, *Aqueous Solubility of Calcium l-Lactate, Calcium d-Gluconate, and Calcium d-Lactobionate: Importance of Complex Formation for Solubility Increase by Hydroxycarboxylate Mixtures.* Journal of Agricultural and Food Chemistry, 2013. **61**(34): p. 8207-8214.
 105. Magalhães, A.C., T.D.A. Furlani, F.D.M. Italiani, F.G. Iano, A.C.B. Delbem, and M.a.R. Buzalaf, *Effect of calcium pre-rinse and fluoride dentifrice on remineralisation of artificially demineralised enamel and on the composition of the dental biofilm formed in situ.* Archives of Oral Biology, 2007. **52**(12): p. 1155-1160.
 106. Liang, C.J., 2013. *In-situ impedance spectroscopy studies of the plasma electrolytic oxidation coating process* (Doctoral dissertation, University of Sheffield).
 107. Sul, Y.-T., E. Byon and A. Wennerberg, *Surface characteristics of electrochemically oxidized implants and acid-etched implants: surface chemistry, morphology, pore configurations, oxide thickness, crystal structure, and roughness.* The International journal of oral & maxillofacial implants, 2007. **23**(4): p. 631-40.
 108. Heyd, D.V. and D.A. Harrington, *Platinum oxide growth kinetics for cyclic voltammetry.* Journal of Electroanalytical Chemistry, 1992. **335**(1–2): p. 19-31.
 109. Liu, B., S. Zheng, S. Wang, Y. Zhang, A. Ortega, N.S. Kim, K. Han, and H. Du, *The redox behavior of vanadium in alkaline solutions by cyclic voltammetry method.* Electrochimica Acta, 2012. **76**(0): p. 262-269.
 110. Makhotkina, O. and P.A. Kilmartin, *The use of cyclic voltammetry for wine analysis: Determination of polyphenols and free sulfur dioxide.* Analytica Chimica Acta, 2010. **668**(2): p. 155-165.
 111. Laurencin, D., N. Almora-Barrios, N.H. De Leeuw, C. Gervais, C. Bonhomme, F. Mauri, W. Chrzanowski, J.C. Knowles, R.J. Newport, A. Wong, Z. Gan, and M.E. Smith, *Magnesium incorporation into hydroxyapatite.* Biomaterials, 2011. **32**(7): p. 1826-37.
 112. Warczak, M., M. Pisarek and A. Sadkowski, *Instability of the anodic oxide layer on Ti as manifest by an anodic peak on the negatively directed branch of the cyclic voltammetry plot.* Corrosion Science, 2014. **89**(0): p. 6-12.
 113. Habazaki, H., M. Uozumi, H. Konno, K. Shimizu, P. Skeldon, and G.E. Thompson, *Crystallization of anodic titania on titanium and its alloys.* Corrosion Science, 2003. **45**(9): p. 2063-2073.
 114. Teh, T.H., A. Berkani, S. Mato, P. Skeldon, G.E. Thompson, H. Habazaki, and K. Shimizu, *Initial stages of plasma electrolytic oxidation of titanium.* Corrosion Science, 2003. **45**(12): p. 2757-2768.
 115. Matykina, E., R. Arrabal, P. Skeldon, G. Thompson and H. Habazaki, *Influence of grain orientation on oxygen generation in anodic titania.* Thin Solid Films, 2008. **516**(8): p. 2296-2305.

116. Pringle, J.P.S., *The anodic oxidation of superimposed niobium and tantalum layers: theory*. *Electrochimica Acta*, 1980. **25**(11): p. 1403-1421.
117. Santos, C.M.M., M.B.Q. Garcia, A.M.S. Silva, R. Santus, P. Morlière, and E. Fernandes, *Electrochemical characterization of bioactive hydroxyxanthenes by cyclic voltammetry*. *Tetrahedron Letters*, 2013. **54**(1): p. 85-90.
118. Hanaor, D.H. and C. Sorrell, *Review of the anatase to rutile phase transformation*. *Journal of Materials Science*, 2011. **46**(4): p. 855-874.
119. Soares, T.A., H. Mozaffari and H. Reinecke, *Generation of microstructures on a Ti–6Al–4V substrate through anodization*. *Surface and Coatings Technology*, 2015. **278**: p. 64-70.
120. Moon, S. and Y. Jeong, *Generation mechanism of microdischarges during plasma electrolytic oxidation of Al in aqueous solutions*. *Corrosion Science*, 2009. **51**(7): p. 1506-1512.
121. Xue, W., C. Wang, R. Chen and Z. Deng, *Structure and properties characterization of ceramic coatings produced on Ti–6Al–4V alloy by microarc oxidation in aluminate solution*. *Materials Letters*, 2002. **52**(6): p. 435-441.
122. Grozovski, V., V. Climent, E. Herrero and J.M. Feliu, *Intrinsic activity and poisoning rate for HCOOH oxidation on platinum stepped surfaces*. *Physical Chemistry Chemical Physics*, 2010. **12**(31): p. 8822-8831.
123. Lu, G.-Q., A. Crown and A. Wieckowski, *Formic Acid Decomposition on Polycrystalline Platinum and Palladized Platinum Electrodes*. *The Journal of Physical Chemistry B*, 1999. **103**(44): p. 9700-9711.
124. Zhao, H., Y. Wang, Q. Tang, L. Wang, H. Zhang, C. Quan, and T. Qi, *Pt catalyst supported on titanium suboxide for formic acid electrooxidation reaction*. *International Journal of Hydrogen Energy*, 2014. **39**(18): p. 9621-9627.
125. Cai, W., J. Li, Y. Jiang, C. Liu, L. Ma, and W. Xing, *Formic acid electro-catalytic oxidation at high temperature in supporting electrolyte free system: Mechanism study and catalyst stability*. *Journal of Electroanalytical Chemistry*, 2016. **761**: p. 68-73.
126. Gottlieb, M., *Anodic oxidation of formic acid at platinum electrodes*. *Journal of The Electrochemical Society*, 1964. **111**(4): p. 465-472.
127. Breiter, M.W., *Anodic oxidation of formic acid on platinum—II. Interpretation of potentiostatic current/potential curves. Reaction mechanism in perchloric acid solutions*. *Electrochimica Acta*, 1963. **8**(6): p. 457-470.
128. Giner, J., *The anodic oxidation of methanol and formic acid and the reductive Adsorption of CO₂*. *Electrochimica Acta*, 1964. **9**(1): p. 63-77.
129. Kolbe, H., *Untersuchungen über die Elektrolyse organischer Verbindungen*. *Justus Liebigs Annalen der Chemie*, 1849. **69**(3): p. 257-294.

130. Vassiliev, Y.B. and V.A. Grinberg, *Adsorption kinetics of electrode processes and the mechanism of Kolbe electrosynthesis*. Journal of Electroanalytical Chemistry and Interfacial Electrochemistry, 1991. **308**(1): p. 1-16.
131. Impey, N.R.M., *The anodic oxidation of calcium lactate : an estimation of the products of electrolysis and an investigation into some of the problems involved* 1950: Rhodes University.
132. Abbona, F., H.E.L. Madsen and R. Boistelle, *The initial phases of calcium and magnesium phosphates precipitated from solutions of high to medium concentrations*. Journal of Crystal Growth, 1986. **74**(3): p. 581-590.
133. Oliveira, C., P. Georgieva, F. Rocha, A. Ferreira and S.F. De Azevedo, *Dynamical model of brushite precipitation*. Journal of Crystal Growth, 2007. **305**(1): p. 201-210.
134. Eliaz, N., *Electrocrystallization of Calcium Phosphates*. Israel Journal of Chemistry, 2008. **48**(3-4): p. 159-168.
135. Eliaz, N. and T. Sridhar, *Electrocrystallization of hydroxyapatite and its dependence on solution conditions*. Crystal Growth and Design, 2008. **8**(11): p. 3965-3977.
136. Bucur, R.V., *Structure of the Voltammograms of the Platinum-Black Electrodes: Derivative Voltammetry and Data Fitting Analysis*. Electrochimica Acta, 2014. **129**(0): p. 76-84.
137. Freund, M.S. and A. Brajter-Toth, *Semiintegral analysis in cyclic voltammetry: determination of surface excess and concentration in presence of weak adsorption and thin films*. The Journal of Physical Chemistry, 1992. **96**(23): p. 9400-9406.
138. Yakovleva, K.E., S.A. Kurzeev, E.V. Stepanova, T.V. Fedorova, B.A. Kuznetsov, and O.V. Koroleva, *Characterization of plant phenolic compounds by cyclic voltammetry*. Applied Biochemistry and Microbiology, 2007. **43**(6): p. 661-668.
139. Sokolová, R., Š. Ramešová, I. Degano, M. Hromadová, M. Gál, and J. Žabka, *The oxidation of natural flavonoid quercetin*. Chemical Communications, 2012. **48**(28): p. 3433-3435.
140. Ikonopisov, S., *Theory of electrical breakdown during formation of barrier anodic films*. Electrochimica Acta, 1977. **22**(10): p. 1077-1082.
141. Moseke, C. and U. Gbureck, *Tetracalcium phosphate: Synthesis, properties and biomedical applications*. Acta Biomaterialia, 2010. **6**(10): p. 3815-3823.
142. Durdu, S., Ö.F. Deniz, I. Kutbay and M. Usta, *Characterization and formation of hydroxyapatite on Ti6Al4V coated by plasma electrolytic oxidation*. Journal of Alloys and Compounds, 2013. **551**(0): p. 422-429.
143. Khan, R., A.L. Yerokhin and A. Matthews, *Structural characteristics and residual stresses in oxide films produced on Ti by pulsed unipolar plasma electrolytic oxidation*. Philos. Mag., 2008. **88**(6): p. 795-807.

144. Mecke, K., *Morphological characterization of patterns in reaction-diffusion systems*. Physical Review E, 1996. **53**(5): p. 4794.
145. Dzhurinskiy, D., Y. Gao, W.K. Yeung, E. Strumban, V. Leshchinsky, P.J. Chu, A. Matthews, A. Yerokhin, and R.G. Maev, *Characterization and corrosion evaluation of TiO₂:n-HA coatings on titanium alloy formed by plasma electrolytic oxidation*. Surface and Coatings Technology, (0).
146. Jin, F., P.K. Chu, G. Xu, J. Zhao, D. Tang, and H. Tong, *Structure and mechanical properties of magnesium alloy treated by micro-arc discharge oxidation using direct current and high-frequency bipolar pulsing modes*. Materials Science and Engineering: A, 2006. **435-436**: p. 123-126.
147. Yerokhin, A., A. Shatrov, V. Samsonov, P. Shashkov, A. Pilkington, A. Leyland, and A. Matthews, *Oxide ceramic coatings on aluminium alloys produced by a pulsed bipolar plasma electrolytic oxidation process*. Surface and Coatings Technology, 2005. **199**(2-3): p. 150-157.
148. Cabrini, M., F. Fontana, S. Lorenzi, T. Pastore and S. Pellegrini, *Effect of Organic Inhibitors on Chloride Corrosion of Steel Rebars in Alkaline Pore Solution*. Journal of Chemistry, 2015. **2015**: p. 10.
149. Valcarce, M.B. and M. Vázquez, *Carbon steel passivity examined in alkaline solutions: The effect of chloride and nitrite ions*. Electrochimica Acta, 2008. **53**(15): p. 5007-5015.
150. Zhai, Z., X. Li, C. Tang, J. Peng, N. Jiang, W. Bai, H. Gao, and Y. Liao, *Decarbonylation of Lactic Acid to Acetaldehyde over Aluminum Sulfate Catalyst*. Industrial & Engineering Chemistry Research, 2014. **53**(25): p. 10318-10327.
151. Fan, Y., C. Zhou and X. Zhu, *Selective catalysis of lactic acid to produce commodity chemicals*. Catalysis Reviews, 2009. **51**(3): p. 293-324.
152. Matykina, E., R. Arrabal, P. Skeldon, G.E. Thompson, P. Wang, and P. Wood, *Plasma electrolytic oxidation of a zirconium alloy under AC conditions*. Surface and Coatings Technology, 2010. **204**(14): p. 2142-2151.
153. Sjöström, T., G. Lalev, J.P. Mansell and B. Su, *Initial attachment and spreading of MG63 cells on nanopatterned titanium surfaces via through-mask anodization*. Applied Surface Science, 2011. **257**(10): p. 4552-4558.
154. Chu, C.L., Z.H. Liu, X. Rao, Q. Sun, P.H. Lin, F. Chen, and P.K. Chu, *Micro-nano hierarchical porous titania modified with ZnO nanorods for biomedical applications*. Surface and Coatings Technology, 2013. **232**: p. 68-74.
155. Khan, R.H.U., A. Yerokhin, X. Li, H. Dong and A. Matthews, *Surface characterisation of DC plasma electrolytic oxidation treated 6082 aluminium alloy: Effect of current density and electrolyte concentration*. Surface and Coatings Technology, 2010. **205**(6): p. 1679-1688.

156. Dean, J.S., J.H. Harding and D.C. Sinclair, *Simulation of Impedance Spectra for a Full Three-Dimensional Ceramic Microstructure Using a Finite Element Model*. Journal of the American Ceramic Society, 2014. **97**(3): p. 885-891.
157. Heath, J.P., J.S. Dean, J.H. Harding and D.C. Sinclair, *Simulation of Impedance Spectra for Core-Shell Grain Structures Using Finite Element Modeling*. Journal of the American Ceramic Society, 2015: p. 98: 1925-1931
158. Gittings, J.P., C.R. Bowen, A.C.E. Dent, I.G. Turner, F.R. Baxter, and J.B. Chaudhuri, *Electrical characterization of hydroxyapatite-based bioceramics*. Acta Biomaterialia, 2009. **5**(2): p. 743-54.
159. Gittings, J.P., C.R. Bowen, I.G. Turner, A.C.E. Dent, F.R. Baxter, and J.B. Chaudhuri, *Dielectric Properties of Hydroxyapatite Based Ceramics*. Structure, 2008: p. 2-5.
160. Sun, C., R. Hui, W. Qu, S. Yick, C. Sun, and W. Qian, *Effects of processing parameters on microstructures of TiO₂ coatings formed on titanium by plasma electrolytic oxidation*. Journal of Materials Science, 2010. **45**(22): p. 6235-6241.
161. Cai, Y., Y. Liu, W. Yan, Q. Hu, J. Tao, M. Zhang, Z. Shi, and R. Tang, *Role of hydroxyapatite nanoparticle size in bone cell proliferation*. Journal of Materials Chemistry, 2007. **17**(36): p. 3780-3787.
162. Catros, S., F. Guillemot, E. Lebraud, C. Chanseau, S. Perez, R. Bareille, J. Amédée, and J.C. Fricain, *Physico-chemical and biological properties of a nano-hydroxyapatite powder synthesized at room temperature*. Irbm, 2010. **31**(4): p. 226-233.
163. Chen, Y.M., T.F. Xi, Y.P. Lv and Y.D. Zheng, *In vitro biological performance of nano-particles on the surface of hydroxyapatite coatings*. Applied Surface Science, 2008. **255**(2): p. 375-378.
164. Dey, A., A.K. Mukhopadhyay, S. Gangadharan, M.K. Sinha, D. Basu, and N.R. Bandyopadhyay, *Nanoindentation study of microplasma sprayed hydroxyapatite coating*. Ceramics International, 2009. **35**(6): p. 2295-2304.
165. Shi, Z., X. Huang, Y. Cai, R. Tang and D. Yang, *Size effect of hydroxyapatite nanoparticles on proliferation and apoptosis of osteoblast-like cells*. Acta Biomaterialia, 2009. **5**(1): p. 338-345.
166. Xu, J.L., K.A. Khor, J.J. Sui, J.H. Zhang and W.N. Chen, *Protein expression profiles in osteoblasts in response to differentially shaped hydroxyapatite nanoparticles*. Biomaterials, 2009. **30**(29): p. 5385-5391.
167. Bai, Y., K.-A. Kim, I.S. Park, S.J. Lee, T.S. Bae, and M.H. Lee, *In situ composite coating of titania-hydroxyapatite on titanium substrate by micro-arc oxidation coupled with electrophoretic deposition processing*. Materials Science and Engineering: B, 2011. **176**(15): p. 1213-1221.
168. Prakash, K.H., R. Kumar, C.P. Ooi, P. Cheang and K.A. Khor, *Apparent solubility of hydroxyapatite in aqueous medium and its influence on the morphology of*

- nanocrystallites with precipitation temperature*. Langmuir : the ACS journal of surfaces and colloids, 2006. **22**(26): p. 11002.
169. Le Guéhennec, L., A. Soueidan, P. Layrolle and Y. Amouriq, *Surface treatments of titanium dental implants for rapid osseointegration*. Dental materials : official publication of the Academy of Dental Materials, 2007. **23**(7): p. 844-54.
170. Kiryukhantsev-Korneev, P.V., *Elemental analysis of coatings by high-frequency glow discharge optical emission spectroscopy*. Protection of Metals and Physical Chemistry of Surfaces, 2012. **48**(5): p. 585-590.
171. Kiryukhantsev-Korneev, F., *Possibilities of glow discharge optical emission spectroscopy in the investigation of coatings*. Russian Journal of Non-Ferrous Metals, 2014. **55**(5): p. 494-504.
172. Osathanon, T., K. Bepinyowong, M. Arksornnukit, H. Takahashi and P. Pavasant, *Human osteoblast-like cell spreading and proliferation on Ti-6Al-7Nb surfaces of varying roughness*. Journal of oral science, 2011. **53**(1): p. 23.
173. Beck, G.R., *Inorganic phosphate as a signaling molecule in osteoblast differentiation*. Journal of cellular biochemistry, 2003. **90**(2): p. 234-243.
174. Aniket, R. Reid, B. Hall, I. Marriott and A. El-Ghannam, *Early osteoblast responses to orthopedic implants: Synergy of surface roughness and chemistry of bioactive ceramic coating*. Journal of Biomedical Materials Research Part A, 2015: p. 103:1961–1973